OÉ Gaillimh
NUI Galway

AN EXPERIMENTAL AND COMPUTATIONAL INVESTIGATION OF THE HIGH TEMPERATURE BEHAVIOUR OF MARBN STEEL WITH APPLICATION TO EFFECTS OF MANUFACTURING

Eimear M. O'Hara B.E. (2014)

Academic Supervisors: Prof. Sean Leen, Dr Richard Barrett and Dr Noel Harrison

Industrial Supervisors: Mr. Rod Vanstone, Mr. Bartosz Polomski and Dr. Steve Osgerby

A thesis submitted to the National University of Ireland Galway

as fulfilment of the requirements for the degree of Doctor of Philosophy

Mechanical Engineering

National University of Ireland Galway

October 2018

ABSTRACT

The key step for next generation power plants is the development of advanced materials capable of achieving high flexibility and efficiency at increased steam temperatures and pressures. Such operating conditions will cause increased fatigue and creep degradation of plant components, where a key limitation of operating under such conditions is the capability of the current generation of materials. Consequently, multi-scale characterisation via experimental and computational methods is necessary to both characterise and predict next generation material behaviour under flexible plant operating conditions at increased temperatures. Attention is focussed here on MarBN, a new precipitate-strengthened 9-12Cr martensitic steel, with improved strength and microstructure stabilisation under long-term loading via increased tungsten solute strengthening and boron enriched grain boundary precipitates.

High temperature low cycle fatigue, creep-fatigue, oxidation and corrosion testing is performed on cast MarBN, and compared to both a forged equivalent, and current state-of-the-art material, P91. Microstructural analysis allows identification of micro- and nano-scale strengthening and degradation mechanisms, as a result of high temperature exposure. Quantification of the shapes and volume fractions of defects in cast and forged MarBN, before and after high temperature low cycle fatigue testing, is performed via 3D X-ray micro-computed tomography. Based on these experimental methods, uniaxial and multi-axial life prediction and damage models, in conjunction with a unified cyclic viscoplastic material model, are developed and applied to cast MarBN at 600 °C and 650 °C.

3D X-ray micro-computed tomography, in conjunction with microstructural analysis, has identified manufacturing defects, in both cast and forged MarBN, as a primary source of fatigue crack initiation. Both idealised (spherical) and measured (complex) defects, acting as regions of localised stress and strain accumulation, are predicted to cause fatigue crack initiation at less than 12% of total fatigue life in all cases. However, forging is found to significantly reduce the volume fraction and complexity of manufacturing defects, compared to the cast material, and as a result, increases fatigue life by approximately double.

ACKNOWLEDGEMENTS

Firstly I would like to thank my supervisors; Sean for always challenging me, Richard for allowing me to build on the work of his PhD, and Noel for support and guidance (and chats about Mayo football). To the IRC and GE Power for providing funding for the research, and advice from Bart, Steve, Rod and the IMPEL Consortium.

The technical staff, William, Pat and Boni, for many test samples, guidance with the INSTRON and technical difficulties. To Eadaoin Timmins and Emma McDermott for direction on microscopy related matters. Thanks also to Dr. Barry O'Brien for advice on microstructural analysis, and Dr. Conor O'Hagan for many top tips on oxidation and corrosion.

To my friends Ed, Hollie, Laura, Lizanne, Maud, Myles, Orla and Sarah, and those in the wider PhD group, as well as members of the 10:30 tea group.

In particular, I would like to thank:
Ciara, for *many* hours drinking tea and going for walks
Eóin, for always being there to chat to and (reluctantly) go for pints
Eoin and Judy, for endless hours of MasterChef, Grand Designs and chats
Emily, for her constant support, particularly encouragement with my literature review

My parents and Granny, for their constant support throughout my Masters/PhD, particularly with an endless supply of teabags.

Finally, to Brían, for supporting, encouraging and putting up with me. I would not have been able to get through this without you.

NOMENCLATURE

A_{eq}	Area of sphere with equivalent volume to defect
A_{defect}	Area of defect
b_i	Isotropic softening rate
c	Coffin-Manson fatigue ductility exponent
C	Ostergren life prediction parameter
C_i	Kinematic hardening modulus
D	Damage
E	Young's modulus
G	Shear modulus
k	Initial yield stress
N	Cycle number
N_f	Number of cycles to failure
n_{pre}	Number of defects pre-test
n_{post}	Number of defects post-test
p	Accumulated effective plastic strain
$\dot{p}$	Accumulated effective plastic strain-rate
Q_i	Saturated isotropic softening stress
R	Isotropic softening
S	Sphericity
$\mathbf{s}$	Deviatoric stress tensor
t	Time

V_{pre}	Volume fraction of defect pre-test
V_{post}	Volume fraction of defect post-test
α	Viscoplastic material parameter
β	Viscoplastic material parameter
γ_i	Kinematic hardening recall parameter
δ	Ostergren life prediction parameter
Δ	Difference
Δ_{area}	Change in area
Δ_{volume}	Change in volume
$\Delta\varepsilon$	Strain-range
$\Delta\varepsilon_{pl}$	Plastic strain-range
$\dot{\varepsilon}$	Strain-rate
$\dot{\varepsilon}^{pl}$	Plastic strain-rate
$\varepsilon_f^{'}$	Coffin-Manson fatigue ductility coefficient
ε_f	Uniaxial failure strain
ε_f^{*}	Multiaxial failure strain
ν	Poisson's ratio
σ	Stress
$\tilde{\sigma}$	Effective stress
σ_{eq}	von Mises equivalent stress
σ_m	Hydrostatic stress

σ_v	Viscous stress
ϕ_i	Chaboche damage material parameter
χ	Kinematic hardening

LIST OF PUBLICATIONS

JOURNAL PUBLICATIONS

Chapter 3 and Chapter 6: O'Hara, E.M., Harrison, N.M., Polomski, B.K., Barrett, R.A., Leen, S.B. The effect of inclusions on the high-temperature low-cycle fatigue performance of cast MarBN: Experimental characterisation and computational modelling. Fatigue & Fracture of Engineering Materials & Structures (2018). DOI: https://doi.org/10.1111/ffe.12864.

Chapter 3 and Chapter 5: O'Hara, E.M., Harrison, N.M., Polomski, B.K., Barrett, R.A., Leen, S.B. Fatigue damage characterisation of MarBN steel for high temperature flexible operating conditions. Proceedings of the Institution of Mechanical Engineers, Part L: Journal of Materials: Design and Applications, 231 (2017) 23-37. DOI: https://doi.org/10.1177/1464420716667759.

Chapter 3 and Chapter 5: Barrett, R.A., O'Hara, E.M., Harrison, N.M., Polomski, B.K., Leen, S.B. High-temperature low-cycle fatigue behavior of MarBN at 600 °C. Journal of Pressure Vessel Technology 138, no. 4 (2016): 041401. DOI: https://doi.org/10.1115/1.4031724

INTERNATIONAL CONFERENCE PROCEEDINGS

Chapter 3 and Chapter 6: O'Hara, E.M., Harrison, N.M., Polomski, B.K., Barrett, R.A., Leen, S.B. Effect of Voids and Inclusions on the High Temperature Localised Cyclic Behaviour of a Next Generation Power Plant Material. *Engineering Integrity Society Fatigue 2017 Conference,* July 3rd to July 5th 2017, Cambridge, UK.

Chapter 3 and Chapter 5: O'Hara, E.M., Harrison, N.M., Polomski, B.K., Barrett, R.A., Leen, S.B. Fatigue damage characterisation of nano-strengthened 9Cr steels under high temperature flexible operating conditions. *1st International Conference on Materials Design and Applications,* June 30th to July 1st 2016, Porto, Portugal.

Chapter 3 and Chapter 5: Barrett, R.A., O'Hara, E.M., Harrison, N.M., Polomski, B.K., Leen, S.B. High-temperature low-cycle fatigue behavior of MarBN at 600 °C. *ASME 2015 Pressure Vessels and Piping Conference*, July 19th to July 23rd 2015, Boston, USA.

TABLE OF CONTENTS

1 INTRODUCTION

1.1 General

The highly variable nature of renewable energy sources presents a substantial challenge in the transition of current generation, base-load power plants to highly flexible operating conditions. The EU has committed to a reduction in greenhouse gas emissions by 80% to 95% by 2050, meaning renewable energy sources will produce over 65% of electricity. Significant investments in energy systems (e.g. power plants, grid and insulation materials) are required, with particular emphasis on the research and development of advanced and innovative technologies to reduce emissions and increase efficiency. Decarbonisation of the transport industry will place further pressure on the electricity sector and require increased investment in power generation. This in turn impacts household expenditure, where the cost of energy is predicted to rise by approximately 16% until 2030, and places greater focus on the level of investment required in efficient vehicles, appliances and insulation. In particular, renewable technologies can provide the greatest benefits in terms of reduced energy costs and emissions. However, power plants are still required in the absence of a suitable storage technology and infrastructure that is more efficient than current generation methods (e.g. gas). Decarbonisation will also depend heavily on biomass for heat, transport and electricity production. As a result, gas is likely to remain a critical energy production method past 2050, as an alternative to coal and oil, operating under flexible loading conditions in conjunction with renewable sources [1].

Power plant cycling is defined as a change in the electric load levels (e.g. plant start-up, shut-down and load fluctuation) based on system load requirements. This causes

significant thermal and stress loading of components, leading to increased microstructural damage. Creep-fatigue has been identified as a major contributor to reduced component lifetime, increasing plant costs and outage rates [2]. European energy production from renewables is rising rapidly and prioritised when fed into the grid; however, their variable nature means alternative methods are still required to ensure demand is met. The power generation market and plant operators are now facing greater demand for more flexible operation of plant to provide compensation during times of high demand and fluctuating renewable energy sources. Improved technology and sophisticated operating procedures (e.g. overnight shut-down) allow increased flexibility and contribute to reduced costs in such areas [3].

Microstructural degradation of power plant components, as a result of severe operating conditions, is a primary factor limiting operating temperatures and pressures necessary for increased efficiency and reduced emissions. The drive to increase the amount of energy generated through renewable energy sources means that traditional base-load power plant operation is no longer a viable option. Transitioning to more flexible operation will increase degradation of plant components through a combination of fatigue, corrosion and thermal gradients, and further increases the complexities associated with material characterisation, component design and plant operation.

Two key factors influencing the development and implementation of new materials in power plants are (i) analysis of as-received and post-test (e.g. creep, fatigue and oxidation) material to identify microstructural strengthening and degradation mechanisms (e.g. voids and inclusions) to further inform the manufacturing process, and (ii) fatigue life characterisation to identify suitable design limits for flexible operation in plant. The effect of high temperature creep loading on power plant materials has been extensively investigated, in line with the typical loading conditions a traditional base-load power plant component would encounter; however, as plant operation becomes more flexible, a new area of research, in terms of the effect of both room and high temperature cyclic loading and thermal transients, must be investigated.

This chapter discusses the changing face of power generation and the effects of the global need to reduce emissions on the operational modes for fossil fuel power plants. Following this, the typical materials used for such applications and the influence of cost on material selection will be discussed, as well as the development of alternative advanced materials. Finally, the aims and objectives of this thesis and an overview and scope of research work are presented.

1.2 The Effect of Renewable Energy Sources

The future of energy in Europe has changed substantially as a result of European Union (EU) regulations on emissions standards (i.e. taxation of CO_2) and subsidies on renewable energy generation methods. In 2008, an EU target to reduce 2020 greenhouse gas levels by 20%, relative to the levels measured in 1990, was agreed [4]. Further EU targets to increase the share of renewables to at least 27% by 2030 were also agreed in 2014 [5]. Consequently, significant declines in global coal consumption have occurred over the past number of years, particularly in the UK, where usage fell by 52.5%, to its lowest ever level [6].

In Ireland, fossil fuel import dependency has varied between 85% to 90% since 1990, due to a combination of increased demand and reduced indigenous production i.e. gas and peat. In 2016, this dropped to 69% as a result of natural gas production, but the rate of supply of natural gas is expected to reduce sharply in the coming years. Peat production levels have continually fallen since 2013, leaving the renewable sector as the primary alternative for national production [4]. The major impact this will have on current and future generations of power plants is (i) transition to highly flexible plant operation, as the amount of energy produced from renewable energy sources increases and (ii) a new generation of advanced materials which must resist increased fatigue and oxidation/corrosion effects.

Figure 1.1 depicts the contribution from renewable energy sources (hydroelectric, wind, biomass, landfill and biogas) to the gross electricity consumption in Ireland from 1990 to 2014. Wind is shown to dominate, overtaking hydroelectric, in recent years and in 2014, renewable energy generated by wind accounted for 18.2% of all electricity generated, compared to gas (45.8%) and coal (14.3%). Increased co-firing of biomass in peat generating stations also contributes to reduced fossil fuel dependency [4]. This is a clear indication of how flexible operation of power plant will be increasingly necessary in the coming years.

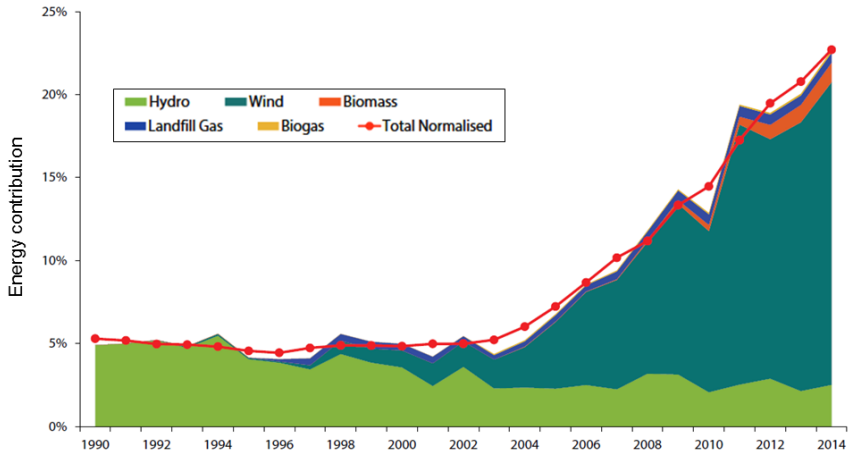

Figure 1.1 Renewable energy contribution to gross electricity consumption from 1990 to 2014 in Ireland. Adapted from [4].

Figure 1.2 depicts the direct effect of increased renewable energy sources on the decrease in CO_2 production, with wind and biomass the most significant contributors to reduced CO_2 emissions. The total energy-related emissions for 2016 are approximately 37 mega-tonnes. The use of renewables resulted in a reduction of nearly 4 mega-tonnes of CO_2 emissions and reduced the cost of fossil fuel imports by approximately €342 million in 2016 alone [4]. This is further motivation to increase the share of renewables and, therefore, transition power plants from base-load to intermittent-mode operation.

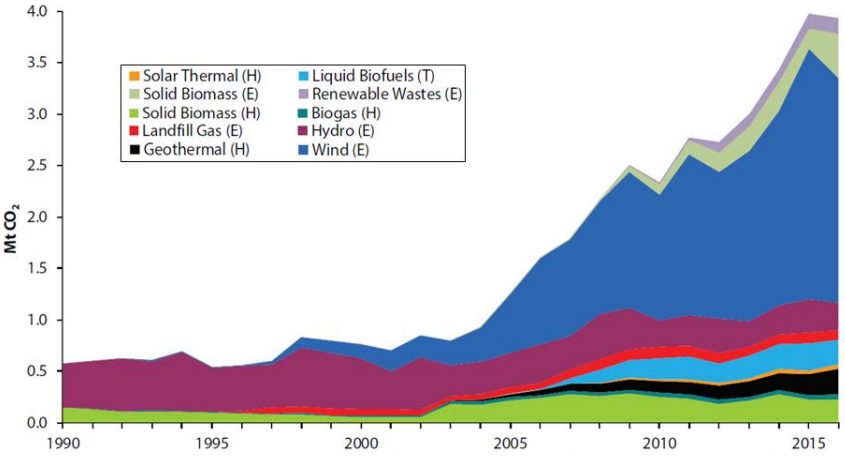

Figure 1.2 Mega-tonnes of CO_2 (Mt CO_2) avoided due to renewable energy sources in Ireland from 1990 to 2016. Adapted from [4].

Subcritical power plants of the 1980s operated at approximately 550 °C and 40% thermal efficiency, compared to current ultra-supercritical (USC) plants at between 44% and 46%. Such increased operating conditions can in turn lead to a reduction of 2.5 million tonnes of CO_2 over plant lifetime [7]. USC plant conditions have a main steam temperature of 600 °C, with steam pressures up to 28.5 MPa and reheat steam

temperatures of 620 °C, but are limited by the lack of a suitable range of cost-effective materials capable of operating at increased loading conditions. The design life of USC power plants is approximately 30 years and is a key factor influencing material development and component design [8]. Based on this, plant operators may run at subcritical loading conditions to prolong component lifetime and reduce outage frequency, which can cost over €500,000 per day [9], further motivating the requirement for enhanced materials. Figure 1.3 shows how greater reductions in emissions can be made through increased efficiency of fossil fuel based plants. The benefits include prolonged fuel reserves (e.g. coal), increased power output and reduced emissions and operational costs [10].

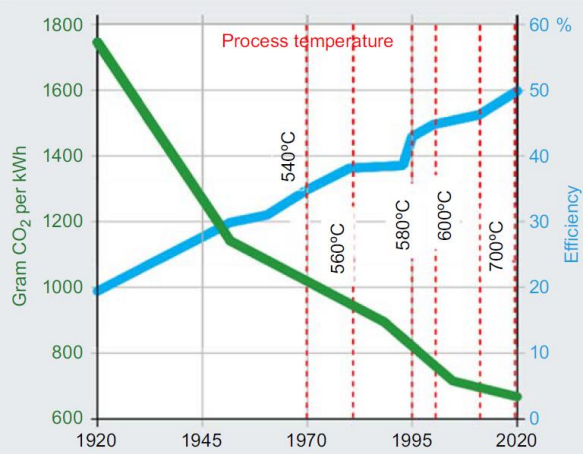

Figure 1.3 Relationship between emissions, efficiency and operating temperature in power plants [10].

1.3 Component Degradation under Flexible Loading

One of the primary limitations to plant start times is the resulting level of component stress due to thermal fatigue, arising from plant cycling. Start-up and shut-down can occur multiple times a day and reduce component lifetime below 200,000 cycles. Component and plant designers must consider factors such as material properties, wall thickness and yield stress to optimise thermal cycling [3]. Figure 1.4 presents the breakdown in power generation by various sources throughout one day, indicating the many energy production methods and factors which must be considered for flexible operation [11].

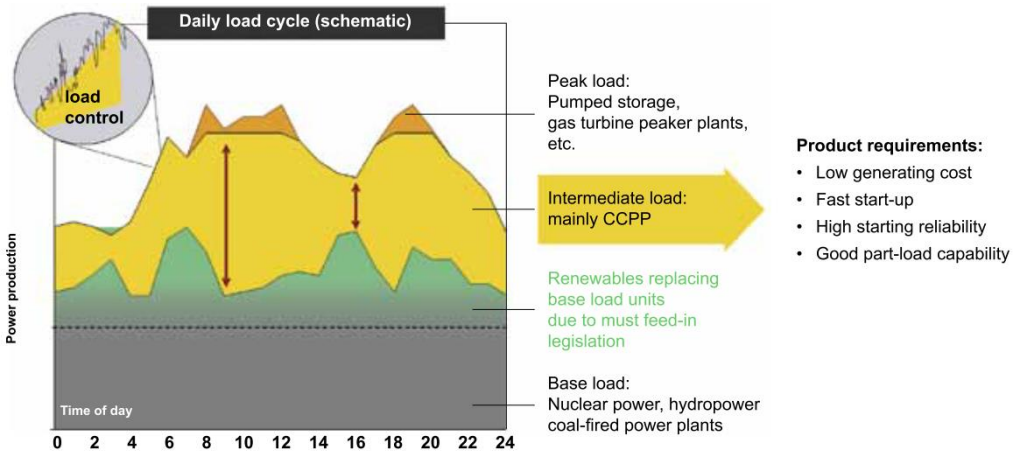

Figure 1.4 Schematic of a daily load cycle and its impact on combined cycle power plants (CCPP) [11].

The number of forced outages, due to unplanned component failure or other factors requiring component removal, has increased due to flexible operation. Greenhouse gas emissions have risen also e.g. nitrogen oxide emissions rose 10% due to larger fuel consumption on start-up in a coal generating plant; however, the emissions avoided due to renewables far outweigh this increase [12]. Modifications to current base-load power plants for flexible operation will include changes to both hardware and operational practices. To date, a number of issues have been identified as a result of cycling a coal generating station at low loads (<40% capacity), including increased stress, wear and tear, and corrosion of components due to large temperature swings [12]. Some examples of the effect of cyclic loading on specific components include (i) boiler tube failure due to fatigue, corrosion-fatigue and pit formation, (ii) cracking of thick-walled components (e.g. headers and valves) and dissimilar metal welds, due to steam temperature fluctuation, (iii) generator rotor cracking during slow turning, due to rotor and casing movement, (iv) oxidation during start-up, and draining or dislodging of oxides from the boiler wall due to thermal variation, and (v) corrosion of turbine components due to wet steam and oxides [12].

Start-up and shut-down of plant causes thermal cycling of the hot-gas-path components and can lead to increased cost in terms of reduced component life and time-value for money. Other issues include (i) chemical disturbances in feed-water and boiler water, (ii) excessive corrosion during start-up and shut-down, and (iii) increased levels of deposits, build-up and under-deposit corrosion in the boiler. Computational modelling and prediction of component performance in real-time, in terms of damage accumulation, requires an understanding of the damage mechanisms associated with

specific temperatures and pressures. This will provide plant designers and operators with a more realistic cost prediction of components operating at flexible USC loading conditions [2,13].

Combined cycle gas turbines (CCGT), containing a gas turbine, water/steam cycle with a steam turbine and heat recovery steam generator (HRSG), provide the fastest response time under flexible operation to date, with efficiency up to 60% and less than half the emissions of an equivalent steam driven plant. A schematic of the basic layout is shown in Figure 1.5. CCGT development has vastly improved in the last 20 years and offers significant improvements in efficiency, as well as increased flexible operation in terms of (i) rapid start-up, shut-down and load variation, (ii) improved start-up reliability and load predictability and (iii) grid system support [3].

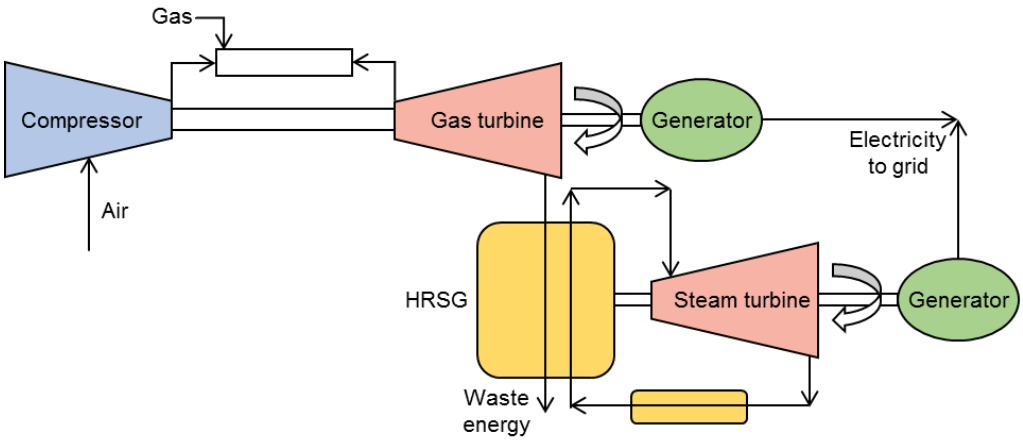

Figure 1.5 Schematic of a combined cycle gas turbine plant. Adapted from [14].

HRSG in new combined cycle units, originally designed for base-load operation, are a key component in providing increased efficiency. However, early failure due to cycling has been found to occur, indicating the limited knowledge of the effect of low cycle fatigue in terms of component design and performance in-service. Both the tubes and casings of HRSGs are primary locations of component failure in flexible power plants. Failure of HRSG tubes (Figure 1.6) often results in a full section being replaced, as limited space means significant cutting and welding of the existing system and increased costs [2,13]. In particular, a range of issues with HRSG systems under flexible operation have been observed in industry, including (i) oxide scale cracking and corrosion-fatigue of thin wall components during cycling at low loads, (ii) valve and turbine casing cracking due to increased start-ups and shut-downs, (iii) internal and external boiler cracking due to thermo-mechanical fatigue (TMF) and increased ramp

rates, and (iv) fatigue cracking of components due to boiler resonance, vibration and component movement during high-load operation [15].

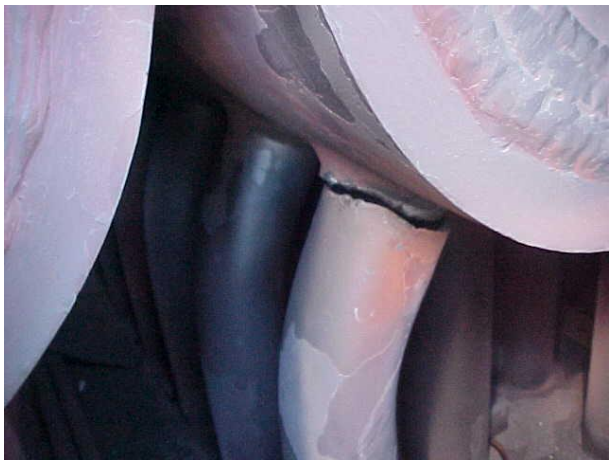

Figure 1.6 Tube failure in a HRSG system [16].

The effects of fatigue at current and increased loading conditions must be identified to allow component designers and plant operators to accurately identify suitable design limits and reduce outage times. Furthermore, increased loading of components requires an improved range of materials, capable of withstanding such harsh conditions, for upgrading of current and future plant.

1.4 History and Development of 9Cr Steels and Alternative Alloys

9Cr steels were originally developed in the 1930s as a tube alloy. Alloying elements, such as vanadium and tungsten, were investigated in terms of improving the long-term creep performance, but molybdenum was found to provide the most economical improvement in creep strength and corrosion resistance, through solid solution strengthening and precipitation of $M_{23}C_6$ particles. Such materials are known as modified 9Cr steels. This eventually led to the development of T/P9, a standard material for super-heater and boiler components. In the 1970s, nuclear power plant development intensified and a large development program in the United States of America resulted in the production of modified 9Cr-1Mo steel, P91, at the Oak Ridge National Laboratory [8]. Strict control of alloying elements produced enhanced creep rupture strength compared to other materials at the time. American Society of Mechanical Engineers (ASME) code approval was acquired in 1984 and this material has since been widely implemented in fossil fuel power plant applications at operating temperatures of up to 580 °C. In Japan, further improvements on P91 have been made via optimised

molybdenum and tungsten content and the addition of boron, leading to an enhanced strength steam pipe steel, P92, with operating temperatures of up to 620 °C. However, implementation beyond such temperatures is hindered by steam oxidation resistance, and increasing the chromium content was insufficient in producing a steel with equivalent strength to P92, hence the requirement for a cost-effective alternative remains [8].

Nickle-based superalloys can provide many of the desired material properties for application at elevated loading conditions, but the significant cost associated with these materials means retrofitting of an entire plant is not economically viable. As such, substantial resources have been focused on the development of further modifications to 9Cr alloys for these applications [8]. Table 1.1 highlights the significant expense associated with Ni-alloys (top row) and, therefore, the use of such components must be limited to the highest temperature regions in plant. This is further validation for the use of 9Cr steels as a significantly cheaper alternative [17].

Cast components have widespread applications across power plants and, in the past, were manufactured from Cr-Mo and Cr-Mo-V for sub- and supercritical conditions. However, these materials have insufficient strength for operation at USC conditions; as a result, modified 9Cr steels have become a favoured choice. Martensitic 9-12Cr steels have application in some of the hottest areas in plant (e.g. steam lines, outlet headers and super-heaters) due to their high creep strength, thermal properties and oxidation and corrosion resistance, in conjunction with relatively low cost. There are many benefits to cast components including the ability to produce intricate geometries, reproducible shape and cost-effectiveness, but some issues can occur during manufacturing, such as dendritic shrinkage and inclusion formation [8].

Table 1.1 Cost per kilogram of various nickel-based alloys and steels [17].

Grade	A740®	A263	A617	A625	A230	A155
€/kg	19.36	19.36	19.12	17.84	17.51	14.46
Grade	MarBN	E911	P92	P91	CMV	Cr-Mo
€/kg	2.76	1.76	1.79	1.39	0.92	0.91

Research and development programs, running since the early 1970s, have focussed on advanced materials for power plant applications, to allow the maximum operating conditions to be increased, therefore, improving efficiency and reducing emissions. The European COST (Cooperation in Science and Technology) project, which began in the early 1970s until the early 2000s, has been followed by KMM-VIN (Knowledge-based Multifunctional Materials Virtual Institute) [8]. This includes UK-based IMPACT (Innovative Materials Design and Monitoring of Power Plant to Accommodate Carbon Capture) [18] and follow-on IMPULSE (Advanced Industrial Manufacture of Next-Generation MarBN Steel for Cleaner Fossil Plant) projects [19], both of which focussed on the development of MarBN steel. The industry-funded associated project IMPEL [20] also has a similar goal in terms of the development of MarBN as an improved high temperature material for welded components (i.e. boiler, pipe and turbine). This demonstrates the international scope for research and development of MarBN steel, from its origin in Japan to widespread investigation across Europe.

MarBN is a martensitic, ferritic steel originally developed at the National Institute for Materials Science (NIMS) in Japan, with a focus on improving (i) microstructural stability during long-term creep loading, (ii) oxidation and corrosion resistance, (iii) Type IV cracking resistance in welded components, and (iv) flexible operation [21]. Welding of modified 9Cr steels is known to produce a fine-grained structure in the heat affected zone (HAZ), replacing the hierarchical microstructure, and is a common cause of component failure (i.e. Type IV cracking). Figure 1.7 compares the stress versus rupture time for parent metal and welded MarBN and P92 at 650 °C. MarBN shows almost identical performance between parent and weld metal, and an increase in rupture stress of approximately 30%, indicating the importance of preserving the hierarchical microstructure for long-term macroscale strength [21].

Significant research has been conducted on the creep performance of MarBN; however, there remains a requirement to improve the understanding of the effects of (i) manufacturing process (i.e. casting and forging), (ii) fatigue loading and oxidation performance, compared to current generation materials, and (iii) associated mechanisms of degradation. Furthermore, the development of a computational model capable of capturing the phenomenological behaviour and damage evolution, across a range of loading conditions, is a key requirement for design of next generation power plant components for advanced modified 9Cr steels.

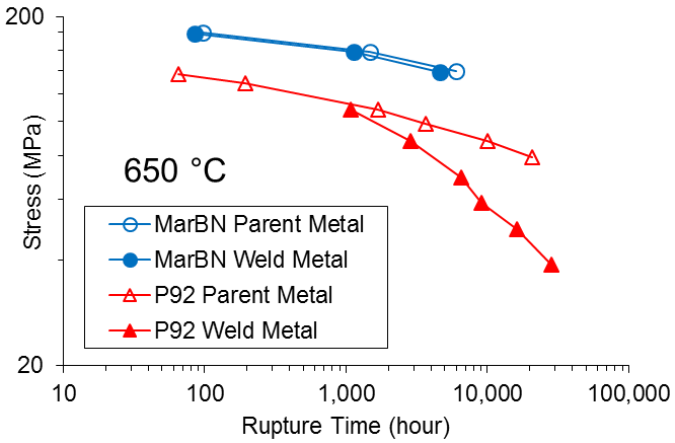

Figure 1.7 Stress versus rupture time for MarBN and P92 parent and weld metal samples at 650 °C. Adapted from [21].

1.5 Aims and Objectives

The primary aim of this thesis is to experimentally characterise the high temperature cyclic response of cast and forged MarBN steel via (i) a program of high temperature low cycle fatigue (HTLCF) and creep-fatigue (CF) testing, (ii) microstructural analysis and 3D X-ray micro-computed tomography (µCT) scanning, and (iii) oxidation and corrosion studies. A secondary aim is the development of computational models of the constitutive behaviour, including isotropic and kinematic hardening, and life prediction and fatigue damage behaviour. The key aspects focused on are as follows:

1. Experimental testing to characterise the fatigue response of MarBN at high temperature. HTLCF and CF testing of cast and forged MarBN steel, with a view to understanding the effect of manufacturing process and temperature on the cyclic response of the material. HTLCF testing of ‘as-received’ (AR) P91 steel, a widely used material in current generation power plants, is performed for comparison.
2. Microstructural analysis of pre- and post-test MarBN samples to identify mechanisms of strengthening and degradation. In particular, the role of manufacturing defects (i.e. voids and inclusions) on fatigue crack initiation (FCI) and component failure at high temperature will be investigated.
3. 3D X-ray micro-computed tomography (µCT) scanning of cast and forged MarBN, before and after HTLCF testing, will provide a greater understanding of the influence of manufacturing process on defect formation and associated FCI. Identification of defect volume fraction and shape characterisation will be

performed. A 3D analysis of the primary crack path, and micro-cracking between defects, away from the primary crack, will be investigated also.

4. Oxidation and corrosion studies on cast and forged MarBN, as well as AR P91 steel, in air and with a corrosive ash applied are performed. The rate of oxide scale growth and oxide pit formation, particularly around inclusions, is investigated. Oxidation and corrosion resistance at high temperature is critical for USC application.
5. Calibration and validation of a unified cyclic viscoplastic material model, including uniaxial life prediction and damage effects, is performed for cast MarBN at 600 °C and 650 °C, based on the experimental HTLCF and CF testing. Material parameter optimisation is performed to ensure accurate and unbiased prediction of material behaviour across a range of loading conditions, due to the strain-rate sensitivity of the material at high temperature.
6. Development of coupled and uncoupled multiaxial life prediction and damage accumulation methodologies is performed, to quantify the microscale effects of manufacturing defects, in terms of localised stresses and strains. Ideal and complex defect geometries (identified from 3D X-ray μCT scanning) are modelled under HTLCF loading conditions, as part of a HTLCF dog bone specimen and power plant component. A robust material model is vital for understanding the effect of cyclic loading on components with defects.

1.6 Thesis overview and scope

Chapter 2 presents background and a review of the literature related to this work, including descriptions of creep, fatigue, oxidation and microstructural strengthening and degradation mechanisms in 9Cr steels. The various modelling techniques developed to date to describe fatigue loading are also presented, in terms of constitutive behaviour, life prediction and damage accumulation. Methods of characterisation of manufacturing defects and modelling are also presented.

Chapter 3 discusses the role of the various alloying elements and heat treatment procedures. The results of the HTLCF and CF test program on cast and forged MarBN, with comparisons to current generation material, P91 steel, across a range of strain-rates and strain-ranges are presented and discussed. This is followed by microstructural analysis of pre- and post-test samples (MarBN and P91). Scanning electron microscopy (SEM), back-scatter electron (BSE) microscopy, element dispersive X-ray (EDX)

spectroscopy and transmission electron microscopy (TEM) techniques are employed to identify the primary strengthening and degradation mechanisms, and the role of manufacturing defects in sample failure. Oxidation and corrosion studies performed on cast and forged MarBN at 600 °C and 650 °C, with comparisons to P91 at 600 °C, are then presented. The rate of oxide scale growth is characterised from 1 to 28 days and the role of inclusions in terms of oxide pit formation is investigated. BSE is applied to identify Laves phase formation as a result of thermal, HTLCF and CF exposure.

Chapter 4 describes the programme of 3D X-ray μCT scanning of pre- and post-test HTLCF cast and forged MarBN samples to identify the role of manufacturing defects in crack initiation and propagation under cyclic loading. This is compared with microstructural analysis of manufacturing defects in post-test samples. The volume fraction of manufacturing defects, and the amount of void growth as a result of HTLCF testing, is quantified. Sphericity of each defect, as a result of the respective manufacturing process, is calculated and compared also.

Chapter 5 presents the phenomenological model, and material parameter identification and optimisation process, based on HTLCF and CF experimental data for cast MarBN at 600 °C. Calibration and validation of a uniaxial hyperbolic sine unified cyclic viscoplastic material model for cast MarBN is described, along with the development of a uniaxial life prediction and damage evolution material model.

Chapter 6 presents a computational study of the effect of manufacturing defects on the local fatigue cracking behaviour of cast MarBN under HTLCF conditions, using an uncoupled life prediction and damage methodology based on experimentally identified material parameters. Following this, a coupled critical-plane Ostergren life prediction and damage accumulation model is developed as part of a user-material subroutine (UMAT) in Abaqus and applied to uniaxial and multiaxial cases, including single and multiple manufacturing defect geometries.

Chapter 7 describes advanced material modelling of complex manufacturing defects, identified during 3D X-ray μCT scanning, in HTLCF gauge length models and plant component geometries, to identify localised stress and strain concentrations and associated damage accumulation and fatigue crack initiation.

In Chapter 8, the key conclusions of the work are presented and recommendations for future work are discussed.

2 BACKGROUND AND LITERATURE REVIEW

2.1 Introduction

There are several aspects to be considered in terms of the design and characterisation of high temperature materials including (i) greater flexibility of power plants as the contribution from renewable energy sources is increased, (ii) the role of chemical composition, manufacturing process and heat treatment, (iii) the complex hierarchical microstructure of 9Cr steels, (iv) the range of experimental testing necessary to fully characterise the material and (v) calibration and validation of computational models to predict component performance.

The following chapter describes the complexity of these materials in terms of manufacturing process, heat treatment, mechanical and high temperature loading, as well as the influence of various alloying elements and related strengthening mechanisms. An overview of numerical and computational modelling techniques, in terms of cyclic plasticity, isotropic and kinematic hardening, life prediction and damage are then presented. Finally, manufacturing defects and void formation are discussed in terms of their role in crack initiation, and the various methodologies employed to characterise their presence.

2.2 Manufacturing and Heat Treatment

2.2.1 Manufacture of Castings and Forgings

Due to the strict levels of chemical control necessary in manufacturing modified 9Cr steels, an increased level of skill is required during melting and refinement of the material. Small variations in chemistry throughout the material can have adverse effects under ultra-supercritical (USC) loading. Furthermore, trace elements must be stringently controlled during deoxidisation of the steel. Secondary refinement is typically required for USC grade materials, for example via argon oxygen decarburisation or vacuum oxygen decarburisation. The fabrication of a highly homogeneous material, with uniform elemental distribution is a vital requirement in the production of a high quality steel for USC applications [8].

Figure 2.1 is a flowchart of the manufacturing process for forged tempered martensitic steel, FB2 [8]. The steel is melted in an electric arc furnace (EAF) and refined in a ladle furnace (LF) with deoxidising agents (e.g. aluminium, calcium), followed by argon oxygen decarburisation (AOD), and LF, with vacuum degassing (to remove gases such as oxygen and hydrogen). The ingot is then cast, hot forming is applied and the material is heat treated. Pre-machining is performed, followed by ultrasonic (US) testing to identify defects, and further heat treatment. Final machining and testing of the material are then performed. This complex and highly skilled process indicates the importance of strict chemical control during manufacturing.

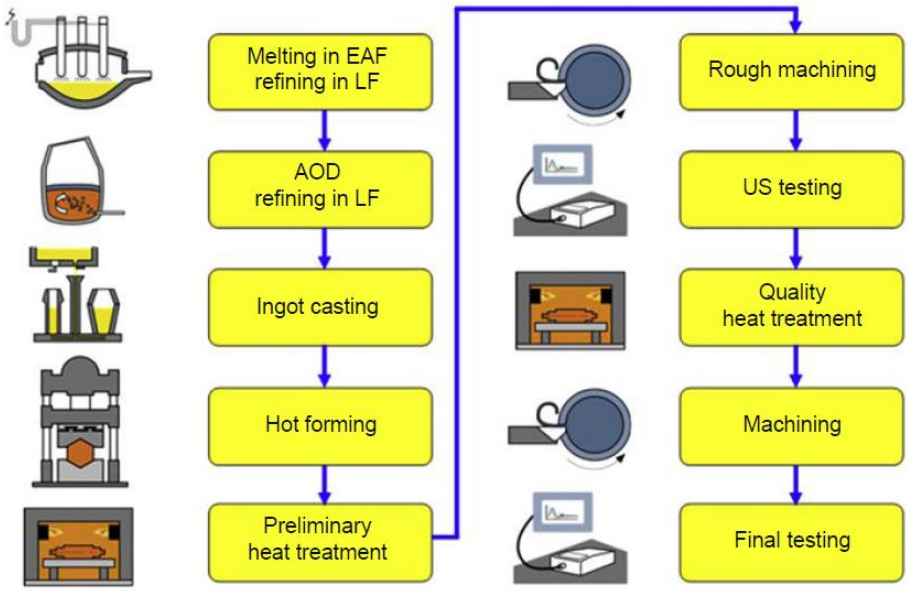

Figure 2.1 Flowchart of the manufacturing process of FB2 [8].

Forging of the material can then be performed, through heating of the ingot to the desired temperature and forging on a forging press. The temperatures must be strictly controlled to produce the desired microstructure and avoid δ-ferrite formation. Further heat treatment processes are then applied, followed by machining. Finally, US testing is performed, based on a minimal detectable defect size (MDDS). This typically ranges from 1.5 mm (for a part diameter of 860 mm) to 2.2 mm (for part diameters between 1,120 mm and 1,200 mm) [8]. Although this is not the exact manufacturing process for the cast and forged MarBN examined in this work, it provides an example of the complexities associated with the manufacture of advanced martensitic steels for USC applications.

Formation of manufacturing defects (e.g. inclusions) is a common occurrence during steel manufacture. $CaO\text{-}Al_2O_3$ inclusions have been identified in linepipe steel (X80), following the LF-degassing-Ca treatment stage of manufacture, by Wang *et al.* [22]. Modifications to the manufacturing process were investigated and it was suggested that an inclusion removal step, before Ca treatment and following a longer degassing step, should be performed, reducing the number of inclusions by over 40%, as well as reducing their size.

2.2.2 Heat Treatment

Figure 2.2 is a phase diagram for Fe-Cr steel, based on Cr content. Austenite (γ) formation can occur up to 12% Cr, between temperatures of ~1,200 K and 1,400 K. Air cooling allows martensitic transformation above ~7%Cr, as bainitic transformation is suppressed due to the interaction between Cr and C atoms. Increasing the Cr content to above 9% enhances the oxidation resistance of the material also. As the steel cools, δ-ferrite can form due to an imbalance of alloying elements and transform to γ-austenite, through a slow diffusion-controlled growth process. Dissolution of δ-ferrite during normalising is also a slow process, meaning it may remain in the finished steel, providing soft regions that can promote component failure [8].

Figure 2.3 presents the effect of different heat treatment processes on P92 steel, in terms of grain size and dislocation density. Grain size is shown to rapidly increase above normalising temperatures of 1,100 °C (Figure 2.3(a)) and dislocation density is found to rapidly decrease at higher normalising and tempering temperatures, due to sub-grain

formation (Figure 2.3(b)). Little change in particle ($M_{23}C_6$ and MX) diameter was observed as a result of increased tempering temperature [23].

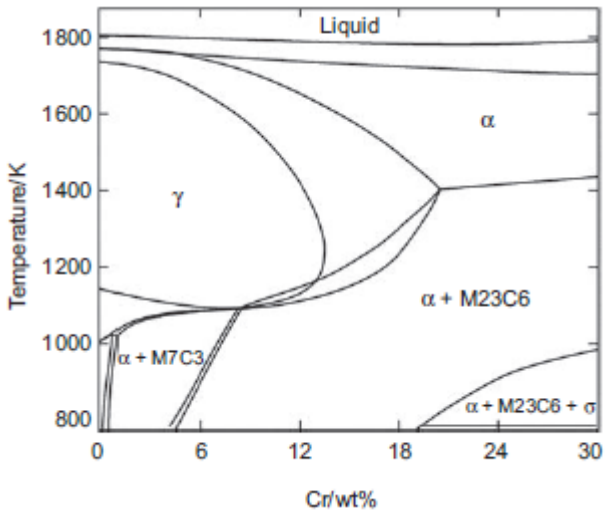

Figure 2.2 Phase diagram for Fe-Cr steel, as a function of Cr, with 0.1%C [8].

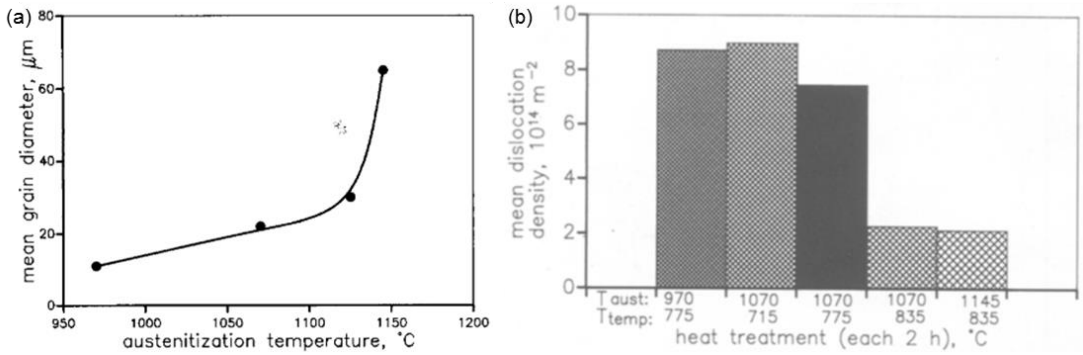

Figure 2.3 Effect of heat treatment temperatures on (a) grain size and (b) dislocation density [23].

High dislocation density is a characteristic feature of 9-12Cr steels following low temperature tempering (~750 °C) [8]; however, if dislocations glide from the sub-grain interior to the sub-boundary, annihilation of dislocations can occur, reducing dislocation density, leading to a reduction in the strength of the component and more rapid microstructural degradation [24]. Li *et al*. [25] investigated the effect of an extended pre-service heat treatment on the creep performance of T91 and T92 steel at 650 °C. Figure 2.4 compares rupture stress for the materials tested in the as-received condition (T91 and T92), with the same material having undergone an additional 16 hour heat treatment at 765 °C (T91-16 and T92-16), as well as the mean lines from the European Collaborative Creep Committee (Grade 91 and Grade 92). A reduction of 20% to 30% in rupture stress occurs in all cases; this is attributed to coarsening of $M_{23}C_6$ particles

(T91-16), and rapid nucleation and growth of Laves phase particles (T92-16). This indicates the importance of an optimised heat treatment process and the substantial effect it can have on the microstructure, particularly due to the significant strengthening effect of nano- and microscale features in martensitic steels.

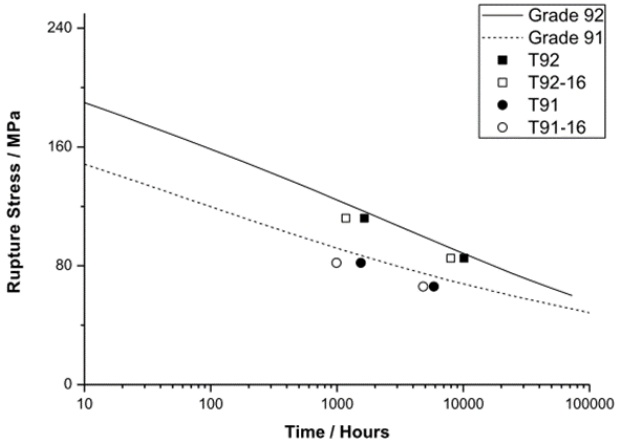

Figure 2.4 Rupture stress versus time for T91 and T92 in the as-received and post-heat treated condition (T91-16 and T92-16), with comparison to mean code data [25].

2.3 Creep of Power Plant Materials

2.3.1 Introduction

Creep at high temperature is defined as the slow, continuous deformation of a material over time. In general, creep occurs once the temperature exceeds 0.3 to 0.4 of the melting temperature of the metal. At room temperature, strain, ε, is only dependent on stress, σ; however, at high temperature, time, t, and temperature, T, are also influencing factors [26], such that:

$$\varepsilon = f\left(\sigma, t, T\right) \tag{2.1}$$

The complex response of metals under stress at high temperature is presented schematically in Figure 2.5, where three distinct regions of conventional creep deformation are shown to occur. After a short period of elastic strain, an initially high period of creep occurs, known as the primary creep region (I). This is followed by a steady state region, known as secondary creep (II), and can be described using the Norton power-law relation:

$$\dot{\varepsilon}_{\mathrm{c}} = B\sigma^{n} \tag{2.2}$$

Finally, a period of accelerated creep and rupture is defined as the tertiary region (III).

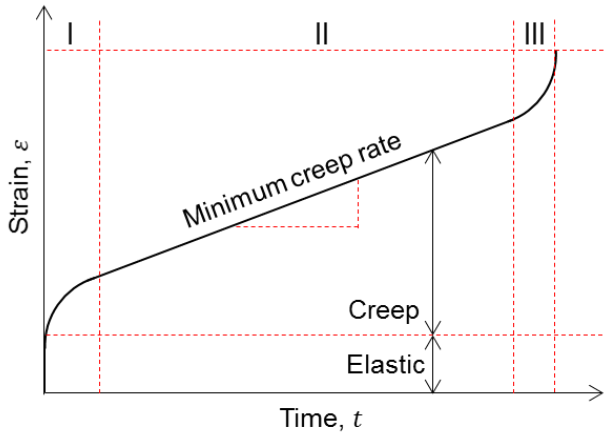

Figure 2.5 Strain-time creep curve. Adapted from [27].

Creep in-service causes a reduction in the maximum stress, as well as stress redistribution, particularly during tertiary creep. However, more complicated design procedures are often necessary, due to highly conservative and cost ineffective life predictions as a result of simple, elastic designs, based on a needlessly high maximum stress [28].

2.3.2 Mechanisms of Degradation

The influence of stress and temperature on the resulting creep degradation mechanism is described in Figure 2.6. The primary mechanisms are diffusional creep (linear-viscous response) and dislocation creep (power-law type behaviour). At lower stress levels, diffusion creep is the dominant mechanism (Figure 2.7). Crystal deformation under loading leads to grain elongation and atomic diffusion between grain faces. To resist hole formation between grains, grain-boundary sliding must occur [26].

Dislocation creep occurs as a result of dislocation motion due to the diffusion of atoms under loading. Precipitates act as obstacles to dislocation motion, but a process known as climb and glide, shown in Figure 2.8, describes the nature of dislocation creep. Climb and glide can occur independently also. Furthermore, bulk crystal diffusion in regions of void formation, typically along grain boundaries, leads to a reduced area to withstand degradation and eventually fracture occurs [26].

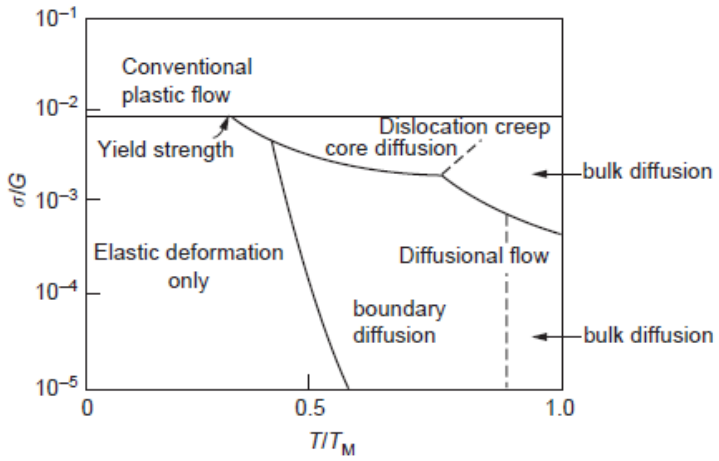

Figure 2.6 Schematic of the degradation mechanisms associated with various stresses and temperatures under creep loading [26].

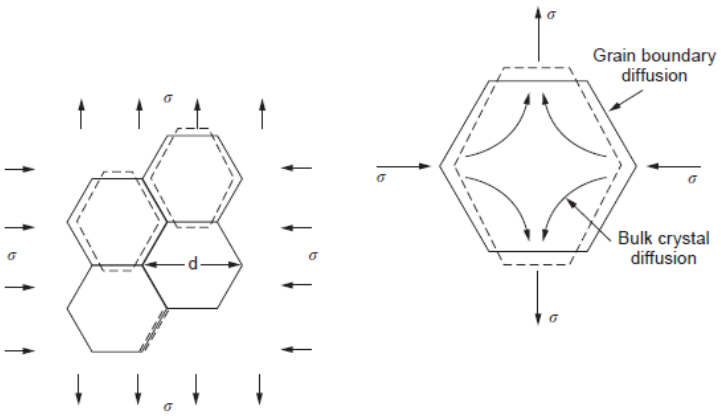

Figure 2.7 Schematic of the diffusion creep process [26].

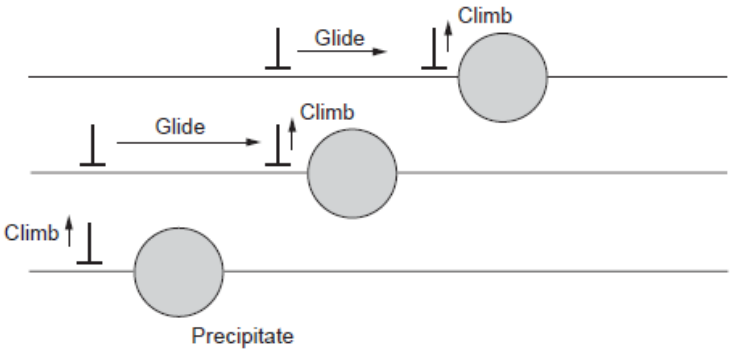

Figure 2.8 Schematic of the climb and glide mechanism of dislocation creep [26].

Furthermore, three major categories of creep damage have been defined by Dyson [28] in relation to component failure; namely (i) loss of external section (due to uniform straining or corrosion-product failure), (ii) microstructural degradation (i.e. particle coarsening and loss of dislocation density), and (iii) loss of internal section (as a result of environment, cavity nucleation and growth).

2.3.3 Creep Testing of Current Generation Materials

Extensive creep testing of 9Cr steels for power plant applications has been performed to date. Microstructural evolution under constant load conditions is a key area of interest in identifying the primary microscale strengthening and degradation mechanisms in these complex materials [29]. In Figure 2.9, the maximum operating temperature of current generation power plant materials is presented, based on an average stress rupture strength of 100 MPa after 100,000 hours [30]. Austenitic steels are shown to provide comparable performance to martensitic steels, but the large increase in thermal expansion coefficient (at least 50%) means that flexible operation of such components may lead to excessive thermal stresses and, hence, premature fatigue failure. The high creep rupture strength associated with martensitic steels is dependent on the martensitic transformation and related strengthening mechanisms, generally associated with a reduced martensitic lath width. As early as 3,000 hours, a decrease in dislocation density of 75% has been observed in P92 steel, indicating the importance of experimental testing and extensive microstructural characterisation [30].

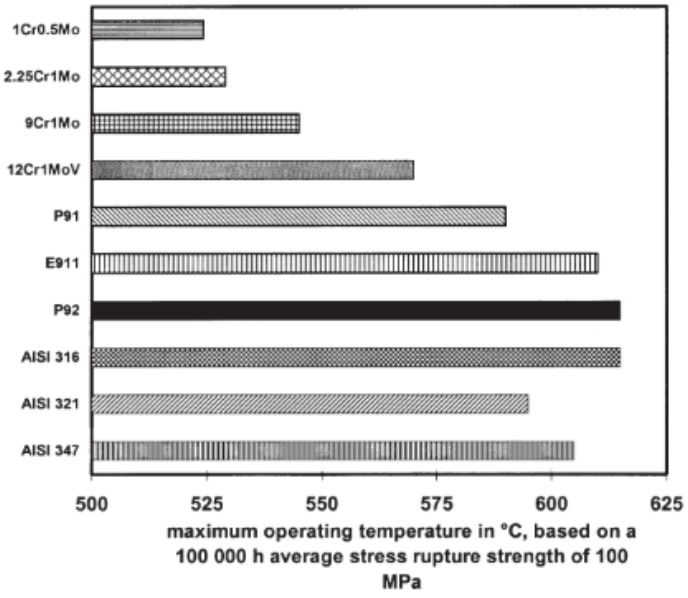

Figure 2.9 Maximum operating temperature of various current generation power plant steels [30].

The effect of both stress and temperature are presented in Figure 2.10 for P91 steel. It should be noted that the specific P91 steel tested by Hyde *et al.* [31] has a significantly lower creep rupture strength than specified in the mean code data. Further evidence of the detrimental effects of stress and temperature, as a result of increased strain, is shown in Figure 2.11 for P92 steel. The broad range of loads applied indicate the importance of

loading level and long-term testing of materials to accurately identify safe loading limits at various temperatures. While performance at low stress levels at 600 °C provides satisfactory results, the inability of the material to endure a 50 °C increase in temperature is a key limiting factor for application of such materials at USC loading conditions [23].

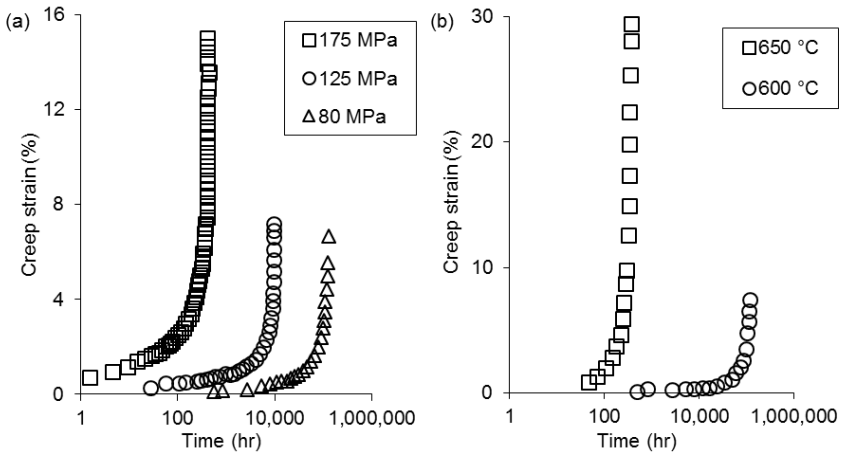

Figure 2.10 The effect of (a) stress at 600 °C (175 MPa and 125 MPa [32], and 80 MPa [33]) and (b) temperature at 600 °C [33] and 650 °C [31] on P91 steel.

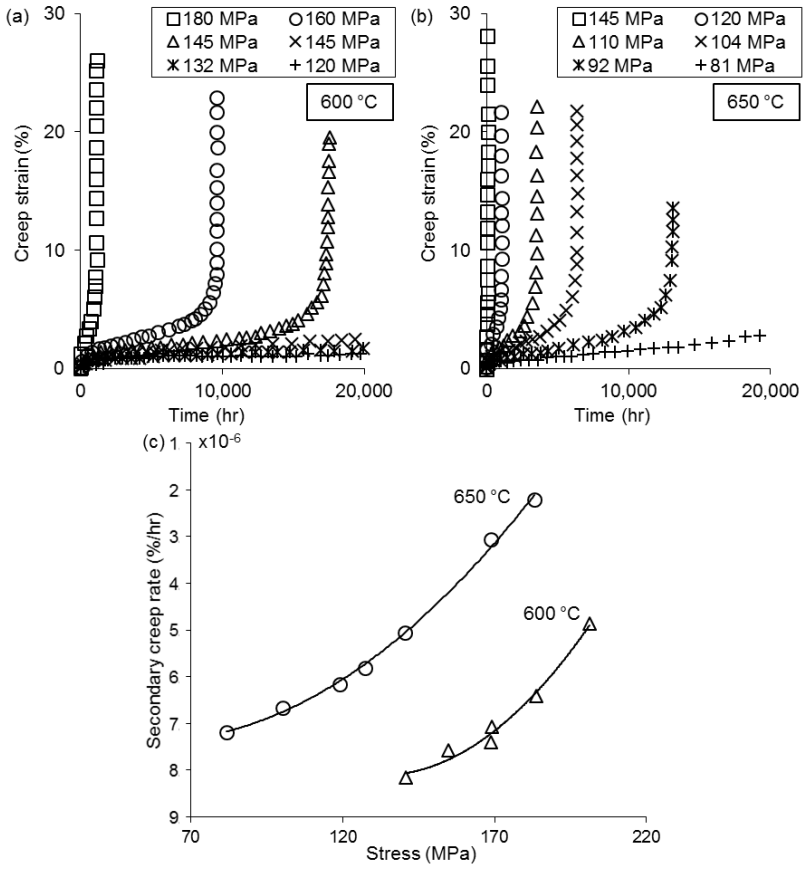

Figure 2.11 (a, b) Creep strain versus time for P92 at 600 °C and 650 °C, and (c) comparison of the minimum creep rate at both temperatures. Adapted from [23].

Figure 2.12 indicates both the effect of tungsten as well as temperature on various 9Cr martensitic alloys. The creep rupture stress is greatly improved due to the microscale strengthening mechanisms provided by tungsten, in particular at 600 °C [30].

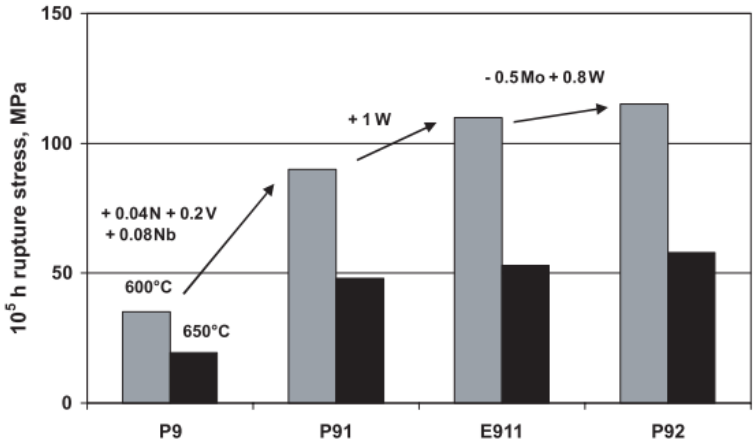

Figure 2.12 Influence of alloying elements and temperature on the rupture stress of various modified 9Cr martensitic alloys [30].

Laves phase formation in P92 steel has been observed up to 10,000 hours during thermal aging or creep exposure at 600 °C and 650 °C, with particles growing to significantly larger dimensions at 650 °C [30]. In the case of current generation material P91, the precipitation of Laves phase during creep after 100,000 hours at 600 °C, in conjunction with $M_{23}C_6$ carbide coarsening, was identified as the key cause of reduced creep strength [29]. However, such particles have been identified as early as 2,000 hours in 9-12Cr steels [34], indicating the importance of a stabilised microstructure and thermally-stable particles.

2.3.4 Next Generation Ultra-Supercritical Steels

The main advantage of USC loading is increased plant efficiency and reduced emissions. The next generation of advanced materials for USC plant applications must possess a number of key material properties for successful, long-term and flexible operation; namely (i) high temperature capability, (ii) oxidation and corrosion resistance, (iii) weldability, (iv) cost-effective and (v) ease of manufacture and fabrication. There are a number of benefits associated with modified 9Cr steels, compared to conventional ferritic steels. This includes (i) increased rupture strength for elevated steam temperatures and pressures (ii) enhanced oxidation and corrosion resistance due to Cr content, (iii) longer component life for creep and fatigue loading and (iv) reduced wall thickness in components (leading to reduced thermal storage and

stress). Wall thickness is particularly important, as it reduces cost and manufacturing time, as well as requiring less time to reach thermal equilibrium and, therefore, the effects of thermo-mechanical fatigue are reduced. Figure 2.13 describes the development of creep-resistant martensitic 9Cr steels over the past 50 years in terms of operating temperature, particularly as part of the European Cooperation in Science and Technology (COST) project [8]. The creep performance of these materials has been the primary focus in terms of mechanical testing.

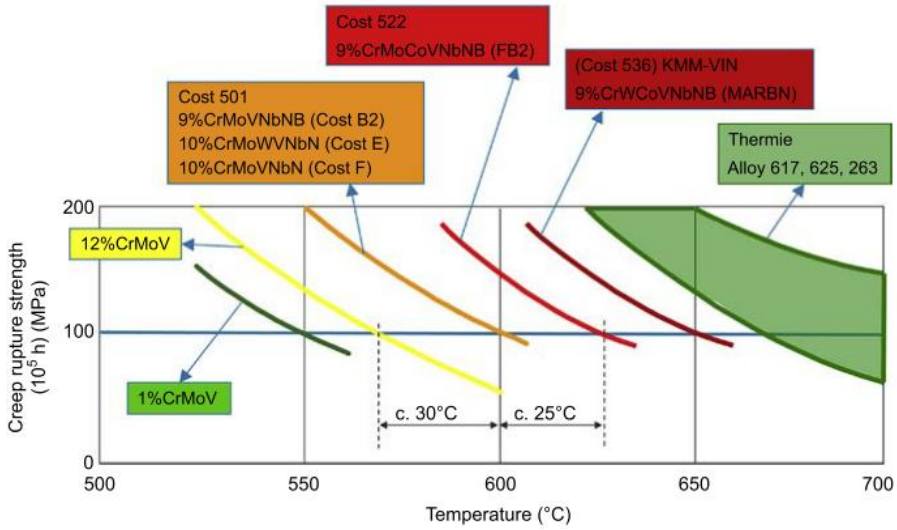

Figure 2.13 Creep rupture strength versus temperature for various power plant steels [8].

Compared to cast P91, the key changes in the chemical composition of Cost B2 (CB2) are reduced nickel to improve creep strength, controlled amounts of boron and as a result, reduced nitrogen. Cobalt is added to counteract δ-ferrite formation, and molybdenum content is increased. Jandová *et al.* [35] have performed creep testing of CB2 samples at various applied stress levels at 650 °C, as per Figure 2.14. Samples A and B are extracted from a pilot valve at different wall thickness locations, and compared to a trial melt.

FB2 is the forged version of CB2 and has been creep tested by Di Gianfrancesco *el al.* [36], with comparison to Grades 91 and 92 at 600 °C and 650 °C (Figure 2.15). FB2 is shown to produce enhanced creep strength for up to 100,000 hours (also compared to CB2 in Figure 2.14) and is recommended for applications up to 625 °C, due to its superior creep strength compared to current generation materials [36].

In Figure 2.16, the creep rupture behaviour of SAVE12AD (9Cr-3W-2.6Co) is presented at 600 °C and 650 °C, and is approximately 1.6 and 1.3 times higher than that

of Grades 91 and 92 at 600 °C, respectively. This is attributed to long-term microstructural stability and reduced precipitate coarsening, for over 45,000 hours at 600 °C [37].

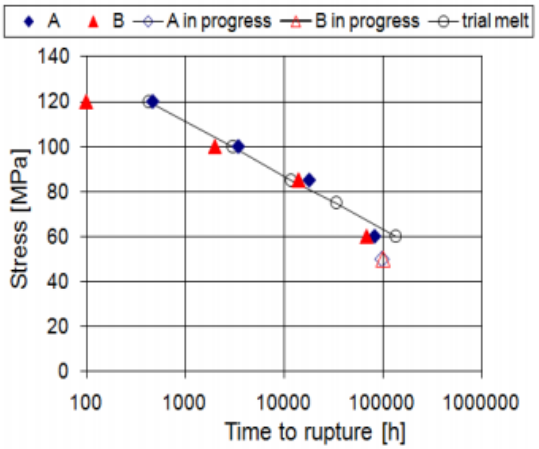

Figure 2.14 Applied stress versus rupture time for various CB2 samples [35].

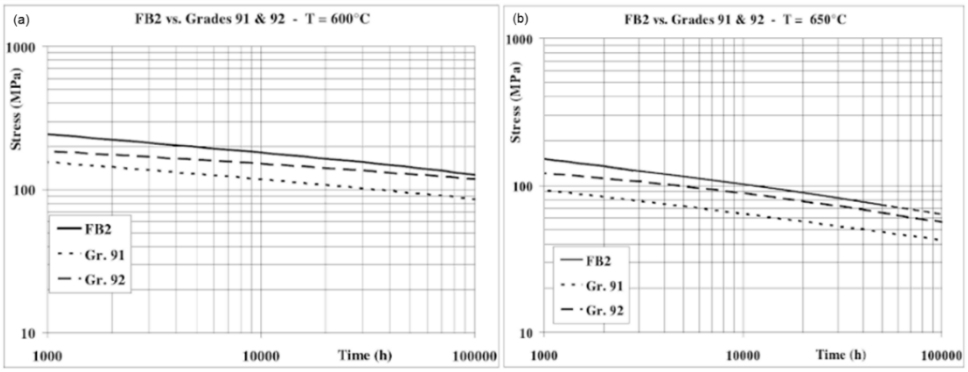

Figure 2.15 Stress versus time for FB2 and Grades 91 and 92 at (a) 600 °C and (b) 650 °C [36].

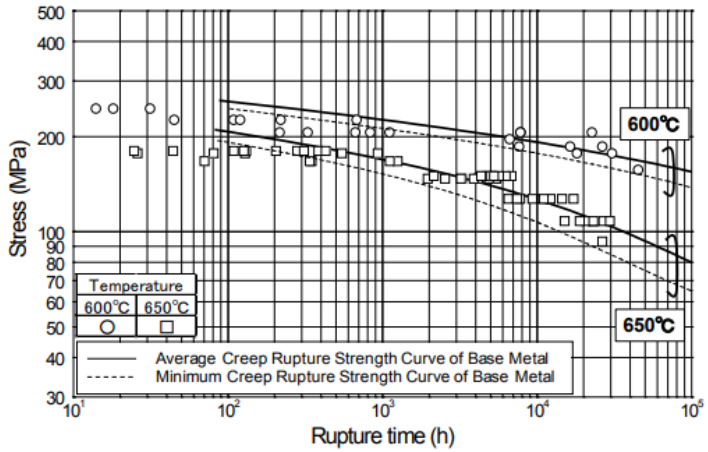

Figure 2.16 Creep rupture strength versus time for SAVE12AD at 600 °C and 650 °C [37].

In Figure 2.17, creep testing of advanced modified 9Cr steels, with 3% tungsten, by Abe *et al.* [38] at 650 °C is presented, with comparison to alternate advanced materials. The creep strength is significantly increased and is attributed to precipitate design for optimised creep performance.

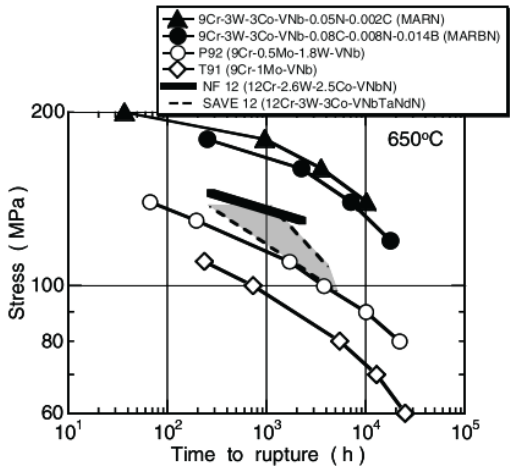

Figure 2.17 Creep rupture strength of various advanced martensitic steel alloys [38].

Shingledecker *et al.* [39] performed short-term testing of advanced austenitic alloy HR6W (23.4Cr-44.8Ni-0.12Ti-6.0W). Figure 2.18 shows the stress-time plot for HR6W at a variety of temperatures, with the relevant failure mechanisms. Temperature is shown to have a significant effect on both the rupture stress and mode of failure of the material. Similar rupture times are observed compared to SAVE12AD (Figure 2.16) and MarBN (Figure 2.17). However, the coefficient of expansion of austenitic steels is higher than for martensitic steels, leading to increased thermal stresses. Thermal fatigue has been identified as a source of component failure in plant under cyclic operation using austenitic steels [40] and may cause further issues under USC conditions.

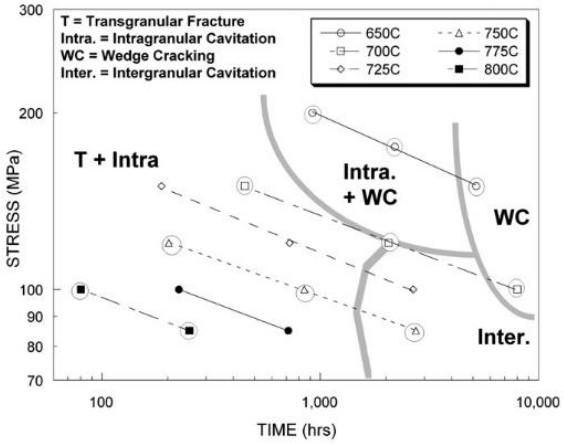

Figure 2.18 Stress versus time for HR6W at a variety of temperatures and mapping of the related failure mode [39].

2.4 Oxidation & Corrosion

2.4.1 Introduction

Oxidation is the process whereby a chemical reaction of the material with oxygen occurs, and corrosion is the irreversible degradation of metals as a result of chemical reactions with the environment. Both mechanisms have a significant impact on the in-service performance of plant components and can cause premature failure if not taken into account during the design phase. The matrix material properties determine the rate at which oxidation or corrosion will occur e.g. transition metals, such as iron, nickel and chromium, have moderate resistance, while alkali and alkaline earth metals, such as magnesium and calcium, oxidise more rapidly [41].

9 to 12Cr steels have been identified as an alternative to expensive Ni-based superalloys for plant components up to 650 °C. To ensure sufficient long-term performance, the oxidation resistance of such materials must be understood for USC loading conditions. Chromium is a key alloying element, however, increasing the content above 12% prevents formation of the martensitic microstructure and results in degradation of creep strength. This level of chromium is generally too low to allow formation of the protective Cr_2O_3 oxide scale [42]. Three factors are of concern in terms of the oxidation and corrosion behaviour of high temperature materials; (i) reduced wall thickness can increase stress and, hence, reduce time-to-rupture, (ii) the reduced thermal conductivity of an oxide layer provides increased insulation of tube material from cooling fluid, therefore increasing metal temperature and corrosion and creep rates, and (iii) spallation is more likely as the oxide scale thickness increases during thermal cycling of plant components i.e. start-up and shut-down cycles, leading to repeated exposure of the matrix material [43].

2.4.2 Structure and Effect of Alloying Elements

The diffusion coefficient of a material will control the rate at which an oxide scale forms and motion of various alloying elements. A lower diffusion coefficient results in oxide formation closer to the surface compared to materials with a high diffusion coefficient [26]. For Fe-Cr alloys, the structure of the oxide scale generally occurs as follows: close to the surface consists of primarily chromium oxide, the outer layer is primarily iron oxide with a mixed chromium and iron spinel between the two. Chromium has a lower vapour pressure than iron and therefore, forms closer to the

surface [44]. An example of this can be seen in Figure 2.19 for ferritic-martensitic steel, HCM12A. In the diffusion layer, oxide-formation occurs preferentially along lath boundaries, indicating the influence of microstructure on the oxidation behaviour of the material [45].

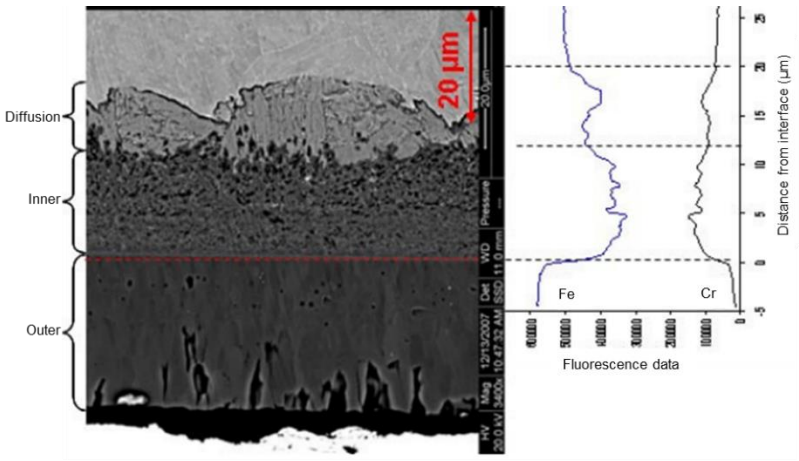

Figure 2.19 Scanning electron microscope (SEM) image of the oxide scale in HCM12A, and element line map of Fe and Cr distribution. Modified from [45].

In some cases, an oxide layer that forms close to the surface can be highly beneficial in protecting the material from further oxide scale formation and material diffusion e.g. chromium and aluminium oxide scales. However, materials with a higher vapour pressure travel further from the surface and offer little protection e.g. at high temperature, molybdenum and tungsten are extremely volatile and evaporate once they form oxides, providing no resistance to oxidation. Oxide films are usually brittle and if there is a low volume of oxide, relative to the material, it will crack to relieve strain. For the opposite case, the scale will break away from the surface. Thermal gradients can cause cracking of the oxide scale and can, in some cases, propagate into the alloy depending on the strength of adhesion. A coating is essential to maintaining constant molybdenum and tungsten compositions in the matrix and preventing rapid evaporation during oxidation (500 °C to 600 °C for tungsten carbides [46]), but breaking of the coating can cause significant localised oxidation. The crack growth rate during cyclic loading is often largely increased when combined fatigue and corrosion occur, and failure due to localised attack, such as pitting, is more likely than under uniform conditions [26,47].

2.4.3 Mechanisms of Corrosion

The factors influencing protective and non-protective oxidation of materials, in terms of alloying elements and discontinuities, are of prime importance. Increased degradation of high temperature alloys due to thermal cycling occurs as a result of oxide scale cracking and spallation. This is due to the mismatch in the coefficient of thermal expansion (COE) between the oxide scale and the alloy in conjunction with stresses generated from oxide scale growth. In general, high temperature components are exposed to multiple atmospheres containing various oxidising components. This can change the material response from that observed in air to a less stable rate of oxide scale growth, with corrosion products containing the alternative oxidising compounds. As a result, the ability of a material to form a protective oxide scale is of great importance for high temperature applications in a complex environment [48]. Two main factors govern the failure of oxide scales: (i) stresses in the oxide scale and (ii) quality of the scale and interface with the matrix. The primary factors influencing the stress situation have been identified as:

$$\sigma_{\text{Total}} = \sigma_{\text{IntrGrth}} + \sigma_{\text{GeomGrth}} + \sigma_{\text{Therm}} + \sigma_{\text{Creep}} + \sigma_{\text{Microcrck}} + \sigma_{\text{Mech}} \tag{2.3}$$

where σ_{IntrGrth} is the stress that occurs during oxide growth and formation of new oxides, σ_{GeomGrth} describes the surface geometry (e.g. roughness) during oxide growth, σ_{Therm} occurs due to a mismatch in COE between the oxide and metal, σ_{Creep} and $\sigma_{\text{Microcrck}}$ are the stresses due to oxide creep and microstructural damage, and σ_{Mech} is as a result of mechanical loading [49]. Some types of corrosion related to high temperature applications are listed below:

(i) Uniform corrosion: occurs evenly across the component surface at a predictable rate and can be protected against using coatings, inhibitors or cathodic protection.

(ii) Stress corrosion: due to tensile stresses in conjunction with a corrosive environment can cause crack initiation and propagation from a metal surface i.e. stress corrosion cracking (generally localised).

(iii) Intergranular corrosion: grain boundary corrosion can cause grain removal, weakening the material to further corrosion attack.

(iv) Pitting corrosion: localised corrosion phenomenon that is highly destructive to the component and is largely unpredictable.

(v) Erosion-corrosion: flow of solid, liquid or gas occurs around a metal component, causing grooves similar to its directional pattern.

Examples of this are shown schematically in Figure 2.20 [26].

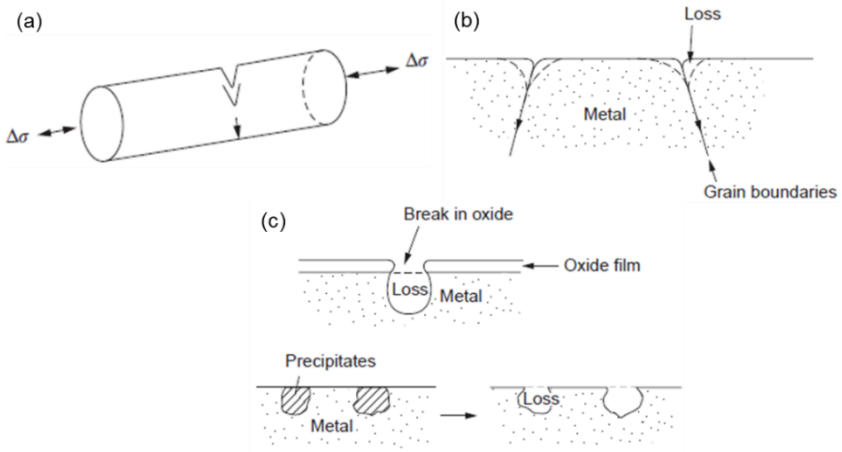

Figure 2.20 Schematic of different types of corrosion: (a) stress, (b) intergranular and (c) pitting. Adapted from [26].

Stresses due to oxidation can occur due to a mismatch in the volume of oxide layer and metal from which it forms. If this ratio is greater than unity (which it generally is), compression of the oxide occurs during inward migration of oxide ions, and results in oxide growth at the oxide-gas interface [50]. This can have a number of effects in terms of the behaviour of the oxide layer, as shown in Figure 2.21 [26]. Inclusions at or near the surface have also been found to contribute to oxide pit formation, as well as oxide scale fracture due to a mismatch in COE [44].

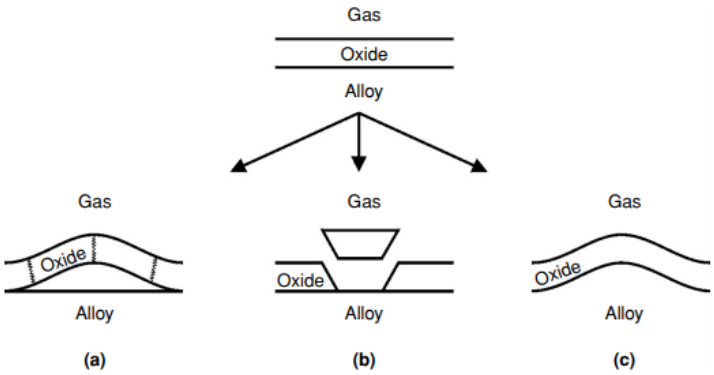

Figure 2.21 Effect of loading on the oxide scale: (a) buckling, (b) shear cracking and (c) plastic deformation of the oxide and alloy [26].

Oxide scale formation on the surface of steel components is dependent on chromium content, environment and temperature. Development of a continuous Cr_2O_3 scale on the

surface of components improves oxidation resistance and is aided by increased chromium content in the material (Figure 2.22). Once the chromium scale is no longer present, iron oxide forms leading to scaling and increased oxidation rates, known as breakaway oxidation or corrosion. Figure 2.23 shows mushroom-type oxide nodule formation in two layers. Once the outer surface (Fe-rich) formed, accelerated inner oxidation occurred and these weakened regions are sites for early crack initiation under mechanical loading. Annealing in air can cause heavy Cr-oxide scale formation, leaving the subsurface depleted. This becomes critical for thin-walled components, such a sheet or tubular products [41].

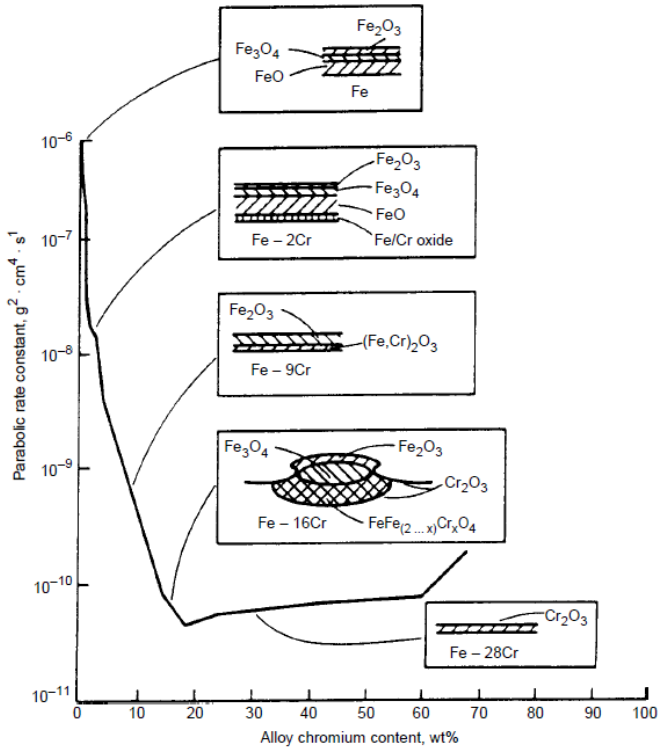

Figure 2.22 Oxidation behaviour as a function of chromium content in Fe-Cr alloys at 1,000 °C in 0.13 atm O_2 [41].

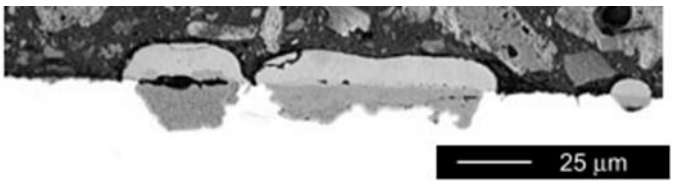

Figure 2.23 Formation of mushroom-type oxide nodules due to an accelerated oxygen attack on the surface of a heat exchanger tube, after heating between 620 °C and 670 °C in air for over 1,000 hours [41].

High temperature components in plant are generally under both thermal and mechanical loading. The mechanical loading can cause stresses in the component as a result of welding (residual) or manufacturing processes prior to service, and can remain in the component if the operating temperature is too low. Stresses can also occur due to external loads during service and can interact with the oxidation or corrosion processes due to temperature. Stress-corrosion cracking can occur in a metal under tensile stress and may experience cracking of the protective oxide layer as the tensile stresses or strains become higher. Abe *et al.* [41] observed significant internal oxidation in conjunction with loading; however, under no load, there was no change in oxide penetration depth up to 1,000 hours (Figure 2.24).

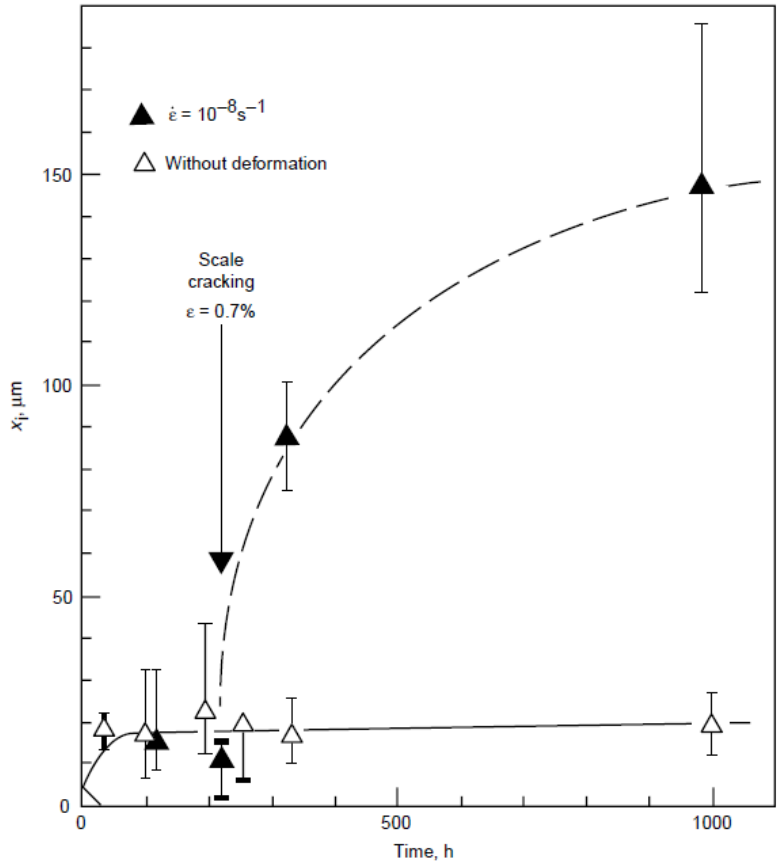

Figure 2.24 Internal corrosion depth in undeformed (open data points) and deforming (closed data points) 18%Cr specimens at 800 °C and $\dot{\varepsilon} = 10^{-8}$ s^{-1} [41].

2.4.4 Effect of Fuel Type

Components in high temperature environments under fossil fuel combustion undergo accelerated oxidation levels due to salt deposits, known as Hot Corrosion 1. Melting of the deposit usually occurs and the rate is approximately linear. Hot Corrosion 2 occurs at temperatures below the deposit melting point and is initially slow, then suddenly

increases as the salt reacts with the oxidation products, resulting in a lower melt temperature [41]. Oxide scale formation is identified as a primary factor in the significantly reduced creep strength at 650 °C in a 2.25Cr-1.6W steel for USC power plant applications. The long-term creep strength degrades rapidly at 625 °C and upwards, in conjunction with microstructural degradation [51].

The fuel used in power plants can have a substantial effect on the corrosion resistance of materials. For example, coal burning is quite different from other fuels and is largely dependent on the sulphur (flue gas), sodium and potassium (ash) content. Quantification of the effect of these elements is necessary to more realistically identify the response of components in-service at high temperature. Design of high temperature alloys for the next generation of power plants must achieve at least equivalent levels of oxidation and corrosion resistance e.g. Figure 2.25. The effects of varying chemical composition and heat treatment, as well as consideration of the service conditions and environment the component will experience in plant, must be accounted for. This alone requires a substantial amount of research for design of a single alloy and highlights the need for improved predictive capabilities in terms of material models [40]. The increased use of biomass will further complicate the rate and methods of corrosion in plant and increase the range of materials components must be resistant to [44,52,53].

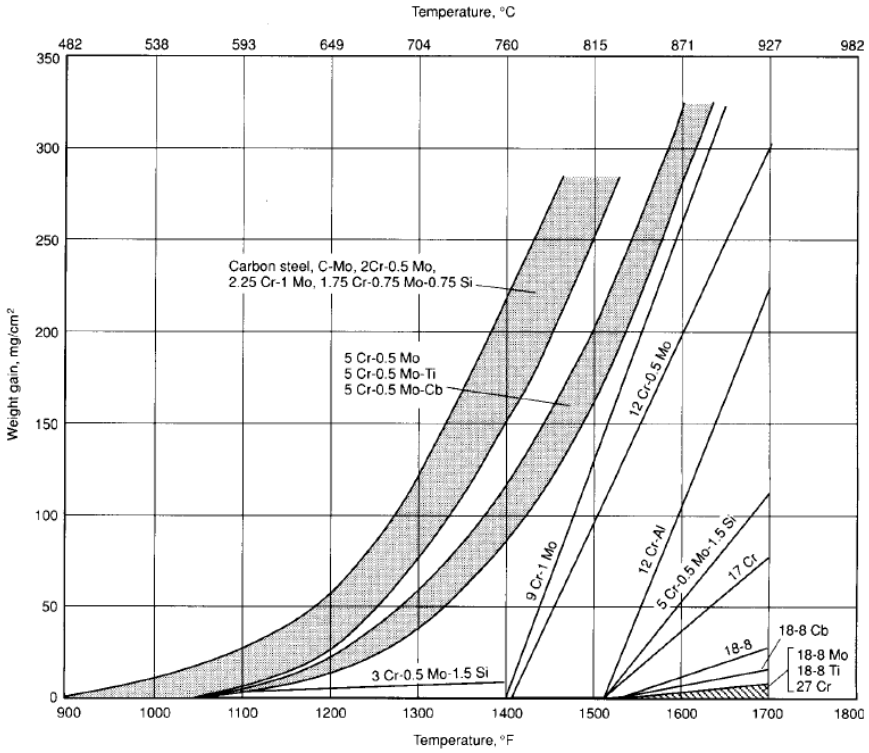

Figure 2.25 Oxidation resistance of various steels in air after 1,000 hours between 482 °C and 927 °C [41].

In service, components are exposed to an array of harsh chemicals. For example, coal is generally classified into 4 categories, from the lowest rank (lignite) to the highest (anthracitic). Properties such as moisture content, volatile matter and sulphur content vary between each group and can significantly affect component performance. Sulphur content is most detrimental in terms of corrosion in high temperature boiler components in plant, as well as the amount and type of emissions generated. Ash generated from coal combustion, in conjunction with flue gases, can cause fly-ash erosion on heat-absorbing surfaces e.g. superheater and furnace wall, leading to heat transfer problems (i.e. raising the temperature of the component and reducing the rate of cooling) and require regular removal (Figure 2.26). The temperature of components can affect whether ash is easily removed or not, as at melting temperature it can form a tightly-bonded slag on the component wall [41].

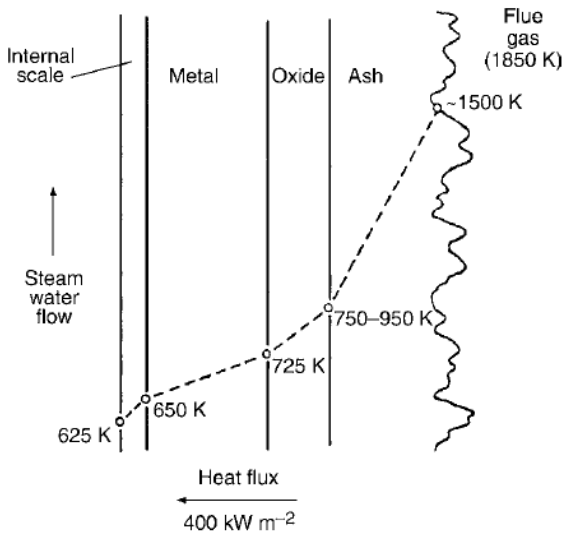

Figure 2.26 Schematic of temperature gradient from the inner to the outer oxide scale and ash/slag deposits on a tube [41].

In an effort to further reduce emissions, the use of carbon-neutral fuel biomass (i.e. organic materials such as wood and agricultural crops) has been implemented in some plants. However, this has been found to lead to accelerated corrosion of plant components due to an altered ash composition. O'Hagan *et al*. [54] applied salts, representative of ash produced during biomass co-firing of peat, to P91 steel at 600 °C up to 28 days. In Figure 2.27(a, b), oxide scale spallation and cracking is observed in a multi-layer structure. Furthermore, both chlorine and temperature are found to promote significant oxide scale growth under short-term conditions (Figure 2.27(c, d)).

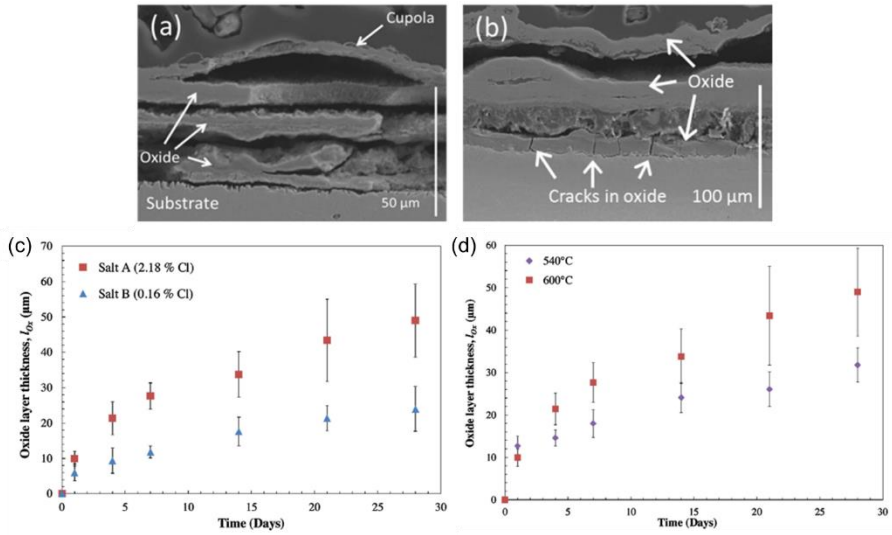

Figure 2.27 Oxide scale structure of P91 at 600 °C for (a) 7 and (b) 28 days, and (c) effect of chlorine content and (d) temperature on oxide scale thickness over time [54].

Skrifvars *et al.* [55] applied a salt (25Na-11K-21S-1.3Cl) with a melt temperature of 526 °C to a range of power plant steels at various temperatures. In general, oxide scale thickness increases rapidly in a short time span (Figure 2.28), as the temperature approaches the melt temperature of the salt, indicating the potentially detrimental effect of biomass on component performance. Such studies indicate the complexities associated with chemical composition of power plant fuels in relation to the oxidation and corrosion resistance of components, and the importance of adequate corrosion resistance, particularly as temperature increases.

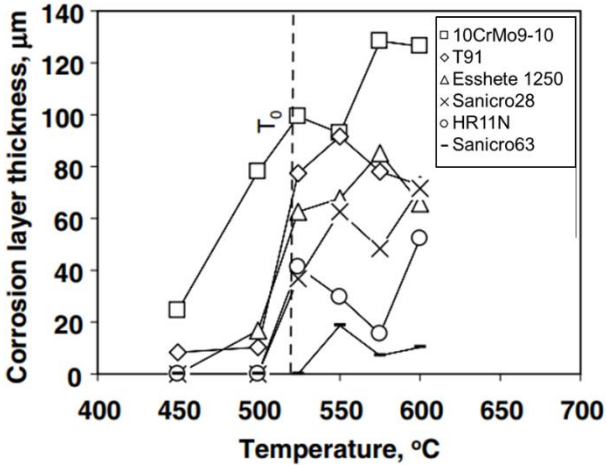

Figure 2.28 Oxide scale thickness as a function of temperature, after 168 hours, for a range of steels with salt applied. T_0 is the melt temperature of the salt [55].

2.5 High Temperature Low Cycle Fatigue

2.5.1 Introduction

Fatigue is the cyclic loading of a component that can lead to failure below the tensile strength of the material (and possibly below yield strength) due to fluctuation of mechanical or thermal loads. The main classes of fatigue are high cycle and low cycle fatigue. High cycle fatigue occurs below yield stress and typically above 10,000 cycles, whereas low cycle fatigue is the converse and incorporates plastic deformation. Crack growth under low cycle fatigue loading occurs due to tensile stresses in a plastic zone at the crack tip, leading to propagation under loading, perpendicular to the loading direction [26]. Under compressive loading, crack growth cannot occur as the crack faces are in contact, causing crack closure. When inclusions or voids are present in the material, hole formation can occur and allow linkage between defects and the crack tip (Figure 2.29), increasing the crack growth rate. Local plasticity around a stress concentration (e.g. a notch or an inclusion) leads to initially slow crack propagation, but eventually increases and component failure occurs [26].

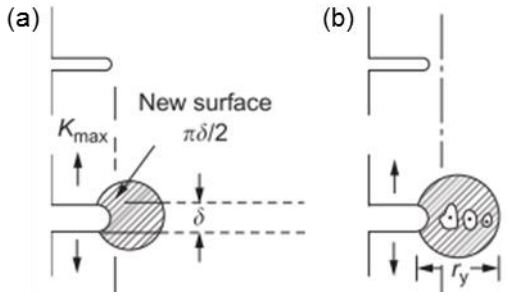

Figure 2.29 Fatigue crack growth (a) without and (b) with the presence of defects [26].

2.5.2 Experimental Testing and Microstructural Analysis

Low cycle fatigue testing of current state-of-the-art 9Cr steels (e.g. P91 and P92) has been performed to identify the effect of various alloying elements, in conjunction with microstructural analysis to understand the nano- and microscale strengthening and degradation mechanisms in operation under high temperature cyclic loading [9,47,64,56–63].

Low cycle fatigue (LCF) testing of 9Cr steel with varying tungsten content was performed by Park *et al.* [65] at room temperature and 600 °C. Significant cyclic softening and a reduction in fatigue life is observed at high temperature, with a tungsten content of 1.8% identified as the optimal amount for enhanced strengthening effects (Figure 2.30) and prevention of δ-ferrite formation. Softening is attributed to a decrease

in dislocation density due to redistribution from low to high density regions, forming low-energy dislocation configurations, and dislocation annihilation. A combination of solid solution and precipitate strengthening are identified as key contributors to the improved cyclic strength of the material as tungsten content increases. Mroziński *et al.* [63] investigated the influence of temperature on cyclic strength. In Figure 2.31, cyclic softening is clearly observed in all cases for a cast P91 material tested across a range of loading conditions, and oxide layer formation further contributes to a reduction in fatigue life as temperature increases.

Nagesha *et al.* [66] have identified similar behaviour in terms of microstructural evolution of 9Cr steels for in-phase (IP) and out-of-phase (OP) thermo-mechanical fatigue (TMF) loading, as well as isothermal fatigue. Figure 2.32 shows the effect of cyclic loading on the microstructural evolution of the material, where lath widening indicates annihilation of lath boundaries. Subgrain growth provides soft regions and contributes to the macroscale softening effect observed under cyclic loading. This indicates the complexities associated with such materials.

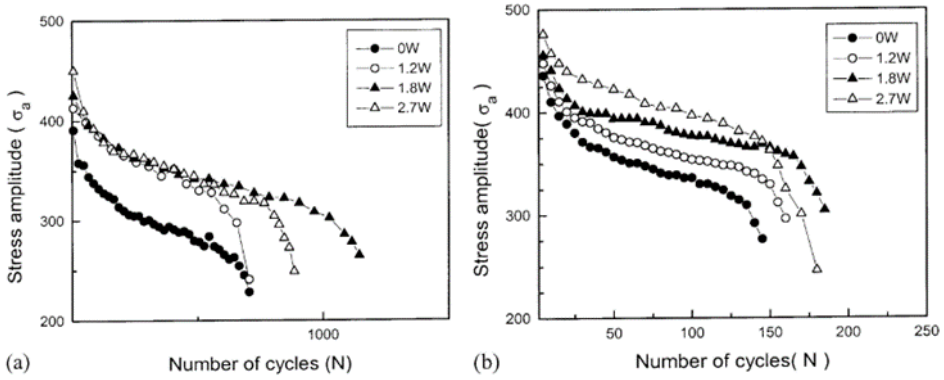

Figure 2.30 Effect of W content on stress amplitude with cycles at 600 °C and a total strain-range of (a) 0.5% and (b) 1.5% [65].

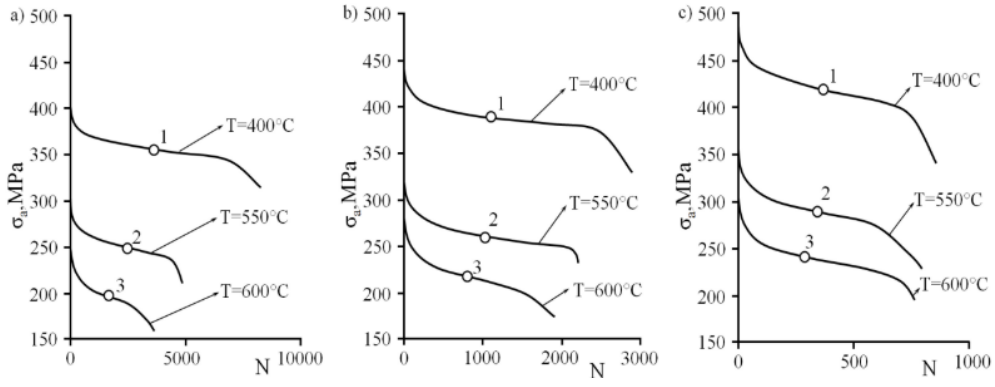

Figure 2.31 Influence of temperature on the stress evolution of cast P91 at a strain-range of (a) ±0.25%, (b) ±0.35% and (c) ±0.6% [63].

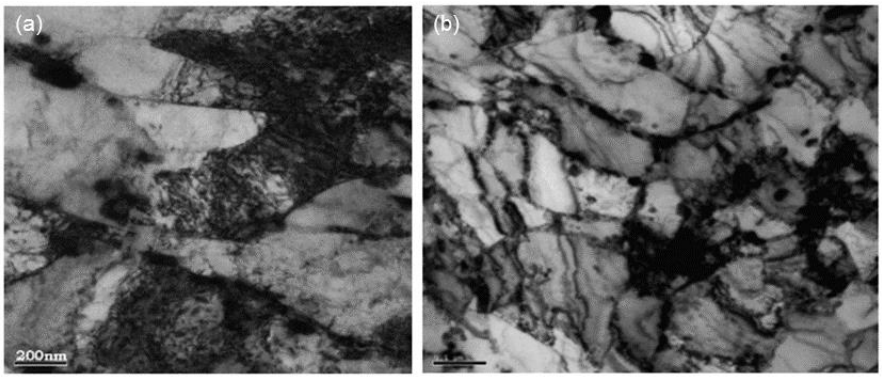

Figure 2.32 Transmission electron microscope (TEM) images of the microstructure of (a) as-received P91 steel with a high dislocation density, and (b) lath coarsening and reduced dislocation density due to out-of-phase TMF loading from 300 °C to 500 °C [66].

Thermo-Calc simulations of Laves phase formation in a 12Cr steel (up to 4% tungsten) predict increased thermal stability at higher temperatures, compared to those containing molybdenum. As the tungsten content increases, so too does the amount of Laves phase and the driving force for nucleation. This can produce an increased and finer precipitate distribution, complementing the strengthening due to $M_{23}C_6$ particles [67]. The role of Laves phase in 9-12Cr steels containing tungsten is not fully understood due to the combined effects of depletion of tungsten from the matrix (reducing the contribution of solid solution strengthening), while also increasing the contribution of precipitation strengthening [68].

2.6 Creep-Fatigue-Oxidation Interaction

Under realistic plant loading conditions, a component will experience creep, fatigue and oxidation effects. Therefore, it is vital to understand the role each of these will have, both individually and together, for material and component design. Fournier *et al.* [56–58] investigated the combined influence of creep, fatigue and oxidation on the behaviour of P91 steel at 500 °C. The influence of a hold period (particularly in compression), in conjunction with increased strain-range, is found to have a detrimental effect on the fatigue life of the sample (Figure 2.33). This has been attributed to a combination of environmental factors and the presence of a positive mean stress under compressive loading. Furthermore, the oxide scale is primarily subjected to tensile stresses and promotes crack initiation. Figure 2.34 presents measured oxide scale thickness as a result of both high temperature loading and static oxidation exposure. Formation of a multi-layered morphology (Fe-Cr spinel and magnetite), possibly due to

repeated oxide scale cracking, is observed under creep-fatigue conditions at a high strain-range. Fatigue and creep-fatigue testing (at lower strain-ranges) results in an oxide scale thickness similar to static oxidation testing, highlighting the influence of loading level on oxidation behaviour.

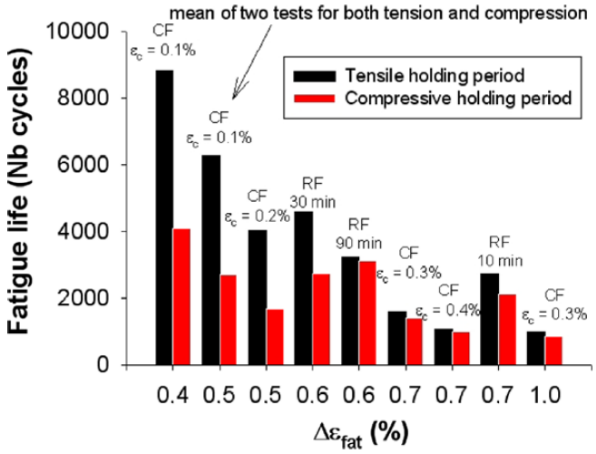

Figure 2.33 Effect of tensile and compressive hold periods on fatigue life for a variety of strain-ranges under creep-fatigue (CF) and relaxation-fatigue (RF) conditions [57].

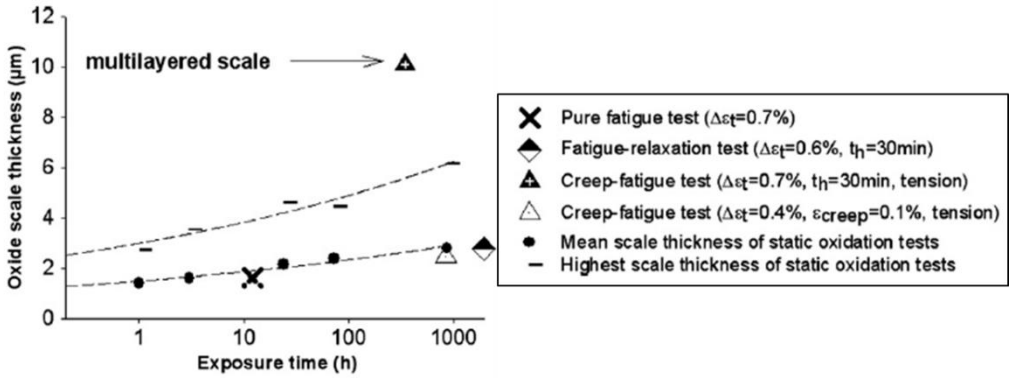

Figure 2.34 Oxide scale thickness as a function of exposure time for samples tested under fatigue, creep-fatigue and static oxidation conditions [56].

Similar results were observed by Shankar *et al.* [60] for a modified 9Cr-1Mo steel at 600 °C, with further reductions in fatigue life due to combined tension and compression holds in conjunction with oxidation effects. The influence of hold time on the dwell sensitivity factor (the ratio of the number of cycles to failure with a hold to the number of cycles to failure without a hold) is shown in Figure 2.35. A variety of 9-12Cr steels tested under pure fatigue and creep-fatigue loading at high temperature identified cyclic softening, due to reduced dislocation density, and subgrain coarsening as the primary degradation mechanism in all cases. A comparison of the as-received and post-test microstructure is presented in Figure 2.36 for P91, where significant coarsening of the

low angle boundary (LAB) microstructure is observed [69]. Figure 2.37 indicates the effect of a hold period on base metal and welded samples of P91, with a greater influence observed at higher temperature [70].

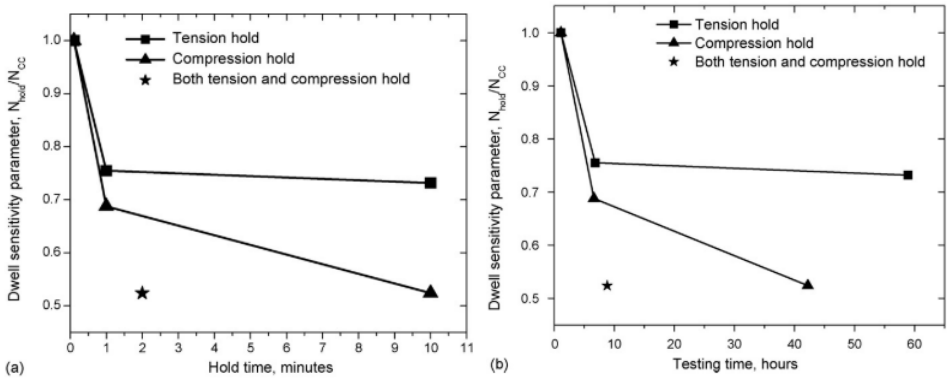

Figure 2.35 Influence of (a) hold time and (b) testing time on the dwell sensitivity parameter [60].

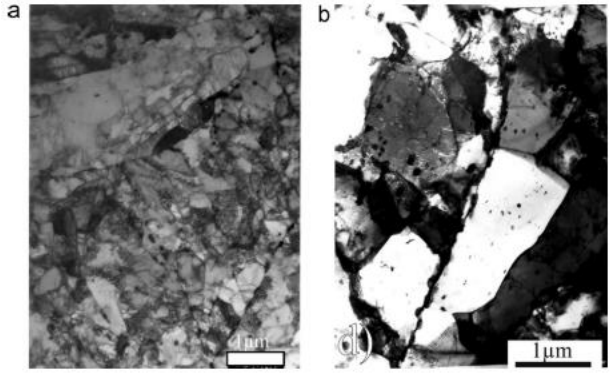

Figure 2.36 TEM of the microstructure of P91 (a) as-received and (b) post creep-fatigue test at 550 °C [69].

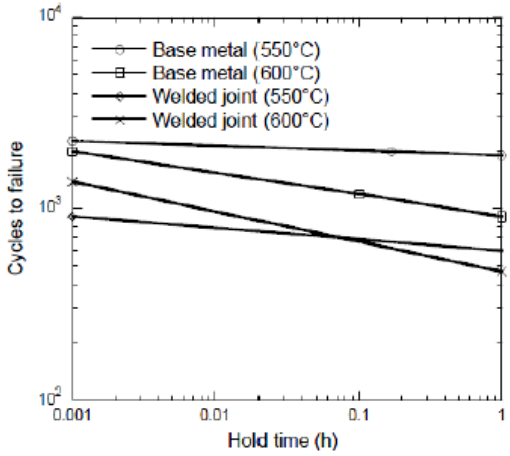

Figure 2.37 Creep-fatigue life as a function of hold time for P91 base metal and welded samples at 550 °C and 600 °C [70].

The effect of different loading types is presented in Figure 2.38 as a function of temperature; compared to OP, IP loading produces a greater rate of reduction in fatigue life with increasing temperature due to enhanced oxidation kinetics and, therefore, the concentration of key strengthening elements is reduced, leading to a weaker matrix material [66].

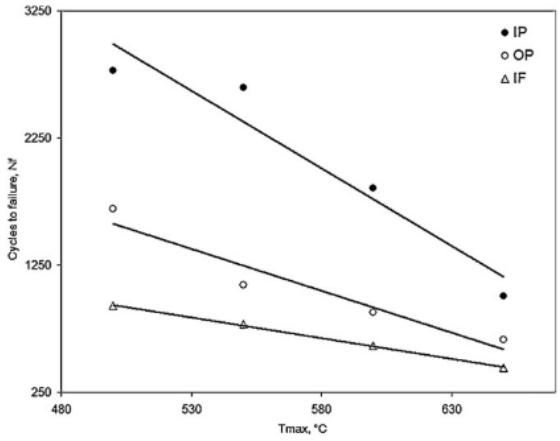

Figure 2.38 Effect of different loading regimes (in-phase, out-of-phase and isothermal fatigue) on fatigue life as a function of temperature [66].

2.7 Microscale Strengthening Mechanisms in 9Cr Steels

2.7.1 Martensitic Microstructure

9Cr tempered martensitic steels have a hierarchical microstructure comprising of prior austenite grains (PAG), packets, blocks and laths, as shown in Figure 2.39. A packet is a region of parallel laths with the same habit planes; depending on the degree of misorientation, laths with similar orientations are subdivided into blocks. Packets and blocks are defined as high angle boundaries, where neighbouring packets or blocks have angles of misorientation greater than 15°, and laths are low angle boundaries with angles of misorientation less than 5° [71–73]. Creep loading has been found to cause martensitic lath transformation to equiaxed subgrains due to dislocation motion, leading to a reduced creep rate [74]. There are a number of complex strengthening mechanisms associated with the hierarchical microstructure. However, it is difficult to quantify the individual contribution from each mechanism. Strengthening occurs due to a combination of grain boundary (GB) strengthening, precipitates distributed along boundaries and within the lath, dislocation substructure and solute atoms [71,72].

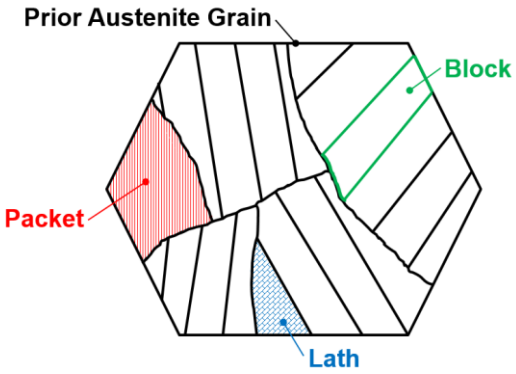

Figure 2.39 Schematic of the hierarchical microstructure of martensitic steels, adapted from [9].

2.7.2 Precipitate and Solute Strengthening

During heat treatment, precipitation occurs of $M_{23}C_6$ (M = Cr, Fe, W, Mn, Mo) carbides along boundaries and MX (M = V, Nb, and X = C, N) carbonitrides distributed throughout the matrix. $M_{23}C_6$ carbides are a primary source of creep strength in 9-12Cr martensitic steels, as they (i) reduce dislocation motion and subgrain growth and (ii) pin boundaries, hence reducing grain growth (Figure 2.40). MX carbonitrides act in a similar manner, and have a high thermal stability compared to $M_{23}C_6$ carbides [24,75]. A comparison between steels with and without $M_{23}C_6$ particles by Maruyama *et al.* [24] shows improved creep resistance through a reduced rate of recovery of the dislocation substructure due to the presence of $M_{23}C_6$ carbides. The addition of MX particles was found to significantly reduce the creep rate, where the particles act as obstacles to dislocation motion, as well as (i) reducing the rate of dislocation substructure recovery and (ii) retaining dislocation hardening for increased time.

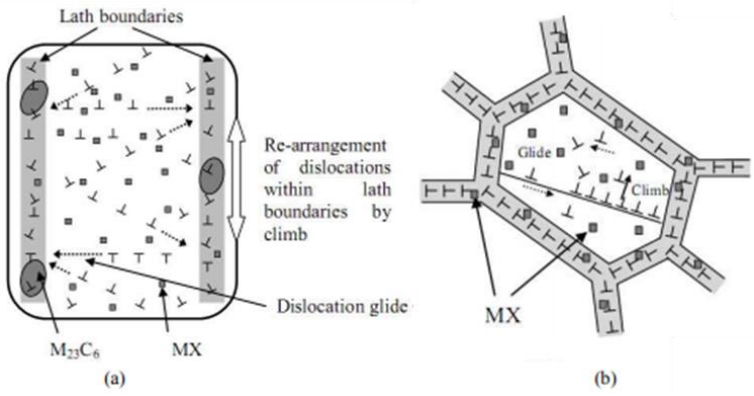

Figure 2.40 Schematic of a martensitic lath after tempering and (b) during subgrain coarsening. Adapted from [74].

Solid solution hardening occurs when larger atoms (e.g. Mo and W) replace solvent atoms in the lattice and produce distortion. As with precipitation strengthening, these particles contribute to reduced dislocation motion and resulting plastic deformation [8]. The effect of W on the macroscale component performance was presented in Section 2.3 and Section 2.5 for creep and fatigue loading. However, solid solution hardening can lead to the precipitation of Fe_2M (M = Mo, W) particles, also known as Laves phase. They form along boundaries during service conditions, as the heat treatment temperatures are often too high to allow precipitation. Their presence has been shown to be both detrimental (rapid particle coarsening and reduced solution hardening) and beneficial (refined precipitate diameter and enhanced GB strengthening) to creep behaviour, depending on saturated particle diameter and tungsten content in the material [23,24,76]. Z-phase (Cr(V, Nb)N) particles can also precipitate in high Cr ferritic steels during service and rapidly coarsen, reducing the effect of MX carbonitrides [24]. Phase equilibrium diagrams for both P91 and P92 are presented in Figure 2.41, indicating the conditions necessary for Laves phase and Z-phase formation.

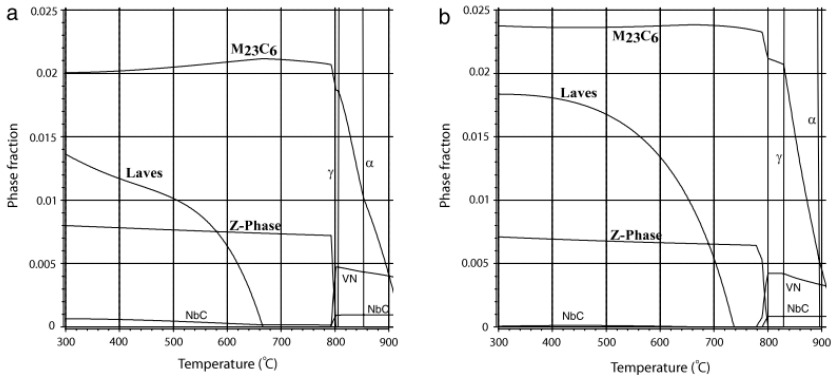

Figure 2.41 Phase equilibrium diagrams for (a) P91 and (b) P92 steel [77].

2.7.3 Dislocation Hardening

At intermediate temperatures, mobile dislocations pass through the dislocation substructure through the aid of an applied stress. However, at elevated temperatures, mobile dislocation motion occurs via diffusion, where particles at a region of high concentration move to a region of lower concentration, hence reducing yield stress. The dislocation substructure is shown to be the primary obstacle to dislocation motion during creep testing, where the accumulation of creep strain corresponds to recovery of the dislocation substructure [24]. Plastic deformation of the dislocation substructure promotes recovery, where subgrain width increases and the dislocation density decreases as creep deformation progresses. Two processes that occur during the

recovery of the subgrain substructure are (i) annihilation of dislocations on a sub-boundary, hence annihilating the sub-boundary, and (ii) mutual sub-boundary annihilation due to opposite signs (Figure 2.42). Process (i) is dominant in the early recovery stage [24]. Guguloth *et al.* [78] investigated the low cycle fatigue behaviour of a modified 9Cr-1Mo steel. Microscale mechanisms of degradation (e.g. dislocation annihilation and precipitate coarsening) were identified as primary contributors to cyclic softening, particularly as test temperature increased from 500 °C to 600 °C.

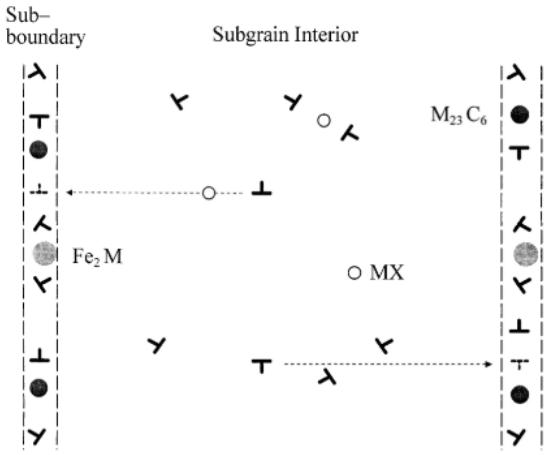

Figure 2.42 Schematic of dislocation recovery along boundaries [24].

2.8 Effect of Alloying Elements

2.8.1 Introduction

This section discusses the effect of various alloying elements on the microscale strengthening of modified 9Cr steels. For reference, the chemical compositions of various modified 9Cr alloys are presented in Table 2.1.

Table 2.1 Chemical composition of modified 9Cr steel P91 [59], P92 and MarBN [38]. Balance is Fe and * denotes mass (%).

	Al	**B***	**C**	**Co**	**Cr**	**Mn**	**N**	**Nb**	**P**	**Si**	**V**	**W**
P91	0.007	-	0.12	-	8.60	-	0.060	0.07	0.017	0.34	0.24	0.03
P92	-	0.002	0.09	-	8.72	0.47	0.050*	0.06	-	0.16	0.21	1.87
MarBN (min)	-	0.005	0.074	2.91	8.77	0.48	0.001*	0.046	-	0.3	0.18	2.85
MarBN (max)	-	0.018	0.081	3.1	9.08	0.51	0.065*	0.055	-	0.31	0.2	3.13

2.8.2 Chromium

Figure 2.43 indicates the effect of chromium content in bainitic (low Cr) and martensitic (high Cr) steels without MX precipitates. The decrease in creep rupture strength and increase in ductile-to-brittle transition temperature (DBTT) at chromium content above 10% is due to δ-ferrite formation, as no carbides, subgrains and significantly reduced dislocation densities are present in these regions. This further indicates the importance of the hierarchical microstructure in providing resistance to plastic deformation [38].

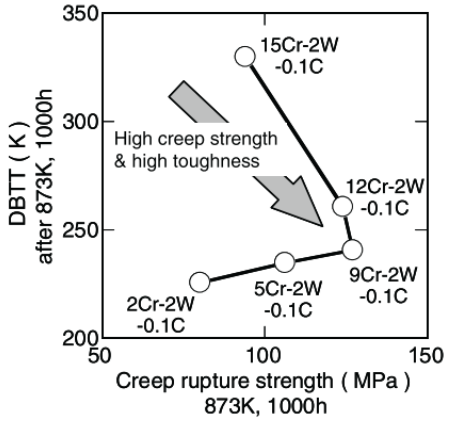

Figure 2.43 The effect of Cr content on creep rupture strength and DBTT at 600 °C for 1,000 hours [38].

2.8.3 Tungsten

Tungsten has been identified as a key component in providing enhanced high temperature creep performance in modified martensitic steels. Figure 2.44 shows TEM images of steels containing 1% and 4% tungsten, post-creep test at 600 °C. For 1% tungsten (Figure 2.44(a)), a significant reduction in $M_{23}C_6$ carbide distribution along boundaries and increased lath coarsening is observed compared to the 4% tungsten sample (Figure 2.44(b)).

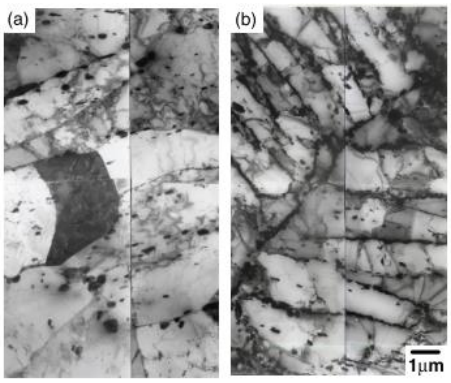

Figure 2.44 TEM images of creep samples tested at 600 °C containing (a) 1% tungsten and (b) 4% tungsten [38].

In Figure 2.45, the effect of tungsten on creep rupture strength, and precipitate and lath evolution is presented. Formation of significant quantities of δ-ferrite occurs after the concentration of tungsten exceeds 3%. Tungsten reduces the coarsening rate of $M_{23}C_6$ carbides and laths, enhancing the precipitation hardening effect, but this effect reduces with increasing temperature, indicating the enhanced strength due to tungsten occurs from a combination of solid solution, precipitation and sub-boundary hardening [38].

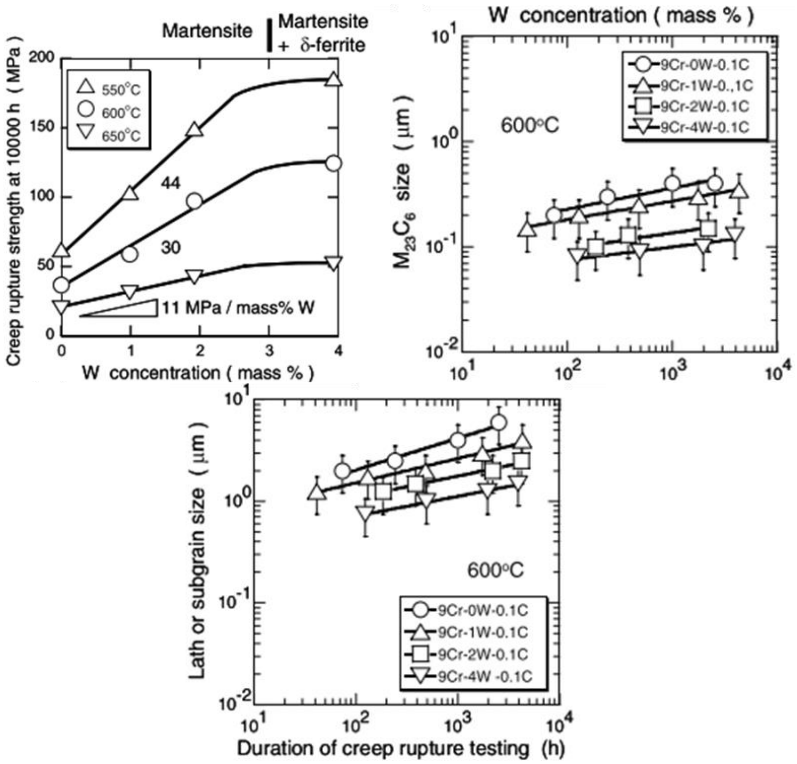

Figure 2.45 (a) Effect of tungsten on the creep rupture strength of martensitic steel at 10,000 hours, and (b, c) evolution of $M_{23}C_6$ and lath or subgrain size with increasing time [38].

2.8.4 Boron and Nitrogen

Grain boundary segregation of boron occurs during normalising. This is followed by $M_{23}C_6$ carbide formation along boundaries, as the tempering temperature is reduced, resulting in boron enrichment of carbides and reduced coarsening [38].

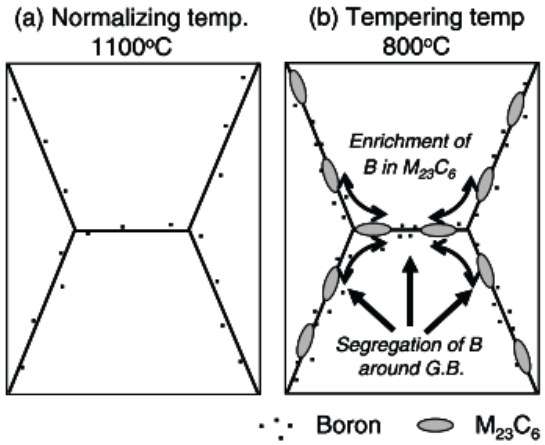

Figure 2.46 $M_{23}C_6$ carbide formation during (a) normalising and (b) tempering [38].

Figure 2.47 shows that for a 9Cr-3W-3Co steel (excluding nitrogen), increasing the amount of boron concentration produces a lower creep rate and increased time to rupture. Boron provides increased stabilisation of $M_{23}C_6$ carbides along boundaries and, hence, reduced lath and block boundary coarsening, preventing recovery of the microstructure for longer [8].

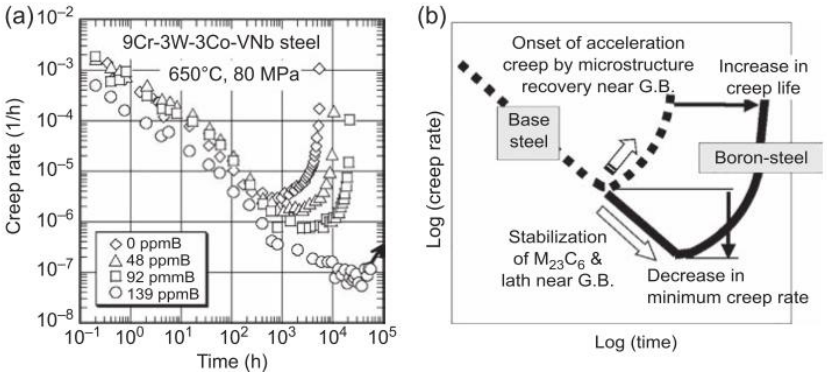

Figure 2.47 (a) Effect of increased boron on the creep rate of 9Cr steel at 650 °C and 80 MPa, and (b) schematic of the mechanism of boron stabilisation of the microstructure in terms of creep rate [8].

Figure 2.48 shows the effect of nitrogen concentration in a steel containing 140 ppm boron, in terms of creep behaviour and BN formation. The peak minimum creep rate and rupture time are found to occur between 80 ppm and 100 ppm nitrogen, and BN formation during normalising at 1100 °C is dependent on the maximum solid solubility of nitrogen and relevant boron content. The amount of nitrogen must be carefully controlled to prevent BN formation, that can lead to boron and nitrogen consumption and reduced creep strength [79–81].

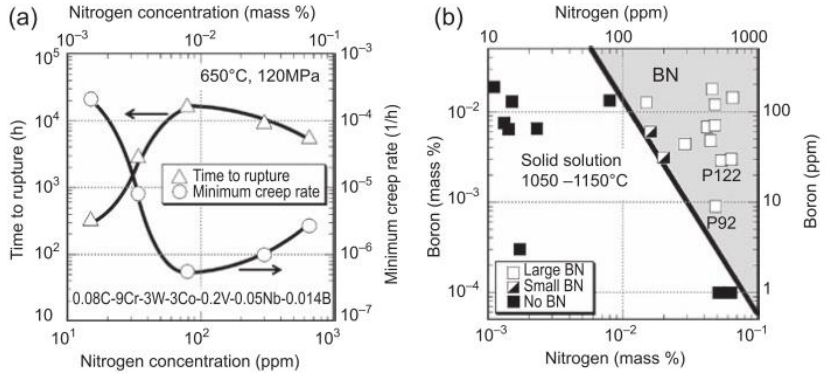

Figure 2.48 (a) Effect of nitrogen content on rupture time and minimum creep rate of 9Cr steel, and (b) BN formation as a function of nitrogen and boron content at a normalising temperature between 1050 °C and 1150 °C [79,80].

Such research and development on the effect of various alloying elements has led to the production of MarBN steel; the name denotes a martensitic 9Cr steel, with controlled levels of boron and nitrogen. Figure 2.49 compares both base metal and welded joints for MarBN, P92 and P122 at 650 °C. Failure of welded P92 and P122 occurs much more rapidly compared to the base metal, whereas MarBN maintains increased strength for the duration of testing, as well as almost identical performance between base metal and welded components, indicating Type IV cracking has been suppressed and preservation of the hierarchical microstructure in the heat affected zone [82]. Type IV fracture in the heat affected zone of 9-12Cr steels at elevated temperatures is a known issue, where the hierarchical microstructure is replaced by a weaker fine-grained zone during welding, and results in premature cracking and failure. This is a serious issue in terms of flexible plant operation, as increased thermal cycles can accelerate damage in these areas and further reduce component life [83]. To date, research has focused largely on the creep behaviour of MarBN material, but as power plants move toward increased flexible operation, the effect of cyclic loading on MarBN must be investigated.

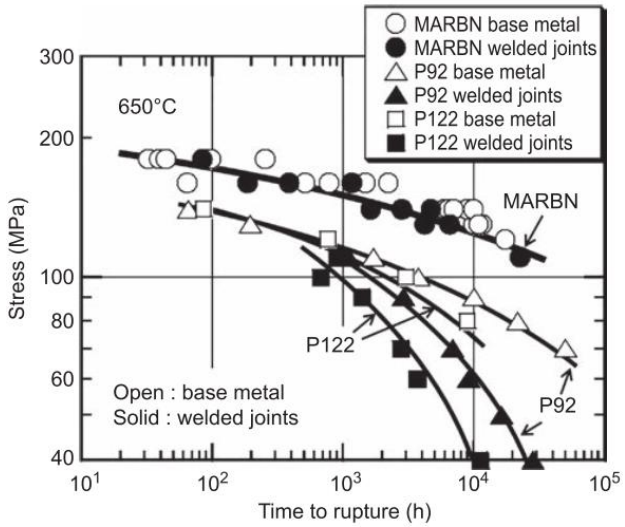

Figure 2.49 Creep rupture curves for MarBN, P92 and P122 base metal and welded joints at 650 °C [82].

2.9 Constitutive Modelling

2.9.1 Introduction

Modelling of 9Cr steels is an important tool in understanding the material behaviour under high temperature loading, in terms of (i) uniaxial and multiaxial macroscale response, (ii) microstructure evolution, and (iii) localised behaviour in the region of manufacturing defects. Based on experimental testing, a number of models have been developed to predict and understand the fatigue response of various materials, as well as predict rates of damage accumulation and failure.

2.9.2 High Temperature Low Cycle Fatigue Modelling

The unified model of Chaboche [84,85], based on a power law flow rule, is broadly used to predict the cyclic viscoplastic behaviour of metals. The constitutive equation is as follows:

$$\dot{p} = \left\langle \frac{f}{Z} \right\rangle^{n} = \left\langle \frac{\mathrm{J}_2(\mathbf{s}-\mathbf{x}) - R - k}{Z} \right\rangle^{n} \tag{2.4}$$

where $\dot{p}$ is the accumulated effective plastic strain-rate, $\mathbf{s}$ is the deviatoric stress tensor, $\mathbf{x}$ is the kinematic back-stress tensor, R is isotropic hardening, k is the initial yield stress, Z is a material constant and n is the cyclic viscoplastic exponent. The various stress components are described graphically in Figure 2.50 [84].

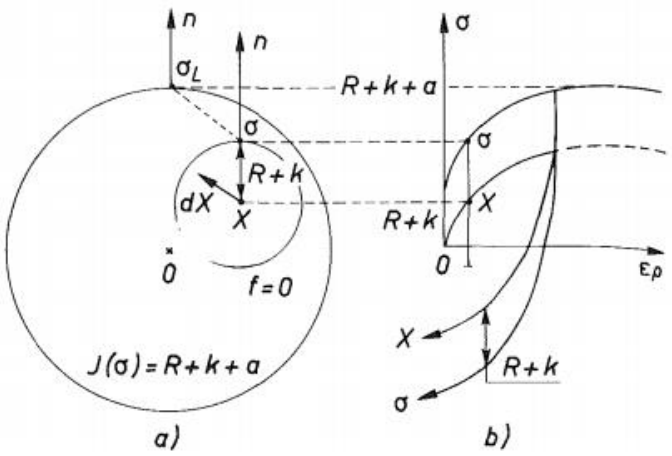

Figure 2.50 Influence of the non-linear kinematic rule for (a) two-surfaces theory and (b) fully-reversed cyclic loading [84].

The rate of isotropic hardening evolution, $\dot{R}$, is calculated as per:

$$\dot{R} = b(Q - R)\dot{p} \tag{2.5}$$

where b is the rate of softening and Q is the asymptotic value of R. The isotropic hardening rule assumes equal expansion of the elastic domain in tension and compression during plastic flow, as described graphically in Figure 2.51 [86].

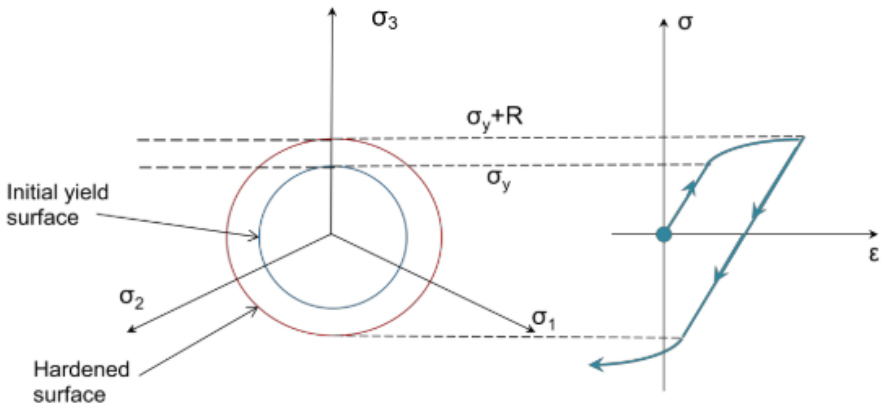

Figure 2.51 Schematic of isotropic hardening and associated stress-strain response [86].

Kinematic hardening, based on the Armstrong-Frederick model [87], is calculated as:

$$\dot{\chi} = \frac{2}{3} c\dot{\varepsilon}_{\text{pl}} - \gamma \chi \dot{p} \tag{2.6}$$

where c and γ are material constants, and $\dot{\varepsilon}_{\text{pl}}$ is plastic strain-rate. Translation of the yield surface occurs during kinematic hardening, as per Figure 2.52. The materials resistance to yielding in compression, as a result of loading in tension, is therefore reduced; this is known as the Bauschinger effect [86].

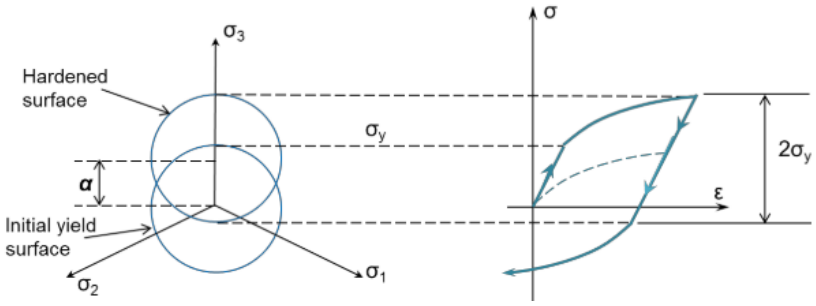

Figure 2.52 Schematic of kinematic hardening and associated stress-strain response [86].

This use of this type of model (i.e. power law flow rule) has been effectively implemented previously for intermediate to high strain-rate cases [88–92]; however, it cannot allow reliable extrapolation to more typical plant conditions, as described in Figure 2.53. As a result, the use of a hyperbolic sine material model has been implemented by Barrett *et al.* [93,94], based on the experimentally observed non-linear stress-strain behaviour of 9Cr martensitic steels at high temperature.

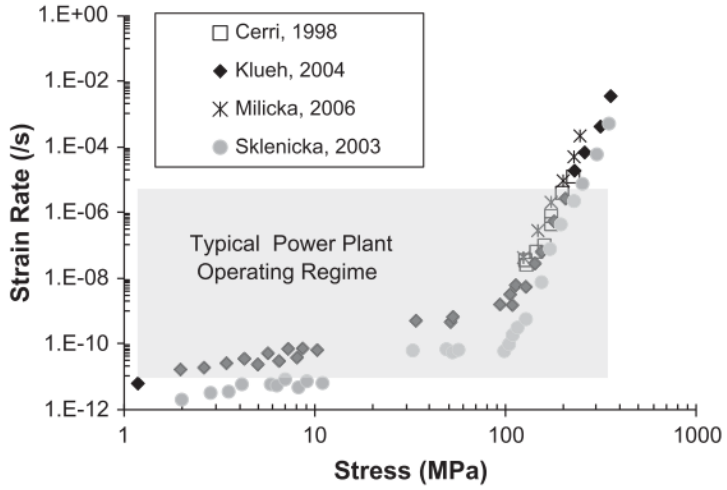

Figure 2.53 Strain-rate versus stress for 9Cr steels at 600 °C [93].

Based on the complex nature of the microstructure of advanced 9Cr martensitic steels, modelling of microstructural evolution has been performed from a physical basis to identify the individual contribution of the various strengthening mechanisms [95–98]. Precipitate and lath coarsening are primary degradation mechanisms associated with high temperature cyclic loading of modified 9Cr steels. Crystal plasticity modelling by Li *et al.* [96] of P91 under cyclic loading conditions has predicted a considerable effect of both factors, in terms of number of cycles to fatigue crack initiation. In the case of prior creep loading of a power plant component under flexible loading conditions, this could be detrimental to component lifetime.

Barrett *et al.* [72] implemented a dislocation-based methodology, in conjunction with a cyclic viscoplasticity model, to predict the effect of dislocation density and precipitate size on cyclic softening and kinematic hardening under high temperature low cycle fatigue (HTLCF) loading in P91 steel. This model has been further developed to be more physically representative of the microstructural evolution and predict the complete effects of various strengthening mechanism, with application to both HTLCF and CF loading [97]. In Figure 2.54, the effect of block size predicts that a coarser microstructure will reduce stress-range and increase plastic strain-range under strain-controlled LCF conditions. After 1,000 cycles, an increased volume fraction of precipitates (MX and $M_{23}C_6$), is predicted to provide enhanced cyclic strength and a reduced plastic strain-range (Figure 2.55). Furthermore, lath width is predicted to be dominant in producing enhanced cyclic strength and reducing plastic strain under cyclic loading; the rate of cyclic softening is reduced as lath width decreases and, therefore, an increase in LCF life is assumed.

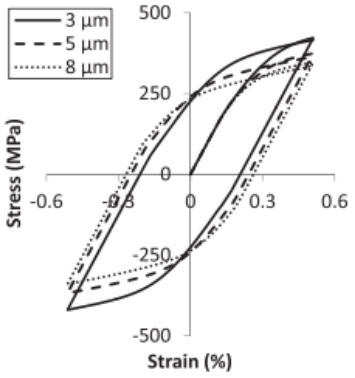

Figure 2.54 Influence of block width on the initial stress-strain loop at 600 °C, $\dot{\varepsilon}$ = 0.1 %/s and $\Delta\varepsilon$ = ± 0.5 % [97].

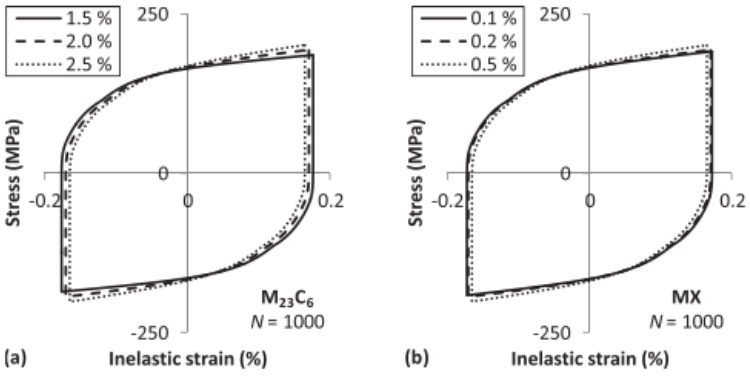

Figure 2.55 Influence of the volume fraction of (a) $M_{23}C_6$ carbides and (b) MX carbonitrides in P91 at 600 °C, for N = 1,000, $\dot{\varepsilon}$ = 0.025 %/s and $\Delta\varepsilon$ = ±0.3% [97].

2.9.3 Life Prediction

Calibration and validation of models to predict damage accumulation and cycles to failure (typically based on uniaxial experimental data) allows greater understanding of the effect of loading when applied to multiaxial geometries and plant components. Figure 2.56 is a schematic of the Basquin and Coffin-Manson laws for each type of fatigue loading. In Figure 2.56(a), high cycle fatigue is shown to occur below the yield stress of the material, for over 10,000 cycles. The Coffin-Manson law (Figure 2.56(b)) is based on the linear relationship obtained by plotting log of the plastic strain-range versus log of number of cycles to failure.

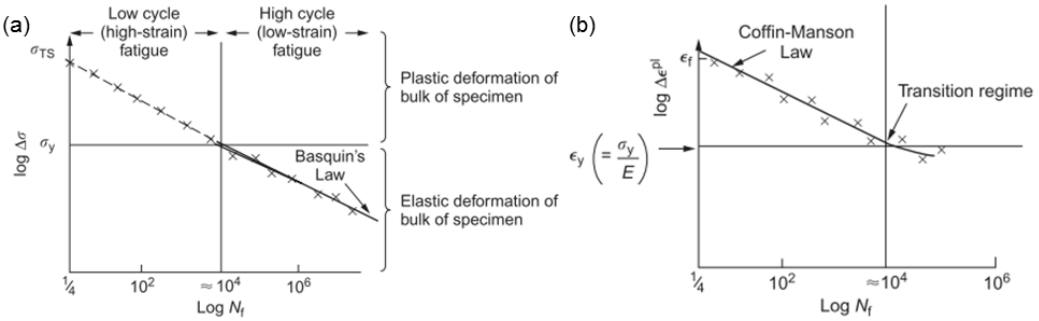

Figure 2.56 Schematic of (a) Basquin law for high cycle fatigue and (b) Coffin-Manson law for low cycle fatigue loading [26].

The Basquin equation [99] is defined as follows:

$$\Delta\sigma N_{\mathrm{f}}^{a} = C_1 \tag{2.7}$$

where the stress range is $\Delta\sigma = \sigma_{\max} - \sigma_{\min}$, N_{f} is number of cycles to failure and a and C_1 are material constants. A similar relationship exists for low cycle fatigue loading, whereby the Coffin-Manson Law [100] is:

$$\Delta\varepsilon^{\mathrm{pl}} N_{\mathrm{f}}^{b} = C_2 \tag{2.8}$$

where $\Delta\varepsilon^{\mathrm{pl}}$ is the plastic strain-range, and b and C_2 are material constants. The Smith-Watson-Topper [101] fatigue parameter combines the Basquin and Coffin-Manson approaches, as per:

$$SWT = \sigma_{\max}\frac{\Delta\varepsilon}{2} = \frac{\sigma_{\mathrm{f}}^{'2}}{E}\left(2N_{\mathrm{f}}\right)^{2d} + \sigma_{\mathrm{f}}^{'}\varepsilon_{\mathrm{f}}^{'}\left(2N_{\mathrm{f}}\right)^{d+f} \tag{2.9}$$

where $\sigma_{\max}$ is maximum stress, $\Delta\varepsilon$ is maximum strain-range, E is Young's modulus, the Basquin coefficients are $\sigma_{\mathrm{f}}^{'}$ and d, and the Coffin-Manson constants are $\varepsilon_{\mathrm{f}}^{'}$ and f.

This model has been implemented by Zhang *et al.* [102], in conjunction with elastic modulus reduction due to fatigue damage.

In terms of energy based models, Ellyin and Kujawski [103] developed a fatigue model dependent on plastic strain energy per cycle, as follows:

$$W = KN_{\mathrm{f}}^{a} \tag{2.10}$$

where W is plastic strain energy per cycle, and K and a are material parameters identified by plotting experimental data for plastic strain energy per cycle versus cycles to failure. The Ostergren [104] model is a strain energy based model, which takes into account both the stress and plastic strain per cycle, to predict number of cycles to failure.

$$N_{\mathrm{f}} = C\left(\Delta\varepsilon^{\mathrm{pl}}\Delta\sigma_{\max}\right)^{\beta} \tag{2.11}$$

where $\Delta\sigma_{\max}$ is the maximum stress range and C and β are material constants. This method has been found to give improved fatigue life prediction compared to the Coffin-Manson equation, particularly in terms of thermo-mechanical fatigue loading [105].

2.9.4 Damage

To identify the effect of increasing cycles on the degradation of the material, a relatively large number of models have been developed with respect to simulating fatigue damage. The concept of a damage parameter was first introduced by Kachanov [106] and following this, Rabotnov [107] introduced an effective stress concept for a material under tensile loading, based on the growth of microdefects. A linear damage summation rule created by Miner [108] is described by:

$$D = \sum \frac{n_{\mathrm{i}}}{N_{\mathrm{f}}} \tag{2.12}$$

where D is damage and n_{i} is cycle number at a given stress amplitude ($\Delta\sigma_{\mathrm{i}}$). However, this method does not account for load history and can produce non-conservative predictions of life [109]. Damage can be regarded as the degradation of the Young's modulus of the material [110], whereby an effective Young's modulus is defined as:

$$\tilde{E} = \frac{\Delta\sigma}{\left(\Delta\varepsilon - \Delta\varepsilon_{\mathrm{pl}}\right)} \tag{2.13}$$

and, therefore, damage is calculated as:

$$D = 1 - \frac{\tilde{E}}{E} \tag{2.14}$$

This concept has been implemented in a damage model, based on the total strain approach, by Lu *et al.* [111] for P91 steel at 600 °C under uniaxial cyclic loading conditions, in conjunction with a Coffin-Manson law (Equation 2.8), where damage is assumed to initiate at the start of loading.

The Chaboche [112] equation for damage accumulation, based on the current cycle and number of cycles to failure, is described as follows:

$$D = 1 - \left[1 - \left(\frac{N}{N_\mathrm{f}} \right)^{\frac{1}{1-\alpha}} \right]^{\frac{1}{\beta-1}} \tag{2.15}$$

where N is cycle number, and α and β are material constants. Lemaitre [113] developed a damage rate term incorporating the effects of both stress and strain per cycle:

$$\dot{D} = \left(\frac{\sigma_{\max}^2 R_\mathrm{v}}{2ES\left(1-D\right)^2} \right)^s \dot{p} \tag{2.16}$$

where $\sigma_{\max}$ is the maximum stress in the cycle, R_v is the triaxiality ratio, and S and s are material constants. Nayebi *et al.* [114] applied this to life assessment of a gas turbine rotor steel, and Kyaw *et al.* [115] implemented this method in conjunction with a unified viscoplasticity model for P91 steel. The calculation of damage begins once an experimentally identified value of accumulated effective plastic strain has been reached. Priyaajit *et al.* [116] implemented a modified version of this in a plasticity coupled continuum damage mechanics model for 1020 steel.

The work of Neu *et al.* [47,117] analysed damage in 1070 steel due to fatigue, creep and oxidation under isothermal, in-phase and out-of-phase loading. Damage is calculated as:

$$D_\mathrm{tot} = D_\mathrm{fat} + D_\mathrm{creep} + D_\mathrm{ox} \tag{2.17}$$

where D_tot is total damage, and D_fat, D_creep and D_ox are damage due to fatigue, creep and oxidation. D_fat is calculated using the Smith-Watson-Topper approach. The interaction between creep and fatigue loading has also been investigated using a number

of approaches, including strain range partitioning and linear damage summation [89,118,119].

2.10 Influence of Manufacturing Defects and Void Growth

2.10.1 Introduction

The presence of manufacturing defects (i.e. voids and inclusions) is often related to the reduced cyclic strength of high strength alloys. A number of factors including matrix material, inclusion type and interface properties effect the fatigue cracking behaviour [120]. Inclusions occur in metallic alloys as a result of chemical reactions with the environment during manufacture and substantial financial resources have been invested in reducing such discontinuities in steels. The presence of inclusions leads to void formation during loading and results in premature cracking of components. The strength and toughness of steels, and benefits of microstructural refinement, are detrimentally affected, and increased plastic deformation and stress and strain localisation occur at the interfaces between inclusions and the matrix [54,121–125]. These regions have been found to influence the direction of crack propagation, causing a crack to preferentially move from the matrix towards an inclusion. It is important to understand the effect of inclusions and voids for various in-service loading conditions via experimental and computational methods [54,126–129].

2.10.2 Experimental Testing and Analysis

In Figure 2.57, the variation of different shapes of creep cavities is defined by Isaac *et al.* [130] for a brass alloy using synchrotron X-ray tomography, where complex cavities are found to occur due to coalescence of multiple cavities.

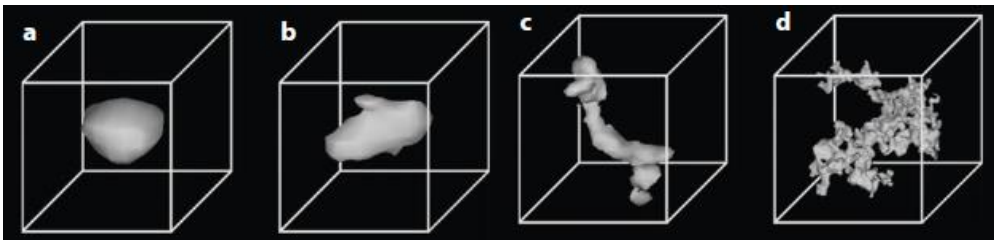

Figure 2.57 (a) Spherical, (b) ellipsoidal, (c) rod and (d) complex creep cavities [130].

Kuwazuru *et al.* [131] have performed 3D X-ray computed tomography (CT) scanning of a cast aluminium alloy in the as-received state and after fully reversed fatigue testing at room temperature. A combination of fractography (Figure 2.58) and 3D X-ray

computed tomography (CT) scanning (Figure 2.59) indicates that near-surface pores were the dominant factor influencing fatigue crack initiation; however, clustering towards the inner regions was also found to produce cracking and can be related to the magnitude of stress concentration in this region.

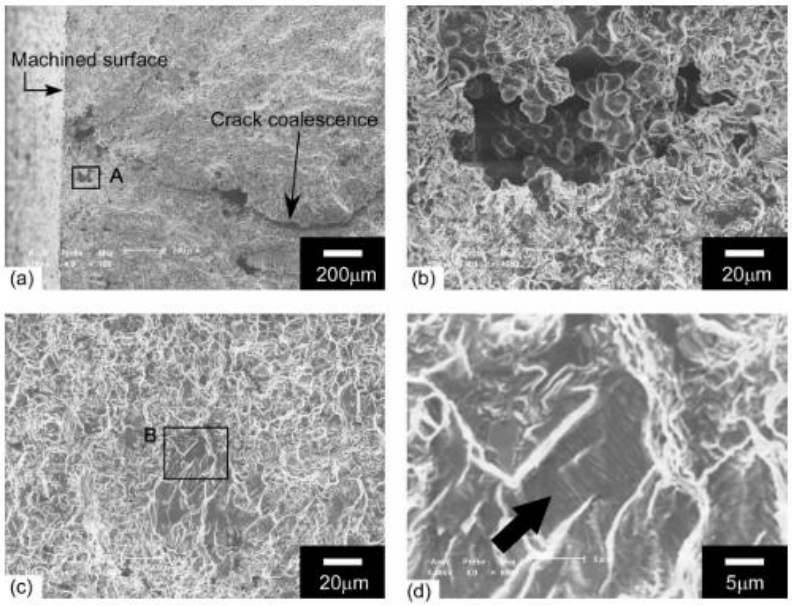

Figure 2.58 SEM images of the fracture surface post-fatigue test showing (a) the location of crack initiation and pores, (b) a shrinkage pore, (c) crack propagation site and (d) fatigue striations [131].

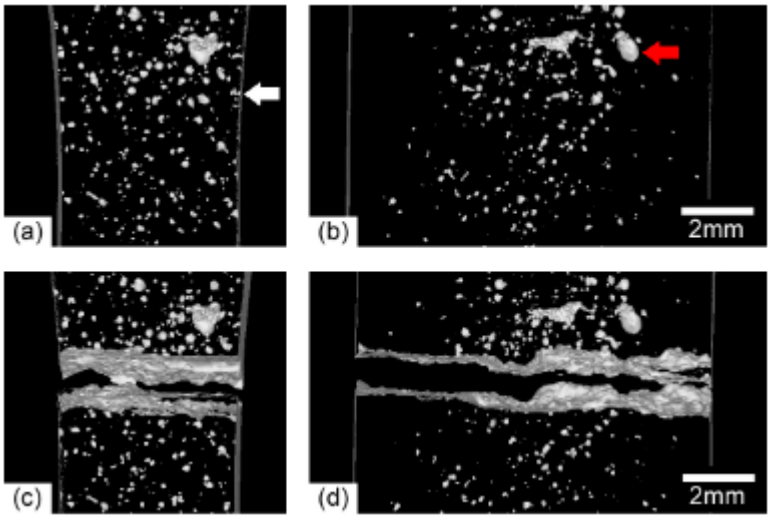

Figure 2.59 Reconstruction of porosities in a cast aluminium alloy (a) frontal view and (b) side view in the as-received state, and (c) frontal view and (d) side view post-test [131].

Schlacher *et al.* [132] used synchrotron μCT, in conjunction with electron back-scatter diffraction (EBSD), to quantify creep void volume in the heat affected zone of a gas

tungsten arc welded forged MarBN sample. Localised pore formation is identified at the fusion line and along grain boundaries, due to fine grain formation as a result of welding. However, scanning of the sample before testing was not performed to identify pre-existing manufacturing and welding induced defects.

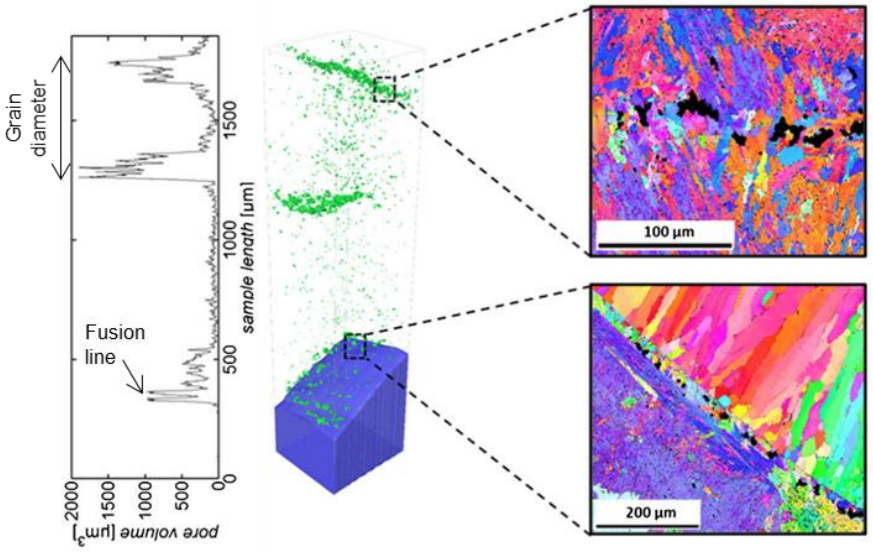

Figure 2.60 Void distribution in a fractured welded MarBN sample, creep tested at 70 MPa and 650 °C for ~17,000 hours, and corresponding EBSD maps at the heat affected zone. Modified from [132].

In Figure 2.61, results by Pessard *et al.* [133] show anisotropic fatigue behaviour of a bainitic steel under fully-reversed high cycle loading conditions, attributed to elongated MnS inclusions in the direction of rolling. Similar results were also observed by Temmel *et al.* [134] for a range of 50CrMo4 steel specimens and varying orientations.

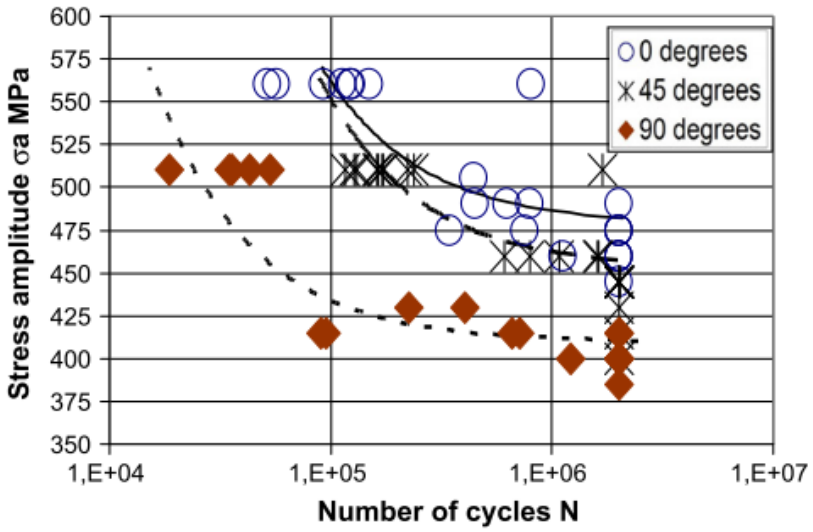

Figure 2.61 Wöhler curves for a bainitic steel with different specimen orientations in relation to the direction of rolling [133].

2.10.3 Modelling of Manufacturing Defects

Modelling of idealised (i.e. spherical) defect geometries has been performed by multiple authors [127,129,135,136] to identify the localised effects of such discontinuities on the matrix and fatigue crack initiation. This has provided insight into the primary micro-scale mechanisms of degradation occurring; primarily, the influence of the localised stress-strain field on decohesion of the inclusion from the matrix, as well as strain accumulation (ratchetting) and the importance of defect shape, size and location.

The modelling of inclusions was first investigated by Eshelby [137] in 1957 and has since become a widely investigated research topic under thermal and mechanical loading. A mismatch in the material properties of inclusions and the matrix during high temperature loading (e.g. heat treatment or power plant start-up and shut-down) can cause decohesion of the inclusion from the matrix material. A greater mismatch in these properties can further increase the localised stress and strain concentrations at the interface and promote early crack initiation [54,126,133,138–140]. Fatigue crack nucleation is further promoted when decohesion of the inclusion from the matrix occurs, and sufficiently large inclusions, in conjunction with clustering, are found to have detrimental effects under cyclic loading [54,123,125,127–129].

Common pores identified in a cast aluminium alloy are presented in Figure 2.62 [141] and can range in size from 10 µm to 1,000 µm. Such locations are preferential for localisation of damage, leading to crack initiation and propagation under cyclic loading and as a result of residual stresses. 2D methods are lacking in terms of identification and characterisation of the complex morphology of shrinkage pores, indicating the importance of 3D methods. In Figure 2.63, modelling of shrinkage pores via plane strain 2D finite element (FE) methods indicates the localised stress concentration factor associated with these complex shapes. Further to this, modelling of the gas pore in 3D (Figure 2.64) indicates both the local notch root radius and the loading direction can produce stress concentration factors of between 3 and 3.5. Similar results are predicted for both gas and shrinkage pores. 3D modelling predicts half the stress concentration of that in 2D and indicates the importance of 3D computational modelling [141,142].

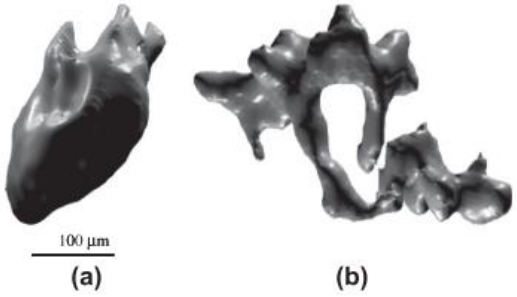

Figure 2.62 Reconstructed X-ray CT images of (a) gas and (b) shrinkage pores in a cast aluminium alloy [141].

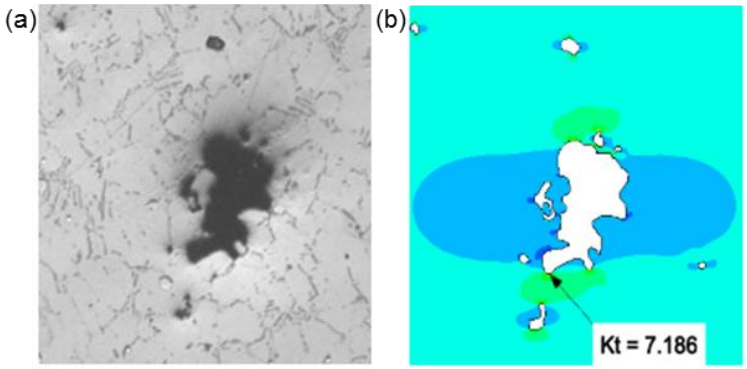

Figure 2.63 (a) SEM image of shrinkage pore and (b) predicted 2D stress distribution (loaded horizontally) [142].

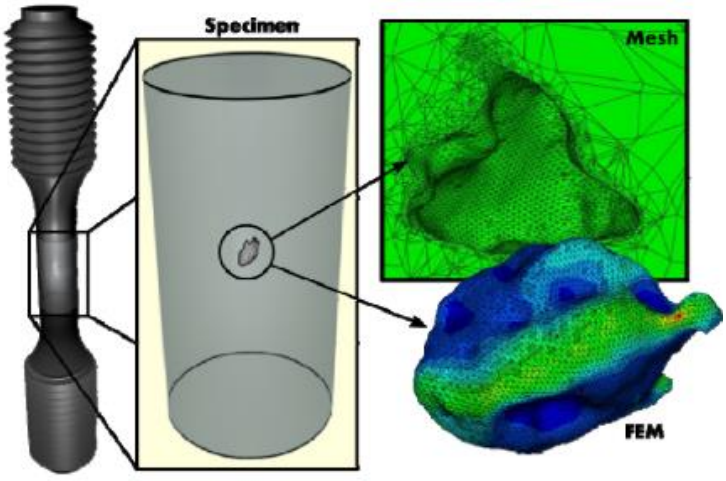

Figure 2.64 von Mises equivalent stress distribution around the surface of a gas pore in a uniaxial fatigue specimen [42].

Hardin *et al.* [143] investigated the relationship between elastic modulus and non-uniform porosity distributions for a range of cast steel specimens, with varying porosity levels (0.08 – 0.2) [128]. The elastic modulus, based on porosity, is defined as:

$$E(\phi) = E_0\left(1-\frac{\phi}{\phi_0}\right)^n \tag{2.18}$$

where E_0 is the elastic modulus of a material with negligible porosity, ϕ is porosity fraction, ϕ_0 is the critical porosity fraction and n is a power exponent. Mapping of the measured tomographic porosity field onto a finite element mesh is performed, for node spacing between 0.2 mm to 2 mm, with local degradation of the elastic modulus using Equation 2.18. Results for the predicted stress and strain distributions are shown in Figure 2.65, indicating non-uniform stress and strain concentrations in the region of porosities. Furthermore, Young's modulus is predicted to decrease non-linearly with increasing porosity fraction.

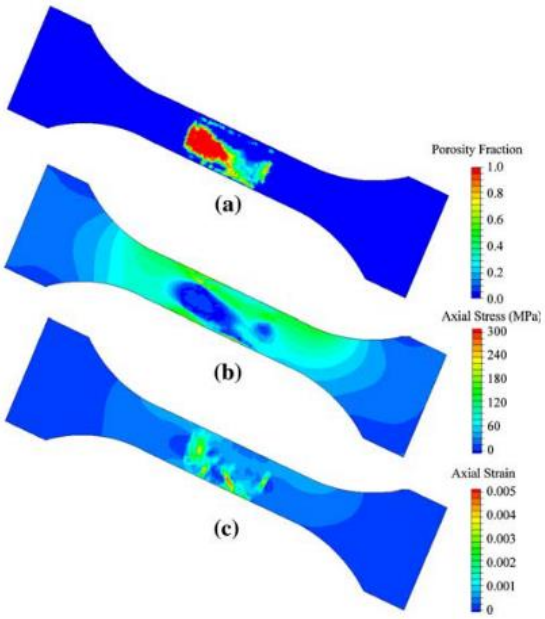

Figure 2.65 Abaqus predicted (a) porosity fraction, (b) axial stress and (c) axial strain in a cast steel under a nominal stress of 96 MPa at room temperature [128].

2.11 Conclusions

There is an extensive amount of literature available in relation to the high temperature experimental characterisation and computational modelling of 9Cr steels, in particular under creep loading conditions and the related mechanisms of degradation. However, as power generation transitions to flexible operation to accommodate the increased contribution from renewable energy sources, the need for fatigue characterisation of current and next generation materials becomes increasingly obvious. Furthermore, as the requirement to operate under higher temperatures and pressures increases, the key

role of oxidation and corrosion is highlighted. As a result, there is increased importance on the role of manufacturing process, chemical composition and heat treatment in terms of microstructurally-driven component performance, and with the development of improved non-destructive test methods (i.e. 3D X-ray CT scanning), characterisation of the role of manufacturing induced defects in component failure is becoming more widespread. The main conclusions from the current literature are:

- The influence of chemical composition and heat treatment can greatly affect the resulting material microstructure (e.g. dislocation density) and in-service performance. Therefore, strict control of the manufacturing process and optimisation of the resulting heat treatment is necessary to ensure maximum component life.
- Significant creep testing of 9Cr steels has been performed, and is a common method for experimental characterisation of current and next generation advanced martensitic steels for power plant applications.
- Microstructural analysis is a necessary tool in understanding the nano-scale strengthening and degradation mechanisms (e.g. void growth, particle coarsening and loss of dislocation density) in tempered martensitic steels, to aid future material design and development.
- Preservation of the martensitic microstructure is vital to long-term macroscale component performance under high temperature loading, primarily due to combined precipitate, dislocation and solute strengthening mechanisms. The addition of tungsten, in conjunction with controlled amounts of boron and nitrogen (i.e. MarBN), has been found to produce an advanced martensitic steel with enhanced creep strength, capable of operating up to 650 °C.
- As operating temperatures are increased, in conjunction with the use of alternative fuel sources (i.e. biomass), understanding the resulting oxidation and corrosion behaviour of martensitic steels is vital for preventing premature component failure.
- Computational modelling, based on experimentally observed phenomena, can provide enhanced insight into the influence of microstructural strengthening mechanisms on macroscale component performance (e.g. precipitate size on cyclic strength). Furthermore, implementation of damage and life prediction methods allows greater understanding of failure mechanisms during loading.

- Non-destructive 3D analysis (i.e. CT scanning) is a powerful tool in quantifying and understanding the role of manufacturing-induced defects and void formation in crack initiation and failure. In conjunction, modelling of idealised and experimentally-measured defect geometries can provide more realistic representation of the as-received material, and greater understanding of their influence on the localised matrix response.

The gaps in the literature to date relate to the following topics:

- Experimental testing of 9Cr steels is primarily related to creep, with little analysis of the role of fatigue or combined creep-fatigue loading. Understanding the cyclic behaviour of the material, and related strengthening and degradation mechanisms (via microstructural analysis), is necessary for material development and component design for USC loading conditions.
- Characterisation of the oxidation and corrosion performance of next generation materials at USC loading conditions, in terms of oxide scale growth and oxide pit formation, to ensure equivalent performance to current generation materials.
- 3D X-ray CT scanning has identified manufacturing defects as a primary source of crack initiation under creep and fatigue loading in various materials. However, the role of manufacturing process on defect formation has received relatively little attention, particularly for 9Cr steels, where variation in chemical composition and manufacturing method can strongly influence the resulting microstructure and, therefore, component performance.
- 9Cr steels are strain-rate dependent materials and cyclically soften at high temperature. Therefore, the development and implementation of phenomenological models, in conjunction with life prediction and damage methodologies, are of particular importance in accurately predicting component performance and failure. Furthermore, computational modelling of components with manufacturing defects can provide enhanced insight on the resulting in-service behaviour.

3 High Temperature Experimental Testing and Microstructural Analysis of MarBN

3.1 Introduction

In this chapter, a high temperature low cycle fatigue (HTLCF) and creep-fatigue (CF) test program for MarBN is presented in conjunction with oxidation and corrosion testing, and compared to current generation material, P91 steel. The application of a range of microstructural analysis techniques are presented for pre- and post-test samples, including optical microscopy, scanning electron microscopy (SEM), energy dispersive X-ray spectroscopy (EDX), back-scatter electron microscopy (BSE) and transmission electron microscopy (TEM), to characterise the nano- and microscale phenomena.

The fatigue response of cast MarBN at 600 °C and 650 °C was investigated across a range of loading conditions to identify the effects of cyclic loading, tensile hold periods and temperature on the material response. Initial testing of forged MarBN at 600 °C is also performed. The fatigue life and cyclic viscoplastic response of materials is a key aspect in terms of component design and also provides the necessary data for calibration and validation of material models with application to more realistic plant conditions and geometries. The cast and forged MarBN material presented and tested here was

produced by Goodwin Steel Castings as part of the IMPACT project [18], and the work presented in this chapter is part of a collaboration between NUI Galway and GE Power, UK. Comparisons are made between test results from the NUI Galway and GE Power test rigs, and repeat testing is performed to establish consistency. MarBN test results are compared to corresponding results for P91 produced at NUI Galway.

Cast and forged MarBN was tested under high temperature oxidation and corrosion conditions to investigate the performance of MarBN in relation to a current power plant material, rolled P91 steel. It is essential that next generation materials display at least equivalent performance in this area, as plant operators look to increase loading conditions, as well as variation in fuel type e.g. biomass.

Microstructural analysis is a key aspect in understanding and characterising the behaviour of advanced martensitic steel. A short summary of the principle of operation of each technique is provided, and the sample preparation method for each type of analysis is also described in detail; this includes polishing, etching, carbon replica and twin-jet polishing. Key strengthening and degradation mechanisms in MarBN in the as-received and post-test condition are identified in terms of fatigue, creep-fatigue, oxidation and corrosion. This chapter identifies manufacturing defects (generally inclusions) as the primary mechanism of degradation in cast and forged MarBN, based on their role in crack initiation and propagation under high temperature loading, and their relationship with oxide pit formation and oxide scale fracture.

3.2 Chemical Composition and Heat Treatment

As discussed in the previous chapter, preservation of the microstructure of 9Cr steels is critical to long-term high temperature performance. The different strengthening mechanisms (e.g. precipitate and dislocation) interact to provide resistance to plastic deformation via resistance to or retardation of dislocation motion under loading. This is attributed to the carefully controlled chemical composition, followed by heat treatment to ensure sufficient strength and ductility. The chemical composition and heat treatment for cast and forged MarBN is confidential information as part of the IMPACT project [18] and, therefore, cannot be disclosed here. A similar composition was presented in Chapter 2 (Table 2.1) for MarBN, as published by Abe *et al.* [38], with comparison to P91 [59] and P92 [38]. The most notable changes to MarBN, in relation to P91 and P92, are the addition of increased tungsten, boron and cobalt, and reduced vanadium and carbon content.

Chromium is known to enhance oxidation and corrosion resistance at high temperature through the formation of a protective chromium oxide scale on the surface of components, as well as contributing to enhanced creep strength (between 10% and 12% concentration). Tungsten and molybdenum also contribute to the strength of the material through solute strengthening. Vanadium and niobium combine with carbon and nitrogen to form MX carbonitrides, dispersed throughout laths to resist dislocation motion. Boron and nitrogen content is strictly controlled to prevent BN particle formation during heat treatment. Boron also reduces the minimum creep rate via providing enhanced stabilisation of carbides along boundaries, and hence, preventing lath coarsening for longer periods of time. Nitrogen further contributes to improving the long-term creep strength, and cobalt has been found to inhibit δ-ferrite formation and enhance material toughness [40,79,80,144].

The heat treatment for cast MarBN, undertaken at NUI Galway, is similar to the process described by Li *et al.* [81], to ensure that BN formation does not occur. Figure 3.1(a) shows the phase transformation diagram for chromium containing steel with 0.1% carbon. Normalisation (in the 850 °C to 1250 °C temperature range) is required to produce a martensitic transformation upon rapid cooling, as well as providing increased yield and tensile strength. Upon removal from the furnace, transformation of austenite to martensite occurs as the material air cools below approximately 380 °C (martensitic transformation temperature for 9Cr steel), as shown in Figure 3.1(b) [30,145]. The hierarchical microstructure of martensite is key to the enhanced creep performance of 9Cr steels via the various micro-strengthening mechanisms. Minimal, if any, δ-ferrite, which can cause severe degradation of high temperature strength at increased quantities, is expected to occur [30]. Once the steel has cooled to room temperature, tempering is performed, at a lower temperature than that of normalizing, to increase toughness and improve ductility. This also reduces the dislocation density of the material and allows precipitation of carbides ($M_{23}C_6$) and carbonitrides (MX), which are essential to the long-term creep strength of the material [30].

To manufacture samples for testing at NUI Galway, cast MarBN bars were extracted from the cast plate shown in Figure 3.2 and heat treatment was performed using a UAF 14/10 Lenton high temperature oven for normalization, followed by an AWF 130/12 Lenton high temperature oven for tempering. A similar geometry was produced for testing at GE Power. The forged MarBN was received in the heat treated condition (a different procedure to that of the cast material). Casting allows the manufacture of large,

complex geometries generally at a reduced tooling cost compared to forged components; in contrast, forging produces a refined grain structure, with increased material toughness and reduced porosity [146]. Therefore, it is expected the forged material will exhibit superior fatigue performance due to the reduced grain size and number of defects.

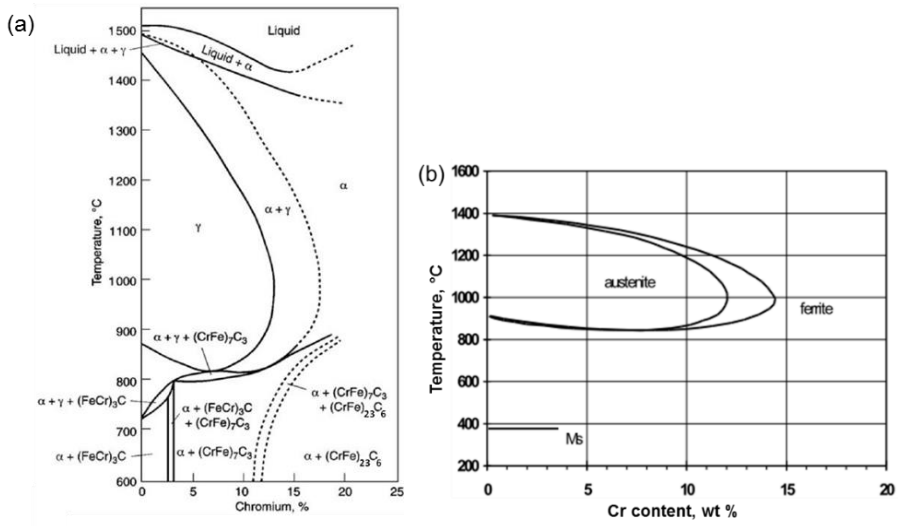

Figure 3.1 (a) Phase transformation diagram for Fe-Cr-0.1C steel [145] and (b) temperature versus chromium content and the regions where austenite, ferrite and martensite occur [30].

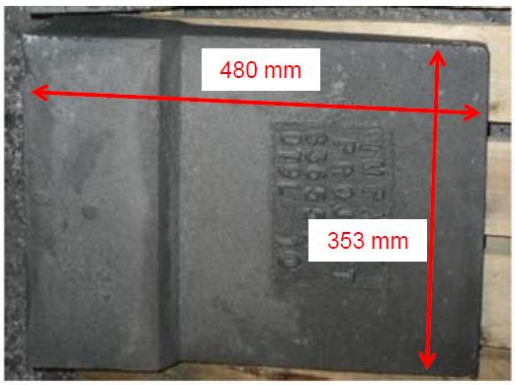

Figure 3.2 As-received cast MarBN plate at NUI Galway, manufactured by Goodwin Steel Castings (UK) [9].

3.3 High Temperature Strain-Controlled Testing Facilities

Following heat treatment and cooling, HTLCF specimens were machined from the bars at NUI Galway, as per the dimensions in Figure 3.3 and according to standard ASTM E606 – 04 for strain-controlled fatigue testing. A similar component geometry is used at GE Power. Strain-controlled HTLCF testing is performed at NUI Galway and GE

Power (UK). At NUI Galway, the test rig is an INSTRON 8500, and a Denison Mayes Group cyclic test machine is used at GE Power, both in conjunction with an INSTRON 8800 controller, as shown in Figure 3.4. Thermal calibration was previously performed for MarBN up to 700 °C at NUI Galway using high temperature thermocouples [9]. Three blind holes and one through the gauge length of the sample were drilled into a cylindrical dog bone specimen and high temperature K type stainless steel sheathed thermo-couples were inserted. Soak times of between six and twelve hours were identified for stabilisation and uniform temperature distribution for P91 and MarBN [9,86]. For the current test program, the oven controller was set to the appropriate temperature based on this study and soaking of the samples was performed overnight in all cases. It is assumed that the mechanical properties of the sample are not affected during this time.

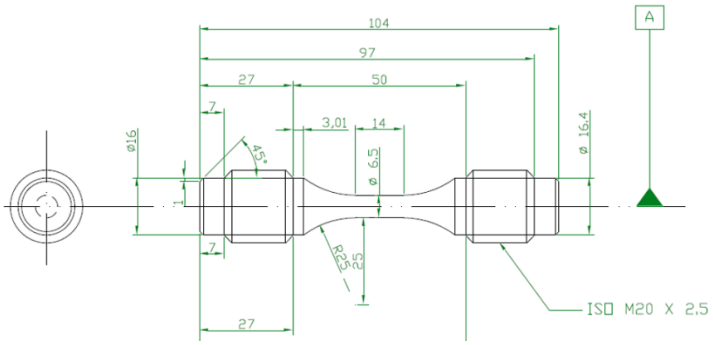

Figure 3.3 HTLCF specimen geometry for testing at NUI Galway [86].

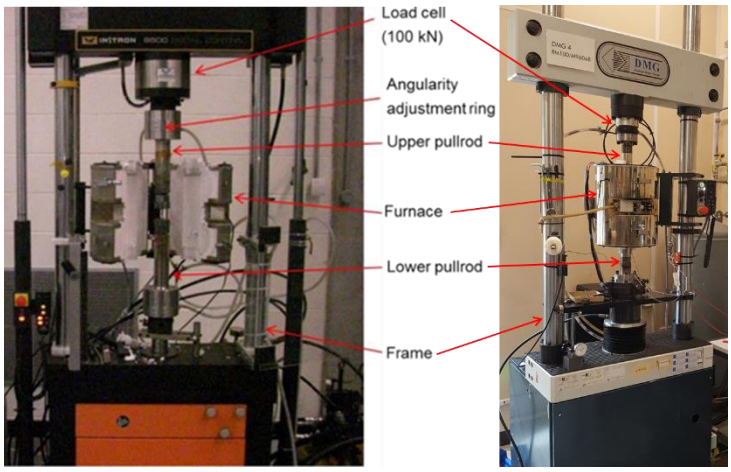

Figure 3.4 NUI Galway (left) and GE Power (right) high temperature strain-controlled test rigs.

At GE Power, high temperature thermocouples are attached to the top and bottom shoulders of the sample throughout testing and secured with high temperature string (Figure 3.5); therefore, thermal calibration was not necessary. The samples is allowed to

soak overnight. Following this, thermocouple data is monitored and adjustments are made manually to the top and bottom furnace inputs, to ensure that the sample is at the correct, uniform temperature. Following each temperature adjustment, the sample is left for one hour to reach steady-state. Heating of both set-ups is performed at a slow rate over-night to allow a uniform temperature distribution throughout the sample.

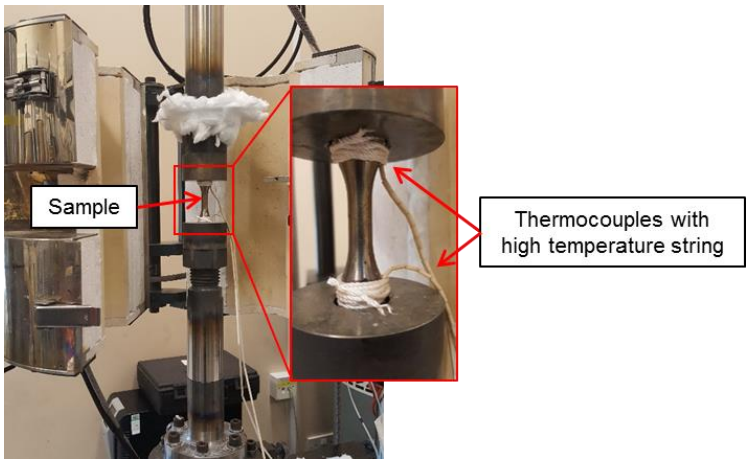

Figure 3.5 Thermocouples attached to the HTLCF sample at GE Power.

Figure 3.6 compares testing performed at NUI Galway and GE Power under the same loading conditions. Repeat testing was performed to ensure confidence in the results produced between both test facilities, with almost identical maximum stress evolution and similar plastic strain evolution; a difference of approximately 2.5% in stress and 4.7% in plastic strain was measured at the 300th cycle.

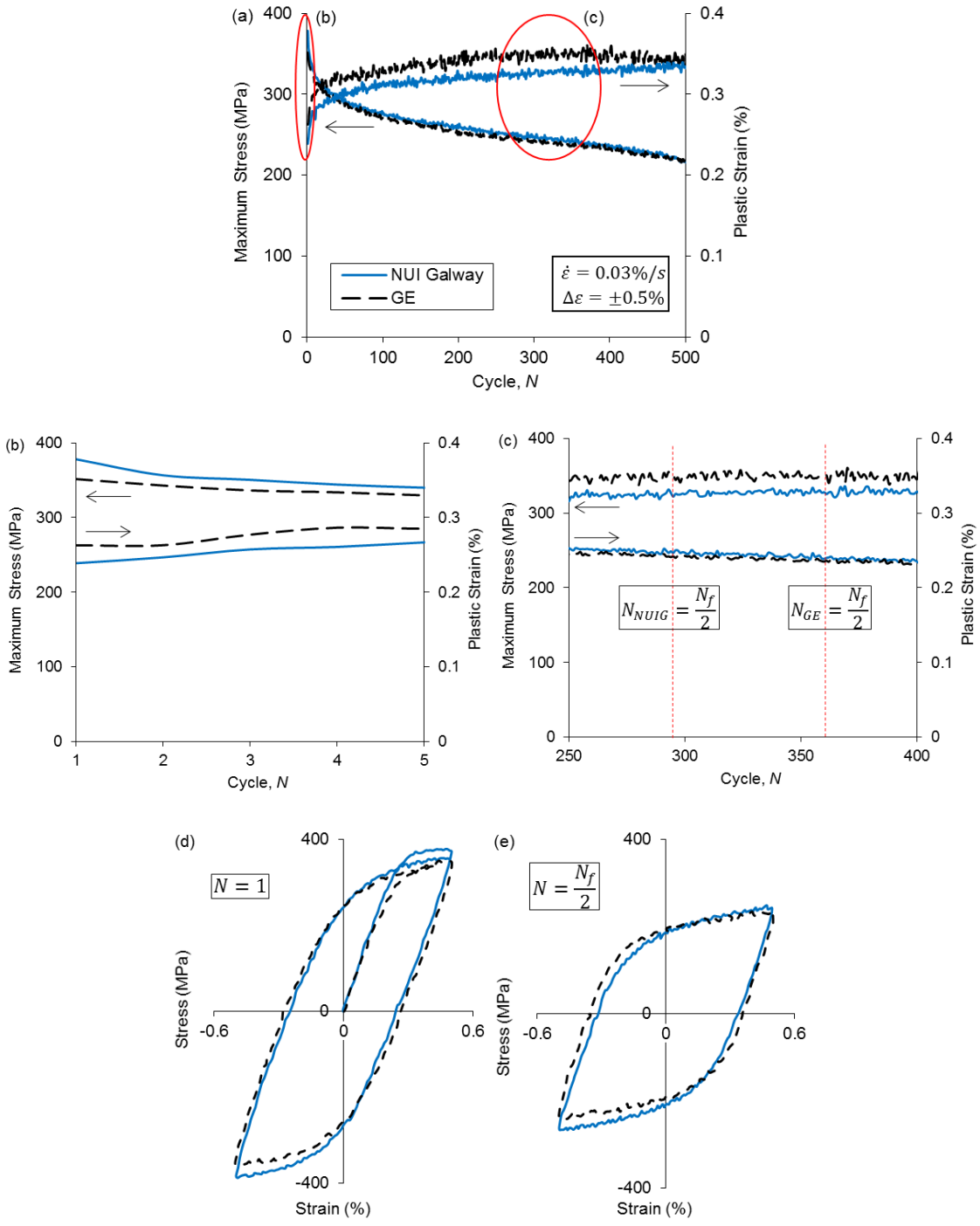

Figure 3.6 Repeat HTLCF test of cast MarBN at 650 °C, at NUI Galway and GE Power, comparing (a) maximum stress and plastic strain evolution up to 500 cycles, (b) initial cycles, (c) half-life, (d) initial stress-strain loops and (e) half-life stress-strain loops.

3.4 Analytical Methods

3.4.1 Optical Microscopy

Optical microscopy combines visible light with a system of lenses to increase the magnification of the sample of interest. Throughout this work, an Olympus BX51M

optical microscope was used and provides up to 100 times magnification for analysis of polished and etched metal samples. A real image of the sample is focused via a lens close to the surface, which collects light, and increasing the number of lenses produces greater magnification. Figure 3.7 is a schematic representation of this process [147]. An example of an optical microscope image of the grain structure of cast MarBN steel is shown in Figure 3.8, following polishing and etching.

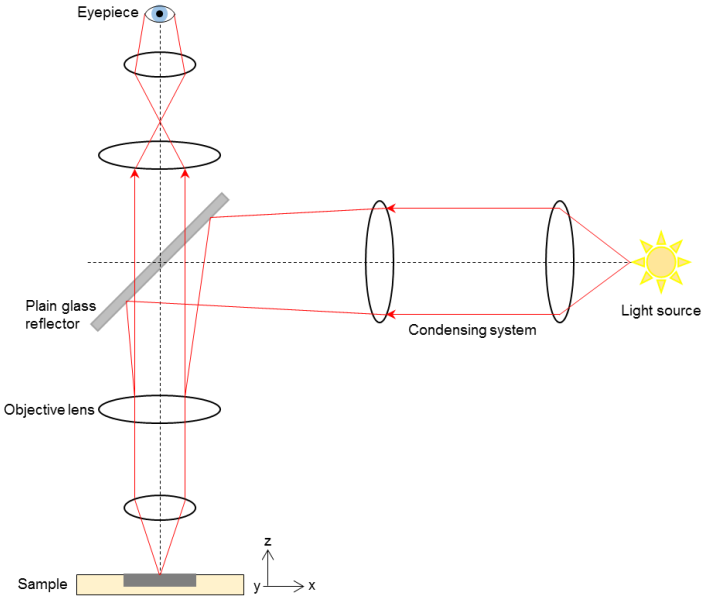

Figure 3.7 Schematic representation of the principle of operation of an optical microscope. Adapted from [147].

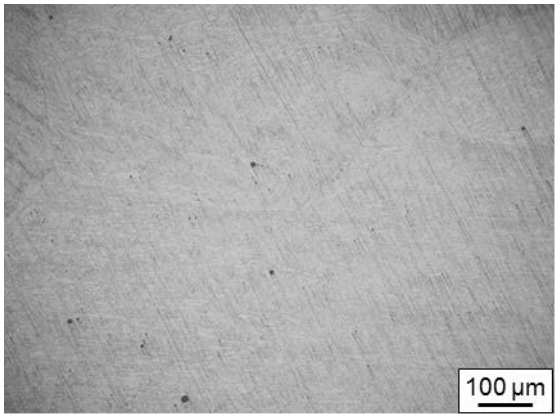

Figure 3.8 Example of an optical microscope image of cast MarBN steel after polishing and etching.

3.4.2 Scanning Electron Microscopy

Figure 3.9 presents the basic operating principle of an SEM with EDX and BSE [148]. For increased magnification requirements (e.g. investigation of crack propagation and oxide scale formation), the Hitachi S-4700 SEM with EDX and Hitachi S2600N

Variable Pressure SEM with backscatter at NUI Galway are used. The increased levels of magnification are, in brief, achieved by emission of electrons from an electron gun and focused through one or multiple condenser lenses (between 0.4 nm and 5 nm diameter). As the beam passes through the scanning coils, it is deflected in the x and y axes and allows the beam to be scanned across the sample surface, providing a large depth of field for analysis, to nanometre resolution. The column and chamber are under vacuum conditions and the level of magnification can be controlled by the user. Upon contact of the beam with the sample, electrons lose energy through repeated scattering and absorption. Secondary electrons are produced if the electrons interact with the nucleus and electrons of the sample. Back-scattered electrons are those reflected back with little interaction with the surface [149,150]. The use of a backscatter detector allows heavier elements (e.g. tungsten) to be viewed with greater contrast compared to lighter elements (e.g. chromium) and can be used to visually identify different precipitate types (e.g. Laves phase) [68]. The chemical composition of a sample can be analysed using SEM in conjunction with an EDX detector, based on the interaction between the electrons in the beam and the atoms in the sample. A histogram of the intensity of various elements is then produced [151]. Figure 3.10 presents an example of an SEM image of the grain structure of cast MarBN steel

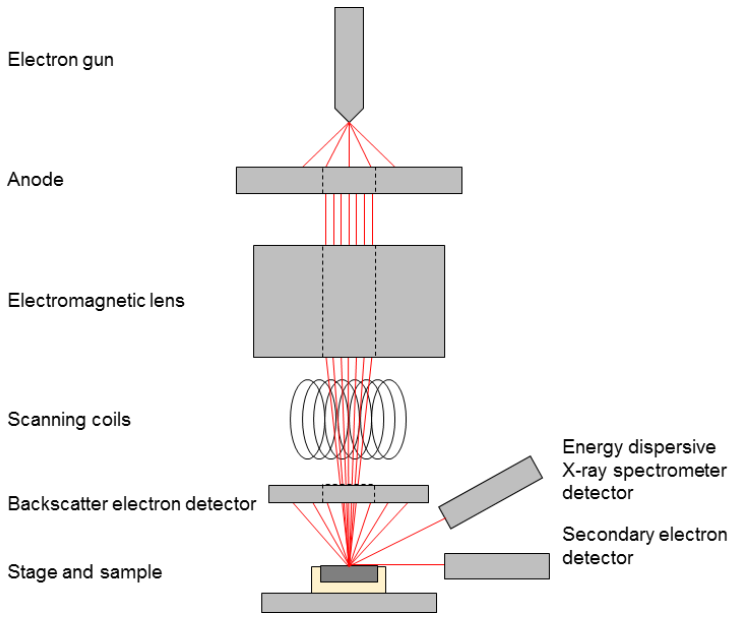

Figure 3.9 Schematic representation of a scanning electron microscope with BSE and EDX detectors. Adapted from [148].

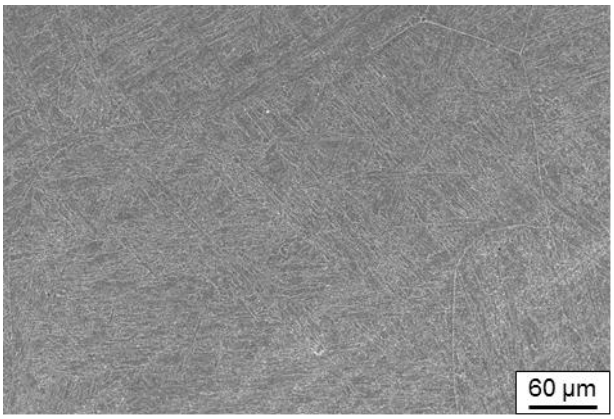

Figure 3.10 Example of an SEM image of cast MarBN steel after polishing and etching.

3.4.3 Transmission Electron Microscopy

The general structure of a TEM is presented in Figure 3.11. In a similar method to SEM, electrons are generated from the electron gun at the top of the electron column and travel through a small hole down the column under vacuum conditions. A number of apertures are located below the gun that can be inserted to vary the precision of the beam. Electromagnetic lenses are used and provide magnification up to 1,000,000 times and a resolution in the range of fractions of nanometres. A key difference is that the beam passes through the samples and projects an image onto a viewing screen at the base of the TEM. This allows very small details, such as precipitates and dislocations, to be analysed, as well as being able to identify the crystal structure of specific artefacts using diffraction patterns [152]. In Figure 3.12, an example of a TEM image of the cast MarBN hierarchical microstructure is presented.

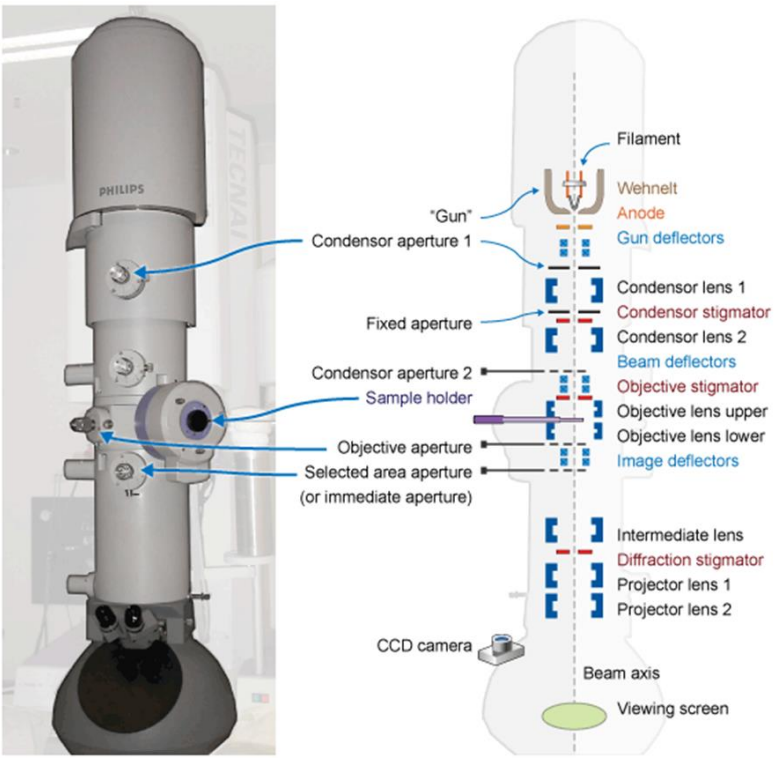

Figure 3.11 Generalised internal structure of a TEM [152].

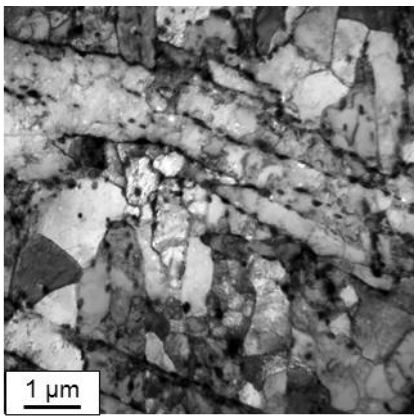

Figure 3.12 Example of a TEM image of thin foil cast MarBN sample.

3.5 Sample Preparation Techniques

3.5.1 Optical and Scanning Electron Microscopy

Samples are cut from (i) as-received heat-treated bars and (ii) the gauge length of post-HTLCF test MarBN samples using a Buehler IsoMet low-speed saw. The extracted samples are then placed in plastic mounts and an epoxy resin is added. Upon hardening, samples are removed from the mounts and polished using a Buehler EcoMet/AutoMet 250 Pro automatic polisher. Initially, grinding of the samples is performed using silicon carbide paper from P200 to P1200 grit. Polishing is then performed, using a diamond suspension, to a 0.06 µm finish. At this point, a mirror-like finish exists on the sample

surface and some of the grain structure becomes visible. The etchant, Vilella's reagent, is applied to the sample for thirty seconds to allow the entire martensitic microstructure to be analysed via optical microscopy and SEM. Vilella's reagent was provided by ESB International (Cork), as per the standard material safety data sheet. Cleaning is performed between all steps using deionised water in an ultrasonic bath. Figure 3.13 shows sample optical microscopy images of the surface of cast MarBN; a rough surface finish is observed following grinding up to P1200 grit (with all lines in the same direction), a smooth surface finish is then produced with some evidence of the grain structure following polishing up to 0.06 µm, and finally etching allows the entire microstructure to be analysed.

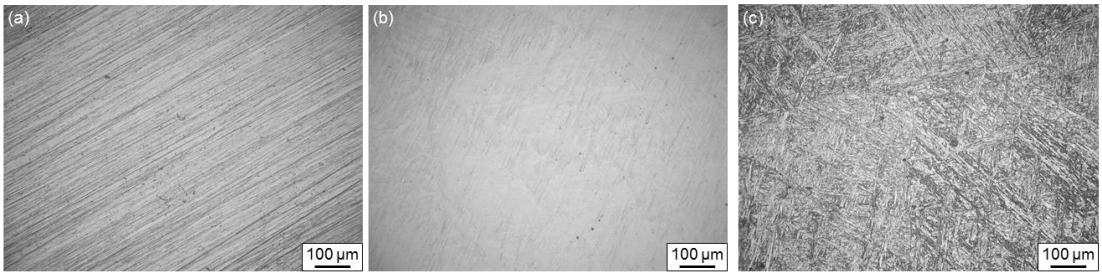

Figure 3.13 Optical microscopy images of cast MarBN after (a) grinding up to P1200 grit, (b) polishing to a 0.06 µm finish and (c) etching.

3.5.2 Transmission Electron Microscopy

Two methods of sample preparation were used for TEM analysis: (i) carbon replica and (ii) twin-jet polishing. The carbon replica technique specifically allows the precipitate distribution to be analysed, whereas twin-jet polishing produces samples with the entire microstructure exposed (i.e. laths, precipitates, dislocations). Preparation of carbon replica samples is the same as that described above for SEM, followed by application of a continuous carbon layer to the top of the samples using a vacuum carbon evaporator. To extract the carbon replica samples, a grid is cut on the sample surface using a scalpel (approximately 2 mm^2 sections), and the sample is then placed in Vilella's reagent until the carbon layer (containing the precipitates) detaches from the sample. Each carbon film is placed on a copper mesh grid for analysis.

For twin-jet polishing, a thin section of metal is cut from a larger section using a slow speed saw and gradually ground until the thickness of the sample is between 50 µm and 100 µm, and a P4000 grit finish is achieved. Three millimetre discs of metal are extracted from the larger sample using a disc punch. Cleaning in methanol is performed and samples are then placed in the twin-jet polisher, containing a methanol-based

etchant (methanol – 59 %, perchloric acid – 6 %, buchanol – 35 %), at -27 °C and a voltage of 20.5 V. The etchant is fired at both sides of the centre of the sample until a hole is achieved, with a surrounding area thickness of approximately 200 nm. Cleaning is again performed in methanol, followed by water, and then samples are placed in containers with ethanol to prevent rusting. TEM of carbon replica and thin foil samples is performed using a Hitachi H7000 TEM at NUI Galway and a JOEL JEM-2100F TEM at University of Limerick. Figure 3.14 shows sample TEM images of cast MarBN using the above mentioned methods.

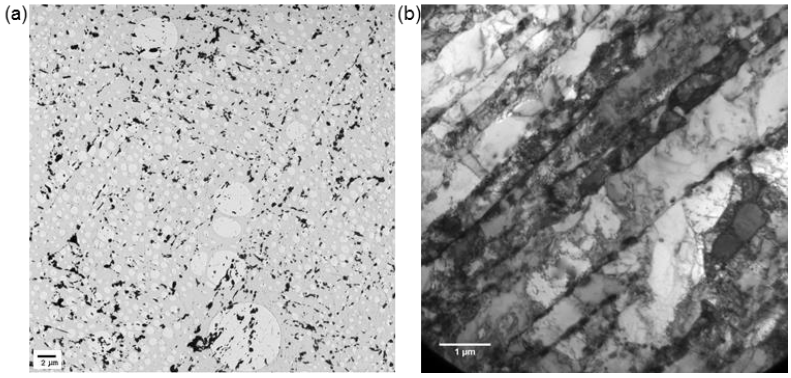

Figure 3.14 TEM images of cast MarBN using the sample preparation method (a) carbon replica and (b) twin-jet polishing.

3.6 Oxidation and Corrosion Test Methods

The oxidation and corrosion experimental method employed here is based on that of O'Hagan [44]. 10 mm × 5 mm × 3 mm samples of cast and forged MarBN and rolled P91 steel were tested in air at 600 °C and 650 °C, with and without power plant ash applied (one sample per loading condition). Before testing, samples were polished using progressively finer SiC grit paper, up to grade P1200, to ensure a uniform surface finish, free of significant roughness. The samples were cleaned in deionised water in an ultrasonic bath and, where appropriate, ash was applied using a spatula. The chemical composition of the ash (obtained from the West Offaly Power Plant) is shown in Table 3.1. All samples were placed in the furnace to be removed at time periods of 1, 7, 14, 21 and 28 days. Replenishment of the ash to the surface of the samples was not necessary over the course of testing. Upon removal, samples were air cooled, then fixed in an epoxy resin. Samples were sectioned and prepared using mechanical polishing with the SiC grit papers mentioned previously, followed by 9 µm, 3 µm and 0.06 µm diamond suspensions. The etchant, Vilella's reagent, was applied to the samples to reveal the microstructure and any possible defects. Analysis was then performed using optical

microscopy, SEM, BSE and EDX to identify the detailed mechanisms of oxidation and corrosion occurring across the given time periods.

Table 3.1 Chemical composition of the power plant ash (as a result of peat burning) applied to MarBN and P91 samples.

Element	Ca	S	Fe	Si	C	Al	Mg	K	Cl	Na
Weight (%)	43.16	15.12	12.77	10.18	5.93	4.80	3.94	2.43	1.33	0.35

3.7 High Temperature Low Cycle Fatigue of MarBN

3.7.1 Introduction

Figure 3.15 shows schematic representations of typical strain-controlled fatigue and creep-fatigue tests. An experimental test program of fully reversed (triangular), strain-controlled HTLCF and CF testing was previously published for cast MarBN at 600 °C [9]. In this work, a similar test program, shown in Table 3.2, has been performed on cast MarBN at 650 °C, as well as testing of cast and forged MarBN at 600 °C, to identify the effect of temperature and manufacturing process on the cyclic response of the material. One sample is tested in all cases, excluding repeat testing of cast and forged MarBN, as presented in Section 3.7.4. Strain-controlled CF testing is also performed on cast MarBN, with a one hour strain-hold period in tension, to identify the effect of a dwell period on failure mechanisms and life. Failure corresponds to a 20% drop in load after the first 150 cycles of testing (i.e. after the primary phase of cyclic softening), where macroscale cracking sufficiently reduces the load bearing capacity of the sample [9], as per the BS7270:2006 standard for constant amplitude strain controlled axial fatigue of metallic materials. Testing is not performed to fracture as it may lead to damage or fracture of the extensometer legs.

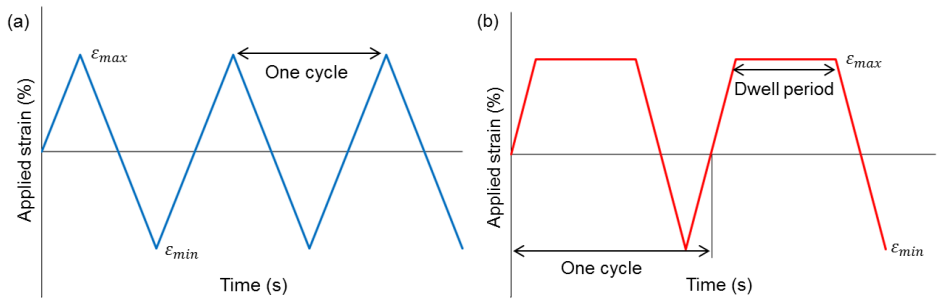

Figure 3.15 Schematic representation of applied strain-time histories for strain-controlled (a) fatigue testing and (b) creep-fatigue testing, with a hold period in tension.

Table 3.2 Test program for HTLCF and CF testing of cast MarBN at 650 °C and corresponding fatigue life.

Type	**Δε (%)**	**ε̇ (%/s)**	N_f **(-)**
HTLCF	±0.5	0.1, 0.03, 0.01	515, 587, 551
	±0.4	0.03, 0.01	861, 809
	±0.3	0.03, 0.01	2091, 1901
CF	±0.5	0.1	389

3.7.2 High Temperature Low Cycle Fatigue Testing

Figure 3.16 compares the stress-strain loops for the initial and half-life cycles for cast MarBN at 650 °C, for two different strain-rates and three different strain-ranges. The strain-rates at which power plants typically operate are much lower than those applied under laboratory conditions, therefore, characterisation of the material across various strain-rates and strain-ranges is essential [153]. The effect of strain-rate in cast MarBN at 600 °C has been presented previously by Barrett *et al.* [9] across two orders of magnitude; similar results are observed here across an order of magnitude, with a greater effect presumed to occur as the strain-rate is further decreased.

Masing behaviour occurs when stress-strain loops (across various strain-ranges) are geometrically coincident with the monotonic stress-strain curve (magnified by two). Non-Masing behaviour is linked to precipitation hardened materials or those with a high dislocation density, leading to cyclic hardening or softening [154]. Such behaviour has been identified previously in P91 steel at 400 °C and 600 °C, and cast MarBN at 600 °C [9], and is again observed here for cast MarBN at 650 °C (Figure 3.16). Figure 3.17 shows the evolution of the maximum stress as a function of cycles for cast MarBN at 600 °C and 650 °C across a range of loading conditions. As the temperature is increased, a significant reduction in cyclic strength occurs, as well as reduced fatigue life.

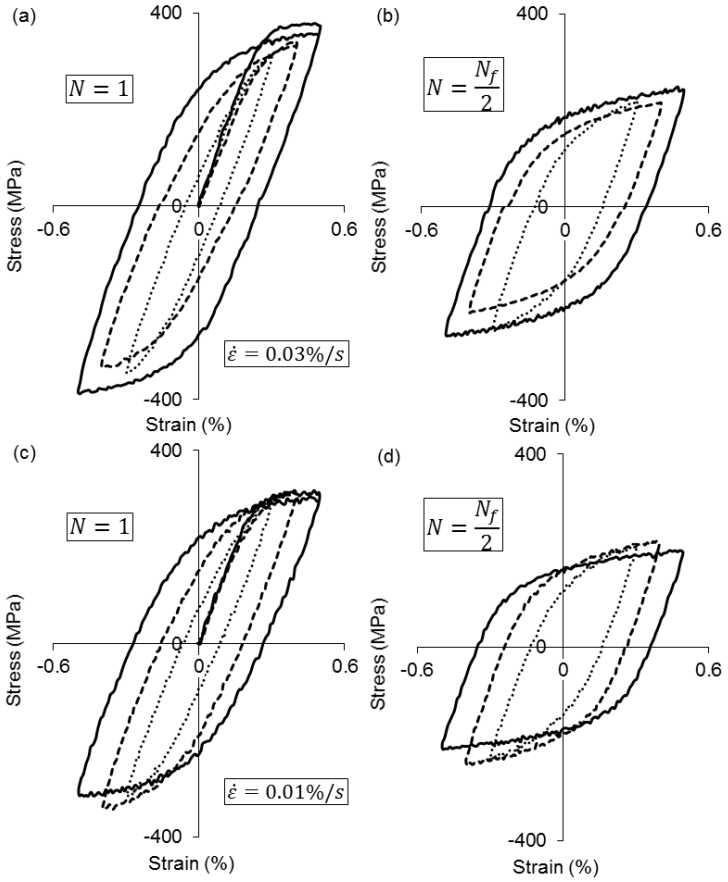

Figure 3.16 (a – d) Stress-strain curves for cast MarBN at 650 °C across a range of strain-rates and strain-ranges at the initial and half-life cycles.

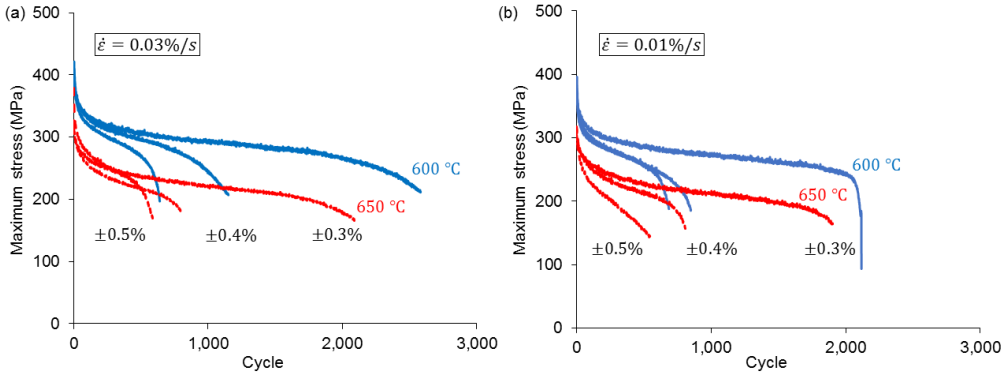

Figure 3.17 Measured evolution of maximum stress with cycles during HTLCF testing of cast MarBN at 600 °C and 650 °C across a range of strain-ranges and (a) $\dot{\varepsilon}$ = 0.03 %/s and (b) $\dot{\varepsilon}$ = 0.1 %/s.

Figure 3.18 compares the cyclic stress-strain behaviour of cast MarBN (600 °C and 650 °C) and rolled P91 (600 °C) for the initial and half-life cycles at multiple strain-rates. Cast MarBN at 600 °C shows superior cyclic strength throughout the test compared to

P91 at the same temperature, with comparable performance between P91 at 600 °C and cast MarBN as the temperature is increased to 650 °C.

In Figure 3.19, the evolution of maximum stress as a function of cycles is shown for cast MarBN (600 °C and 650 °C) and P91 (600 °C) under HTLCF loading, at two different strain-rates and an applied strain-range of ± 0.5%. At the lower strain-rate (Figure 3.19(a)), cast MarBN at 650 °C behaves almost identically to P91 at 600 °C in terms of cyclic strength, with only marginally lower cycles to failure, and has significantly increased cyclic strength at 600 °C. The higher strain-rate results of Figure 3.19(b) show that at 650 °C, cast MarBN exhibits a higher rate of cyclic softening than P91 at 600 °C.

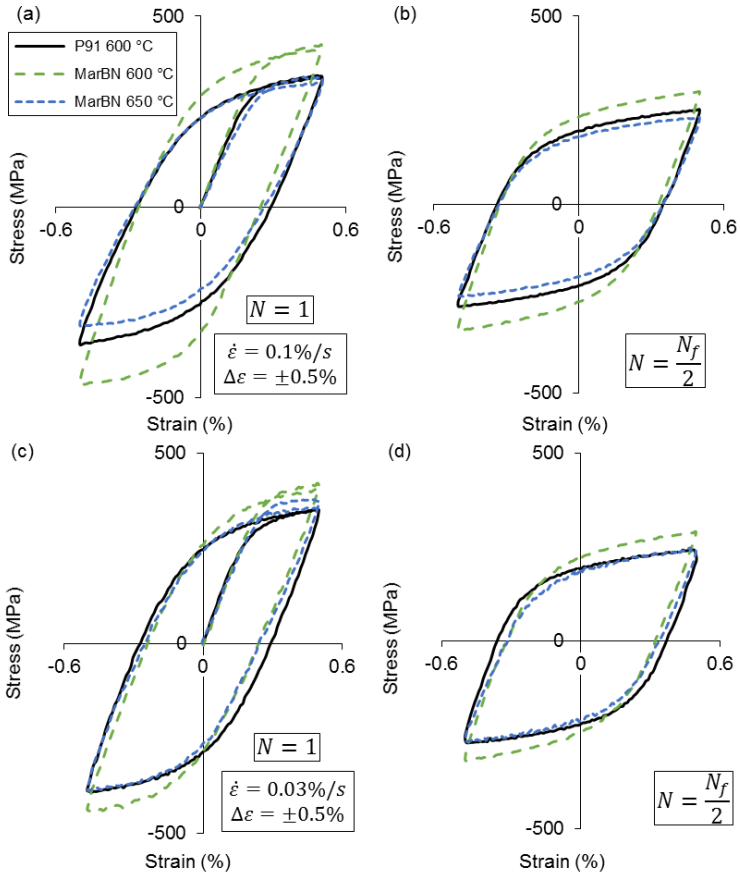

Figure 3.18 Comparison of cast MarBN (600 °C and 650 °C) and rolled P91 (600 °C) for the initial and half-life cycles at a strain-rate of (a, b) 0.1 %/s and (c, d) 0.03 %/s.

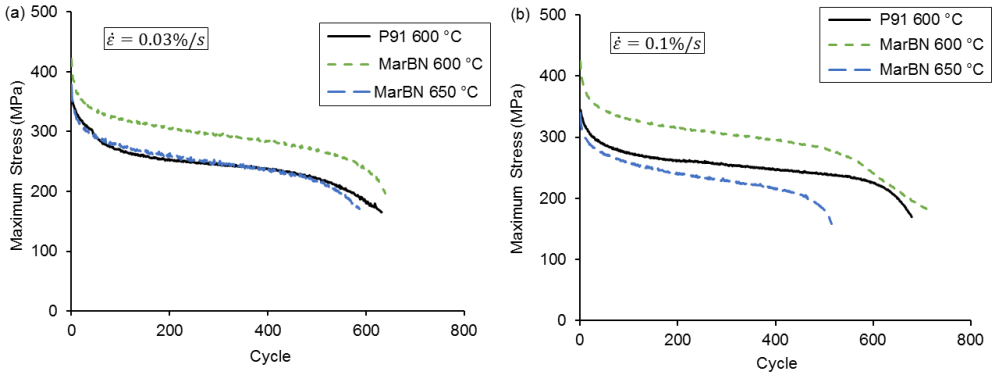

Figure 3.19 Comparison of the maximum stress evolution for cast MarBN (600 °C and 650 °C) and rolled P91 (600 °C) under HTLCF loading at (a) $\dot{\varepsilon}$ = 0.03 %/s and (b) $\dot{\varepsilon}$ = 0.1 %/s and $\Delta\varepsilon$ = ±0.5%.

Figure 3.20 shows the evolution of cyclic softening stress with cycles under the same conditions as Figure 3.17. The cyclic softening stress is the change in maximum stress from the initial cycle ($R = \sigma_{\max,0} - \sigma_{\max}$). A large decrease in maximum stress was observed in Figure 3.17 for the higher temperature cases, but when the softening stress is plotted separately, the results are generally similar for both temperatures, up to the point of fatigue crack propagation and sample failure.

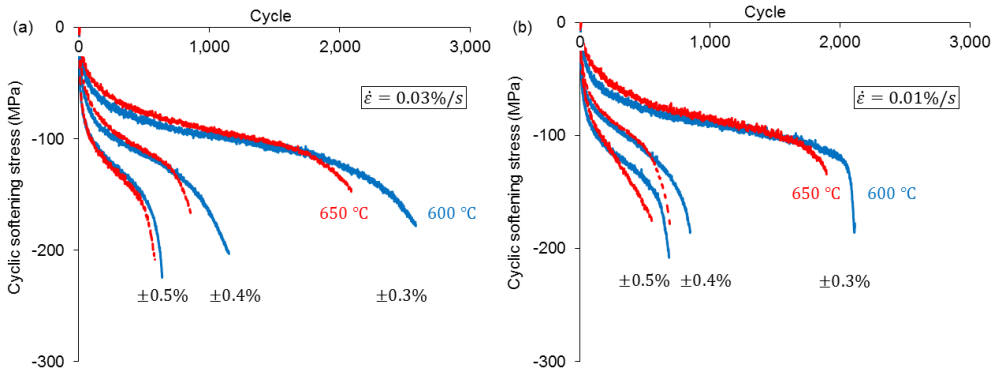

Figure 3.20 Cyclic softening stress evolution with cycles for cast MarBN at 600 °C and 650 °C across a range of strain-ranges and (a) $\dot{\varepsilon}$ = 0.03 %/s and (b) $\dot{\varepsilon}$ = 0.01 %/s.

Figure 3.21 presents the accumulated effective plastic strain with cycles for the data presented in Figure 3.20. The accumulated effective plastic strain is the sum of the absolute plastic strain with increasing cycles $\left(p = \sum_{N=1}^{N_f} 2\Delta\varepsilon^{pl} N \right)$. In general, a similar rate of effective plastic strain accumulation occurs in all cases at a strain-rate of 0.1 %/s (Figure 3.21(b)); however, greater differences are observed as the strain-rate is decreased, particularly at lower strain-ranges (Figure 3.21(a)).

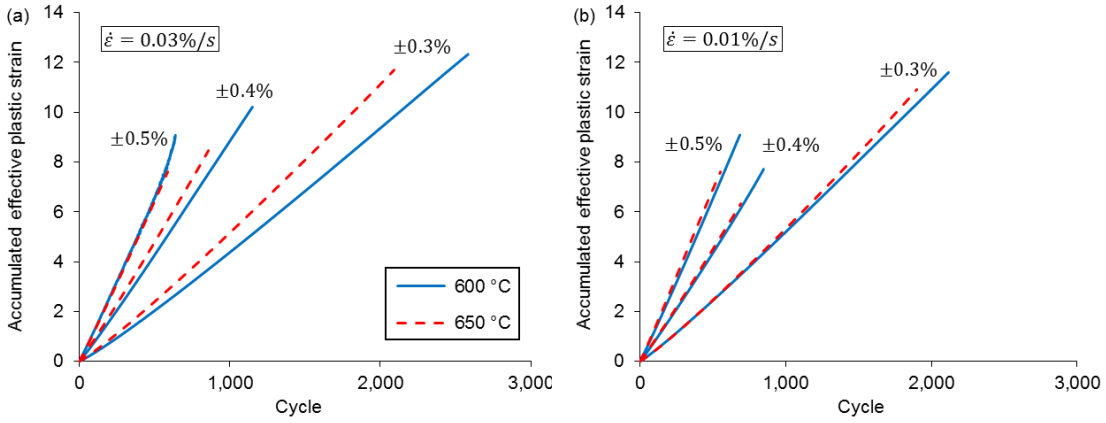

Figure 3.21 Accumulated effective plastic strain with cycles for cast MarBN at 600 °C and 650 °C across a range of strain-ranges and (a) $\dot{\varepsilon}$ = 0.03 %/s and (b) $\dot{\varepsilon}$ = 0.01 %/s.

3.7.3 Effect of a Hold Period

In Figure 3.22, the introduction of a hold period is shown to significantly reduce fatigue life (by 25% compared to the equivalent HTLCF test). An increase in the rate of cyclic softening is also observed, as well as more rapid degradation of the maximum stress towards the end of the test.

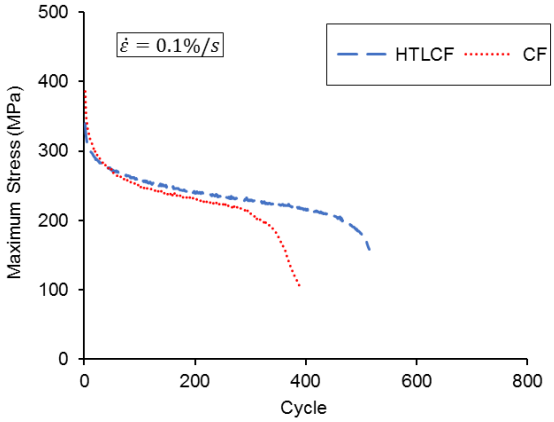

Figure 3.22 Maximum stress evolution for cast MarBN under HTLCF and CF loading at 650 °C, $\dot{\varepsilon}$ = 0.1 %/s, and $\Delta\varepsilon$ = ±0.5%.

The stress-strain loops of the data presented in Figure 3.22, comparing the HTLCF and CF response of cast MarBN, are shown in Figure 3.23 for the initial and half-life cycles. An increase in the plastic strain-range is observed due to CF loading, as well as increased compressive non-zero mean stress (~26% greater than the HTLCF sample) during the initial loading cycle.

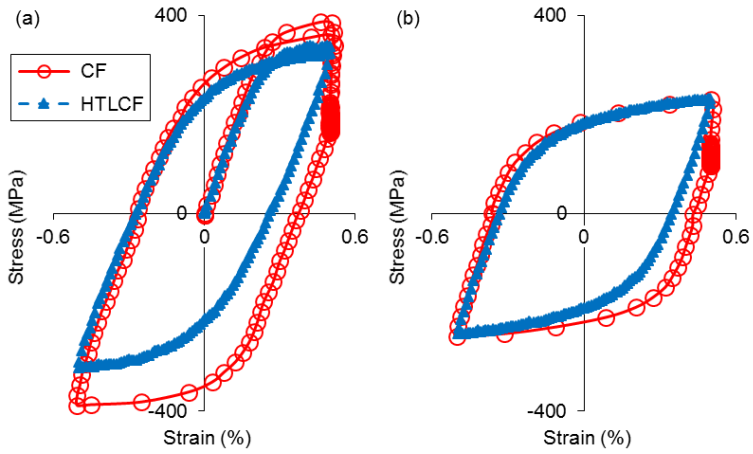

Figure 3.23 Comparison of the stress-strain loops for cast MarBN at 650 °C under HTLCF and CF loading for the (a) initial and (b) half-life cycles.

Figure 3.24 shows the evolution of stress under strain-controlled loading in tension, during the first cycle for MarBN at 600 °C and 650 °C. A reduction in the maximum stress is observed due to the effect of increased temperature on yield stress; a decrease in stress of ~60% and ~43% occurs at 600 °C and 650 °C respectively, compared to the initial maximum stress.

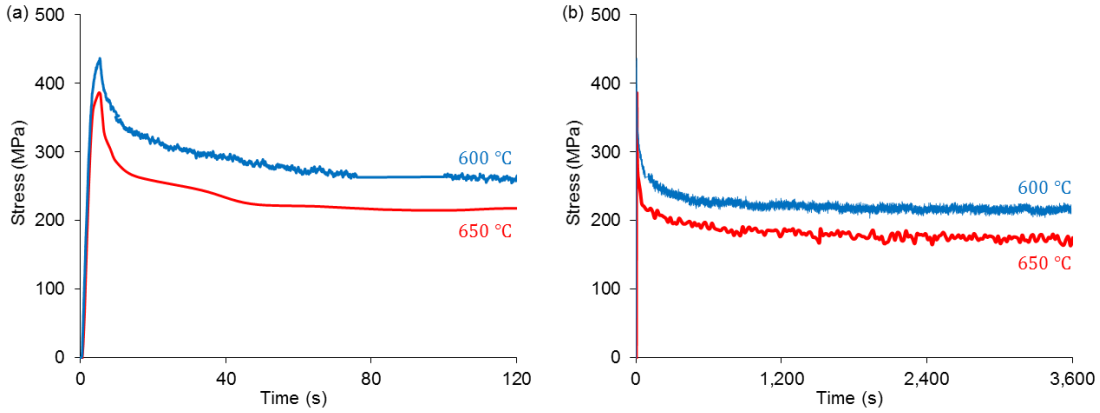

Figure 3.24 Stress evolution in CF testing of cast MarBN during the first cycle under strain-controlled tension loading up to (a) 120 seconds and (b) one hour at 600 °C and 650 °C.

Figure 3.25(a) shows the effect of temperature on the maximum plastic strain evolution for cast MarBN at 600 °C and 650 °C under CF loading during the initial hold period. An increase in plastic strain of ~11% occurs due to a 50 °C increase in temperature. In Figure 3.25(b), the maximum plastic strain evolution during HTLCF and CF testing is compared, and an increase in plastic strain of ~28% is observed due to the hold period, resulting in early failure compared to the same sample under HTLCF loading.

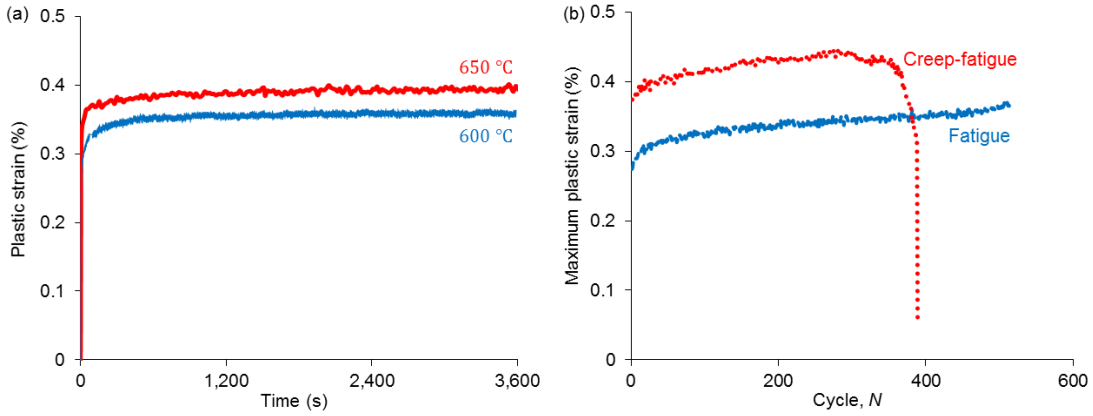

Figure 3.25 (a) Plastic strain evolution with time for cast MarBN at 600 °C and 650 °C and (b) maximum plastic strain evolution with cycles for HTLCF and CF loading ($\dot{\varepsilon}$ = 0.1 %/s, $\Delta\varepsilon$ = ±0.5% and temperature = 650 °C).

3.7.4 Cast versus Forged MarBN

To investigate the influence of manufacturing process on the high temperature cyclic behaviour of MarBN, HTLCF testing of cast and forged MarBN is performed at 600 °C, as described by the test program in Table 3.3. The forged material is produced from the same melt as the cast material and provided by the IMPACT project [18].

Table 3.3 Test program for HTLCF testing of cast and forged MarBN at 600 °C. The '*' denotes samples that are 3D X-ray µCT scanned before and after testing. Δ is percentage difference in cycles to failure between samples.

Material	**$\Delta\varepsilon$ (%)**	**$\dot{\varepsilon}$ (%/s)**	**N_f (-)**	**Δ (%)**
Cast_01	±0.5	0.1	715	13.1
Cast_02*	±0.5	0.1	627	
Forged_01*	±0.5	0.1	987	17.7
Forged_02	±0.5	0.1	1178	

The individual stress-strain loops are presented in Figure 3.26 for the initial, half-life and final cycles. The yield stress of Cast_02 (~250 MPa) is found to decrease by approximately 25% compared to Cast_01 and both forged samples (~330 MPa). Jumps in measured response of the Forged_01 sample (red dashed circle in Figure 3.26(f))

occurred due to cracking at the top extensometer leg in later cycles, as shown in Figure 3.27.

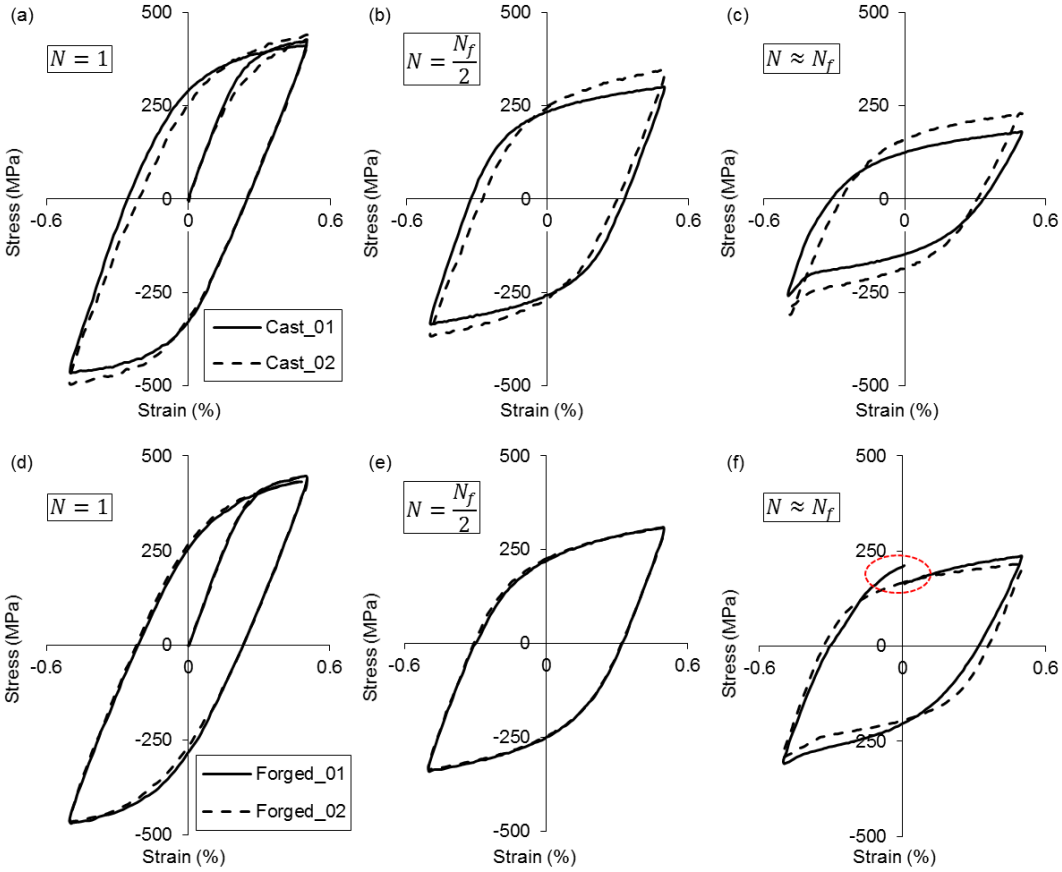

Figure 3.26 Stress-strain evolution of (a – c) cast and (d – f) forged MarBN for the initial, half-life and final cycles at 600 °C, $\dot{\varepsilon}$ = 0.1 %/s and $\Delta\varepsilon$ = ±0.5%.

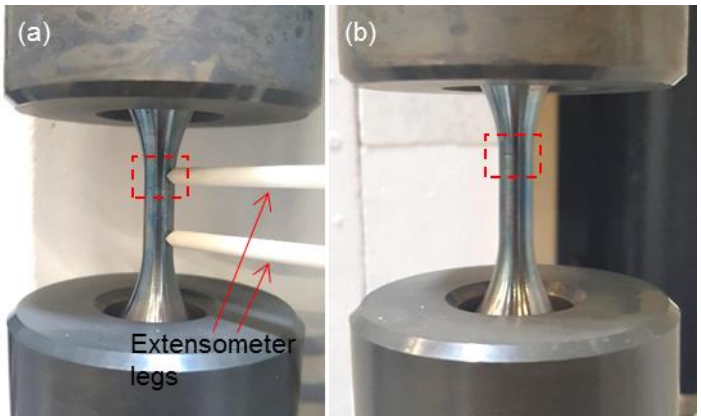

Figure 3.27 Cracking at the top extensometer leg during testing of Forged_01, causing distortion of the measured stress and strain.

Figure 3.28 presents the evolution of maximum stress and plastic strain for two cast and forged MarBN samples. The forged samples exhibit almost identical performance in terms of stress-strain, maximum stress and plastic strain evolution, with greater

variability observed between the cast samples. Forged MarBN has an increased fatigue life compared to cast also (Figure 3.29). These variations (i.e. yield stress, maximum stress and plastic strain evolution) are potentially related to manufacturing defects formed during the casting process. This will be discussed in more detail in Chapter 4, where 3D X-ray micro-computed tomography (µCT) scanning of cast and forged samples is presented (pre- and post-test) to characterise the role of manufacturing defects on fatigue cracking behaviour.

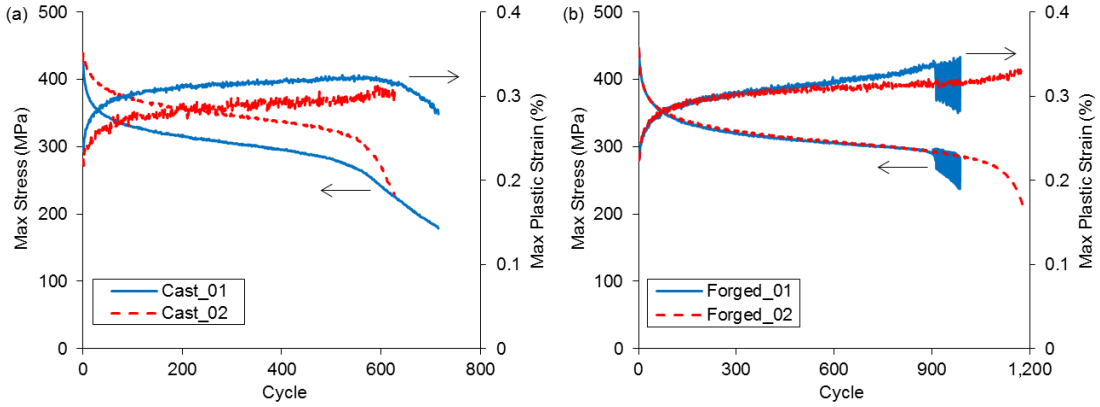

Figure 3.28 Maximum stress and plastic strain evolution with cycles for (a) cast and (b) forged MarBN samples tested at 600 °C, $\dot{\varepsilon}$ = 0.1 %/s and $\Delta\varepsilon$ = ±0.5%.

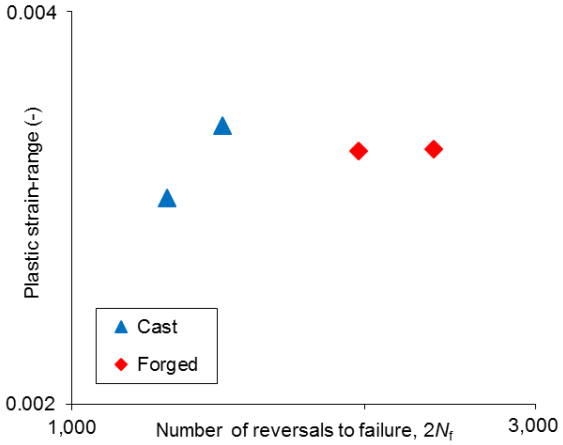

Figure 3.29 Plastic strain versus reversals to failure for cast and forged MarBN at 600 °C, $\dot{\varepsilon}$ = 0.1 %/s and $\Delta\varepsilon$ = ±0.5%.

3.7.5 Damage and Life Prediction

Fatigue damage in metals is primarily attributed to irreversible plastic deformation, generally as a result of dislocation motion, and is dependent on factors such as precipitates, inclusions and grain boundaries in the material [155,156]. At an early stage of fatigue loading, microstructural changes occur in the bulk of the material under cyclic

loading, whereby irreversible dislocation movement occurs [155]. Plastic deformation of ductile materials can cause decohesion of the particle-matrix interface or fracture of inclusions, leading to microvoid growth and microcrack initiation at elevated temperatures. Decohesion or inclusion fracture primarily results from stress concentrations, due to dislocation pile-up at inclusions, for example [121,123,156–158].

A key challenge for the case of 9Cr steels, which cyclically soften due to microstructure evolution, is the identification of macroscale fatigue damage evolution for prediction of crack initiation and hence failure. To separate cyclic softening and damage in 9Cr steels a modified damage term, $D_{\exp}$, is developed and defined as:

$$D_{\exp} = 1 - \frac{Z}{Z_0} \tag{3.1}$$

where

$$Z = \sigma_{\max}(N) - R(N) \tag{3.2}$$

and $\sigma_{\max}$ is the maximum tensile stress per cycle, Z_0 is the maximum value of Z, and R is the isotropic cyclic softening stress, calculated as:

$$\int_0^R \dot{R} = \int_0^p b(Q - R)\dot{p} \tag{3.3}$$

where b and Q are material constants, and $\dot{p}$ is the accumulated effective plastic strain-rate. As illustrated in Figure 3.30(a), the rate of primary cyclic softening is significantly greater than during the secondary phase. This is followed by a rapid decrease in the cyclic softening stress as macroscale crack propagation occurs and the component fails. To demarcate natural material softening from macroscale damage, the Z term is used, as per Figure 3.30(b). Figure 3.31 compares the damage curves for MarBN at 600 °C and 650 °C across a range of loading conditions. The rate of damage accumulation rapidly increases as macroscopic crack propagation occurs and is similar in all cases.

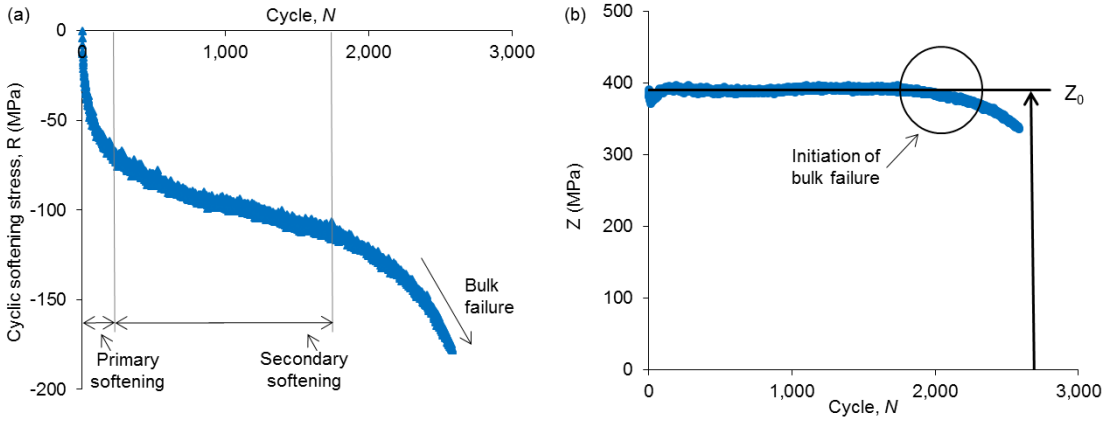

Figure 3.30 (a) Identification of the primary and secondary softening regions under cyclic loading, followed by macroscopic crack propagation and bulk sample failure, and (b) demarcation of softening from the maximum stress evolution and identification of Z_0.

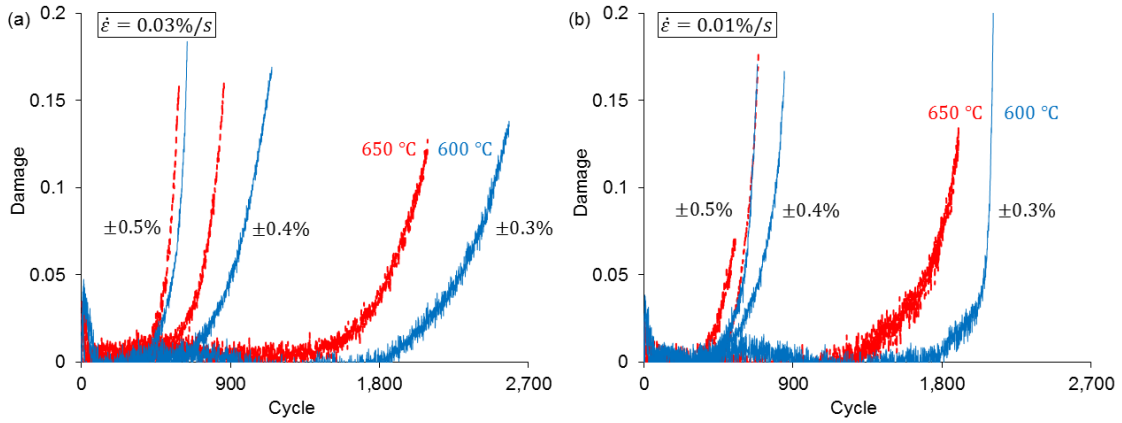

Figure 3.31 Damage accumulation with cycles for cast MarBN at 600 °C and 650 °C across a range of strain-ranges and a strain-rate of (a) 0.03 %/s and (b) 0.01 %/s.

Various methods of life prediction have been discussed in Chapter 2, which are calibrated based on experimental data. The Coffin-Manson [100] relationship is defined as:

$$\frac{\Delta\varepsilon^{\mathrm{pl}}}{2} = \varepsilon_{\mathrm{f}}^{'}\left(2N_{\mathrm{f}}\right)^{c} \tag{3.4}$$

where $\Delta\varepsilon^{\mathrm{pl}}$ is the plastic strain-range, N_{f} is number of cycles to failure, and $\varepsilon_{\mathrm{f}}^{'}$ and c are the fatigue ductility coefficient and exponent. In Figure 3.32, the low cycle fatigue (LCF) strain-life plot for cast MarBN at 600 °C and 650 °C is presented and the Coffin-Manson constants, $\varepsilon_{\mathrm{f}}^{'}$ and c, are identified at half-life. Similar plastic strain-ranges are generally observed in all cases, with a small reduction in number of reversals to failure

as a result of increasing temperature. For MarBN, the constants were identified based on a strain-rate of 0.03 %/s.

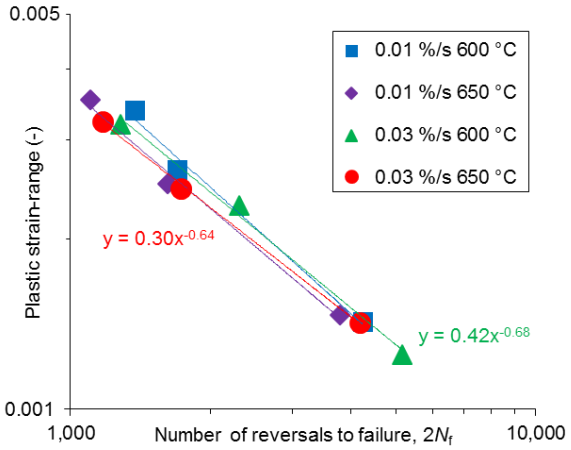

Figure 3.32 Strain-life plot for cast MarBN at 600 °C and 650 °C at various strain-rates and strain-ranges.

The Ostergren [104] life prediction equation (applicable for both thermo-mechanical and isothermal fatigue), based on both plastic strain-range and maximum stress ($\sigma_{\max}$), is given by:

$$N_{\mathrm{f}} = C\left(\Delta\varepsilon^{\mathrm{pl}}\sigma_{\max}\right)^{\delta} \tag{3.5}$$

where C and δ are material parameters. Identification of the Ostergren [104] parameters is performed by plotting the Ostergren product at half-life $\left(\Delta\varepsilon^{\mathrm{pl}}\sigma_{\max}\right)$ against cycles to failure for a set of fatigue tests across various strain-ranges. The identified Coffin-Manson and Ostergren constants for MarBN at 600 °C and 650 °C are presented in Table 3.4.

Table 3.4 Coffin-Manson and Ostergren life prediction constants for MarBN at 600 °C and 650 °C, at a strain-rate of 0.03 %/s.

Temp (°C)	$\boldsymbol{\varepsilon_f'}$ **(-)**	$\boldsymbol{c}$ **(-)**	$\boldsymbol{C}$ **(MPa)**	$\boldsymbol{\delta}$ **(-)**
600	0.42	-0.68	167.30	-0.69
650	0.30	-0.64	152.82	-0.72

3.8 Microstructural Analysis

3.8.1 As-Received MarBN

BSE images of the as-received microstructure of rolled P91, and cast and forged MarBN are shown in Figure 3.33. Significant differences can be observed in terms of grain size as a result of the different manufacturing processes. Rolled P91 has a refined grain size of approximately 20 µm, while cast MarBN has a greater variation in grain size in the range of 200 µm to 400 µm, and forged MarBN has intermediate grains that are approximately 100 µm in length.

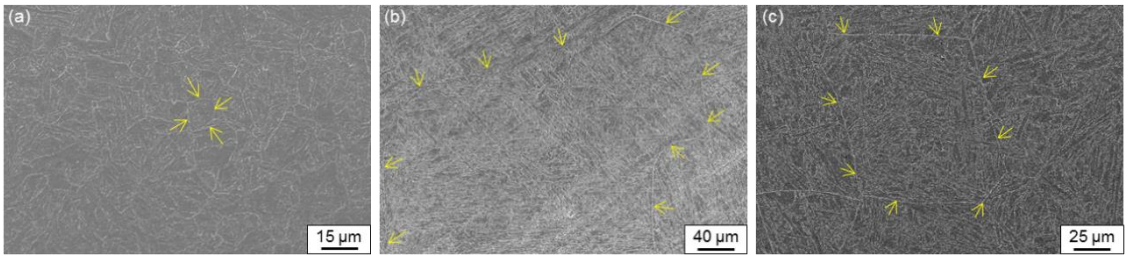

Figure 3.33 As-received microstructure of (a) rolled P91, (b) cast MarBN and (c) forged MarBN.

3.8.2 Fractography of High Temperature Low Cycle Fatigue and Creep-Fatigue MarBN

Fractography of cast MarBN samples post-test, for a range of HTLCF and CF loading conditions at 600 °C and 650 °C, is performed using SEM. Images of the fracture surface of forged MarBN are also presented. Characteristic features of crack initiation and propagation based on HTLCF and CF loading are observed, independent of strain-rate, strain-range and temperature. Figure 3.34(a) and Figure 3.34(b) show fatigue striations in the region of crack propagation in a cast MarBN sample tested under HTLCF loading at 600 °C. In Figure 3.34(c) and Figure 3.34(d), ductile dimples can be seen in in the area of static fracture, and inclusions are also observed in both regions on the cast fracture surfaces examined.

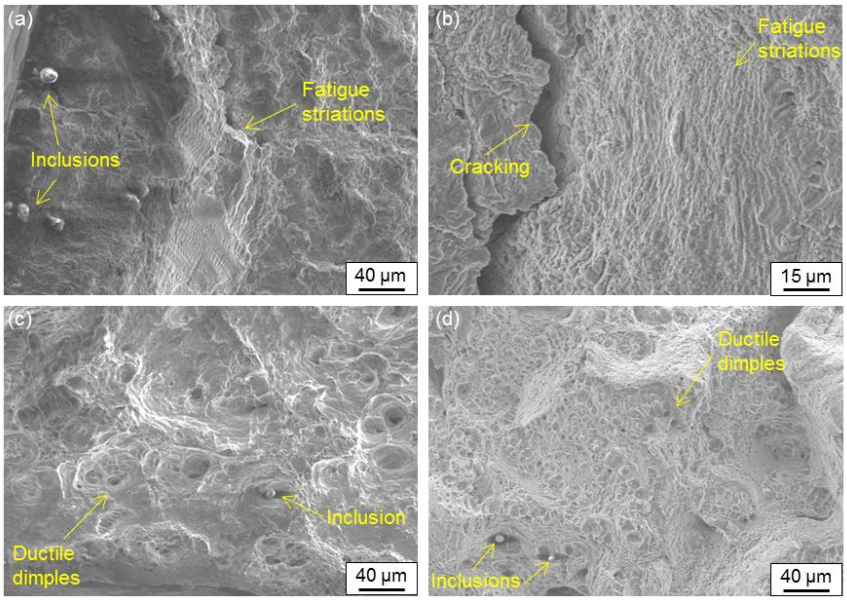

Figure 3.34 SEM images of the fracture surface of HTLCF cast MarBN samples showing (a, b) fatigue striations and (c, d) ductile dimples.

Figure 3.35(a) and Figure 3.35(b) present examples of dendritic shrinkage on the fracture surface of various cast MarBN samples tested under HTLCF loading. Their presence on the fracture surface, as well as crack propagation from these regions, indicates localised stress and strain concentrations, leading to cracking and sample failure under HTLCF loading. Figure 3.35(c) and Figure 3.35(d) show the influence of voids and inclusions on the cracking behaviour in terms of both initiation and propagation. In Figure 3.36, similar features are observed in the case of forged MarBN as a result of HTLCF testing (e.g. cracking at inclusions, ductile dimples). A notable difference is the presence of tear ridges in the region of static fracture (i.e. away from the region of primary cracking), indicating local crack initiation.

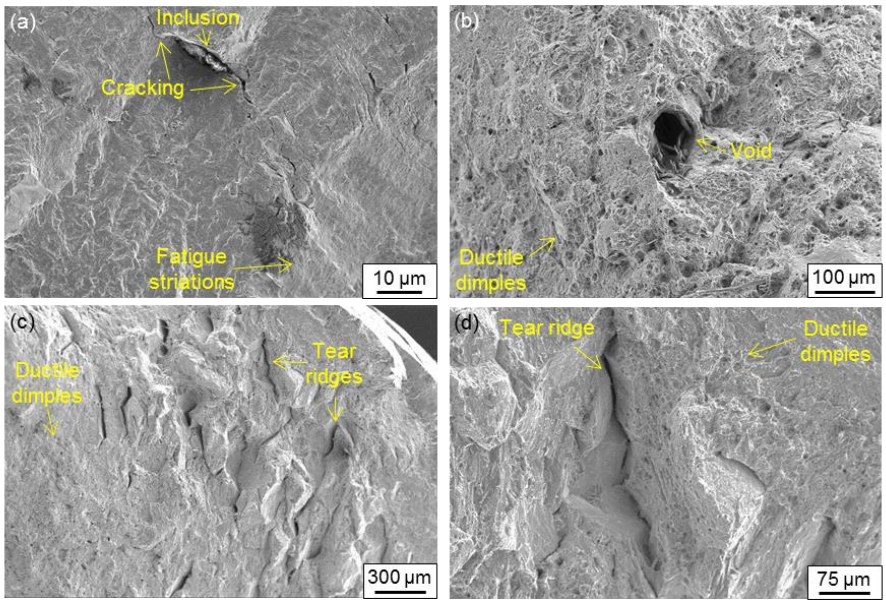

Figure 3.35 (a, b) Dendritic shrinkage and (c, d) cracking at inclusions on the fracture surface of post-HTLCF cast MarBN samples.

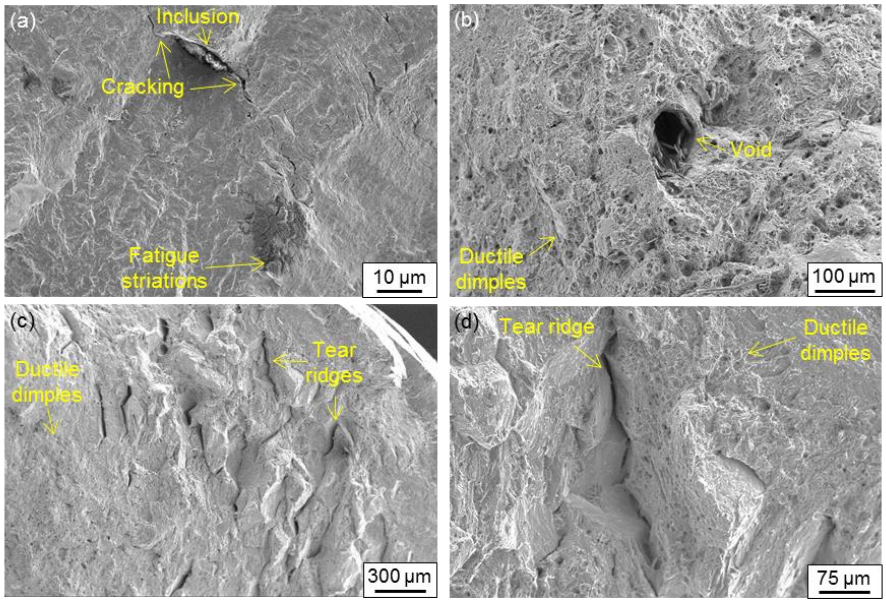

Figure 3.36 SEM images of the forged MarBN fracture surface showing (a) cracking from an inclusion and fatigue striations, (b) a void in the region of ductile dimples, (c, d) tear ridges and ductile dimples.

Fatigue striations and ductile dimples are also observed on the fracture surface of the cast MarBN sample tested under CF conditions at 650 °C; the primary difference between the CF and HTLCF fracture surfaces is the presence of cleavage facets, and associated cracking, in the region of static fracture. Figure 3.37 presents multiple examples of this.

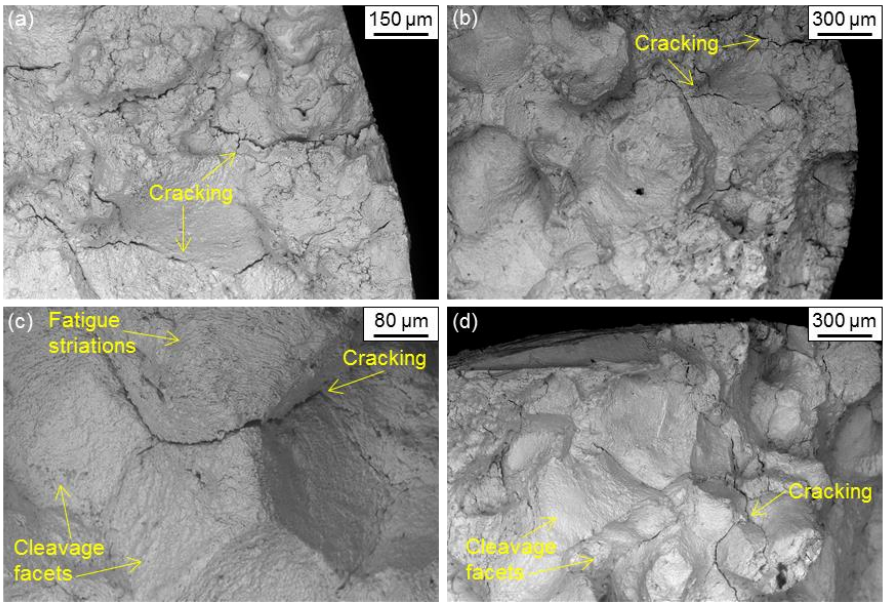

Figure 3.37 (a – d) Cracking and cleavage facets on the fracture surface of the CF cast MarBN sample tested at 650 °C.

3.8.3 Sectioned Post-Test MarBN

Following fractographic analysis, the above samples are placed in resin and polished as described in Section 3.5.1, for sectioned microstructural analysis. Secondary cracking, away from the fracture surface, is observed in all cases. In Figure 3.38, complex shaped Ca-Al-O inclusions are shown to influence cracking behaviour near the surface, whereas cracking at a spherical MnS does not occur. The role of oxidation is also investigated and Figure 3.39 shows an oxygen element map demonstrating oxide penetration of the matrix through a secondary crack.

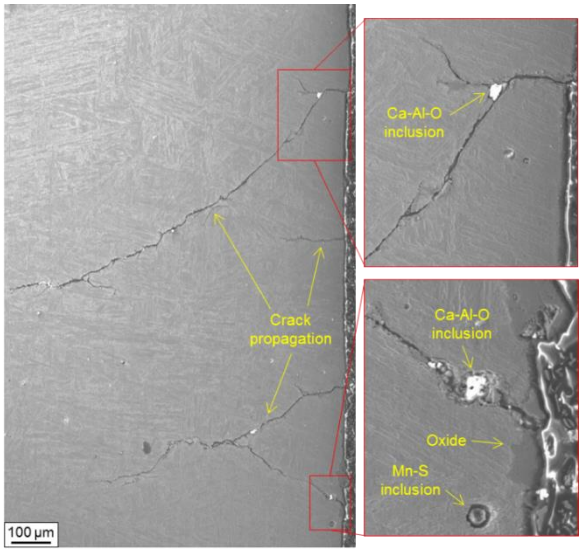

Figure 3.38 SEM image of secondary cracking around complex shaped inclusions in a cast HTLCF MarBN sample tested at 600 °C.

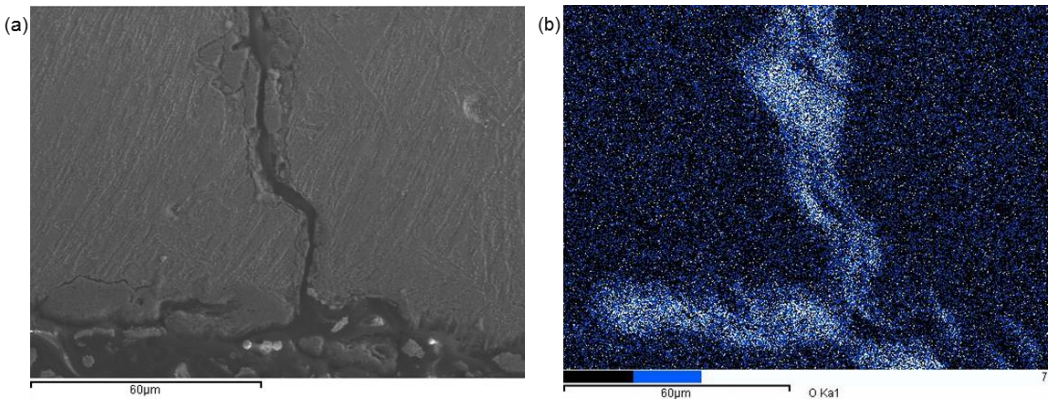

Figure 3.39 (a) Oxide layer growth in a secondary crack of a cast HTLCF MarBN sample tested at 600 °C and (b) the corresponding element map for oxygen.

Further examples of secondary cracking are presented in Figure 3.40 and Figure 3.41, for HTLCF samples at 600 °C and 650 °C. There is no significant difference observed between the amount of secondary cracking or oxide growth for the two temperatures. Similar behaviour is also observed in the forged MarBN sample (Figure 3.42). However, when compared to a sample tested under CF loading conditions (Figure 3.43), the amount of secondary cracking and internal oxidation is found to increase, as a result of prolonged high temperature exposure. Inclusions are seen to play a vital role in terms of both crack initiation at the surface and propagation through the matrix, as well as oxide pit formation, in the majority of cases presented.

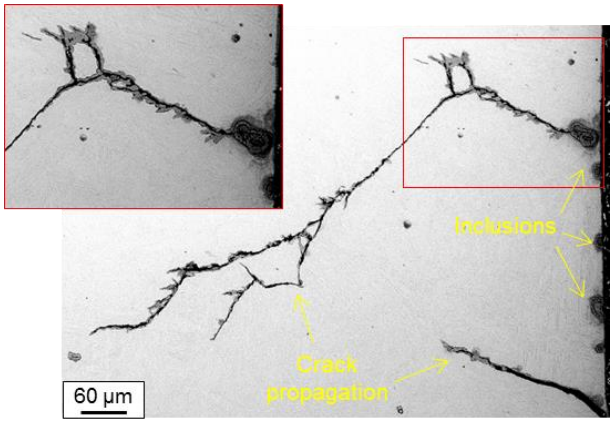

Figure 3.40 BSE image of secondary cracking and oxide scale growth in a cast HTLCF MarBN sample tested at 600 °C.

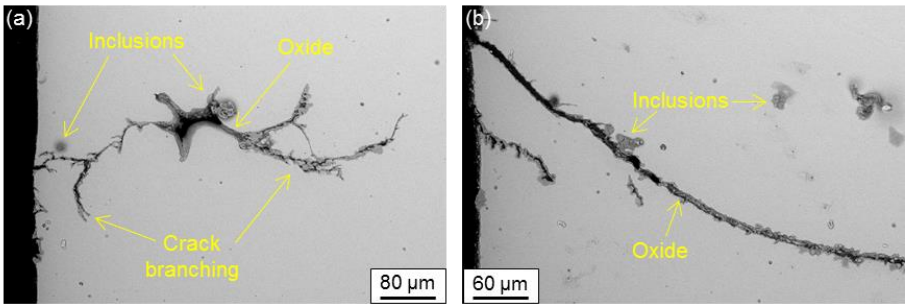

Figure 3.41 BSE images of (a) crack branching along the gauge length at inclusions and a casting defect, with internal oxide scale growth, and (b) crack propagation and internal oxidation in a cast HTLCF MarBN sample tested at 650 °C.

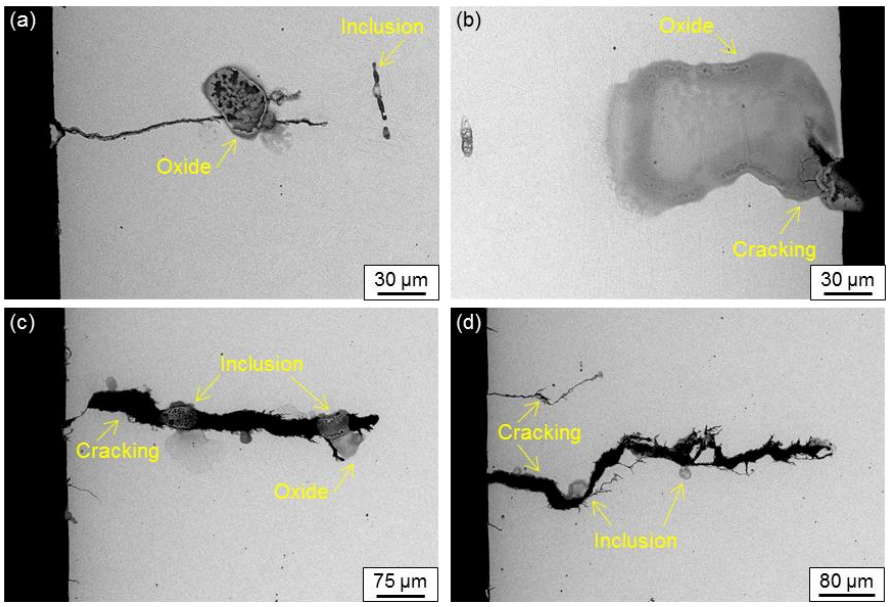

Figure 3.42 BSE images of (a) crack propagation towards a stringer-type inclusion, with oxide pitting, and (b, c, d) secondary cracking at an inclusion, and oxide scale formation and pitting, in a forged HTLCF MarBN sample tested at 600 °C

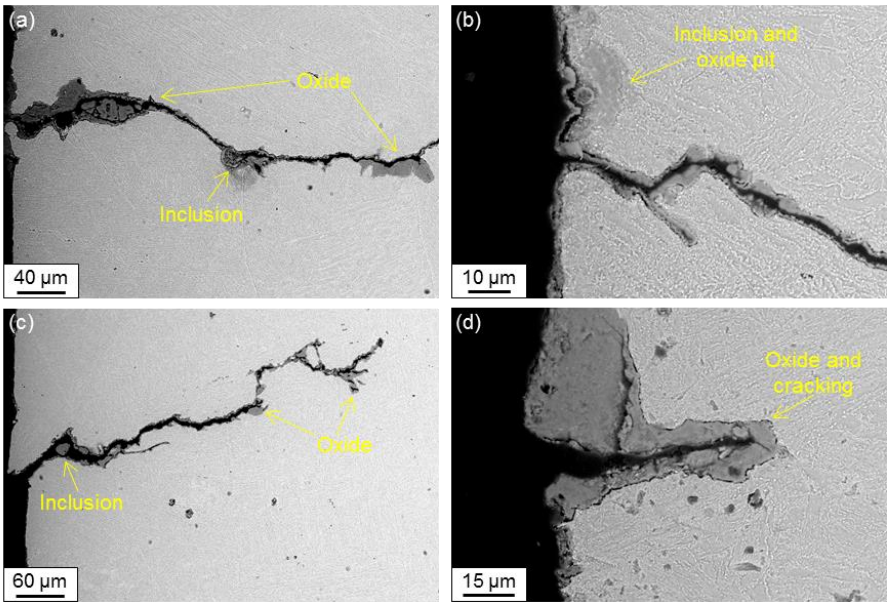

Figure 3.43 BSE images of secondary cracking (a, b, c) at inclusions and oxide scale formation, and (d) oxide scale formation, in the CF cast MarBN sample at 650 °C.

Figure 3.44 shows an element map of the crack in Figure 3.43(a). The distribution of oxygen, iron, chromium and tungsten are presented and confirms oxide growth in the secondary crack, as well as chromium and iron rich layers in the oxide scale. Tungsten is shown to be coarsely distributed and this is assumed to be due to its segregation in solute and precipitate form in the large-grained cast microstructure.

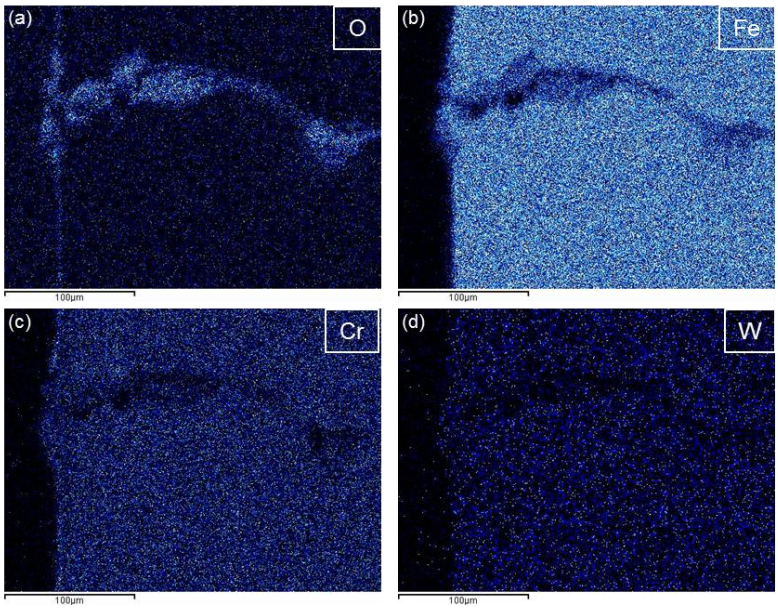

Figure 3.44 Element map of (a) oxygen, (b) iron, (c) chromium and (d) tungsten corresponding to Figure 3.43(a).

3.8.4 Casting Defects and Inclusions

Crack initiation and propagation, due to the presence of manufacturing defects (i.e. voids and inclusions) near the gauge length surface, has been confirmed in both cast and forged MarBN in the previous section. However, alternative factors such as shape and decohesion also play an important role in relation to crack initiation and propagation [155,158]. Figure 3.45 shows examples of the varying complexity of casting defects observed via SEM in sectioned post-test cast MarBN samples under HTLCF loading conditions. Cracking as a result of low cycle fatigue loading typically originates from the sample surface and no internal cracking is observed in the samples examined here. The influence of defects on cracking will be presented in greater detail in Chapter 4. In terms of the manufacturing defects observed in the forged material, complex shaped defects were not typically observed; the geometry was generally identified as either spherical or elongated stringer-type defects. Figure 3.46 presents SEM images of a number of inclusions and voids observed in sectioned cast MarBN samples post-HTLCF testing, where decohesion has occurred or the inclusion has fallen out or become damaged during mechanical polishing. The typical composition of these inclusions is presented in Table 3.5 and shows high calcium content in all cases.

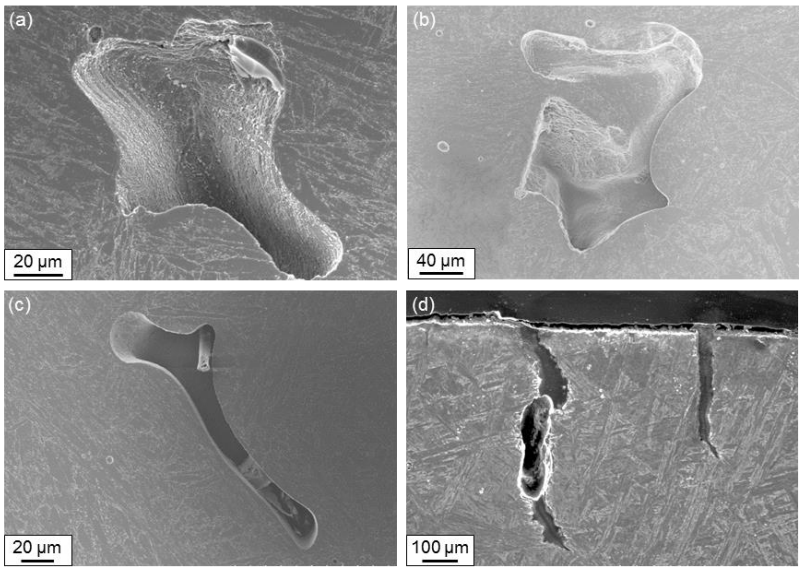

Figure 3.45 (a – d) Examples of various manufacturing defects observed using SEM in sectioned cast MarBN HTLCF samples.

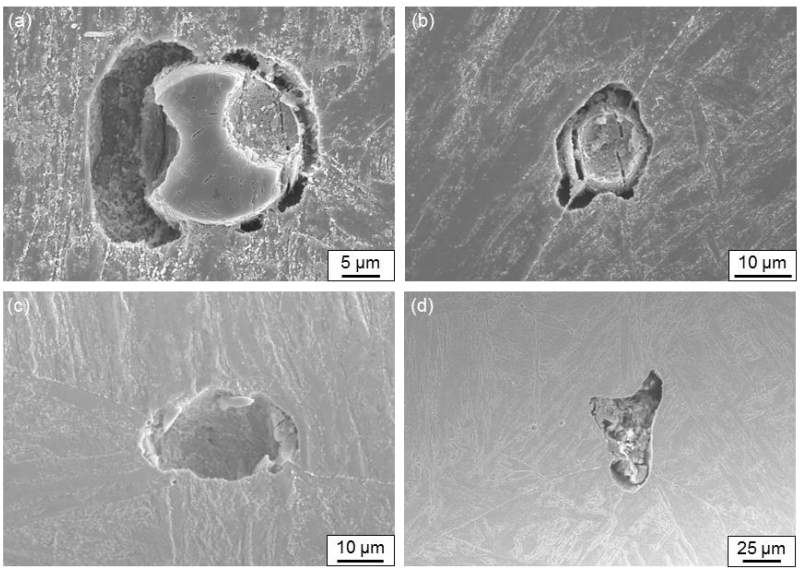

Figure 3.46 (a – d) Examples of various manufacturing defects observed via SEM in sectioned cast MarBN HTLCF samples post-test.

Table 3.5 Elemental composition of the inclusion shown in Figure 3.46(b) (first row), and others identified via EDX in cast MarBN.

Element	**O**	**Al**	**Si**	**S**	**Ca**	**Cr**	**Mn**	**Mg**	**Fe**
Weight%	28.6	7.1	3.4	6.1	36.4	4.0	14.4	-	-
	58.1	16.4	-	0.6	20.2	-	-	2.8	2.1
	35.6	16.7	7.1	-	34.1	-	-	2.5	4.2
	53.1	15.5	4.9	-	23.4	-	-	2.1	1.2

3.8.5 Transmission Electron Microscopy

TEM is used to investigate the effect of cyclic loading at high temperature on precipitate and lath evolution in cast MarBN. In Figure 3.47, bright field images of AR and post-test cast MarBN are presented. Significant lath coarsening is observed to occur as a result of low angle boundary annihilation due to HTLCF loading.

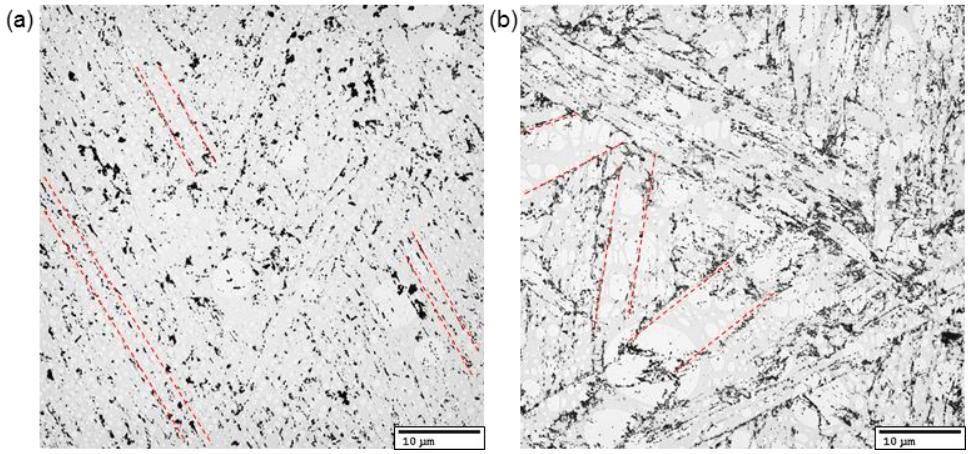

Figure 3.47 Bright field TEM images of carbon replica cast MarBN samples. (a) As-received and (b) post-HTLCF test at 600 °C. Red lines denote lath boundaries.

A histogram of the most common Feret diameters (the longest distance between any two points within a boundary) is presented in Figure 3.48. To perform this measurement, the images are converted to a binary format and watershed segmentation is applied to identify individual particle dimensions using image processing software, ImageJ [159]. The frequency of particles post-test is found to be approximately double that for pre-test, with little change in diameter. It is conjectured that regions of Laves phase have formed along grain boundaries in the post-test MarBN samples as a result of the high temperature loading. Thus, the significant increase in particle density observed via TEM (Figure 3.48) is attributed to Laves phase formation. In Figure 3.49, low angle boundary annihilation and dislocation motion in post-test thin foil MarBN samples is identified, indicating the effect of cyclic loading on the microstructure. Formation of equiaxed subgrains is also observed, as per Figure 3.50.

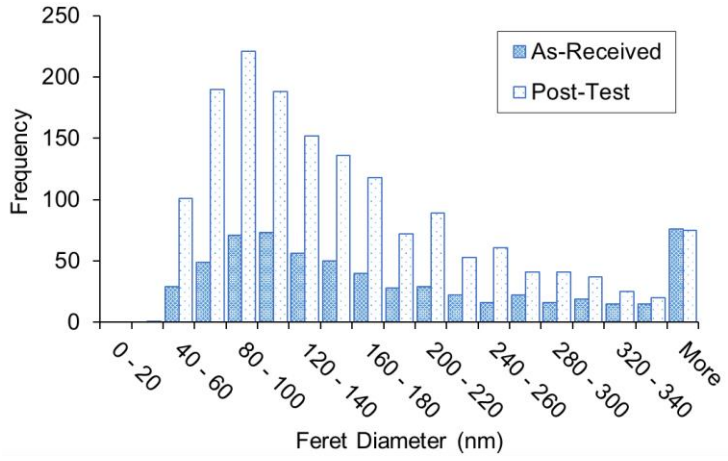

Figure 3.48 Histogram of the frequency of precipitate Feret diameter in carbon replica cast MarBN samples in the as-received and post HTLCF test condition.

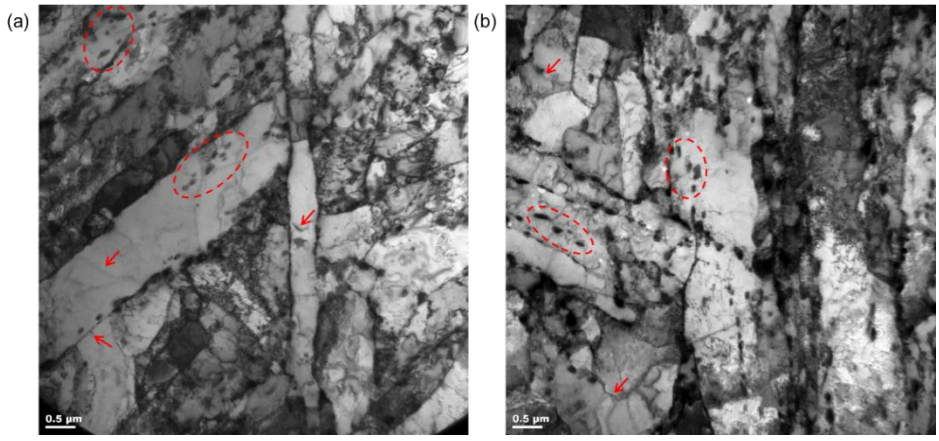

Figure 3.49 (a, b) Bright field TEM images of the lath microstructure in thin foil cast MarBN samples post-HTLCF test at 600 °C. Dashed circles are $M_{23}C_6$ carbides and arrows are dislocation chains within a lath.

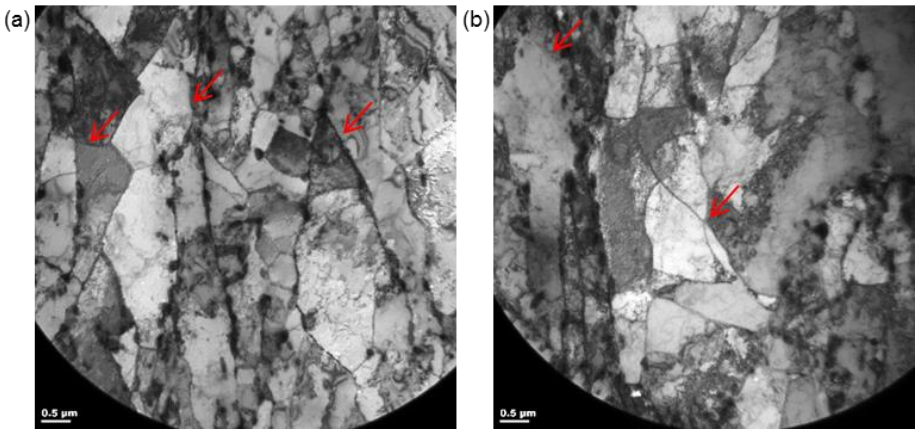

Figure 3.50 (a, b) Bright field TEM images of equiaxed subgrain formation in thin foil cast MarBN samples post-HTLCF test at 600 °C. Red arrows are equiaxed sub-grains.

3.9 Oxidation and Corrosion Testing

To characterise the oxidation and corrosion resistance of MarBN, cast and forged samples were exposed to air and corrosive ash at 600 °C and 650 °C up to 28 days. P91 samples were also exposed to the same conditions at 600 °C, for comparison to a current state-of-the-art power plant material. Figure 3.51 and Figure 3.52 show measured oxide scale thickness with time for oxidation and corrosion MarBN and P91 samples. A loosely adhered and inconsistent scale occurs due to high temperature oxidation exposure. In contrast, the scale thickness dramatically increases for all samples due to the application of corrosive ash (from ~6 µm to ~60 µm in all cases after 28 days exposure). No significant effect on scale thickness is identified due to increased temperature.

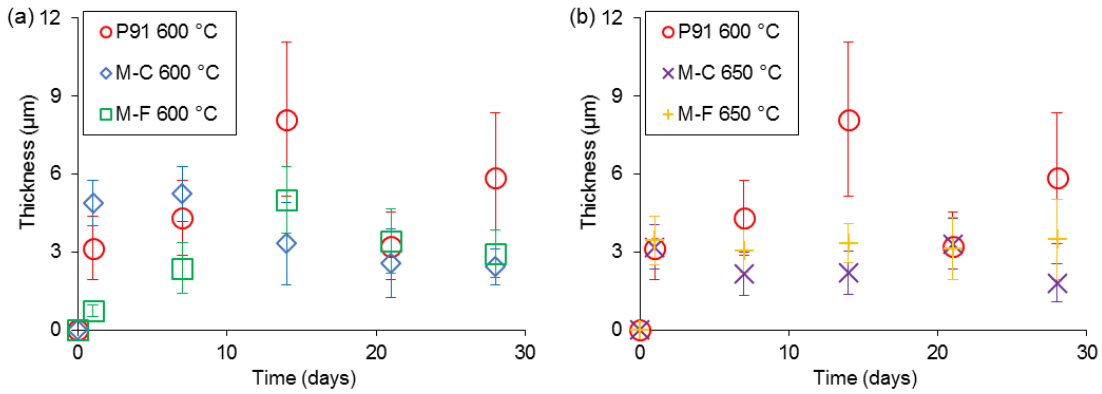

Figure 3.51 Oxide scale growth with time in air for cast MarBN (M-C) and forged MarBN (M-F) at (a) 600 °C and (b) 650 °C, with a comparison to P91 at 600 °C.

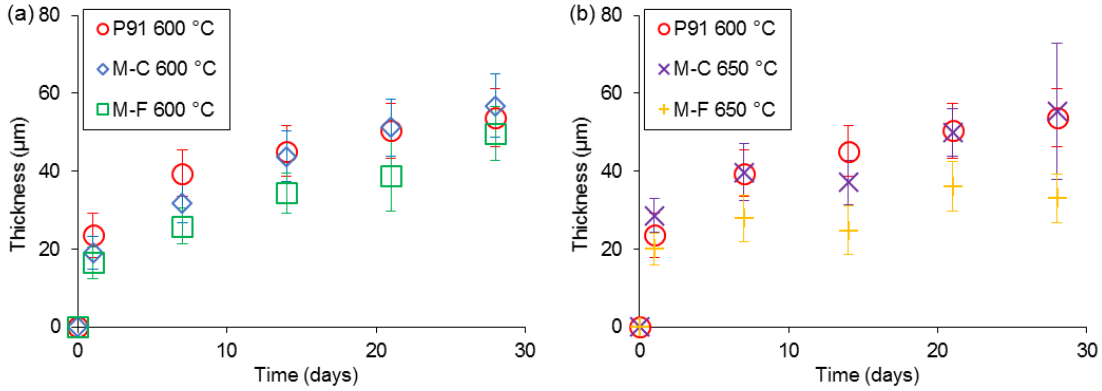

Figure 3.52 Oxide scale growth with time and ash applied, for cast MarBN (M-C) and forged MarBN (M-F) at (a) 600 °C and (b) 650 °C, with a comparison to P91 at 600 °C.

Figure 3.53 shows BSE images of the oxide scale on sectioned corrosion samples of MarBN and P91 after high temperature exposure for 28 days. Spallation of the oxide scale can be seen, as well as oxide pit formation at inclusions, in the case of P91. Figure 3.54 shows examples of oxide pit formation at inclusions, and oxide scale spallation and cracking for P91 and MarBN samples, corrosion tested for 28 days.

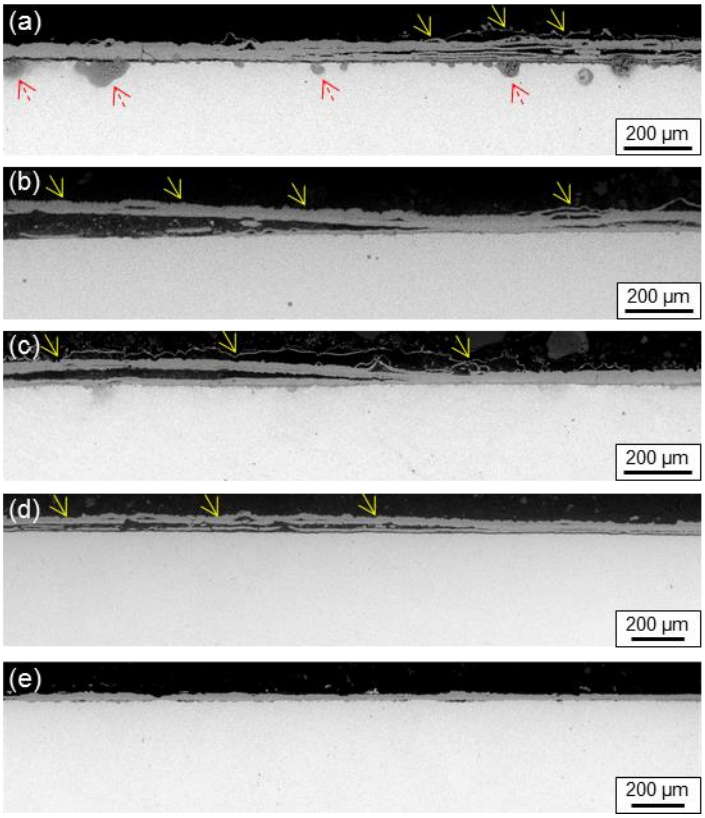

Figure 3.53 BSE images of oxide scale growth on (a) P91, (b) cast MarBN and (c) forged MarBN at 600 °C, and (d) cast MarBN and (e) forged MarBN at 650 °C, corrosion tested for 28 days. Solid yellow arrows denote oxide spallation and dashed red arrows are oxide pits at inclusions.

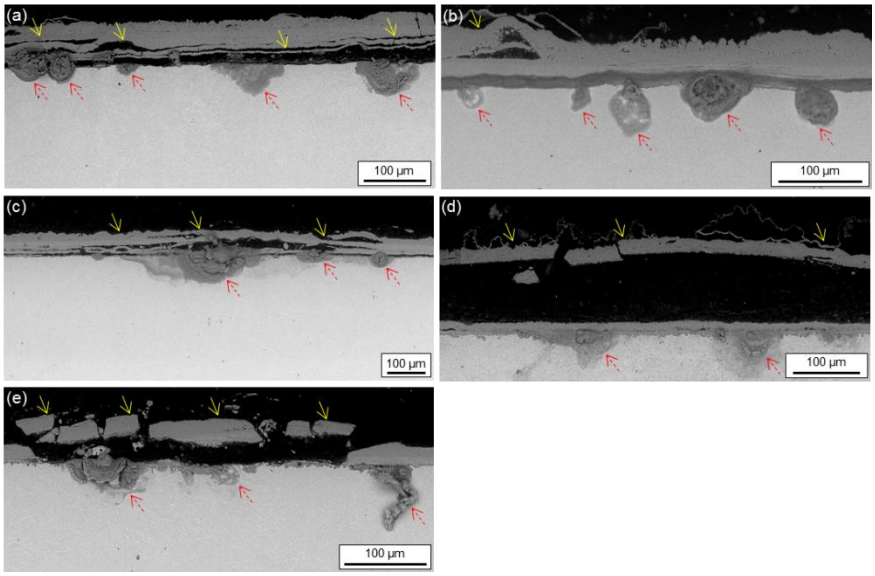

Figure 3.54 Role of inclusions in oxide scale detachment and oxide pit formation at the surface in (a) P91, (b) cast MarBN and (c) forged MarBN at 600 °C, and (d) cast MarBN and (e) forged MarBN at 650 °C for 28 days. Solid yellow arrows denote oxide spallation and dashed red arrows are oxide pits at inclusions.

Figure 3.55(a) shows an SEM image of a cast MarBN sample, tested in air at 600 °C for 28 days. Decohesion of an inclusion at the surface, as well as the oxide scale, is observed. EDX measurements of the chemical composition are taken along the oxide scale and the distribution of tungsten and chromium are plotted in Figure 3.55(b). The distribution of tungsten and chromium approaching the surface is also presented in Figure 3.56 for a cast MarBN sample, oxidation tested at 650 °C for 21 days. The oxide scale is still adherent to the surface in this case. Significant variations in chemical composition are observed close to the oxide scale, compared to the as-received matrix composition (dashed lines).

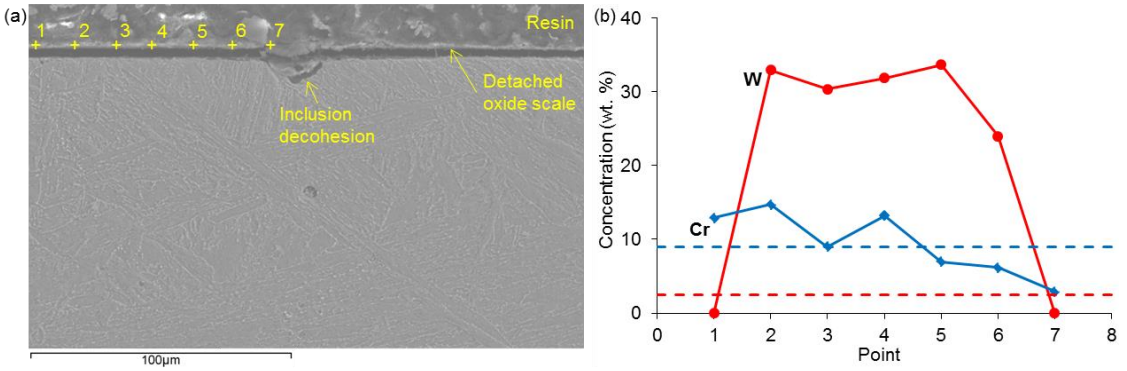

Figure 3.55 (a) SEM image of oxide scale detachment and inclusion decohesion in cast MarBN in air at 600 °C for 28 days, and (b) EDX measured Cr and W concentrations through the oxide scale at locations labelled in part (a). Dashed lines indicate original composition.

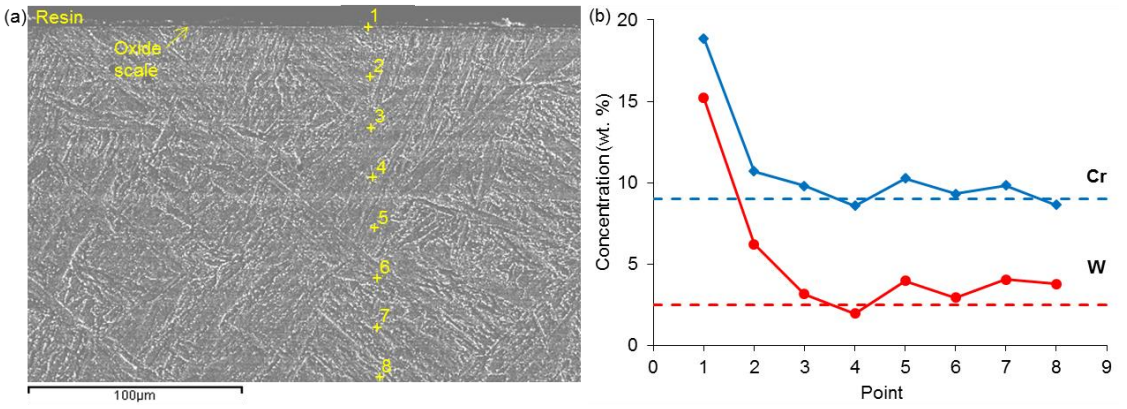

Figure 3.56 (a) SEM image of an oxide scale on cast MarBN in air at 650 °C for 21 days, and (b) EDX measured Cr and W concentrations through the matrix at locations labelled in part (a). Dashed lines indicate original composition.

Figure 3.57 is an element map of oxygen, molybdenum and tungsten in a cast MarBN sample, oxidation tested at 650 °C for 28 days. Although the oxide scale is very thin (~5 µm), an oxide-affected zone is observed adjacent to the oxide scale.

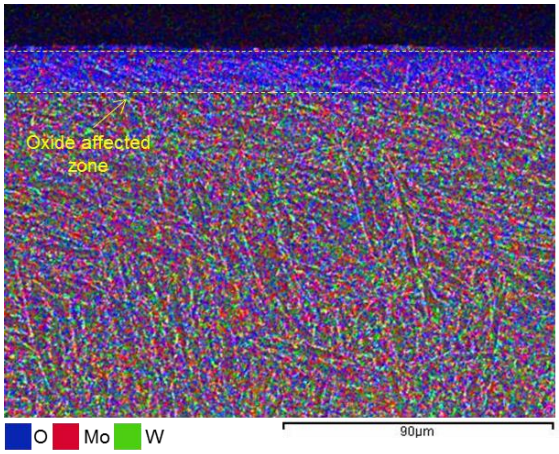

Figure 3.57 Element map of oxygen (blue), molybdenum (red) and tungsten (green) in cast MarBN in air at 650 °C for 28 days.

Figure 3.58 shows element maps of the oxygen, iron and chromium distributions in cast and forged MarBN samples, corrosion tested at 650 °C for 28 days. Iron is found to diffuse to the outer region of the oxide scale, while chromium remains close to the surface. The same maps are shown in Figure 3.59 for P91, corrosion tested at 600 °C for 28 days, and similar distributions are observed.

In Figure 3.60, element maps of cobalt, chlorine and tungsten are presented for cast and forged MarBN samples, corrosion tested at 650 °C for 28 days. Figure 3.60(a) shows high concentrations of chlorine in the oxide scale of cast MarBN that is not observed for forged MarBN (Figure 3.60(b)). For the cases where inclusions are located at the surface (Figure 3.60(c) and Figure 3.60(d)), segregation of chlorine towards inclusions occurs. The presence of tungsten and cobalt in the oxide scale is also observed.

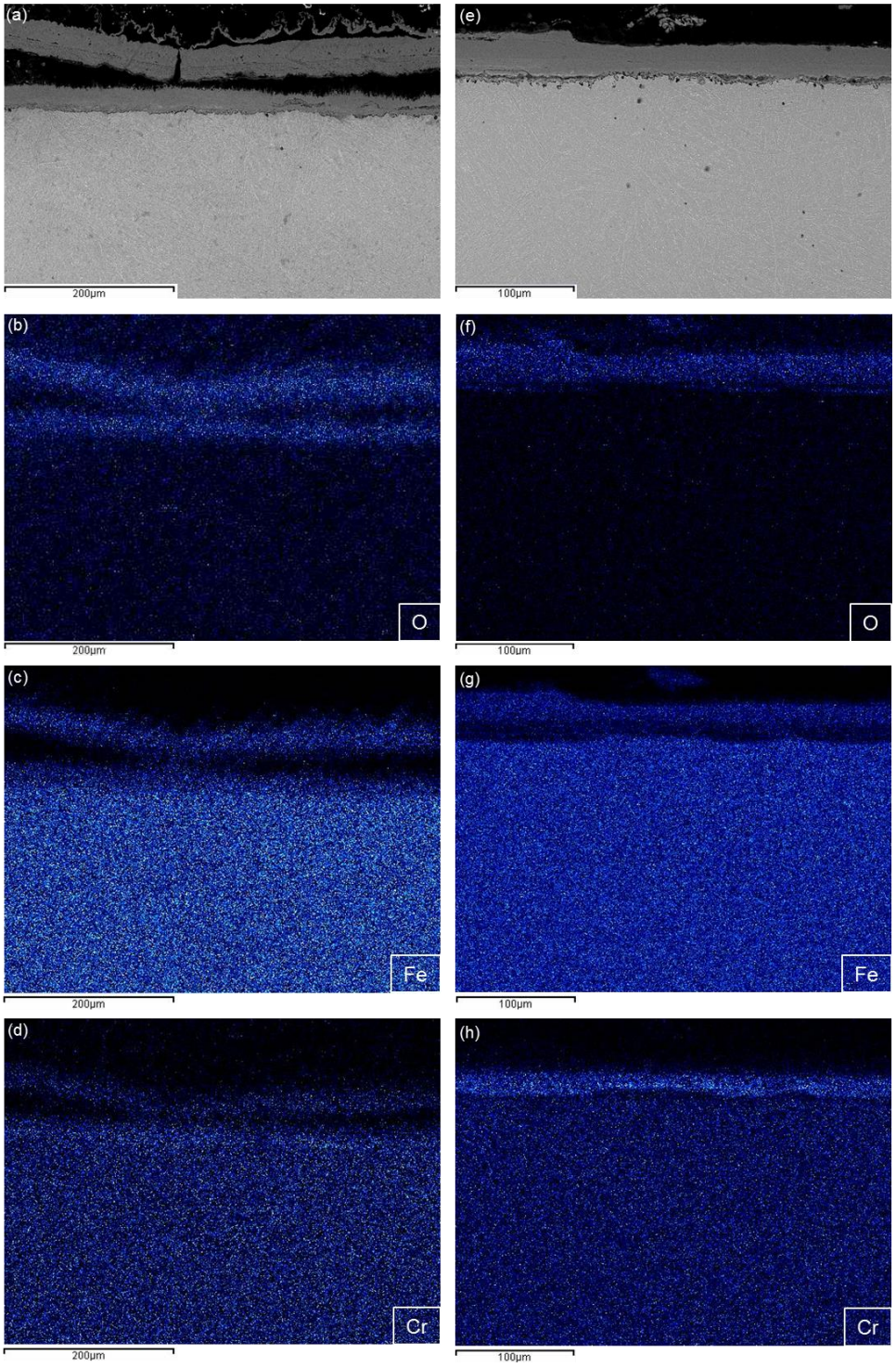

Figure 3.58. Element maps of (a – d) cast MarBN and (e – h) forged MarBN showing the distribution of oxygen, iron and chromium after 28 days at 650 °C with ash applied.

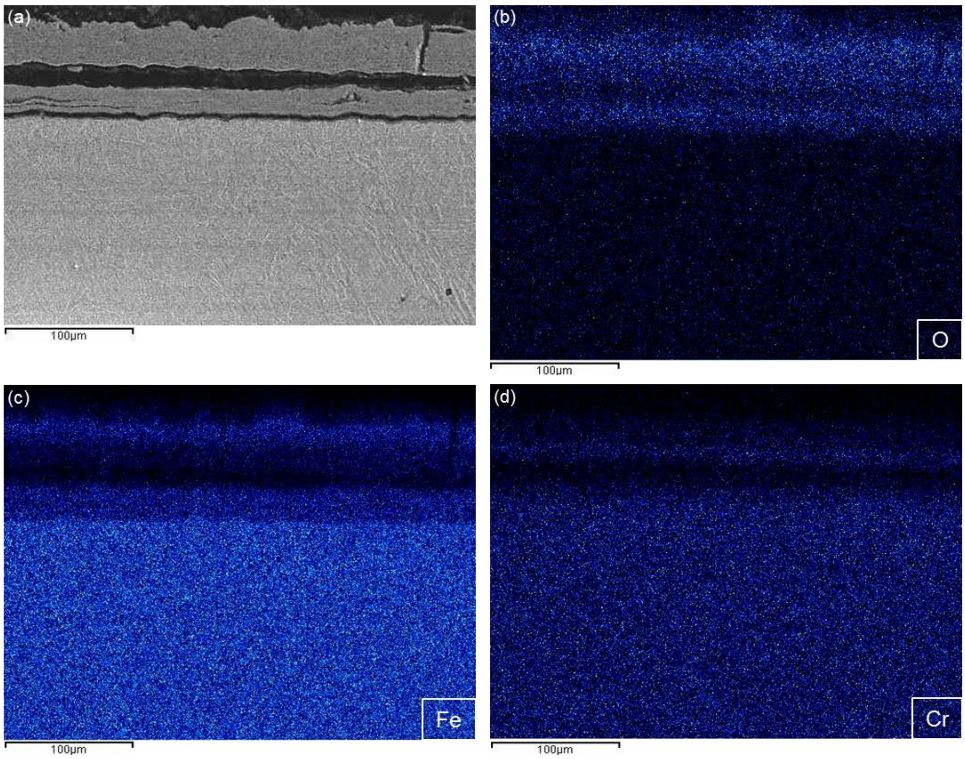

Figure 3.59. Element map of P91 showing the distribution of oxygen, iron and chromium after 28 days at 600 °C with ash applied.

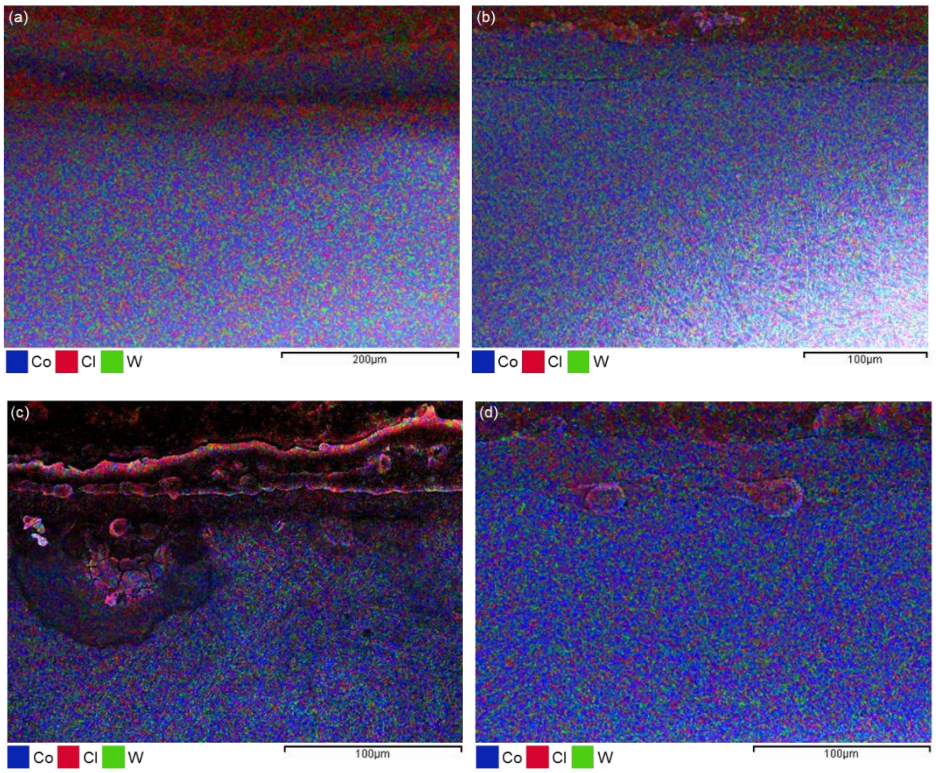

Figure 3.60 Element maps of cobalt (blue), chlorine (red) and tungsten (green) in (a, c) cast and (b, d) forged MarBN at 650 °C for 28 days with ash applied.

3.10 Laves Phase Formation

BSE has been used previously to identify Laves phase (Fe_2W) particles in tungsten containing steels [25,68,160], due to the high atomic weight of tungsten resulting in a high contrast between the particles and matrix. Figure 3.61 shows examples of Laves phase formation along boundaries in cast MarBN samples tested under HTLCF loading at 600 °C and 650 °C. Inclusions near the surface are shown to promote fatigue crack initiation. In Figure 3.62, similar results for Laves phase formation are observed as a result of CF loading at 650 °C. Laves phase formation has also been observed in oxidation (Figure 3.63) and corrosion (Figure 3.64) MarBN samples at both 600 °C and 650 °C. In Figure 3.65, linear regions of Laves phase are identified in the oxide scale, and may explain the high concentration of tungsten previously identified in the oxide scale in Figure 3.55.

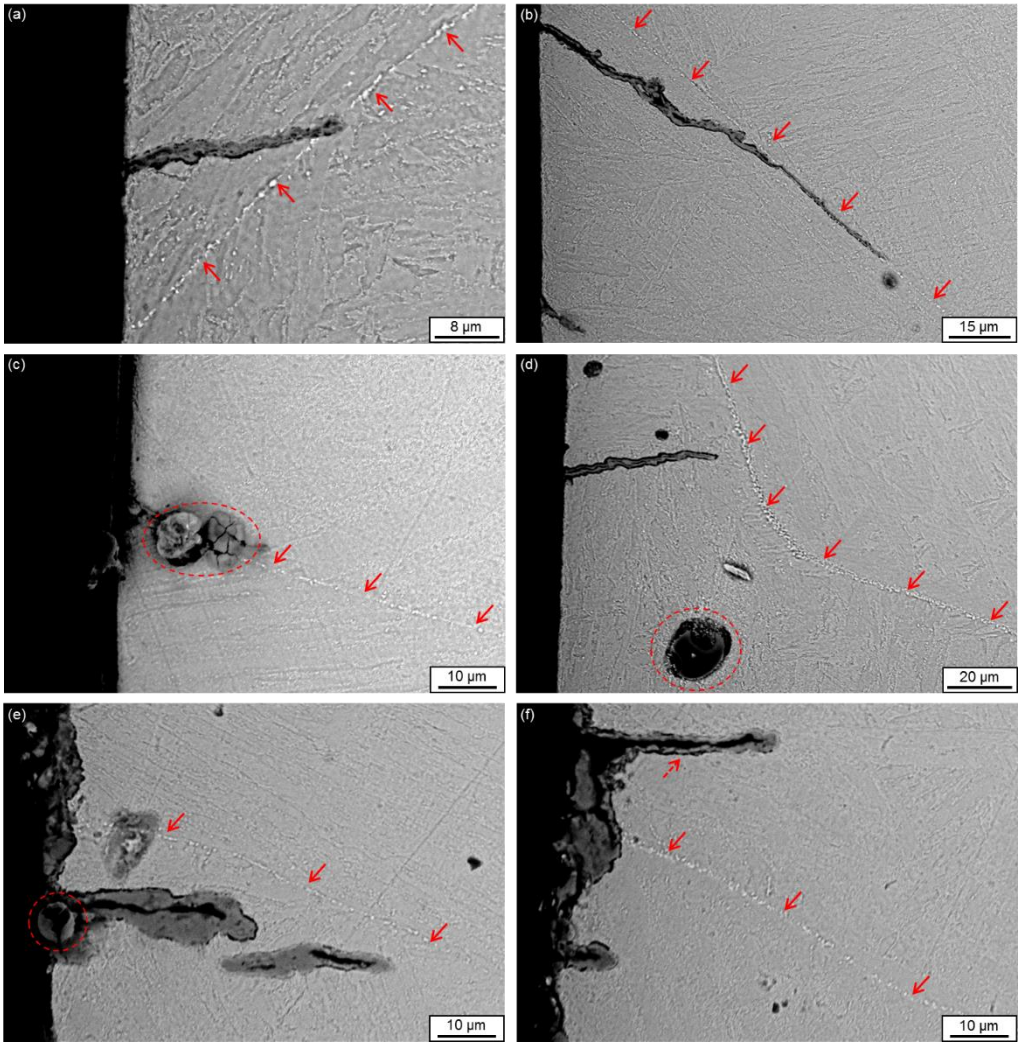

Figure 3.61 BSE images of Lave phase formation in cast MarBN after HTLCF testing at (a – d) 600 °C and (e, f) 650 °C. Red arrows indicate Laves phase along boundaries and dashed circles are inclusions.

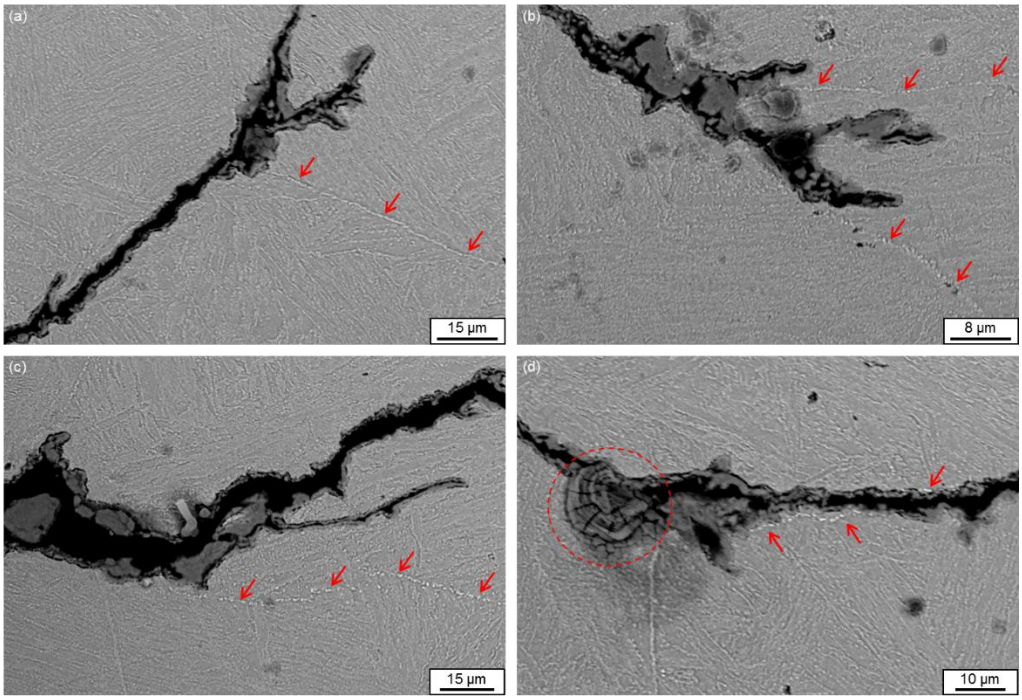

Figure 3.62 (a – d) BSE images of Laves phase formation in cast MarBN after CF testing at 650 °C. Red arrows are Laves phase and dashed circles are inclusions.

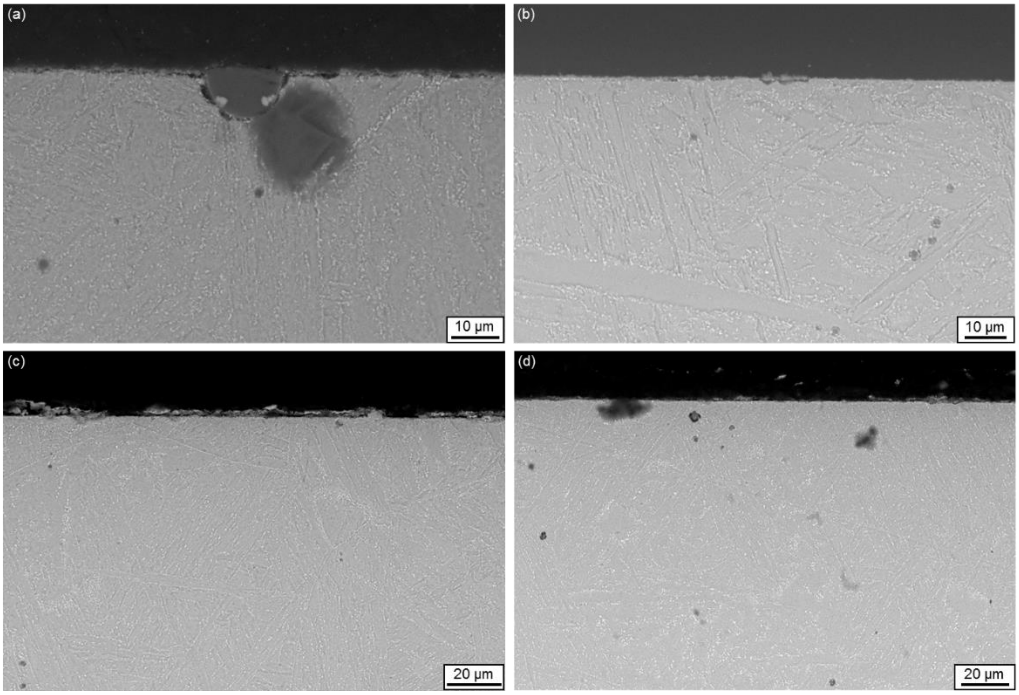

Figure 3.63 BSE images of Laves phase in cast MarBN oxidation samples at (a) 600 °C, and (b) 650 °C, and forged MarBN oxidation samples at (c, d) 650 °C, after 14 days (left) and 28 days (right). Bright regions are Laves phase.

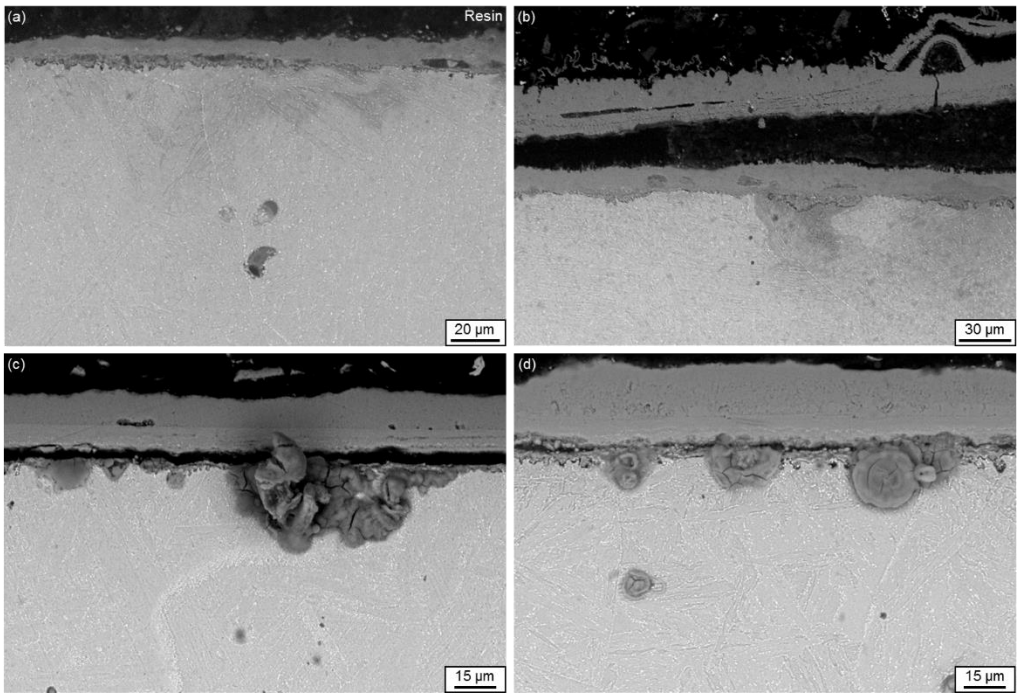

Figure 3.64 BSE images of Laves phase in cast MarBN corrosion samples after (a) 21 and (b) 28 days, and forged MarBN corrosion samples after (a) 7 and (b) 28 days at 650 °C. Bright regions are Laves phase.

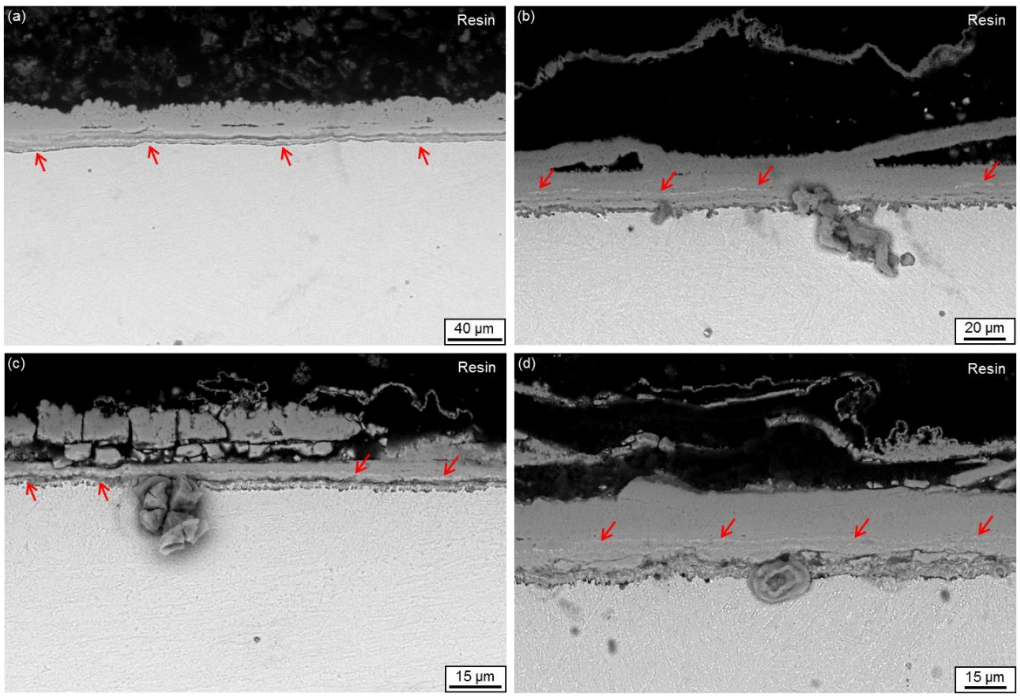

Figure 3.65 BSE images of linear regions of Laves phase (red arrows) in the oxide scale of corrosion samples of cast MarBN at (a) 600 °C after 28 days, and (b) 650 °C after 14 days, and forged MarBN at (c) 650 °C after 1 day and (d) 650 °C after 21 days.

3.11 Discussion

3.11.1 General

The HTLCF behaviour of a cast nano-strengthened martensitic steel, MarBN, has been characterised via a programme of strain-controlled cyclic tests covering different strain-rates and strain-ranges at 650 °C, with comparisons to the same material at 600 °C, as well as a forged equivalent and current generation power plant material, P91 steel. The characterisation includes measurement of cyclic evolutions of stress, plastic strain, softening and fatigue damage. High temperature oxidation and corrosion testing has been performed to identify oxide scale growth rates and the role of inclusions in oxide pit formation and crack initiation. A range of microstructural analysis techniques have been employed to characterise the microstructure, both before and after high temperature exposure. Observation of the influence of manufacturing defects on crack initiation and propagation has also been investigated using these techniques, with a view to identification of key factors affecting high temperature cracking and damage.

3.11.2 High Temperature Low Cycle Fatigue Behaviour of MarBN

Both the manufacturing and heat treatment processes for MarBN steel must be carefully controlled due to the strict limitations on the chemical composition and risk of harmful BN formation during normalizing, that can rapidly coarsen under high temperature loading. Degradation of long term high temperature creep strength can then occur at the expense of (i) thermally-stable $M_{23}(CB)_6$ carbides and (ii) MX (VN) carbonitrides [161]. The optimisation of boron and nitrogen concentration on the creep behaviour of modified 9Cr steels has been extensively investigated [21,71,82,162,163]; however, there is a need to identify the effect of flexible loading on MarBN, as investigated here.

The initial and half-life stress-strain behaviour for cast MarBN and P91 is presented in Figure 3.18. In spite of MarBN being a cast material, compared to rolled P91, MarBN is shown to be superior, with equivalent cyclic strength as the temperature is increased to 650 °C. This can also be seen in Figure 3.19 in terms of maximum stress evolution; however, more rapid failure of the cast MarBN sample occurs at the higher strain-rate at 650 °C. The initial grain size in cast MarBN is shown to be many times larger than for P91, and approximately two to four times larger than the equivalent forged material (Figure 3.33). This result conflicts with the Hall-Petch relationship, where grain size is inversely proportional to yield strength, and is attributed to thermally stable, boron-

enriched $M_{23}C_6$ carbides along boundaries, providing barriers to dislocation motion, combined with enhanced tungsten solute strengthening and high dislocation density. Maruyama *et al.* [24] have shown that tungsten also reduces the coarsening rate of $M_{23}C_6$ carbides, enhancing the effect of precipitate strengthening. This is a key benefit of MarBN for application to higher temperatures and pressures, compared to materials currently used in steam header applications for current generation fossil fuel power plants, and is particularly encouraging considering this work is comparing cast MarBN to rolled P91. Despite a reduced fatigue life at 650 °C, similar rates of softening and effective plastic strain accumulation are identified in cast MarBN for a range of loading conditions across each temperature, prior to failure (Figure 3.20 and Figure 3.21). Cyclic softening is a known phenomenon in 9-12Cr steels and is attributed to dynamic recovery of the microstructure. This involves a reduction in dislocation density, and low angle boundary annihilation due to dislocation annihilation, resulting in lath coarsening, the extent to which depends on temperature and strain amplitude. Therefore, even small-amplitude cycling of plant components (e.g. warm starts, hot starts or fluctuations) can cause microstructural degradation and reduce strength [69,72,164].

The introduction of a hold period is found to further decrease the fatigue life of cast MarBN at 650 °C (Figure 3.22), as a result of increased cyclic softening and plastic strain (Figure 3.23 and Figure 3.25(a)). However, the significant increase of almost 30% maximum plastic strain over the course of testing, compared to HTLCF loading, is a dominant factor in the reduced fatigue performance. The stress range due to CF loading is ~26% greater than for LCF conditions at the initial cycle, whereas the stress range at half-life is approximately equal, although an increased plastic strain-range is observed for CF loading in both cases. This is attributed to significant microstructural changes during the primary cyclic softening phase, namely subgrain boundary annihilation (due to dislocation annihilation) and plastic strain (as a result of dislocation motion), as identified by Fournier *et al.* [165] for 9Cr steel. CF loading generally results in an overall reduction in life, compared to pure fatigue loading [56] and is an important factor to consider in terms of the complex operational cycles plant components will face under flexible loading conditions (i.e. creep-fatigue-oxidation).

HTLCF testing of cast and forged MarBN, manufactured from the same melt, allows the influence of the manufacturing process to be investigated. As shown in Figure 3.33, forging, in conjunction with a shorter heat treatment, results in a reduced grain size compared to cast MarBN. The stress-strain loops (Figure 3.26) and maximum stress and

plastic strain evolution (Figure 3.28) of cast and forged MarBN indicate greater differences in the behaviour of the two cast samples tested, but no significant difference overall in terms of cyclic strength or plastic strain-range. The fatigue life of forged MarBN is increased (Table 3.4 and Figure 3.29), almost double that of the cast in the case of Cast_02 and Forged_02, indicating the substantial influence of manufacturing process on fatigue life. The reasons for this will be discussed in more detail in Chapter 4, based on 3D X-ray μCT scanning and analysis of cast and forged samples.

The initiation point of macroscale crack propagation in MarBN has been defined in Figure 3.30, where the secondary region of cyclic softening ends and a large reduction in maximum stress occurs. It can be seen from Figure 3.31 that damage, and, therefore, macroscale crack propagation, is limited to a small portion of fatigue life. In contrast, crack initiation under low cycle fatigue loading has been found to occur within 3% to 10% of fatigue life [166], indicating the importance of understanding microstructural strengthening and degradation mechanisms to design against premature component failure. Based on experimental testing, life prediction constants are identified that will be implemented in various life prediction models in later chapters.

3.11.3 Microstructural Analysis

To understand the mechanisms of degradation in cast and forged MarBN as a result of high temperature testing, microstructural analysis has been performed. Under LCF loading, fatigue cracking generally initiates on the sample surface, but during high cycle fatigue loading, crack nucleation is found to occur within the sample as a result of discontinuities in the material [124]. Therefore, the location of manufacturing defects, in conjunction with the applied loading conditions, can significantly affect the failure mode of a component.

Fatigue striations have been observed on the fracture surface of 9Cr steels tested at high temperature [75,167,168] and were observed on both the HTLCF and CF MarBN samples parallel to the fatigue crack. The presence of fatigue striations and ductile dimples on the fracture surface of both cast and forged MarBN are characteristic of fatigue failure in metals (Figure 3.34 and Figure 3.36). Fatigue striations are generated by repeated crack blunting and sharpening as a result of dislocation slip in the plastic zone at the crack tip, and can be used as a measure of the rate of microcrack propagation under constant loading. It is estimated from the SEM images presented here, that crack

propagation occurs at approximately 6 μm and 3 μm per cycle for cast and forged MarBN, respectively. Ductile dimples on the fracture surface occur due to localised plastic strain and dislocation accumulation, and void growth around inclusions occurs as a result of decohesion from the matrix. These phenomena have been observed previously on the fracture surface of stainless and martensitic steels [169–171], as well as for the MarBN samples presented here.

Dendritic shrinkage has also been observed on the fracture surface of cast MarBN samples (Figure 3.35). Formation occurs due to shrinkage of the solidified metal during casting, and can cause expansion of porosities i.e. entrapped or discharged gases. This feature has been identified in cast materials as a source of crack initiation, both at the surface and towards the centre of the specimen, as a result of clustering and the complicated shape producing an increased stress concentration. The complexity of the geometry, as opposed to the size of the pore, is identified as the important factor [131], as observed in Figure 3.38.

The main difference between the HTLCF and CF fracture surfaces is the presence of cleavage facets and cracking between adjacent crystals as a result of CF loading (Figure 3.37). The density of cracks, both at the surface and internally, is found to increase due to the tensile hold period. CF testing of P91, with a two minute hold period, produced similar results and is linked to combined creep and fatigue degradation [59]. This highlights the importance of understanding the failure mechanisms in martensitic steels as a result of different loading conditions.

Sectioned images of cast and forged MarBN (Figure 3.38, Figure 3.40 to Figure 3.43) provide further evidence of the role of manufacturing defects in fatigue crack initiation and propagation. The complex shape of inclusions appears to have a greater influence on the cracking behaviour of MarBN under cyclic loading, compared to spherical inclusions i.e. Ca-Al-O compared to Mn-S (Figure 3.38); however, proximity to the gauge length surface is also a factor. The size, shape, location and distribution of manufacturing defects is of particular importance, as impurities have been identified as a primary source of failure, particularly when the defect is located close to the surface [123,155,156,172]. Both shape (Figure 3.45) and decohesion (Figure 3.46) have been identified here as key factors influencing crack initiation under high temperature loading [155,158]. The mechanical properties of inclusions differ from the matrix and there is generally a low-strength interface bond between inclusions and the matrix. Decohesion or inclusion fracture is found to primarily result from stress concentrations

due to dislocation pile-ups at inclusions [21,85,155,156]. In terms of micro-scale mechanisms of degradation in MarBN, inclusions have been identified as playing a primary role in crack initiation under both HTLCF and CF loading. The effects of inclusions in the relatively small samples examined here is possibly greater than for more realistic, thick section components, as in real plant (e.g. a valve chest), particularly as the applied strains tested here are also higher than for typical plant conditions in order to achieve short-term failure. Nevertheless, a more refined manufacturing process would undoubtedly further improve the cyclic and CF response of the material and be advantageous for prolonged life.

Transgranular cracking is observed along the gauge length of cast MarBN samples during mechanical testing, with oxide scale formation in the cracks (Figure 3.38 to Figure 3.44). Oxide scale cracking, due to mechanical loading, promotes diffusion of oxygen along microstructural boundaries, resulting in a weakened matrix material to resist crack initiation and propagation [56]. The oxide scale shown in Figure 3.44, as a result of CF testing for ~14 days, is up to 40 μm thick, with an inner layer of Fe-Cr spinel and an outer layer of primarily iron oxide (magnetite). Oxide penetration of the matrix is also observed, below the Fe-Cr spinel. Similar results have been observed elsewhere, where high strain-range CF testing has been found to produce thicker oxide scale formation, compared to pure fatigue and low strain-range CF loading, due to repeated fracture of the oxide layer [56]. Furthermore, inclusions are shown to promote oxide pit formation; therefore, the likelihood of crack initiation and propagation in such regions of both increased stress concentrations and weakened matrix material is increased.

The effect of cyclic loading on the nano-scale mechanisms of degradation in MarBN has been examined via carbon replica and thin foil sample analysis using TEM. The macro-scale cyclic softening behaviour of MarBN, as discussed earlier in this chapter, can be attributed to a number of micro- and nano-scale mechanisms. Evidence of lath coarsening (Figure 3.47), dislocation motion (Figure 3.49) and subgrain formation (Figure 3.50) has been observed in carbon replica and thin foil samples. The loss of low angle boundaries through dislocation annihilation, resulting in equiaxed subgrain formation, has been identified as a primary mechanism contributing to cyclic softening, as the amount of boundaries available to resist plastic deformation is reduced [173,174]. The initially large grain size in the cast material, compared to forged MarBN, may promote this and be a factor in the reduced fatigue life observed. Boron and tungsten

have been identified as key elements in reducing the rate of precipitate growth and promoting a fine distribution of precipitates along boundaries, hence enhancing the precipitate strengthening effect [38]. In addition, nitrogen promotes a fine dispersion of MX particles through the microstructure and provides increased obstacles to dislocation motion [79,80]. Therefore, a refined grain structure, in conjunction with a thermally-stable precipitate distribution, is a key source of enhanced HTLCF performance for MarBN steel.

3.11.4 Oxidation and Corrosion Performance of MarBN

The rate of oxide scale growth in cast and forged MarBN has been measured for oxidation and corrosion testing conditions at 600 °C and 650 °C, with a comparison to rolled P91 steel at 600 °C. A parabolic rate of oxide scale growth is observed for corrosion samples (Figure 3.52) and is significantly larger (~10 times after 28 days) than for samples tested under oxidation conditions (Figure 3.51). In air, the rate of oxide scale growth is in line with that measured by Fournier *et al.* [175] for a 9Cr steel at 600 °C also.

The corrosive ash applied is more representative of the environment power plant components will be exposed to (i.e. fireside conditions), in particular for biomass, as its use as an alternative fuel source increases. The low melt temperature of the biomass can cause highly-adherent melts to form on the component surface, leading to insulation of the component, an altered coefficient of thermal expansion and enhanced thermal fatigue [44]. Inclusions have been identified as playing a primary role in oxide pit formation, and oxide scale spallation and cracking (Figure 3.54). The repeated fracture and regrowth of the oxide scale exposes the material to increased element diffusion and reduces the load bearing capability of the material. High levels of tungsten, many times that of the original material composition, have been identified in the oxide scale (Figure 3.55) and values of both tungsten and chromium are found to increase approaching the oxide scale from within the matrix material (Figure 3.56). Similar results have been identified for forged MarBN also. Diffusion of chromium, in an attempt to form a protective oxide scale is a known phenomenon; however, high levels of tungsten diffusion also occurs. Degradation of hardness and increased rate of tungsten carbide diffusion has been identified as the temperature exceeds 600 °C [46]. Tungsten is a key element in terms of the strength of MarBN, and this may present issues for long-term performance under ultra-supercritical loading conditions.

Due to the level of chromium in MarBN and P91 (below 12%), a protective oxide scale cannot form [42] leading to the formation of an oxide affected zone, as observed in oxidation samples (Figure 3.57). In the case where the scale remains intact, iron-oxide forms at the outer surface due to diffusion, resulting in a depleted zone in the substrate and internal oxidation of the metal. Otherwise oxide scale cracking occurs, due to stresses or a mismatch in the thermal expansion coefficient, exposing the underlying metal to further oxidation [176,177]. Cracking of the oxide scale occurs in the case of corrosion samples, promoting internal oxidation. This can lead to weakening of the substrate through outward diffusion of elements, such as chromium, iron and tungsten. The structure of the oxide scale is the same across all samples tested here (Figure 3.58 and Figure 3.59), as described previously for the CF sample, with an inner Fe-Cr spinel and an iron oxide outer layer.

The role of chlorine has been found to play a significant role in the corrosion of 9Cr steels, promoting oxide scale detachment and repeated scale formation [54] and has been attributed to the failure of superheater tubes in plant, as early as 6 months [178]. Chlorine has also been identified in concentrated regions at MnS inclusions in 304 SS, and can cause dissolution of inclusions and promote oxide pit formation [179]. Chlorine can penetrate the oxide scale, through pores and cracks, and react with matrix elements to form metal chlorides. At the scale-metal interface, metal chlorides have a high vapour pressure and this promotes both diffusion through the scale as well as evaporation [180]. Chlorine has been identified in both the oxide scale and at inclusions in MarBN corrosion samples. Although the amount of chlorine in the ash applied to samples here is low (~1.3 wt. %), it is identified as a key element in the corrosion behaviour of MarBN. In terms of tungsten carbides, oxidation readily occurs in air between 500 °C to 600 °C, and is susceptible to chlorine attack above 400 °C [46]. Cracking of the cast MarBN oxide scale (Figure 3.60(a)) has allowed chlorine to diffuse through both the inner and outer scales. Preferential diffusion is also observed toward inclusions in both cast and forged samples (Figure 3.60(c) and Figure 3.60(d)), and promotes these location as sites for oxide pit formation and crack initiation.

3.11.5 Laves Phase Formation at High Temperature

In Figure 3.48, little change in the distribution of precipitate Feret diameter was found to occur, although the number of particles in cast MarBN increased with HTLCF exposure; this is attributed to Laves phase (Fe_2W) formation. Laves phase particles are

observed close to the surface and near regions of cracking and oxidation; the high concentration of tungsten in these particles, which commonly grow along grain boundaries, indicates that absorption into the oxide layer would result in reduced strengthening. The presence of Laves phase in cast (600 °C and 650 °C) and forged (650 °C) MarBN has been confirmed through the use of BSE for HTLCF (Figure 3.61), CF (Figure 3.62), oxidation (Figure 3.63) and corrosion (Figure 3.64) samples, as well as in the oxide scale (Figure 3.65). The precipitation hardening effect of boron-enriched $M_{23}C_6$ carbides along boundaries is said to be the primary strengthening mechanism in modified 9Cr steels, and is further enhanced through the addition of tungsten [8,181]; however, tungsten is known to form Laves phase particles, that are prone to rapid coarsening during prolonged exposure under typical service conditions [160]. In P92 steel, these particles have been identified as significant contributors to precipitate strengthening, as particles reach a similar saturated size to $M_{23}C_6$ carbides in less than 10,000 hours and contribute to precipitate strengthening along boundaries [76,182]. The saturated particle size of Fe_2W in cast MarBN, as a result of HTLCF loading, cannot be concluded from this work alone, but presents an interesting focus for future work on the possible effects of Laves phase in modified 9Cr steels under long-term flexible loading.

3.12 Conclusions

The key conclusions of this chapter are:

- Cast MarBN exhibits equivalent fatigue performance to rolled P91 at 600 °C, exhibiting superior cyclic strength at the same temperature and comparable performance at 650 °C.
- The introduction of a tensile hold period increases the rate of plastic strain accumulation, hence reducing fatigue life. This more realistically represents component loading conditions in plant and must be considered for component design, as opposed to pure fatigue or creep loading.
- The mechanisms responsible for cyclic softening are observed at the nano-scale (i.e. low angle boundary annihilation and lath widening). Laves phase particles have been identified, with the measured mean precipitate diameter shown to be equivalent to $M_{23}C_6$ precipitates for short-term HTLCF loading at 600 °C.
- A primary cause of fatigue crack initiation is identified at the micro-scale in the form of manufacturing defects distributed throughout the cast and forged material. The complex shapes of manufacturing defects results in localised stress

and strain concentrations, and strongly influences the crack initiation and propagation behaviour under high temperature loading.

- Both cast and forged MarBN exhibit equivalent oxidation and corrosion resistance, when compared to P91 steel. Inclusions at the surface are identified as key contributors to oxide pit formation, and oxide scale fracture.
- The forging process produces a reduced grain size and approximately doubled fatigue life compared to both cast MarBN and rolled P91. This indicates the importance of a refined manufacturing process in providing resistance to plastic deformation and fatigue crack initiation under HTLCF loading.

4 2D AND 3D MICROSCALE CHARACTERISATION OF MANUFACTURING DEFECTS IN CAST AND FORGED MARBN

4.1 Introduction

Microstructural analysis is adopted for identification of manufacturing defects relevant to fatigue crack initiation in both cast and forged MarBN samples. The effect of manufacturing process on the microstructure and high temperature low cycle fatigue (HTLCF) life of MarBN was presented in Chapter 3. However, the refined grain size as a result of forging may not fully explain the approximately doubled fatigue life, compared to cast MarBN. This chapter presents 3D X-ray micro-computed tomography (μCT) scanning, in conjunction with microstructural analysis, of manufacturing defects in cast and forged MarBN samples, before and after HTLCF testing, to identify the role of such discontinuities in fatigue cracking.

4.2 Principle of Operation

X-ray μCT scanning is a non-destructive method of analysing both the internal and external features of a component. Figure 4.1 is a schematic of the principal imaging components. Radiation is produced in the micro-focus X-ray tube, and aligned in a

parallel trajectory when passed through the collimator. Attenuation (loss of intensity) of the rays occurs as they pass through the sample, resulting in reduced beam intensity. A phosphor-detector then converts the X-rays to visible light, and the level of attenuation is measured by the charge-coupled device camera. 2D grey images are then produced, and mathematical reconstruction of the image set allows the production of a 3D voxel model. A voxel is the 3D equivalent of a pixel and the grey value of the voxel equates to the materials absorptivity (directly related to density). Rotation of the sample allows 3D reconstruction of the sample, through transformation of 2D slices output in the form of dicom files [183,184].

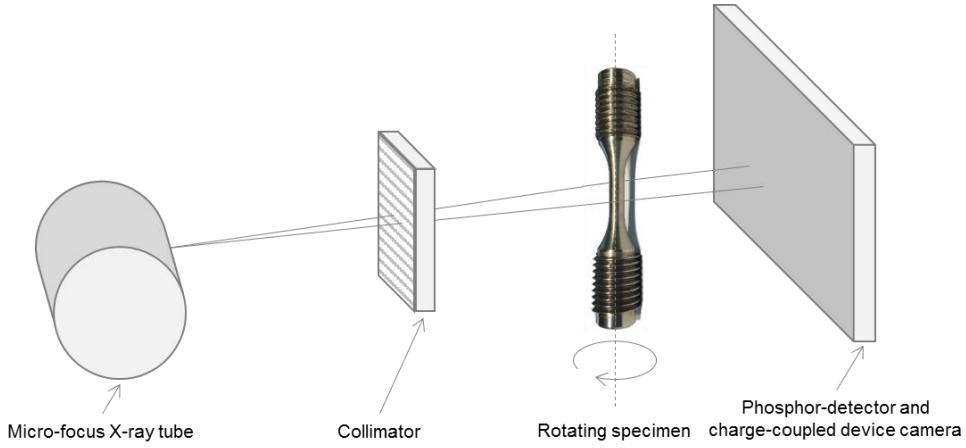

Figure 4.1 Schematic of the principal components of a µCT scanner. Adapted from [183].

Though valuable, this method is not without artefacts and noise. For example, deflection of the X-rays can lead to a halo forming around the workpiece, and noise can occur due to many factors including quantization of X-rays or amplification of signals. Furthermore, beam hardening effects can occur as the X-rays move through the sample, leading to a gradient in grey value from the sample surface towards the centre. This occurs due to low energy photons being more rapidly attenuated than high energy photons. Placing a thin plate (e.g. copper or aluminium) between the X-ray source and sample is one solution to filter out the low energy photons. Beam hardening parameters can also be applied to the software calculation for reconstruction of the scan data [184].

4.3 3D X-Ray µCT Scanning

4.3.1 Methodology

Components were scanned at the South Eastern Applied Materials (SEAM) research centre at Waterford Institute of Technology, before and after HTLCF testing at NUI

Galway. The scanner is a GE VTOMEX L300 (Figure 4.2) and the scan parameters are as follows: voltage = 230 V, current = 65 mAs, resolution = 10 µm and slice thickness = 10 µm. An image of the HTLCF sample is shown in Figure 4.3, highlighting the 20 mm section of the sample that was scanned. Due to beam hardening effects in the top and bottom regions of the sample, only 18 mm of the cast and 16 mm of the forged samples were used for 3D reconstruction. The software used for thresholding and reconstruction of the dicom files was Materialise Mimics 18.0 and Materialise 3-Matic 10.0. Both inclusions and voids are identified (evidence of which has been presented in detail in Chapter 3), as a result of the significant difference in density compared to the matrix material and are referred to collectively as manufacturing defects. A filter is applied in 3-Matic to remove noise and image-based artefacts in the samples below a surface area of 0.005 mm^2 in the cast and 0.0001 mm^2 in the forged samples.

Figure 4.2 GE VTOMEX L300 at SEAM, Waterford Institute of Technology.

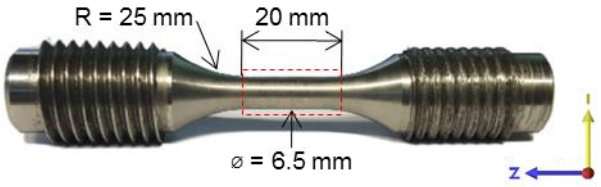

Figure 4.3 HTLCF MarBN sample highlighting the scanned region (red box).

4.3.2 Cast MarBN

Figure 4.4 shows the 3D reconstruction of the cast MarBN sample pre-test (blue) and post-test (red) from the top (Figure 4.4(a, b)) and side (Figure 4.4(c, d)) views. A large crack is clearly visible in the post-test sample, as a result of HTLCF loading at 600 °C, $\dot{\varepsilon}$ = 0.1 %/s and $\Delta\varepsilon$ = ±0.5%.

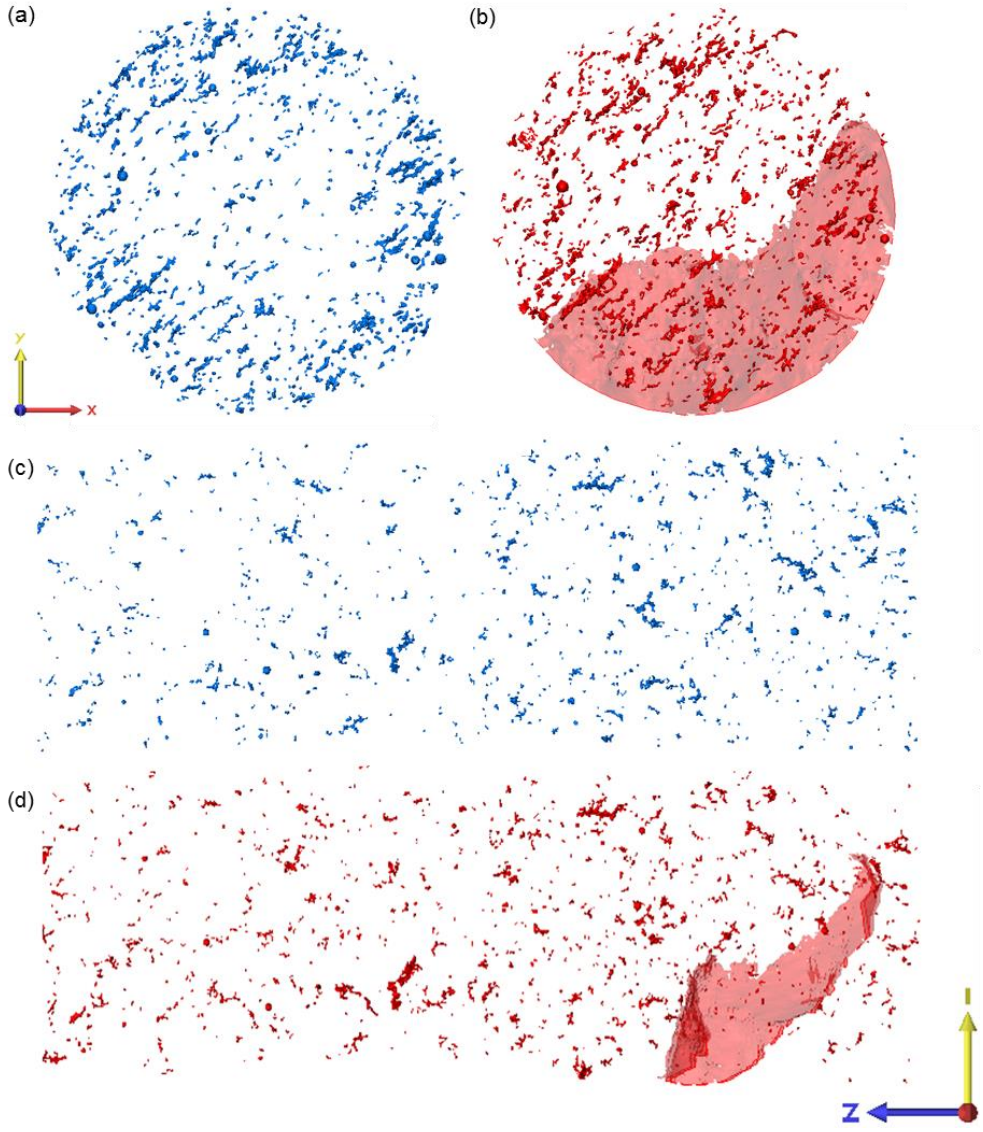

Figure 4.4 3D reconstruction of manufacturing defects in cast MarBN before (blue) and after (red) HTLCF testing, viewed from the (a, b) top and (c, d) side view.

Figure 4.5 shows examples of some of the complex shaped defects in the as-received sample (blue), with a comparison to the same defect post-test (red). They are formed during solidification of the material during casting. Many of the defects are shown to be elongated and have multiple branches. Holes in the defects (e.g. Figure 4.5(c, f)) appear to be prime regions for void growth as a result of HTLCF testing also. Table 4.1 quantifies the change in area and volume of each defect shown in Figure 4.5, and both values are found to increase in all cases. In Figure 4.6, the key pre-test defects (in terms of primary cracking) are highlighted in relation to the crack. In Figure 4.6(c), a scanning electron microscope (SEM) image of one of the defects on the fracture surface is identified in the 3D reconstruction. The crack, with embedded post-test defects, is presented in Figure 4.7.

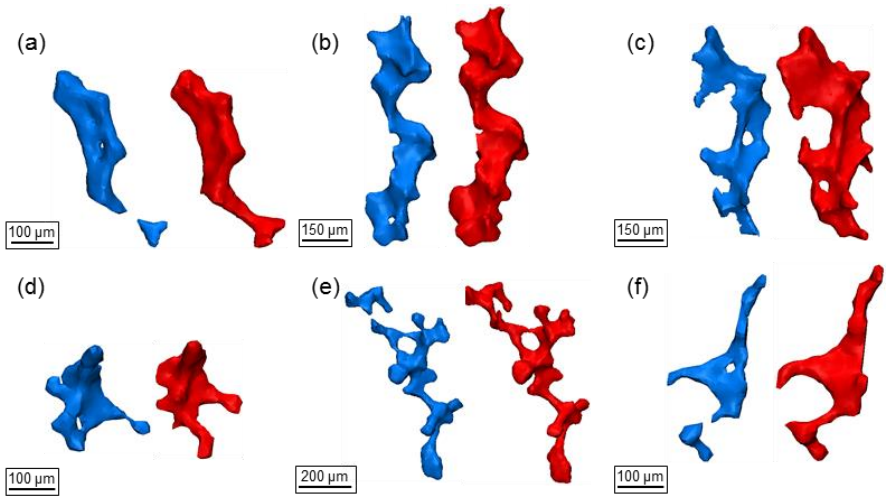

Figure 4.5 (a – f) Comparison of various manufacturing defects in cast MarBN before (blue) and after (red) HTLCF testing.

Table 4.1 Change in cast manufacturing defect area (Δ_{area}) and volume (Δ_{volume}) after testing, as shown in Figure 4.5.

Part	**Δ_{area} (%)**	**Δ_{volume} (%)**	**Part**	**Δ_{area} (%)**	**Δ_{volume} (%)**
(a)	24.9	39.5	(d)	46.8	63.4
(b)	20.1	35.7	(e)	6.6	8.8
(c)	35.1	51.5	(f)	57.2	64.3

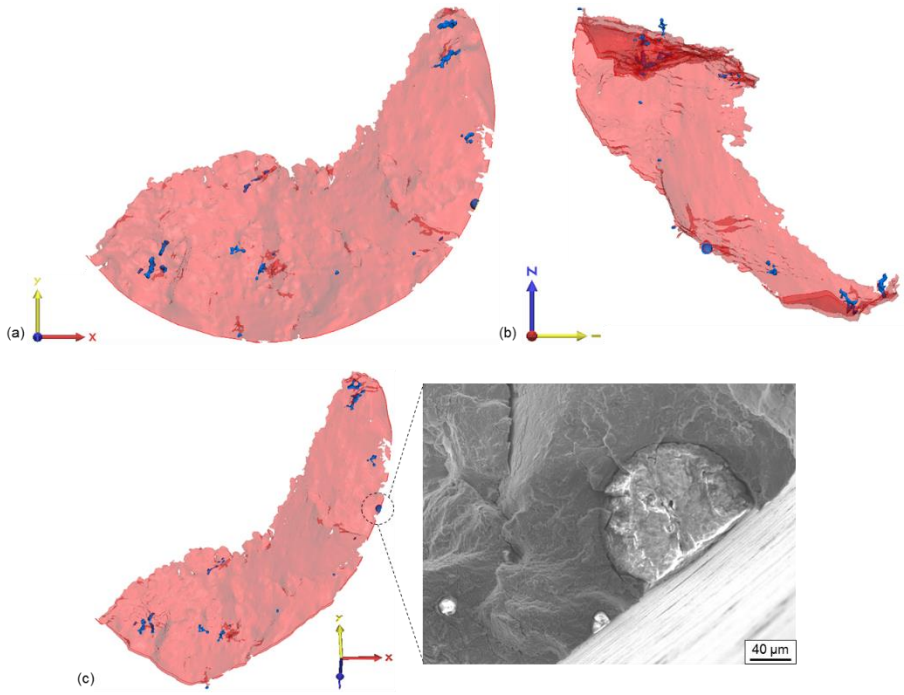

Figure 4.6 (a, b) Top and side views of key manufacturing defects in the pre-test cast MarBN sample, in relation to the post-test crack, and (c) SEM image of a manufacturing defect on the fracture surface, as identified in the 3D reconstruction.

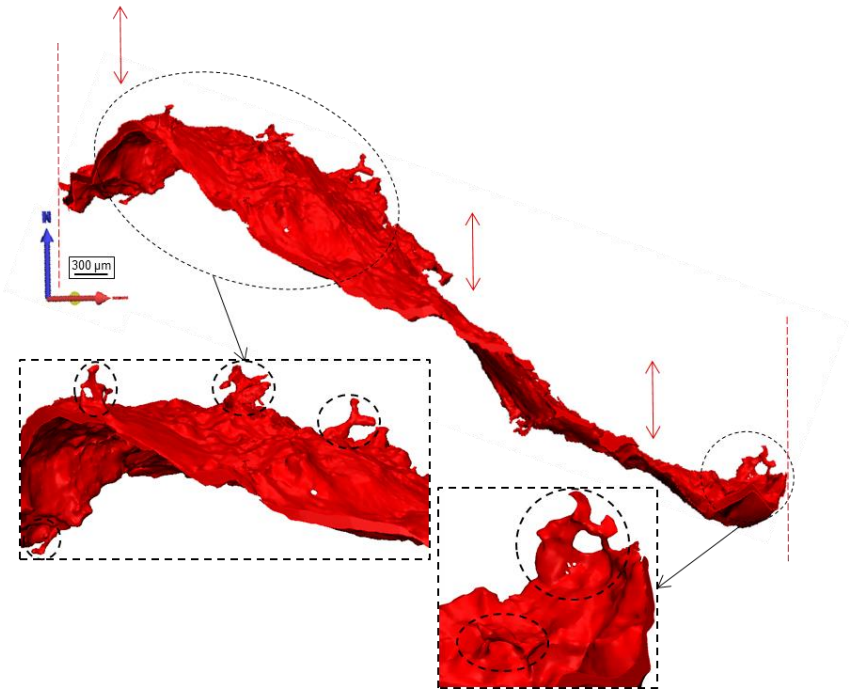

Figure 4.7 3D reconstruction of the primary crack in a post-HTLCF cast MarBN sample, with manufacturing defects highlighted. Dashed red lines indicate the sample surface and red arrows denote the direction of loading.

In Figure 4.8, the pre-test and post-test scans in Figure 4.4 are overlaid on one another, based on the location of a single defect, due to the significant misalignment between defects as a result of HTLCF testing. The arrows in Figure 4.8(a) indicate the location of the post-test defects, relative to the as-received defects. Motion in the radial and axial, as well as tangential directions, is found to occur, and indicates the effect of HTLCF loading and cracking on sample deformation.

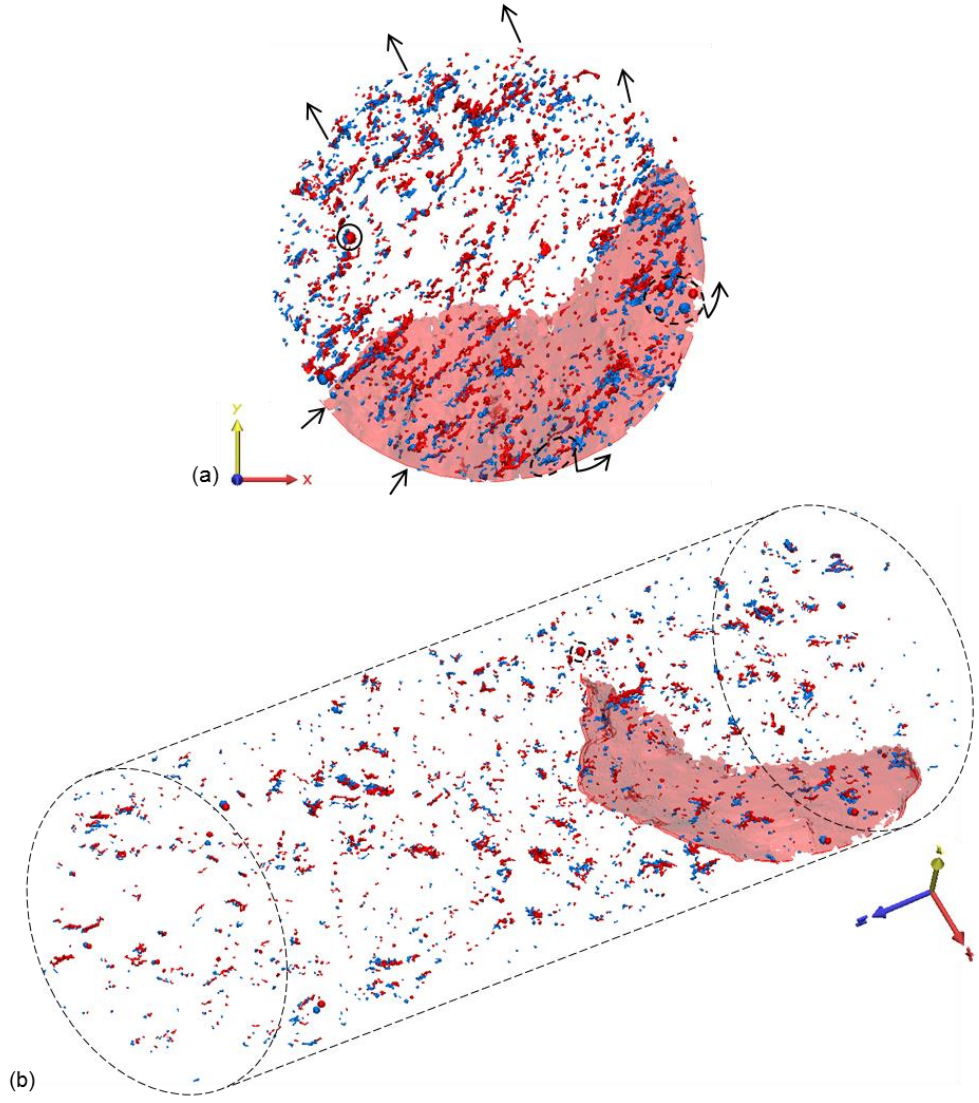

Figure 4.8 Overlap of pre-test and post-test manufacturing defects in cast MarBN, from the (a) top and (b) isometric view. Black arrows denote the direction of motion of defects due to HTLCF testing. Solid black circle denotes the defect aligned pre- and post-test.

4.3.3 Forged MarBN

In Figure 4.9, a 3D reconstruction of the forged MarBN sample before (blue) and after (red) HTLCF testing at 600 °C, $\dot{\varepsilon}$ = 0.1 %/s and $\Delta\varepsilon$ = ±0.5% is presented. Stringer type defects [22], elongated in the direction of forging, are identified, as distinct to the complex shapes in the cast material (Figure 4.5). Multiple cracks are also found to occur in the forged sample around the majority of the circumference, compared to a single large crack in the cast (Figure 4.4).

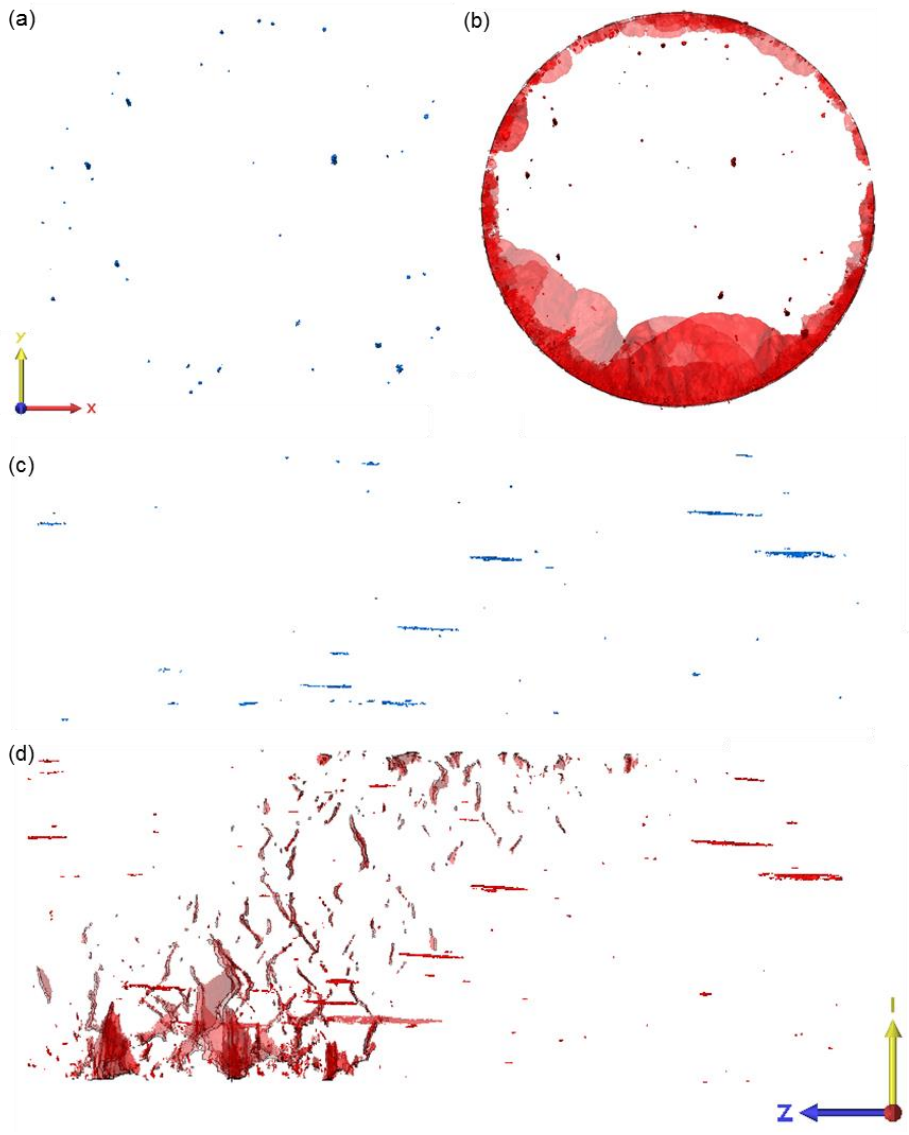

Figure 4.9 3D reconstruction of manufacturing defects in forged MarBN before (blue) and after (red) HTLCF testing, viewed from the (a, b) top and (c, d) side view.

In Figure 4.10, examples of manufacturing defect coalescence and growth, as a result of HTLCF loading, are presented, and the change in area and volume is quantified in Table 4.2.

In Figure 4.11(a), two cracks that propagate towards manufacturing defects are highlighted. Figure 4.11(b) and Figure 4.11(c) show these cracks in greater detail, and the presence of a manufacturing defect in both cracks is identified.

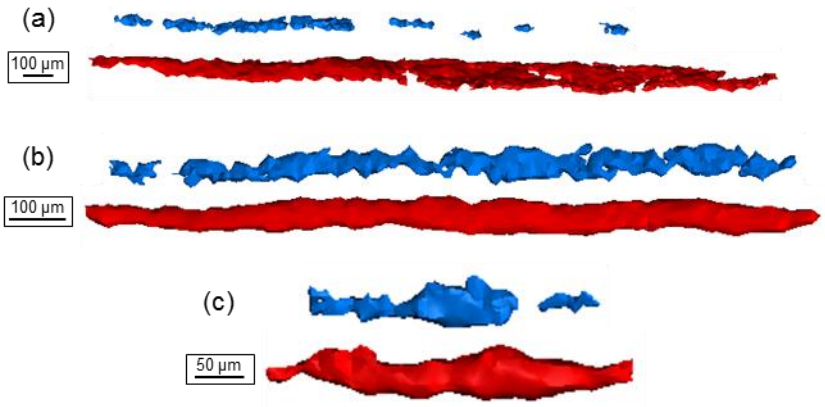

Figure 4.10 (a – c) Comparison of various manufacturing defects in forged MarBN before (blue) and after (red) HTLCF testing.

Table 4.2 Change in forged manufacturing defect area (Δ_{area}) and volume (Δ_{volume}) after testing, as shown in Figure 4.10.

Part	**Δ_{area} (%)**	**Δ_{volume} (%)**
(a)	15.0	46.4
(b)	38.4	58.5
(c)	79.4	89.5

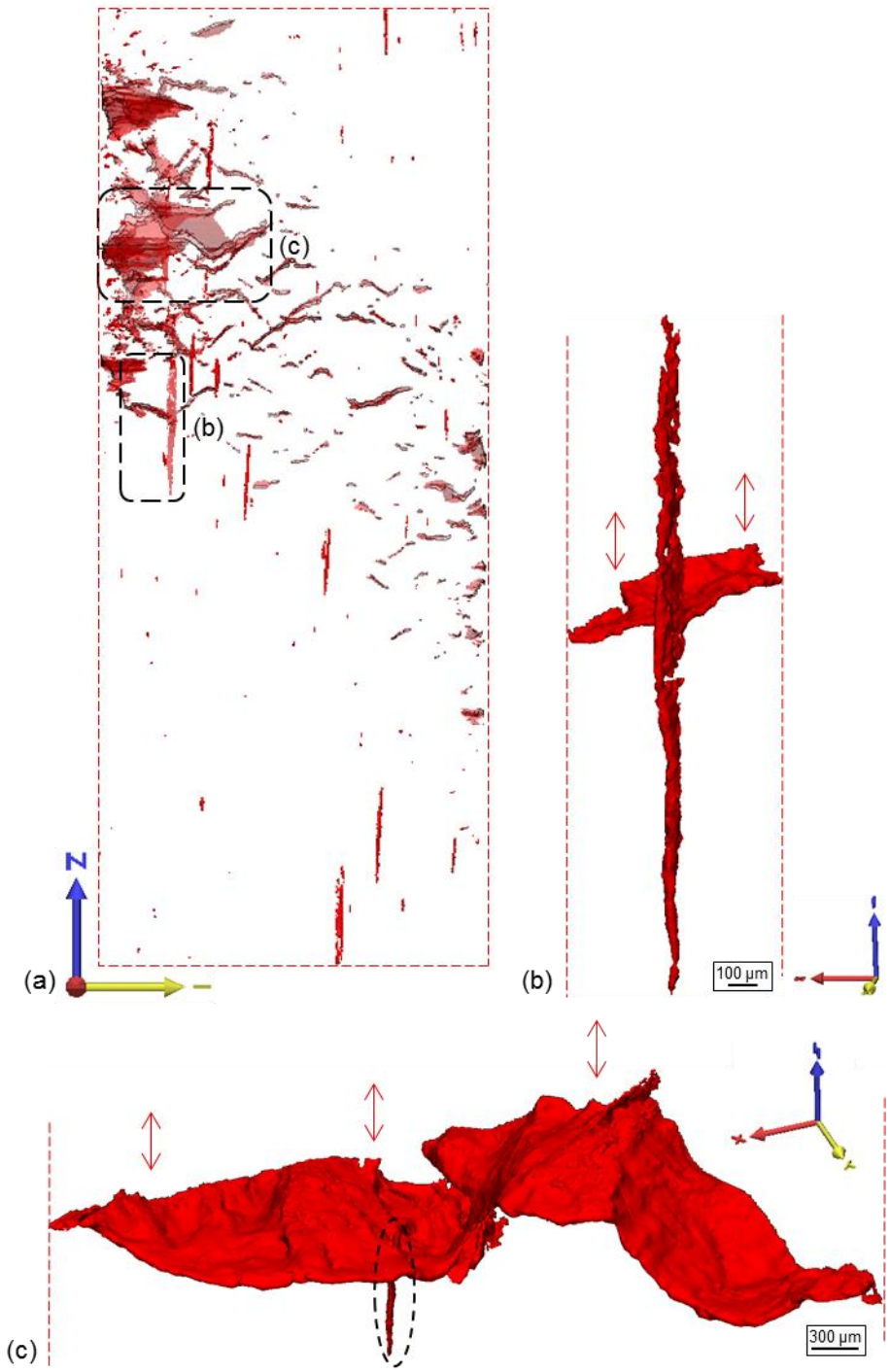

Figure 4.11 (a) Side view of manufacturing defects in the post-test forged MarBN sample, (b) secondary crack and (c) primary crack at a stringer type defect. Dashed red lines indicate the sample surface and red arrows denote the direction of loading.

In Figure 4.12, alignment of the pre-test and post-test defects is presented for forged MarBN, based on a single defect. Similar apparent deformation trajectories to the cast sample (i.e. radial, axial and tangential) are observed.

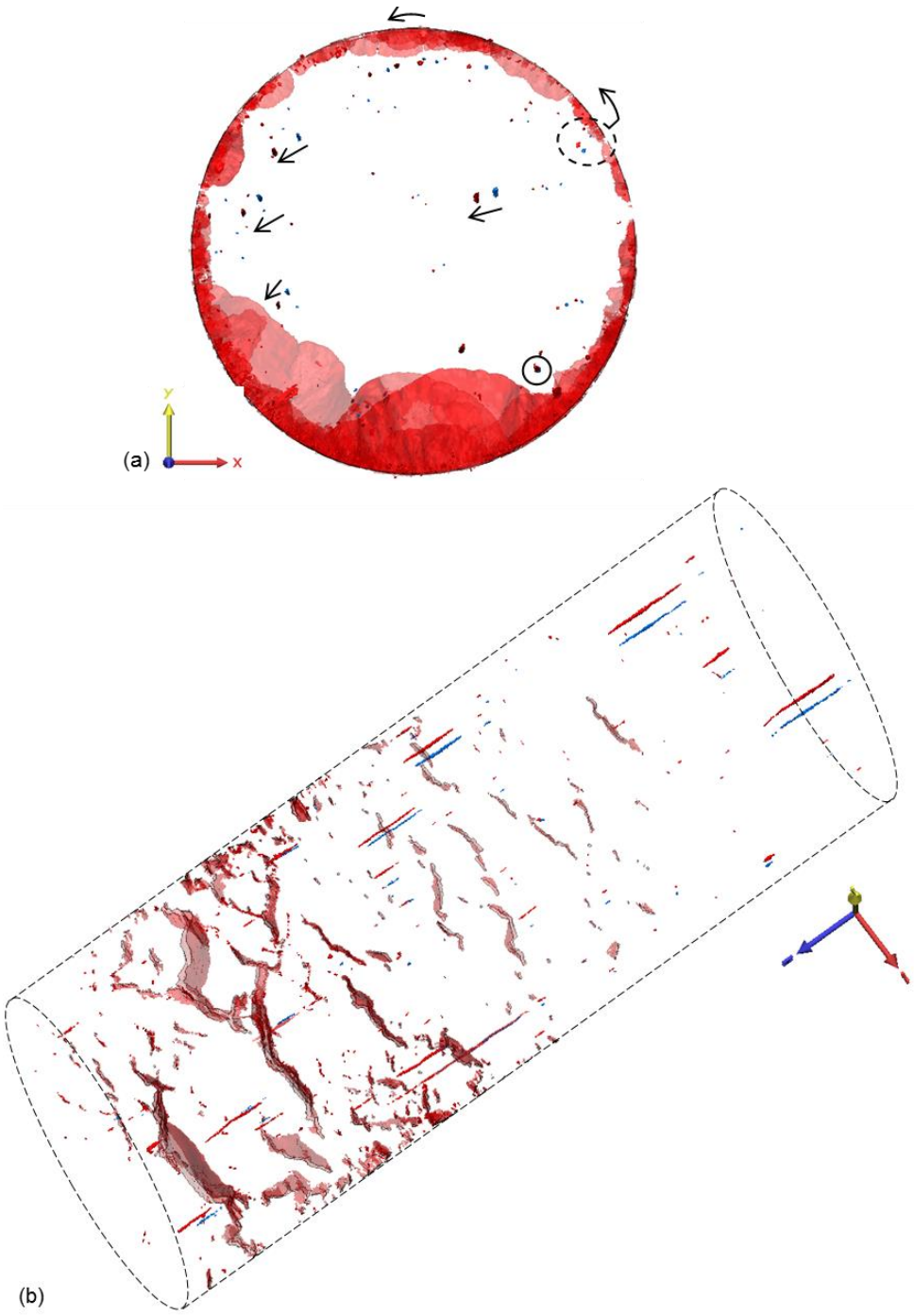

Figure 4.12 Overlap of pre-test and post-test 3D reconstructions of manufacturing defects in forged MarBN, viewed from the (a) top and (b) isometric view. Black arrows denote the direction of motion of post-test defects. Solid black circle denotes the defect aligned pre- and post-test.

4.3.4 Shape Characterisation of Manufacturing Defects

To quantitatively compare the defects identified in the cast and forged MarBN samples, sphericity, S, has been applied. This is the ratio of the surface area of a sphere with the equivalent volume as the defect (A_{eq}), to the surface area of the defect (A_{defect}) and is plotted against the effective radius of the sphere [185]. This methodology has been applied to previously for characterisation of casting defects in Al-alloys [141] and creep cavity formation in 9Cr steels [186]. Sphericity is calculated as per:

$$S = \frac{A_{eq}}{A_{defect}} \tag{4.1}$$

This has been applied to each individual manufacturing defect identified in pre- and post-test cast and forged MarBN samples. Figure 4.13 plots sphericity versus effective radius (of a sphere with an equivalent volume) for the cast (Figure 4.13(a)) and forged (Figure 4.13(b)) defects, before and after testing. Similar trends are observed in both cases, with the least spherical defects typically having an increased effective radius. HTLCF testing appears to have a greater influence on defect growth in the forged sample also. In Figure 4.13(c), the pre-test cast and forged defects with the ten largest volumes have been isolated and similar values of sphericity are calculated for both samples, but the effective radius of cast defects is generally larger.

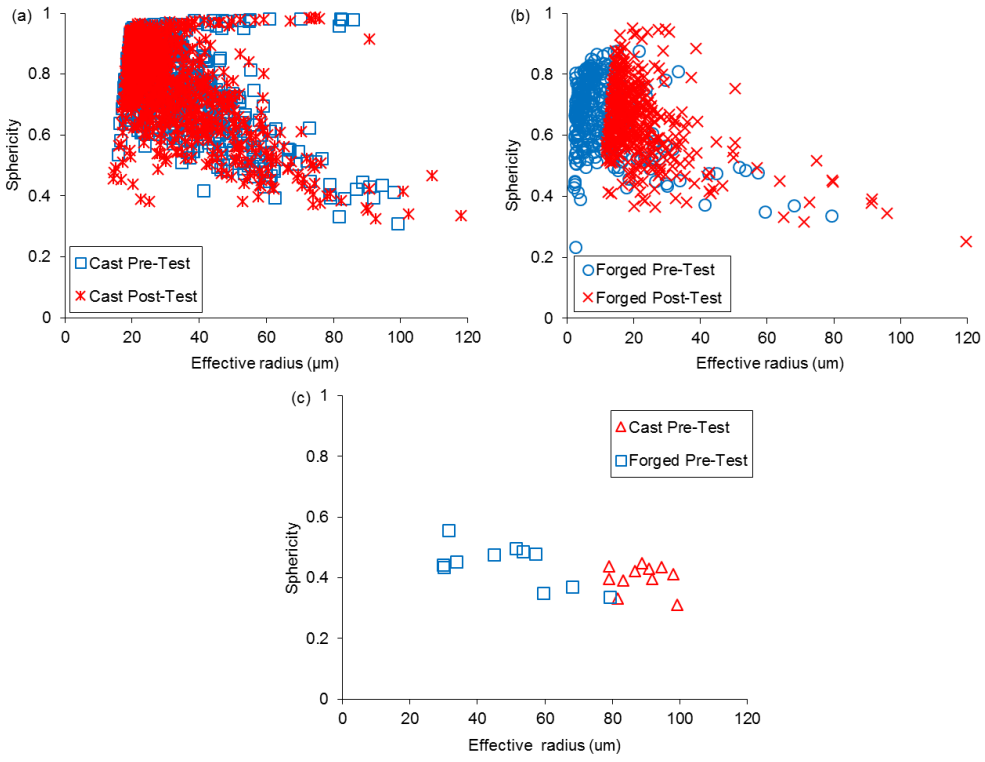

Figure 4.13 Sphericity of manufacturing defects identified in pre- and post-test (a) cast and (b) forged MarBN, and (c) largest volumes in pre-test samples.

Table 4.3 presents the volume fraction of manufacturing defects pre- and post-HTLCF test in cast and forged MarBN samples. The volume fraction after testing includes the crack(s), and is found to increase approximately seven- and five-fold from the as-received cast and forged volume fractions, respectively. In Table 4.4, the number of defects identified in the cast and forged samples are compared, before and after testing, with significantly more defects in the as-received cast sample, compared to the forged.

Table 4.3 Volume fraction of manufacturing defects before and after HTLCF testing.

Sample	$\mathbf{V_{Pre}}$ **(%)**	$\mathbf{V_{Post}}$ **(%)**
Cast	0.0311	0.2276
Forged	0.0019	0.0096

Table 4.4 Number of defects identified in the cast and forged samples before (n_{pre}) and after (n_{post}) testing, including cracks, and percentage increase (Δ).

Type	$\mathbf{n_{pre}}$	$\mathbf{n_{post}}$	Δ **(%)**
Cast	855	978	14.4
Forged	295	445	50.9

4.4 Microstructural Analysis

4.4.1 Fractography

After post-test µCT scanning, samples are fractured at room temperature and the gauge length is removed using a low speed saw, as per Section 3.5.1. SEM images of the influence of manufacturing defects on crack initiation and propagation behaviour on the fracture surface of cast (Figure 4.14) and forged (Figure 4.15) MarBN are presented. In Figure 4.16, some evidence of complex shaped defects on the fracture surface of the cast MarBN sample is presented also. Tear ridges and ductile dimples are observed on both cast and forged samples, as shown in Figure 4.17.

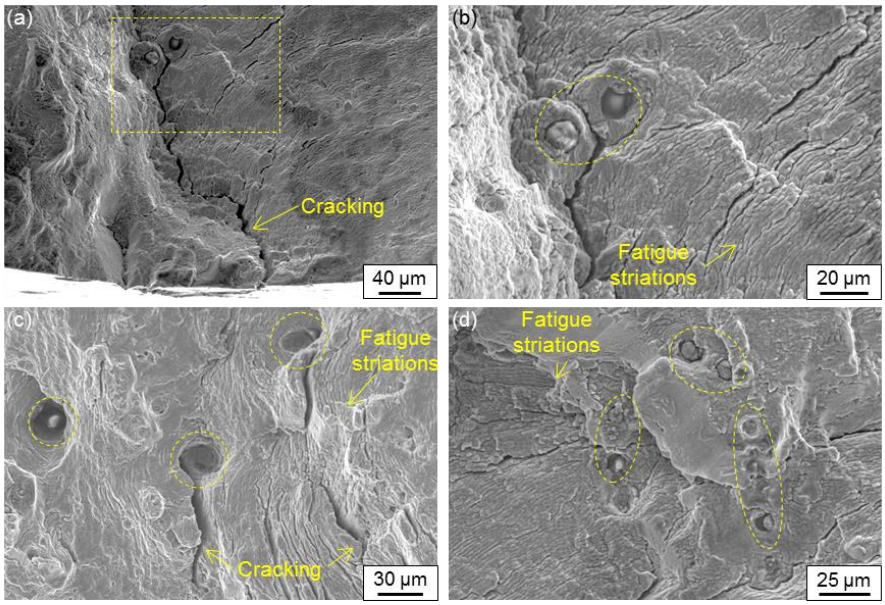

Figure 4.14 (a – d) Cracking around defects (dashed regions) and fatigue striations in cast MarBN.

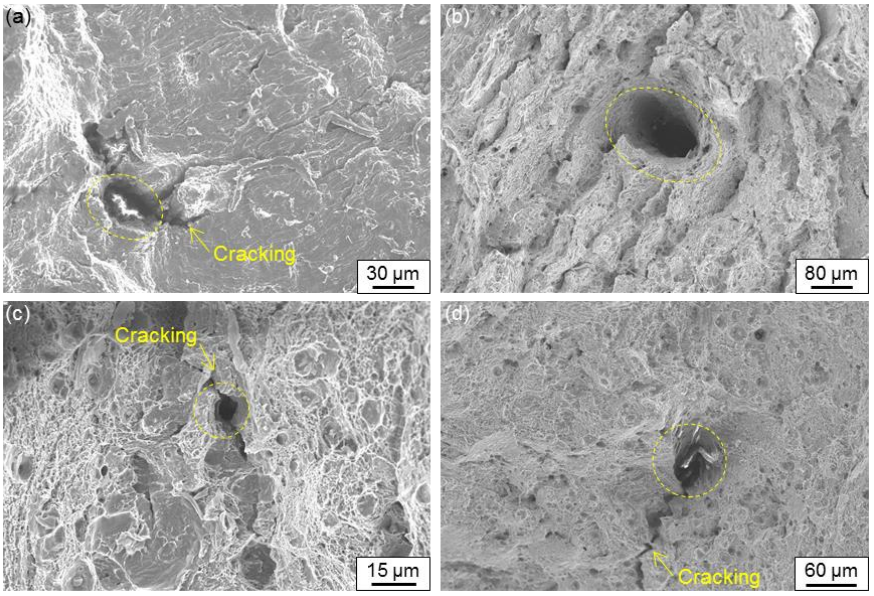

Figure 4.15 (a – d) Cracking around defects (dashed regions) in forged MarBN.

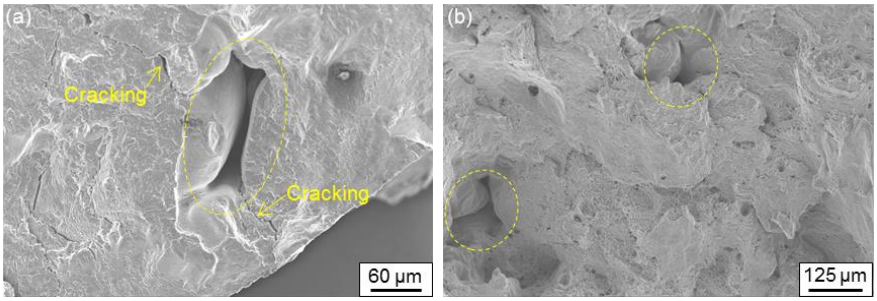

Figure 4.16 (a, b) Complex manufacturing defects on the cast MarBN fracture surface.

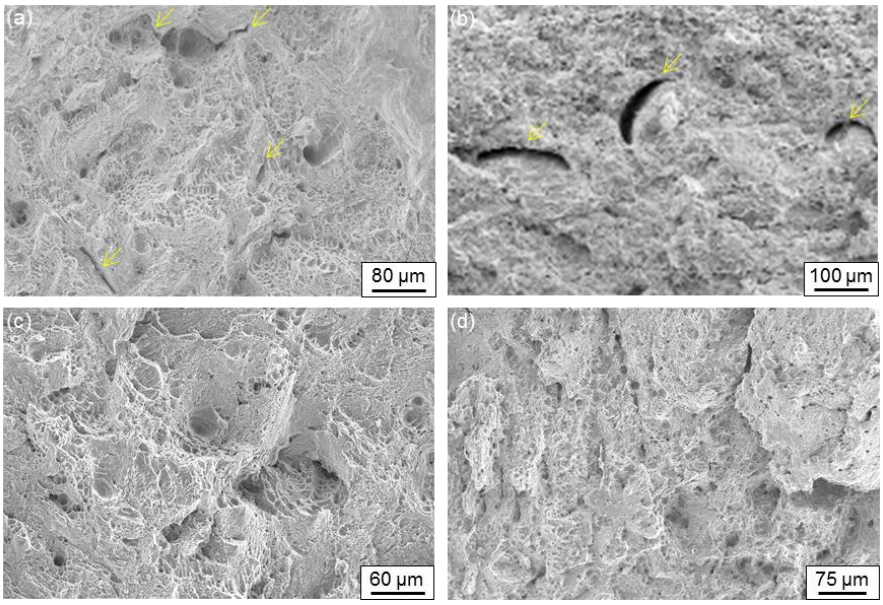

Figure 4.17 SEM images of (a, b) tear ridges (yellow arrows) and (c, d) ductile dimples on the fracture surface of cast (left) and forged (right) MarBN.

4.4.2 Sectioned Analysis

Following fractographic analysis, the cast and forged MarBN samples are prepared for sectioned microstructural analysis using the method described in Section 3.5.1. Backscatter electron (BSE) microscopy images of secondary cracking along the gauge length of cast (Figure 4.18) and forged (Figure 4.19) MarBN samples indicate that manufacturing defects close to the surface are influential in crack initiation and propagation behaviour. Oxide scale growth, in secondary cracks and at defects, has been identified in both samples. Examples of complex shaped defects in the cast sample is presented in Figure 4.20(a, b) and stringer defects are identified in the forged sample in Figure 4.20(c, d), with smaller spherical defects also visible in both cases.

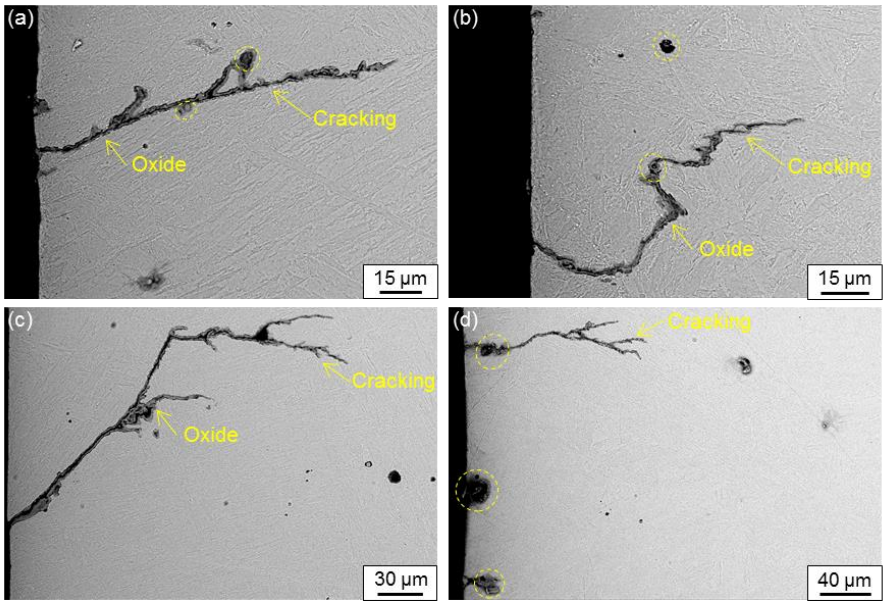

Figure 4.18 (a – d) BSE images of secondary cracking along the gauge length of cast MarBN with oxide scale formation and defects (dashed circles).

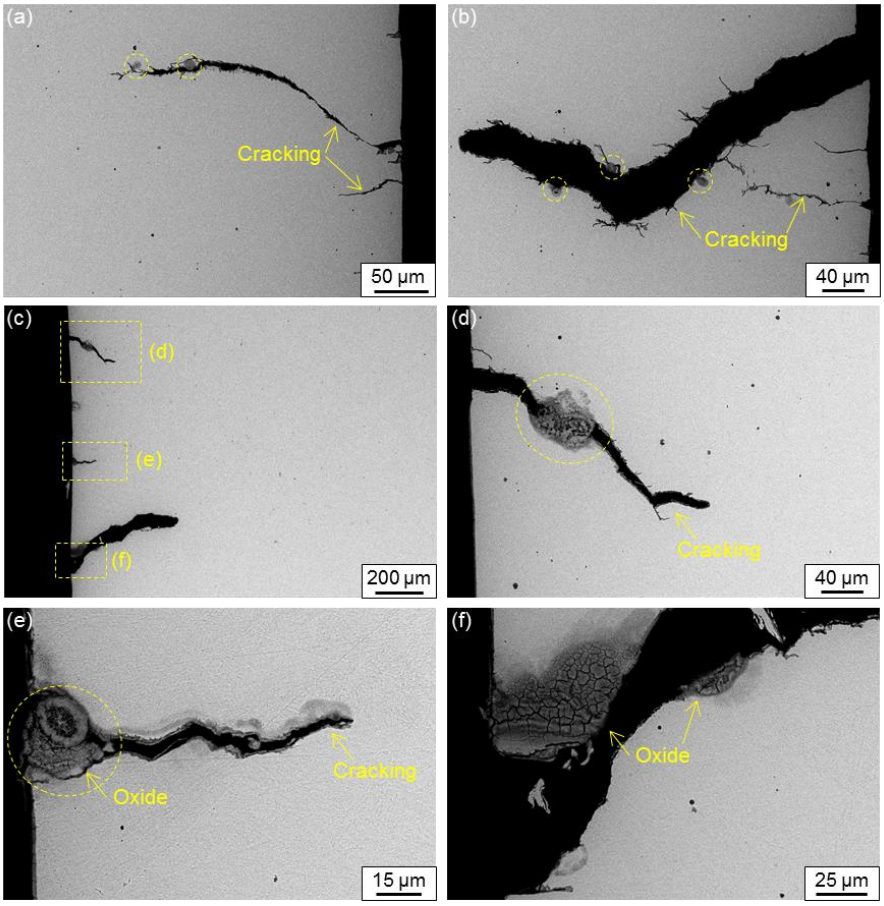

Figure 4.19 (a – f) BSE images of secondary cracking along the gauge length of forged MarBN with oxide scale formation and defects (dashed circles).

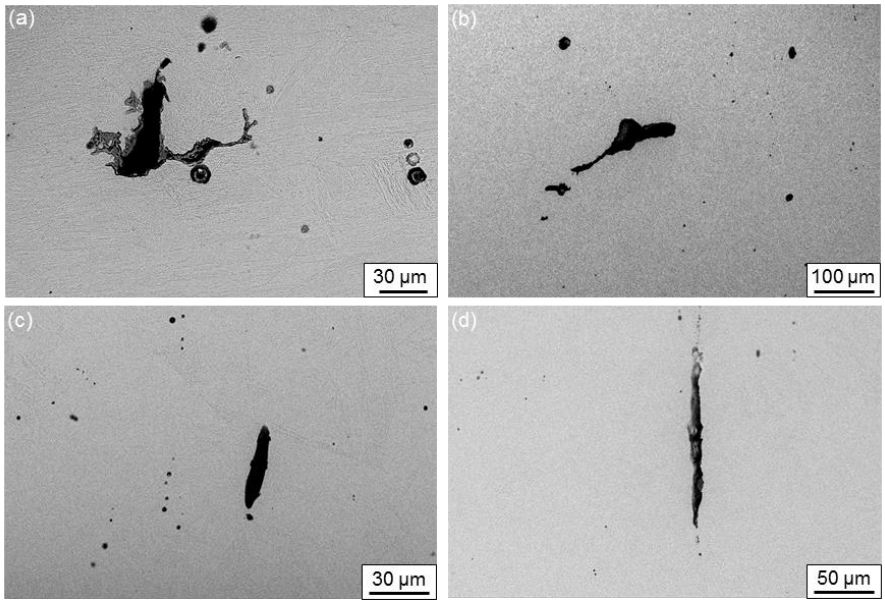

Figure 4.20 BSE images of (a, b) complex-shaped defects in cast MarBN and (c, d) stringer defects in forged MarBN.

4.5 Discussion

Non-destructive imaging has been performed to characterise manufacturing induced defects, formed as a result of casting and forging MarBN steel. Samples were 3D X-ray µCT scanned before and after HTLCF testing to identify the role of defects in failure behaviour. Microstructural analysis of post-test samples has also been performed for comparison between 2D and 3D analysis methods.

The manufacturing process plays a significant role in both the amount and geometry of defects in cast and forged MarBN, as shown in Figure 4.4 and Figure 4.9. The cracking behaviour of both samples is noticeably different also. The cast sample has one large, dominant crack that is 5.5 mm in width and 4.6 mm in height (Figure 4.4). In contrast, the forged sample has multiple smaller cracks, distributed around almost the entirety of the circumference, and the largest is 4.9 mm in width and 1.8 mm in height (Figure 4.9). In Figure 4.4(c), the density of defects is greater in the region where fatigue cracking occurs post-test (Figure 4.4(d)), and void growth around defects can also be seen as a result of HTLCF loading. Similar coalescence of complex cavities has been identified in an Al-alloy for superplastic forming applications using µCT methods, and the rate of growth of cavitation volume increases exponentially as the strain level is increased [187]. Defect geometry in the cast sample is highly complex (Figure 4.5), comprising of multiple branches, and the influence of these discontinuities is clearly identified in Figure 4.7, where multiple complex-shaped defects are identified as part of the primary

crack. Proximity of the defects to the surface, regardless of geometry (Figure 4.6(c)), is also identified as a key factor in crack initiation. Isaac *et al.* [130,188] have used X-ray tomography methods to quantify the volume change of creep cavities in a brass alloy, with void growth occurring below 25% of time to rupture, particularly at complex shaped defects. Although this chapter presents results for samples in the as-received condition and after HTLCF testing, it is assumed that micro-cracking at defects occurs in the primary stages of loading, leading to propagation and coalescence during the remainder of testing.

The forged material is manufactured from the same melt as the cast sample scanned here. Therefore, it is concluded that the forged material originally had the same defect characteristics as the cast (pre-forging). It is interesting to see the dramatic change in defect geometry and distribution as a result of this manufacturing process. The complex shaped defects are now replaced with stringer type geometries, aligned in the direction of forging (Figure 4.9). As per Table 3.4, this results in a significant increase in fatigue life; the number of cycles to failure for the forged sample (Forged_02) is approximately 57% higher than the cast sample (Cast_02). It could be assumed that the more consistent performance of the forged sample, as opposed to the cast (compared in Section 3.7.3 and Figure 3.25), is as a result of (i) reduced complexity in terms of defect geometry and (ii) reduced volume fraction of defects. This study did not examine the effect of orientation on the stringer defects in the forged sample, in relation to the direction of loading. However, fully-reversed fatigue testing of bainitic steel indicates a reduction in the average fatigue limit of ~13% for samples taken perpendicular to the rolling direction of the material [133]. This has not been observed for MarBN for high temperature creep testing, but may be influential under cyclic loading [189].

The forging process is clearly effective in both reducing the amount of defects and altering their geometry. It can be seen from sectioned microstructural analysis (Figure 4.19) that small defects (below the scan resolution) and coalescence of stringer type defects, up to 2.5 mm in length (Figure 4.11(b)), are shown to influence cracking behaviour under cyclic loading. The growth of defects, in terms of area and volume after HTLCF testing, is quantified for the cast and forged samples in Table 4.1 and Table 4.2. Coalescence of multiple defects in the forged sample (Figure 4.10) appears to occur more commonly than in the cast sample and may be due to a combination of geometry and loading direction.

For industrial application of MarBN, in terms of cast components under cyclic loading, it is recommended that a refined manufacturing process be applied to reduce the volume fraction of casting defects, as forging may not be applicable for complex geometries. Forging further increases the cost of component production; however, the enhanced mechanical performance of the material and significantly reduced volume fraction of defects highlights its suitability for highly flexible thin-walled plant components.

Significant differences are observed between the shape of defects identified during µCT scanning of pre- and post-test cast and forged samples cast i.e. complex and stinger. Based on this, sphericity has been used as a method of directly comparing defects based on shape and an effective radius value. In general, similar levels of sphericity and an increase in the effective radius of defects post-test (due to void growth) is observed for all cases, and the amount and size of defects is greater in the cast sample. This trend has been identified elsewhere for carbon fibre/PEEK laminates [185]. The defects with the ten largest volumes have been isolated in Figure 4.13(c), indicating that for similar levels of sphericity, the effective radius is generally larger for cast defects. The number of defects identified before and after testing (Table 4.3 and Table 4.4) increased in both samples, indicating that the rate of defect growth (possibly from defects below the scan resolution of 10 µm), is greater than the rate of defect coalescence. Although similar levels of sphericity are identified between cast and forged defects, this does not quantify the substantial differences in shape between samples. An alternative method, for example the extreme vertices model, may be more applicable for the complex geometries presented here [190].

The effect of loading on both samples (Figure 4.8 and Figure 4.12) leads to misalignment of defects before and after testing. This is not surprising in the axial and radial directions, due to necking during HTLCF loading. However, it is conjectured that as cracks grow under cyclic loading, regions of uncracked matrix material are then subject to increased and non-uniform loading to compensate for the reduced undamaged area. Cracks do not grown uniformly through the sample (Figure 4.6 and Figure 4.11) and, therefore, torsion of the sample and tangential motion of defects occurs.

In contrast to the complex defects observed via 3D X-ray µCT scanning, those identified via fractography (Figure 4.14 and Figure 4.15) and sectioned sample analysis (Figure 4.18 and Figure 4.19) generally appear to be spherical. Similar microstructural features are identified in the post-test cast and forged samples, as those presented in Chapter 3 i.e. cracking at defects, fatigue striations, ductile dimples and oxide scale

growth. This chapter highlights the importance of combined 2D and 3D analysis methods in fully understanding the effect of manufacturing process and resulting defects on component failure, particularly as defects, even smaller than the scan resolution (10 μm), are identified in regions of cracking along the gauge length (Figure 4.18 and Figure 4.19). The development of damage and life prediction models for cast MarBN under HTLCF loading will be presented in Chapters 5 and 6. This is followed by the development and application of a multi-axial damage and life prediction model to the HTLCF gauge length section and plant component geometries, based on the experimentally identified cast and forged manufacturing defects presented in this chapter.

4.6 Conclusions

The key conclusions of this chapter are:

- For the first time, μCT scanning has been applied to cast and forged MarBN before and after HTLCF testing. The complex shape of defects, in conjunction with factors such as coalescence and location, have been identified as key factors promoting fatigue cracking and failure. The various defect geometries provide valuable information for realistic computational modelling of uniaxial test samples and in-service components.
- μCT scanning is a powerful non-destructive tool in understanding the influence of manufacturing process on defect size, shape and distribution. This technique can also be applied to samples after testing to identify the role of defects in component failure.
- Forging reduces the volume fraction of defects by a factor of 16, compared to casting, and reduces the complexity of defect geometry. This contributes to ~57% higher HTLCF life of forged MarBN, when loaded parallel to the forging direction, compared to cast MarBN and P91 steel. The localised influence of defect shape, location and forged manufacturing defect orientation on crack initiation will be investigated in greater detail in Chapter 7 via computational modelling.
- The combined microscopy and μCT scanning results of this chapter provide motivation for further process refinement efforts in order to minimise the number and size of defects due to manufacturing, and maximise fatigue life.

5 DAMAGE AND LIFE PREDICTION MATERIAL MODELLING

5.1 Introduction

In this chapter, a unified cyclic viscoplastic material model, modified to include damage accumulation and life prediction, is presented for cast MarBN (600 °C) and P91 (500 °C and 600 °C) under high temperature low cycle fatigue (HTLCF) conditions, based on experimental testing presented in Chapter 3 and by Barrett [9]. The Coffin-Manson [100] life prediction law has been combined with a variation of the Chaboche [112] damage law, and implemented in a modified hyperbolic sine unified cyclic viscoplastic material model, originally developed by Barrett *et al.* [9,94]. The model is implemented in MATLAB for cast MarBN at 600 °C, based on experimentally identified material parameters. An optimisation procedure has also been developed to automate and expedite material parameter identification, and increase accuracy of prediction of material response. A Chaboche non-linear isotropic softening model is employed, in conjunction with the Z -parameter methodology discussed in Section 3.7.4, to identify the onset of macroscale crack initiation. For subsequent cycles, both cyclic softening and fatigue damage accumulation are assumed to contribute to material degradation and hence failure. This new approach is applied to the cast MarBN and rolled P91 materials for prediction of macroscale cracking and component failure.

5.2 Material Model

The material model is an extension of a hyperbolic sine unified cyclic viscoplastic material model [94], to incorporate life prediction and damage accumulation. A key aspect of the model is the use of strain-rate independent material parameters due to the significant strain-rate effect observed in 9Cr steels above 500 °C. Alternative approaches employ uncoupled creep and plastic strain and this is convenient for application of the strain-range partitioning method [118], for example. However, the unified approach is more generally applicable to combined cyclic fatigue and creep conditions [93] and, more importantly, permits more reliable extrapolation and interpolation to the lower strain-rates observed during power plant operation, based on a relatively small amount of laboratory testing [94]. The model calculates cycles to failure and damage simultaneously, based on a set of optimised material parameters for MarBN and also P91. The plastic strain-rate, $\dot{\varepsilon}^{\mathrm{pl}}$, is defined as:

$$\dot{\varepsilon}^{\mathrm{pl}} = \alpha \sinh\beta\left(\left|\tilde{\sigma}-\chi\right|-R-k\right)\mathrm{sgn}\left(\tilde{\sigma}-\chi\right) \tag{5.1}$$

where α and β are the viscoplastic material constants, $\tilde{\sigma}$ is the effective stress, χ is the kinematic back-stress (accounting for the Bauschinger effect), isotropic softening behaviour is described by the R term, and k is initial cyclic yield stress. Damage is included in the model via an effective stress, as follows:

$$\tilde{\sigma} = \frac{\sigma}{\left(1-D\right)} \tag{5.2}$$

where σ is the stress, and D is damage. The initial and later strain hardening stages are described through the use of two hardening terms in the kinematic hardening evolution model of Armstrong-Frederick, such that $\chi = \chi_1 + \chi_2$. The evolutionary equation for the Armstrong-Frederick [87] model is:

$$\dot{\chi}_{\mathrm{i}} = C_{\mathrm{i}}\dot{\varepsilon}^{\mathrm{pl}}(1-D) - \gamma_{\mathrm{i}}\chi_{\mathrm{i}}\dot{p} \tag{5.3}$$

where C_{i} is the hardening modulus, γ_{i} is a recall parameter and $\dot{p}$ is the accumulated effective plastic strain-rate. Two Chaboche [84,85] isotropic softening terms are used to simulate the primary and secondary stages of softening, such that $R = R_1 + R_2$ [9]. The evolution of R is defined as follows:

$$\dot{R}_{\mathrm{i}} = b_{\mathrm{i}}Q_{\mathrm{i}}(1-D)\dot{p} - b_{\mathrm{i}}R_{\mathrm{i}}\dot{p} \tag{5.4}$$

where the rate of decay is controlled by b_i and Q_i is the saturated cyclic softening stress. The fatigue damage model of Chaboche [112] is defined as:

$$D = 1 - \left[1 - \left(\frac{N}{N_f} \right)^{\frac{1}{1-\phi_1}} \right]^{\frac{1}{\phi_2 - 1}} \tag{5.5}$$

where N is cycle number, ϕ_1 and ϕ_2 are damage constants, and N_f is number of cycles to failure, in conjunction with the Coffin-Manson [100] model for low-cycle fatigue:

$$\frac{\Delta \varepsilon^{pl}}{2} = \varepsilon_f^{'} \left(2N_f \right)^c \tag{5.6}$$

where $\varepsilon_f^{'}$ and c are the fatigue ductility coefficient and exponent, respectively. Differentiation of Equation (5.5), with respect to number of cycles, gives an equation for the damage rate, as follows:

$$\begin{aligned} \frac{dD}{dN} = & \left[\left(\frac{1}{1-\phi_2} \right) \left(1 - \left(\frac{N}{N_f(N)} \right)^{\frac{1}{1-\phi_1}} \right)^{\frac{2-\phi_2}{\phi_2 - 1}} \right] \left[\left(\frac{1}{\phi_1 - 1} \right) \left(\frac{N}{N_f(N)} \right)^{\frac{\phi_1}{1-\phi_1}} \right] \\ & \times \left[N_f(N) - N \left(\frac{1}{2c\left(2\varepsilon_f^{'}\right)^{\frac{1}{c}}} \Delta \varepsilon^{pl\frac{1-c}{c}} \frac{d\Delta \varepsilon^{pl}}{dN} \right) \right] \left[N_f(N) \right]^{-2} \end{aligned} \tag{5.7}$$

5.3 Identification of Initial Material Parameters

The material model, including damage, contains 17 material parameters, which can be classified as follows: (i) elastic (E and k), (ii) isotropic softening (b_i and Q_i) and kinematic hardening (C_i and γ_i), (iii) cyclic viscoplastic (α and β) and (iv) damage and life prediction (ϕ_1, ϕ_2, $\varepsilon_f^{'}$ and c). Poisson's ratio (0.3) is also included. Young's Modulus, E, and the initial cyclic yield stress, k, are determined from the initial stress-strain cycle. Identification of the cyclic viscoplastic material parameters is based on the method developed by Zhan [191] and implemented by Barrett for P91 steel [9].

The Chaboche isotropic softening model [84,85] incorporates two isotropic softening terms to describe the primary and secondary softening behaviour, characteristic of 9Cr steels [94]. The material parameters are identified by integrating Equation (5.4) and fitting this model to experimental cyclic softening data, as per Figure 5.1.

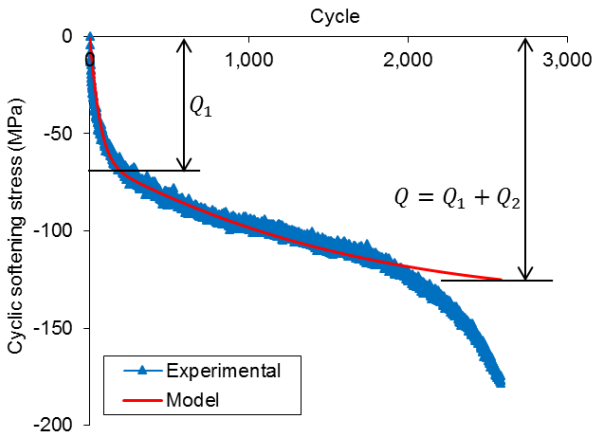

Figure 5.1 Identification of isotropic cyclic softening material parameters for cast MarBN at $\dot{\varepsilon}$ = 0.03 %/s, $\Delta\varepsilon$ = ± 0.3% and 600 °C.

The kinematic hardening constants are identified by dividing the stress into its various components, such that:

$$\sigma = \chi + \left(R + k + \sigma_{\mathrm{v}}\right)\mathrm{sgn}\left(\sigma - \chi\right) \tag{5.8}$$

where σ_{v} is the viscous stress. Differentiation of Equation (5.8) with respect to plastic strain gives:

$$\ln\left(\frac{\delta\sigma}{\delta\varepsilon^{\mathrm{pl}}} - \frac{\delta R}{\delta\varepsilon^{\mathrm{pl}}}\right) = \ln\left(C_{\mathrm{i}}\right) - \gamma_{\mathrm{i}}\varepsilon^{\mathrm{pl}} \tag{5.9}$$

where calculation of $\delta\sigma / \delta\varepsilon^{\mathrm{pl}}$ is performed using a Ramberg-Osgood smoothing function to describe the non-linear stress-strain relationship near the yield point. The kinematic hardening constants are then identified by plotting (i) $\ln\left(\delta\sigma / \delta\varepsilon^{\mathrm{pl}} - \delta R / \delta\varepsilon^{\mathrm{pl}}\right)$ for the later stages of strain hardening, and (ii) $\ln\left(\delta\sigma / \delta\varepsilon^{\mathrm{pl}} - \delta R / \delta\varepsilon^{\mathrm{pl}} - \delta\chi_2 / \delta\varepsilon^{\mathrm{pl}}\right)$ for the initial stages of strain hardening, against $\varepsilon^{\mathrm{pl}}$, as shown below in Figure 5.2.

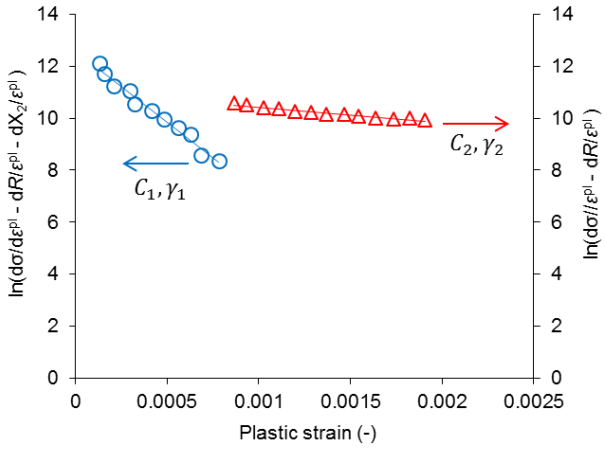

Figure 5.2 Identification of the kinematic hardening material parameters.

The viscoplastic material parameters, α and β are identified using an analytical model for stress as a function of time during a dwell period [9]:

$$\sigma = \frac{2}{\beta}\tanh^{-1}\left(\tanh\left(\frac{\beta\left(\sigma_0 - \chi - k\right)}{2}\right)e^{-\alpha\beta E(t-t_0)}\right) + \chi + k \qquad (5.10)$$

where t_0 and σ_0 are the time and stress at which the hold period begins. Figure 5.3 shows fitting of the model to the stress-relaxation data of the initial cycle of strain-controlled creep-fatigue (CF) testing up to 120 seconds. The Coffin-Manson constants, $\varepsilon_f^{'}$ and c, are determined from the measured plastic strain-range data, $\Delta\varepsilon^{pl}/2$, at half-life and corresponding number of reversals to failure, as shown in Figure 5.4.

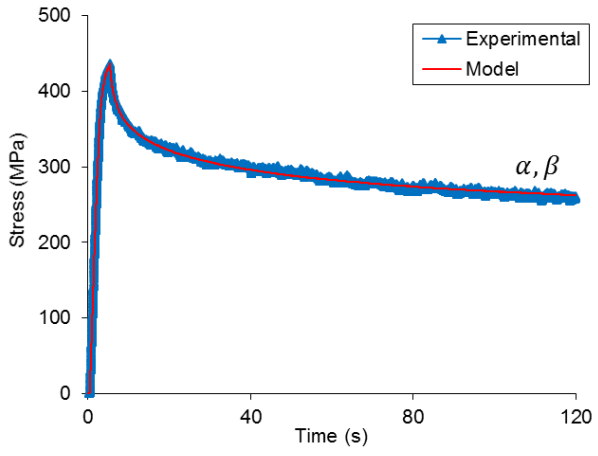

Figure 5.3 Fitting of the model to experimental data to allow identification of the cyclic viscoplastic material constants.

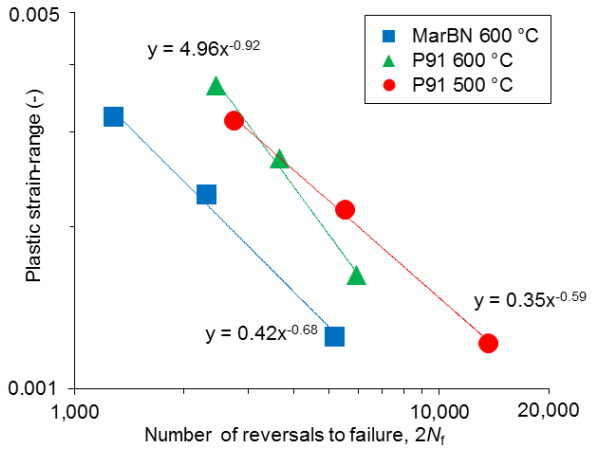

Figure 5.4 Identification of Coffin-Manson constants for cast MarBN and rolled P91.

Calculation of experimental damage is described in Section 3.7.5. The assumption in this model is that softening consists of (i) microstructurally induced softening (such as low angle boundary annihilation and particle coarsening) represented by R and (ii) fatigue damage induced softening represented by Z. The Chaboche damage constants, ϕ_1 and ϕ_2, are identified from the experimentally measured evolution of damage, D_{exp}, with number of cycles, N, via a least squares fitting procedure. All parameters are presented in Table 5.1 and experimental testing (MarBN and P91) and parameter identification (P91) is performed by Barrett [9].

Table 5.1 Coffin-Manson and Chaboche damage constants for cast MarBN at 600 °C and rolled P91 at 600 °C and 500 °C, at $\dot{\varepsilon}$ = 0.03 %/s.

Material	**Temp (°C)**	ε_f' **(-)**	c **(-)**	ϕ_1 **(-)**	ϕ_2 **(-)**
MarBN	600	0.42	-0.68	0.79	15.41
P91	600	0.35	-0.59	0.80	29.23
P91	500	4.96	-0.92	0.85	18.52

5.4 Optimisation Procedure

A flowchart of the material parameter optimisation process, in conjunction with the hyperbolic sine cyclic viscoplastic material model, is shown in Figure 5.5. To increase the accuracy of the material model, and reduce the error between the model and the experimental data, an optimisation procedure is developed using MATLAB for the present viscoplasticity model and applied to cast MarBN at 600 °C. The initial user estimates for the optimisation function correspond to the set of material parameters

identified using the method of the previous section. These are, namely, the initial yield stress, isotropic softening, kinematic hardening and cyclic viscoplastic material parameters. The optimisation procedure is performed using the Levenberg-Marquardt algorithm, as part of the *lsqnonlin* function in MATLAB. The function optimises an array, x_0, of user-defined constants to fit a range of experimental data by minimising the error between the predicted results and experimental data. Optimisation of the cyclic viscoplastic material parameters is based on experimental test data (i) during the initial cycle (k, C_i, γ_i, α and β) and (ii) maximum cyclic values up to macroscale damage propagation (b_i and Q_i). Similar methods for the optimisation of high temperature material parameters for modified 9Cr steel, rolled P91, have been implemented elsewhere [171,192,193].

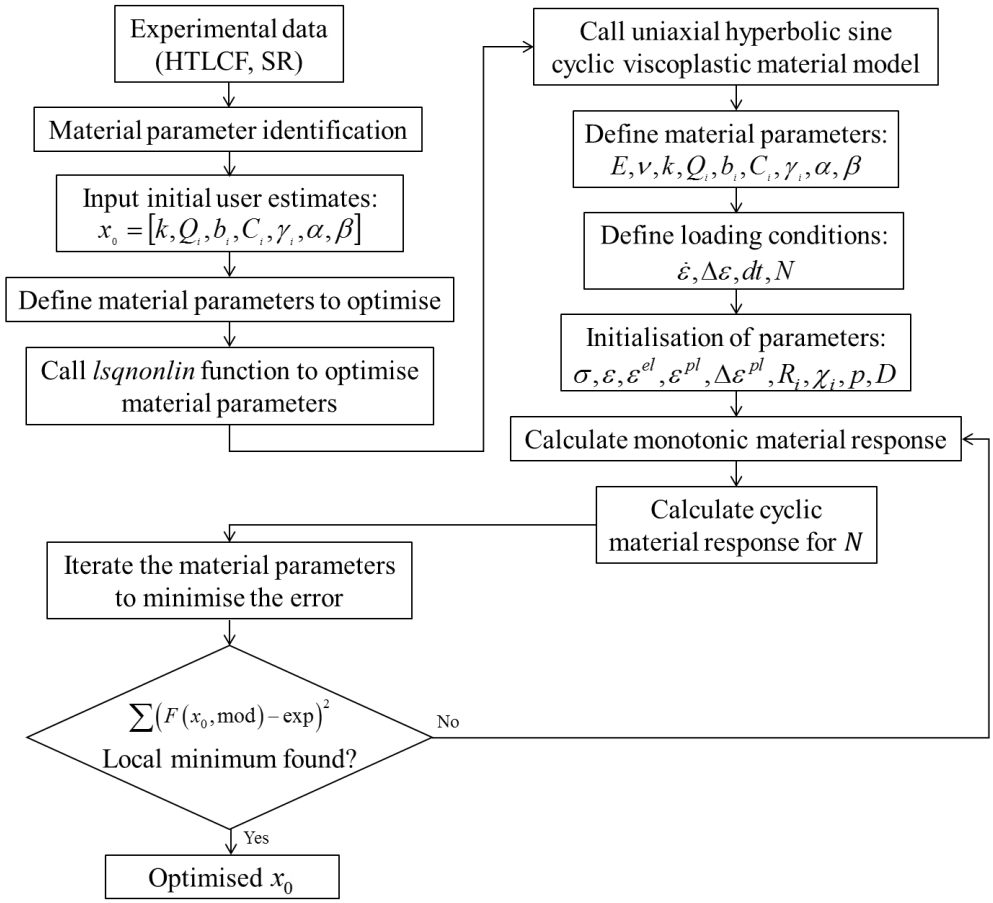

Figure 5.5 Flowchart of the material parameter optimisation process, in conjunction with the cyclic viscoplastic material model, applied to the MarBN material parameters.

5.5 Results

The initial and optimised material parameters for cast MarBN at 600 °C are presented in Table 5.2, as well as the parameters for P91 at 600 °C and 500 °C, previously identified

by Barrett [9]. Figure 5.6 and Figure 5.7 show the results of the optimisation process in terms of model fit to the experimental data for the initial cycle and half-life of MarBN at 600 ℃. The model is shown to accurately capture the stress-strain behaviour across a range of strain-rates and strain-ranges. Figure 5.8 and Figure 5.9 compare the effect of strain-range on the predicted and measured damage evolutions for both MarBN and P91.

Table 5.2 Coffin-Manson life prediction and Chaboche damage constants for cast MarBN at 600 °C and rolled P91 at 600 °C and 500 °C.

Material	E **(GPa)**	k **(MPa)**	Q_1 **(MPa)**	b_1 **(-)**	Q_2 **(MPa)**	b_2 **(-)**
MarBN (Initial)	162	100.0	-74.14	5.90	-73.81	0.25
MarBN (Optimised)	162	100.5	-68.35	11.11	-70.88	0.41
P91 (600 °C)	144	54.04	-72.90	3.02	-52.11	0.13
P91 (500 °C)	173	121.04	-46.67	2.00	-52.11	0.13

Material	C_1 **(MPa)**	γ_1 **(-)**	C_2 **(MPa)**	γ_2 **(-)**	α **(s^{-1})**	β **(MPa^{-1})**
MarBN (Initial)	296,262	5,492.1	61,574.3	601.9	2.0×10^{-6}	0.031
MarBN (Optimised)	296,256	5,610.1	61,545.7	626.3	9.1×10^{-7}	0.035
P91 (600 °C)	275,130	3,397.2	38,101.2	626.6	9.0×10^{-7}	0.055
P91 (500 °C)	304,370	3,422.5	48,484.5	406.7	8.0×10^{-7}	0.055

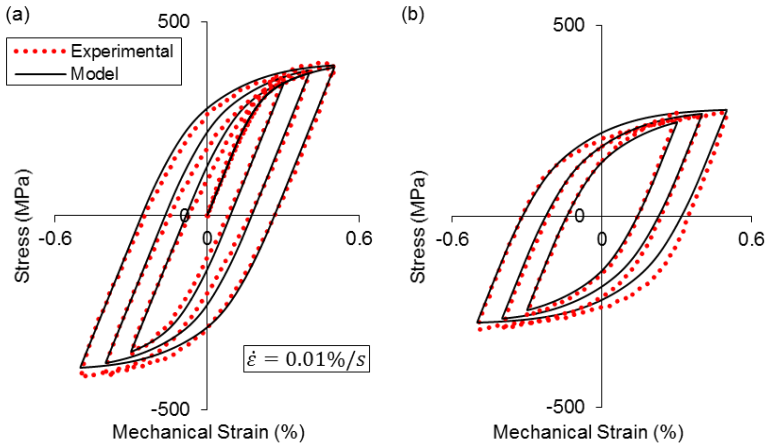

Figure 5.6 Comparison of the model to experimental data for cast MarBN across multiple strain-ranges ($\dot{\varepsilon}$ = 0.01 %/s and T = 600 °C), for the (a) initial cycle and (b) half-life.

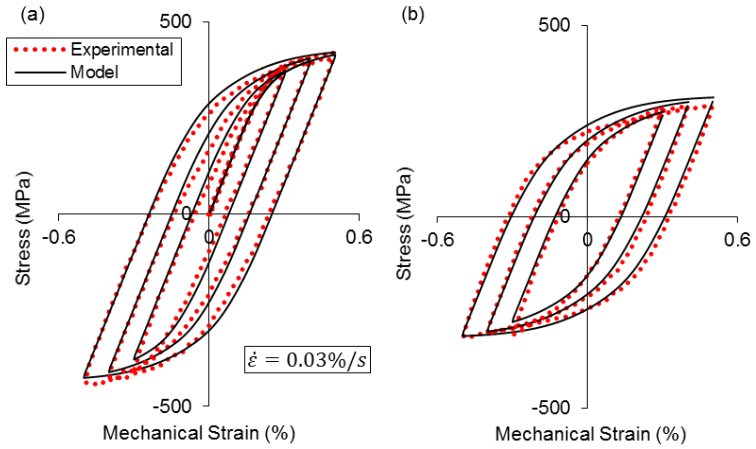

Figure 5.7 Comparison of the model to experimental data for cast MarBN across multiple strain-ranges ($\dot{\varepsilon}$ = 0.03 %/s and T = 600 °C), for the (a) initial cycle and (b) half-life.

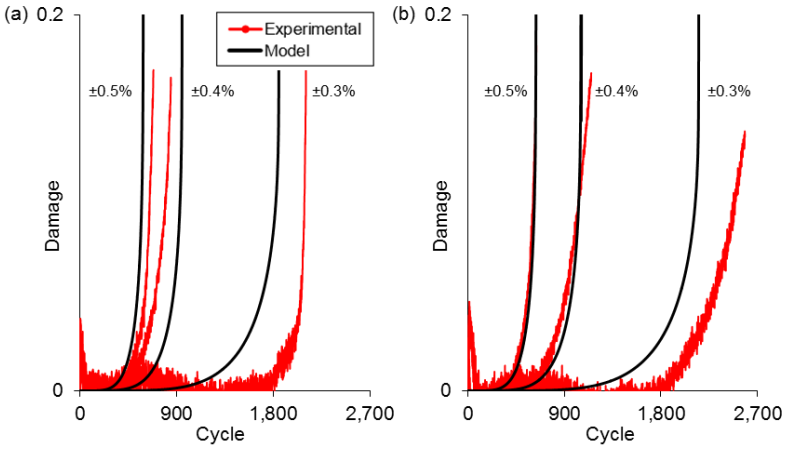

Figure 5.8. Comparison of effect of strain-range on predicted and measured damage evolutions for cast MarBN at 600 °C for strain-rates of (a) 0.01 %/s and (b) 0.03 %/s.

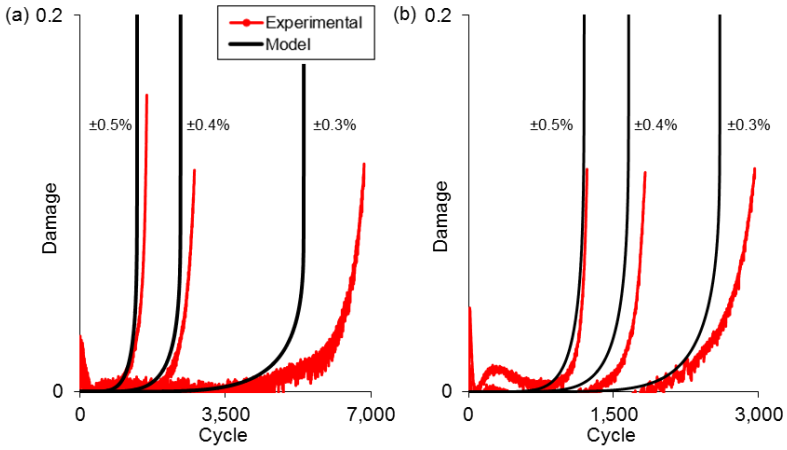

Figure 5.9. Comparison of effect of strain-range on predicted and measured damage evolutions for rolled P91 at a strain-rate of 0.03 %/s and temperature of (a) 500 °C and (b) 600 °C.

Figure 5.10 shows the evolution of the maximum plastic strain for MarBN and P91 at 600 °C, with the model generally capturing the experimental behaviour for the majority of the test. Figure 5.11 demonstrates the effect of increasing cycles on the cyclic stress-strain loop as a result of cyclic softening and fatigue damage accumulation. Figure 5.12 presents a comparison of the predicted number of reversals to failure against the experimental data for all of the above cases. In general, the fatigue life is predicted within ±15% of the experimental data.

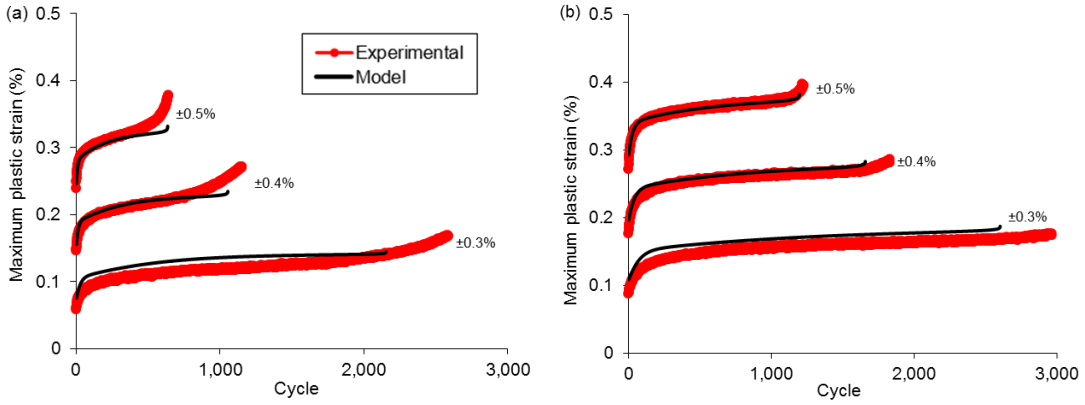

Figure 5.10 Comparison of the predicted and measured maximum plastic strain in (a) cast MarBN and (b) rolled P91 at 600 °C at a strain-rate of 0.03 %/s and multiple strain-ranges.

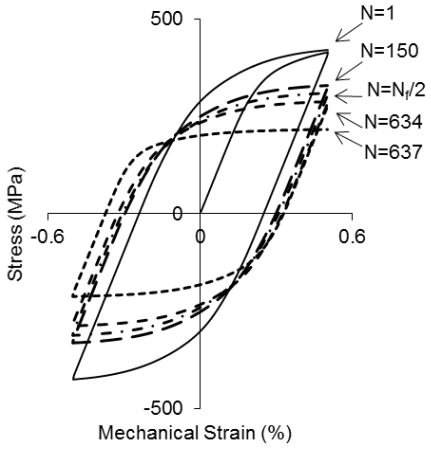

Figure 5.11 Material modelling of cast MarBN at 600 °C for a strain-rate of 0.03 %/s, demonstrating the effect of damage on the cyclic stress-strain loop.

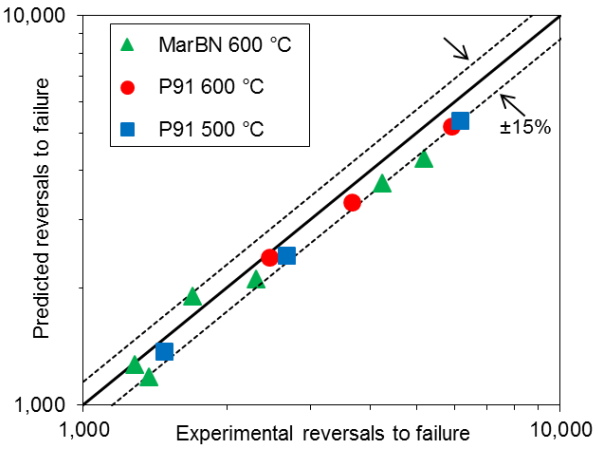

Figure 5.12 Comparison of the predicted and experimental number of reversals to failure for cast MarBN at 600 °C, and rolled P91 at 600 °C and 500 °C.

5.6 Discussion

The material parameter identification and optimisation procedure, outlined here with application to cast MarBN and rolled P91 for high temperature cyclic behaviour and fatigue damage prediction, is shown to provide excellent correlation with the measured failure lives across a range of strain-rates and strain-ranges. A key novel aspect of the present work is the application of the Chaboche non-linear isotropic softening equation, with primary and secondary softening parameters (R_1 and R_2), in comparison to the measured softening behaviour, to demarcate the onset and evolution of fatigue damage-induced softening, characterised by the Z variable. The accuracy achieved in relation to numerical simulation of the evolving cyclic viscoplasticity behaviour of the material (Figure 5.6 and Figure 5.7), preceding fatigue damage, is key to this demarcation process. The increase in plastic strain predicted by the model, as failure begins to occur (Figure 5.10), results in rapid damage accumulation, decreasing the stress range over a small number of cycles (Figure 5.11). Conservative numbers of cycles to failure is generally predicted, particularly at lower strain-ranges (Figure 5.12). Therefore, it is recommended that future calibration and validation of this model is performed based on experimental testing including strain-ranges more typical of plant conditions, to ensure accurate prediction of material degradation for such loading conditions.

A damage rate term (Equation 5.7) has been developed, based on combination of the Chaboche [112] damage law with the Coffin-Manson [100] model for low-cycle fatigue, to predict cyclically evolving damage and cycles to failure, based on the current plastic strain-range. The unified viscoplastic constitutive model used here has been previously applied to multiaxial conditions, without damage and life prediction [93]. Undoubtedly, future work should also focus on the development of more physically-based models, such as the dislocation mechanics based approaches of Fournier *et al.* [194], Giroux *et al.* [195], and more recently Barrett *et al.* [72,95,97]. Nonetheless, from a design perspective, the phenomenological modelling of the present work is ideal for rapid turnaround of results and potential simulation of complex geometries and loading conditions, based on the HTLCF characterisation methods used at NUI Galway and also GE Power, for identification of suitable design limits for plant components. However, again, the Coffin-Manson fatigue model used here has the advantage of facilitating expedient identification of parameters. Interestingly, a key ingredient in the success of the predictive method presented is the accurate prediction of evolving plastic strain range, which is central to the Coffin-Manson equation.

5.7 Conclusions

This chapter presents constitutive modelling of the HTLCF behaviour of cast MarBN and rolled P91, including damage accumulation and life prediction. Some key conclusions are:

- A fatigue life and damage accumulation model is developed for rapid prediction of HTLCF material response across a range of loading conditions, in conjunction with a hyperbolic sine unified cyclic viscoplasticity material model and non-linear combined isotropic softening and kinematic hardening.
- A key aspect of the model is the demarcation of fatigue damage from microstructure-induced softening via comparison of the non-linear isotropic evolution with the measured softening response.
- The new fatigue damage methodology is applied to MarBN at 600 °C and P91 at 600 °C and 500 °C. The results show excellent correlation of predicted and measured fatigue lives for different strain-rate and strain-range conditions as a result of material parameter optimisation processes.
- This model is an initial step in predicting damage evolution and cycles to failure in advanced modified martensitic steels at high temperature for multiaxial loading conditions.

6 CONTINUUM DAMAGE MECHANICS FOR HIGH-TEMPERATURE LOW-CYCLE FATIGUE OF VOIDS AND INCLUSIONS

6.1 Introduction

Microstructural analysis and 3D X-ray micro-computed tomography (μCT) of high temperature low cycle fatigue (HTLCF) MarBN samples have clearly demonstrated the role of voids and inclusions in crack initiation of cast and forged MarBN samples under cyclic loading (Chapter 3 and Chapter 4). This chapter presents the development of both coupled and uncoupled methodologies for the prediction of cycles to crack initiation in the region of voids and inclusions under strain-controlled loading at high temperature. In order to facilitate fitness-for-service of candidate next generation materials, a robust material model that can be calibrated and validated from relatively simple tests, and which can be applied to multi-axial component analysis and design, is required.

An uncoupled approach for prediction of cycles to crack initiation and damage at single inclusions and voids is presented first, based on a localised ductility exhaustion model and the predicted ratchetting behaviour in the region of defects [196,197]. Linear summation of the damage due to both fatigue loading and ratchetting is then performed

to quantify the effect of each mechanism. Conventional uncoupled macro-scale failure prediction methods are applied locally to 2D axisymmetric Abaqus models containing single idealised (i.e. spherical) voids and inclusions, to predict the number of cycles to crack initiation.

Furthermore, in order to design against premature failure, a robust multi-axial fatigue damage methodology is required. The use of the critical-plane method, as an uncoupled tool, has been widely applied [198–200], but has not typically been used for damage calculation within a continuum damage mechanics method. Following on from the uncoupled methodology, a coupled critical-plane method is implemented in a user-material (UMAT) subroutine in Abaqus, in conjunction with Ostergren [104] life prediction and a Chaboche [112] damage law, within a non-linear isotropic and kinematic hardening, cyclic viscoplasticity constitutive equation set. Calibration and validation is performed via comparison with HTLCF and creep-fatigue (CF) experimental data. The UMAT is applied to a cast MarBN section, containing single and multiple idealised inclusions, to identify the micro-scale effects on MarBN during cyclic loading, particularly in terms of damage accumulation and cycles to fatigue crack initiation.

6.2 Uncoupled Life Prediction at Manufacturing Defects

6.2.1 Material Model

The constitutive behaviour of the material is represented using a unified cyclic viscoplastic material model, implemented in an implicit UMAT subroutine for use with the commercial finite element (FE) code Abaqus, as developed by Barrett *et al.* [9,94,201]. The viscoplastic strain-rate, $\dot{\boldsymbol{\varepsilon}}^{\mathrm{pl}}$, is defined as:

$$\dot{\boldsymbol{\varepsilon}}^{\mathrm{pl}} = \frac{3}{2}\frac{\mathbf{s}-\boldsymbol{\chi}}{\mathrm{J}_2\left(\boldsymbol{\sigma}-\boldsymbol{\chi}\right)}\alpha\sinh\beta f = \frac{3}{2}\frac{\mathbf{s}-\boldsymbol{\chi}}{\mathrm{J}_2\left(\boldsymbol{\sigma}-\boldsymbol{\chi}\right)}\alpha\sinh\beta\left(\mathrm{J}_2\left(\mathbf{s}-\boldsymbol{\chi}\right)-R-k\right) \tag{6.1}$$

where $\mathbf{s}$ is the deviatoric stress tensor and α and β are the cyclic viscoplastic material constants. The Bauschinger effect is accounted for using the Armstrong-Frederick model to describe the initial and later strain hardening stages, such that $\boldsymbol{\chi} = \boldsymbol{\chi}_1 + \boldsymbol{\chi}_2$, via the following equation:

$$\dot{\boldsymbol{\chi}}_{\mathrm{i}} = C_{\mathrm{i}}\dot{\boldsymbol{\varepsilon}}^{\mathrm{pl}} - \gamma_{\mathrm{i}}\boldsymbol{\chi}_{\mathrm{i}}\dot{p} \tag{6.2}$$

where C_i is hardening modulus, γ_i is a recall parameter and $\dot{p}$ is the accumulated effective plastic strain-rate. The isotropic softening behaviour is described by the R term, such that $R = R_1 + R_2$. Two isotropic softening terms are used to simulate primary and secondary stages of softening. The evolution of R_i is defined using the Chaboche model as follows:

$$\dot{R}_i = b_i Q_i \dot{p} - b_i R_i \dot{p} \tag{6.3}$$

where b_i is the rate of decay and Q_i is the saturated cyclic softening stress. The iterative increment in accumulated effective plastic strain, $d\Delta p$, is:

$$\mathrm{d}\Delta p = \frac{\varphi - {\Delta p}/{\Delta t}}{\left[\frac{1}{\Delta t} + 3G\Gamma + \Gamma\left(\sum_{i=1}^{2}\left(C_i - \chi_i \gamma_i + b_i\left(Q_i - R_i\right)\right)\right)\right]} \tag{6.4}$$

where $\Gamma = \alpha\beta\cosh\beta f$ and G is shear modulus. φ is the accumulated effective plastic strain-rate for the previous iteration, defined as:

$$\varphi = \alpha\sinh\beta\left(\sigma_e^{tr} - 3G\Delta p - R - k\right) \tag{6.5}$$

where σ_e^{tr} is the effective trial stress (as part of the radial return method [9]). As shown in later sections, localised plasticity for both inclusions and voids is predicted to lead to ratchetting. Hence, a localised ductility exhaustion model is adopted based on the Rice and Tracey [196] void growth model for ductile solids in triaxial stress fields, and the work of Yatomi *et al*. [197] on a C-Mn steel under multiaxial loading and high stress triaxiality states. In this model, the multiaxial failure strain, ε_f^*, is defined as:

$$\frac{\varepsilon_f^*}{\varepsilon_f} = \frac{0.521}{\sinh\left(\frac{3}{2}\frac{\sigma_m}{\sigma_{eq}}\right)} \tag{6.6}$$

The ratio of the hydrostatic stress, σ_m, to the equivalent stress, σ_{eq}, is the triaxiality ratio and ε_f is the uniaxial failure strain, taken here to be 18% for MarBN at 600 °C (based on experimental tensile testing). The number of cycles to crack initiation due to ratchetting, $N_{i,r}$, is calculated based on an approach developed elsewhere [102,202,203], and defined as:

$$N_{\mathrm{i,r}} = \frac{\varepsilon_{\mathrm{f}}^{*}}{\sum_{\mathrm{k=1}}^{N_{\mathrm{i,r}}} \Delta\varepsilon_{\mathrm{r}}} = \frac{\varepsilon_{\mathrm{f}}^{*}}{\sum_{\mathrm{k=1}}^{N_{\mathrm{i,r}}} \sqrt{\frac{2}{3}\Delta\varepsilon_{\mathrm{ij}}^{\mathrm{r}}\Delta\varepsilon_{\mathrm{ij}}^{\mathrm{r}}}} \tag{6.7}$$

where $\Delta\varepsilon_{\mathrm{r}}$ is equivalent (multiaxial) ratchet strain increment, determined from individual ratchet strain components $\Delta\varepsilon_{\mathrm{ij}}^{\mathrm{r}}$. The number of cycles to low cycle fatigue (LCF) crack initiation, $N_{\mathrm{i,f}}$, is calculated here using the local (void and inclusion) hysteresis loops via the Coffin-Manson relationship, and constants identified from uniaxial (macroscale) tests in Chapter 3, as follows:

$$\frac{\Delta\varepsilon^{\mathrm{pl}}}{2} = \varepsilon_{\mathrm{f}}^{'}\left(2N_{\mathrm{i,f}}\right)^{\mathrm{c}} \tag{6.8}$$

where $\varepsilon_{\mathrm{f}}^{'}$ and c are the fatigue ductility coefficient and exponent, respectively. Assuming linear damage summation for ratchetting and LCF, the total damage per cycle for crack initiation is taken here as $D = D_{\mathrm{i,r}} + D_{\mathrm{i,f}} = \frac{1}{N_{\mathrm{i,r}}} + \frac{1}{N_{\mathrm{i,f}}}$. A localised strain concentration factor (SNCF) is identified from the models, and is defined as the ratio of maximum local strain-range ($\Delta\varepsilon_{\mathrm{loc}}$) to nominal applied strain-range ($\Delta\varepsilon_{\mathrm{nom}}$):

$$SNCF = \frac{\Delta\varepsilon_{\mathrm{loc}}}{\Delta\varepsilon_{\mathrm{nom}}} \tag{6.9}$$

6.2.2 Uniaxial Calibration and Validation

Figure 6.1(a) presents a 2D axisymmetric geometry developed in Abaqus for calibration and validation of the material parameters identified for MarBN at 600 °C, as described in Chapter 5, with a UMAT. To date, the UMAT described in the previous section has only been calibrated and validated by Barrett *et al.* for P91 steel [9,94,201]. The MATLAB model, presented in the previous chapter, and unified cyclic viscoplastic UMAT are compared in Figure 6.1(b), in terms of the stress-strain response at the initial and half-life cycles for cast MarBN at 600 °C. Almost identical results are predicted for uniaxial and multiaxial implementation of the model.

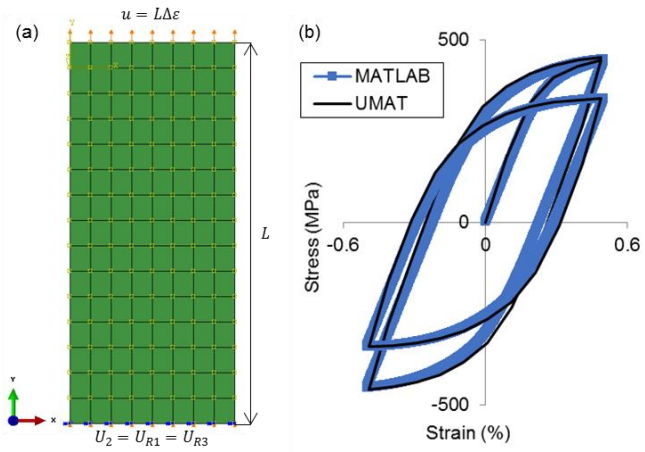

Figure 6.1 (a) 2D axisymmetric geometry with boundary conditions, and (b) comparison of predicted stress-strain response between the UMAT and MATLAB models, for cast MarBN at the initial and half-life cycles ($\dot{\varepsilon}$ = 0.1 %/s, $\Delta\varepsilon$ = ± 0.5%, and T = 600 °C).

Further validation against the measured responses from Chapter 3 are presented in Figure 6.2 for a range of strain-controlled cyclic test conditions, including different strain-rates and strain-ranges at 600 °C, at the initial and half-life cycles. In general, the maximum compressive stress and plastic strain-range are captured by the model. However, greater variation is predicted between the model and the experimental data in terms of the maximum tensile stress. A non-zero mean stress occurs during experimental testing, due to significant cyclic softening, that is not captured by the model, and is a possible source of disagreement between the two.

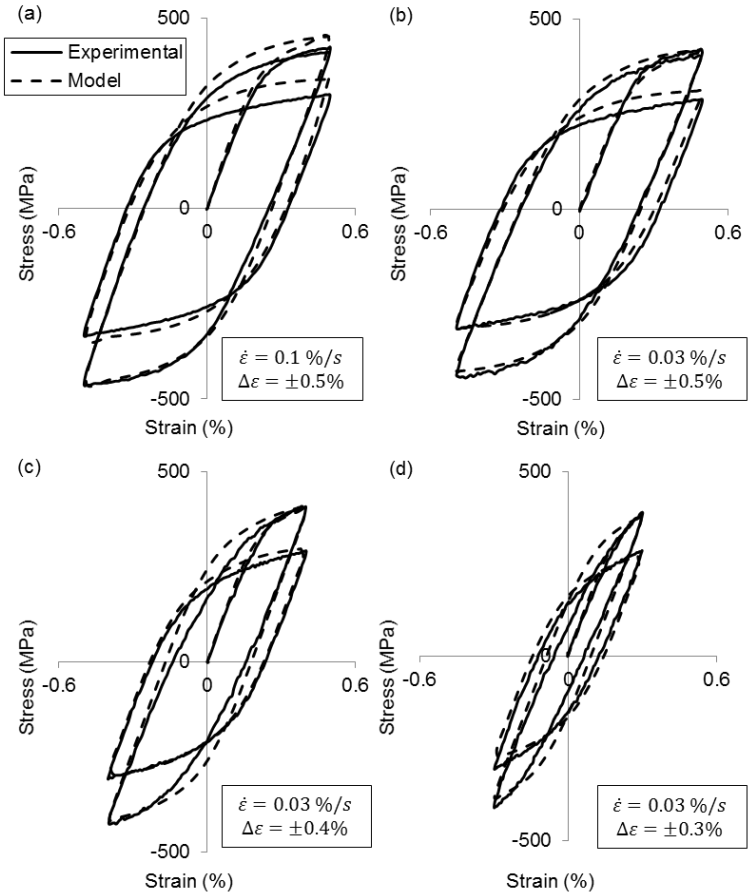

Figure 6.2 (a – d) Calibration and validation of the UMAT for MarBN at 600 °C, across a range of loading conditions, for the initial and half-life cycles.

6.2.3 Multiaxial Model for Manufacturing Defects

The axisymmetric FE model for voids and inclusions is shown in Figure 6.3, including the geometry, symmetric boundary conditions and loading (T = 600 °C, $\dot{\varepsilon}$ = 0.1 %/s and $\Delta\varepsilon$ = ±0.5%). Models are run up to 715 cycles, as per the experimentally determined number of cycles to failure for Cast_01 under the same loading conditions. Based on experimental observations (Figure 3.43), three different void and inclusion diameters are investigated: 12 µm, 23 µm and 30 µm. The model uses axisymmetric stress elements and mesh convergence is achieved to within 1.5% in terms of maximum principal strain (MPS) and axial stress evolution. The inclusion model uses frictionless, hard contact between the inclusion and the MarBN matrix material. The inclusion is assumed to be elastic i.e. very hard compared to the matrix, therefore, a Young's modulus of 390 GPa and Poisson's ratio of 0.35 are assigned to the inclusion, based on experimental measurements by Melander *et al*. [204] of MnS inclusions. The focus is on isothermal fatigue, therefore, thermal loading is not considered at this time.

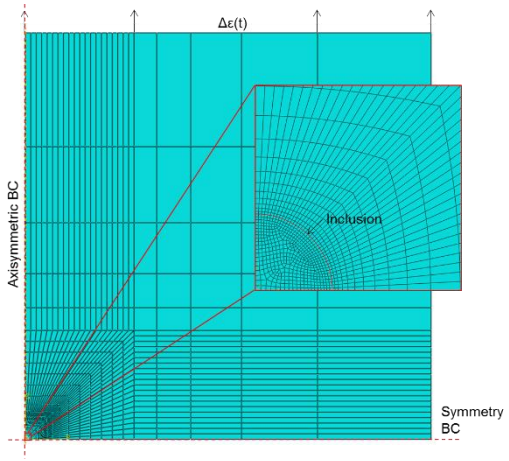

Figure 6.3 Mesh and boundary conditions of the Abaqus model containing an inclusion. The void model is almost identical, except for the omission of the inclusion.

6.2.4 Results

The MPS distributions are presented in Figure 6.4 for a 30 µm void and inclusion for the initial and 50th cycles (T = 600 °C, $\dot{\varepsilon}$ = 0.1 %/s and $\Delta\varepsilon$ = ±0.5%). The location of MPS for the void model is consistent with that of a notch [9,201], i.e. at the minimum section location (labelled 'Root' in Figure 6.4(a)). However, for the inclusion case, the MPS occurs at the top of the inclusion-matrix interface (labelled 'Interface' in Figure 6.4(b)), due to contact during fully-reversed cyclic loading, resulting in a higher SNCF of ~3.7 compared to ~2.5 for the void.

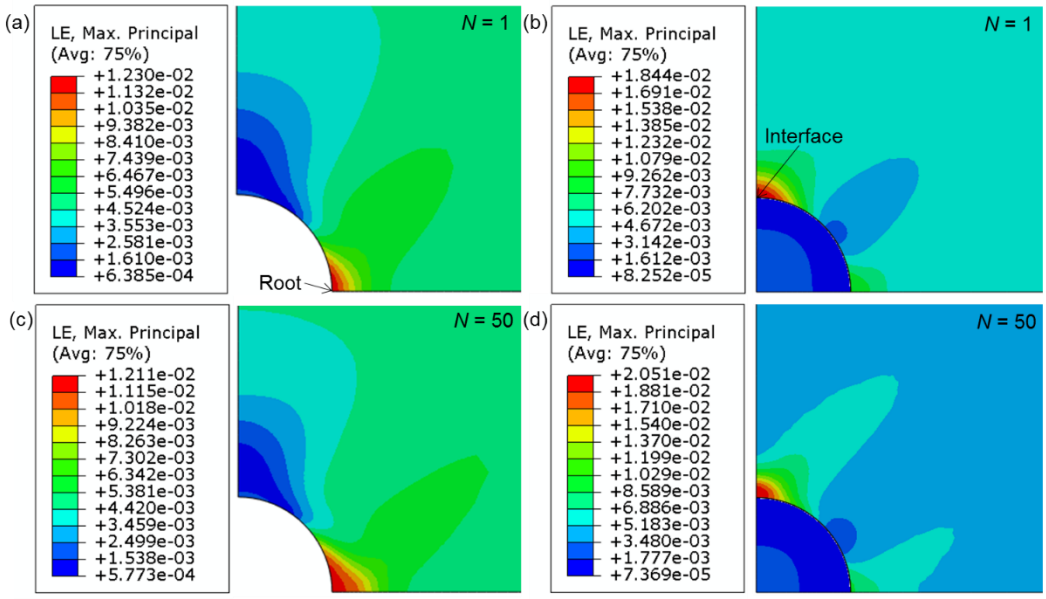

Figure 6.4 MPS distributions for the 30 µm void and inclusion models at (a, b) N = 1 and (c, d) N = 50.

Figure 6.5 compares the predicted MPS distributions for the 12 µm and 23 µm void and inclusion models at the 715th cycle for maximum tension. The maximum value of MPS increases with increasing void or inclusion size, and is higher for inclusions than voids.

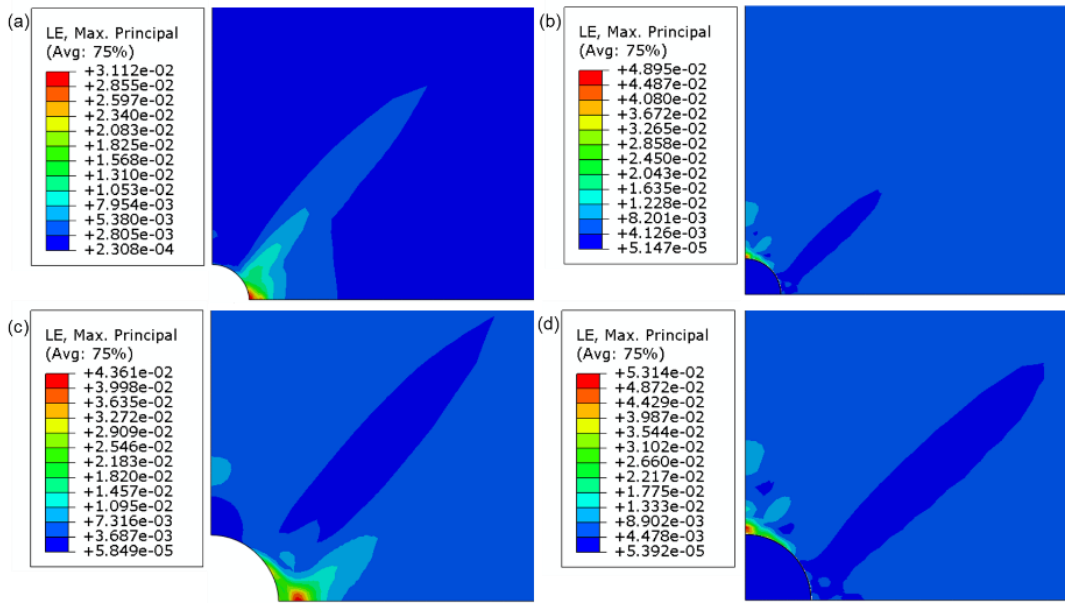

Figure 6.5 MPS distributions at N = 715 for a (a) 12 µm void, (b) 12 µm inclusion, (c) 23 µm void and (d) 23 µm inclusion.

Figure 6.6 presents the MPS distribution for a 30 µm void at N = 715 and the corresponding stress-strain evolution at the void root (labelled 'A' in Figure 6.6(a)) and location of MPS (labelled 'A'' in Figure 6.6(a)); multiple locations are investigated due to strain redistribution during cyclic loading. At location A, ratchetting with increasingly more negative mean strain occurs, and this changes to an increasingly more positive mean strain at location A', away from the root. Figure 6.7 presents the results for a 30 µm inclusion case; only ratchetting with an increasingly more positive mean strain is predicted, and higher strain accumulation than for the void case. As damage is not coupled in this model, saturation of the maximum stress evolution will eventually occur, based on the isotropic hardening constants identified in Chapter 5.

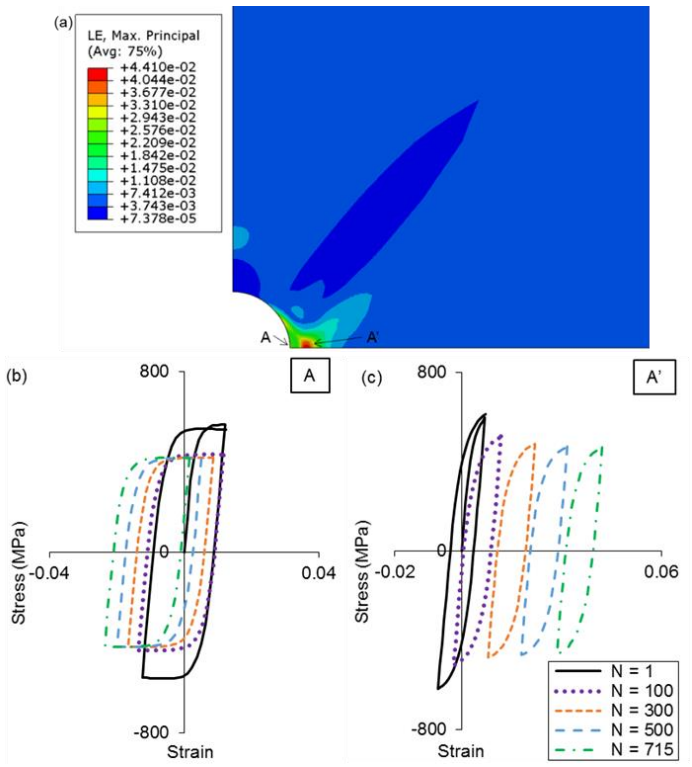

Figure 6.6 (a) Contour plot of MPS at N = 715 for a 30 μm void case, (b) stress-strain evolution at the void root (A) and (c) stress-strain evolution at the site of MPS (A').

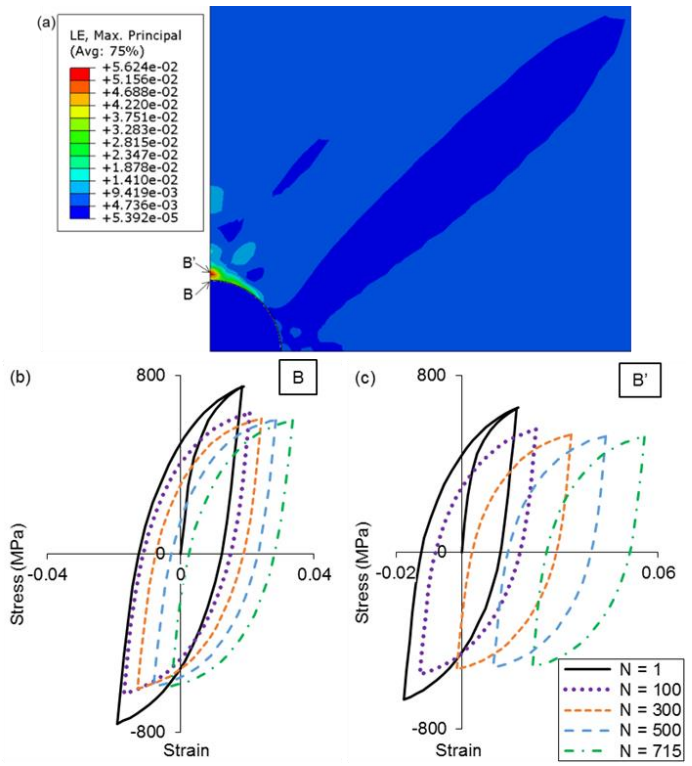

Figure 6.7 (a) Contour plot of MPS at N = 715 for a 30 μm inclusion case, (b) stress-strain evolution at the top of inclusion-matrix interface (B) and (c) stress-strain evolution at the site of MPS (B').

The increment in ratchetting strain with cycles in the axial direction is compared for a 30 µm void and inclusion in Figure 6.8(a). Similar significant reductions in the rate of ratchet strain increment are seen experimentally by Zhang *et al*. [205] for P91 during initial cycles and this slowly increases over later cycles due to cyclic softening. Figure 6.8(b) compares SNCF in the axial direction for each void and inclusion case, and is shown to increase linearly with cycles up to a SNCF of ~10 after 715 cycles. Similar behaviour is predicted between the 23 µm and 30 µm voids and inclusions, particularly when compared to the 12 µm cases at later cycles. Larger inclusion and void diameters are generally predicted to increase the SNCF, with a greater concentration at inclusions than voids in all cases. A slightly larger SNCF is predicted for the 23 µm inclusion than the 30 µm inclusion case; however, the value of MPS is greater for the 30 µm inclusion; therefore, it is assumed that during redistribution of the location of MPS with cycles, strains in the non-loading directions are increased at larger inclusions.

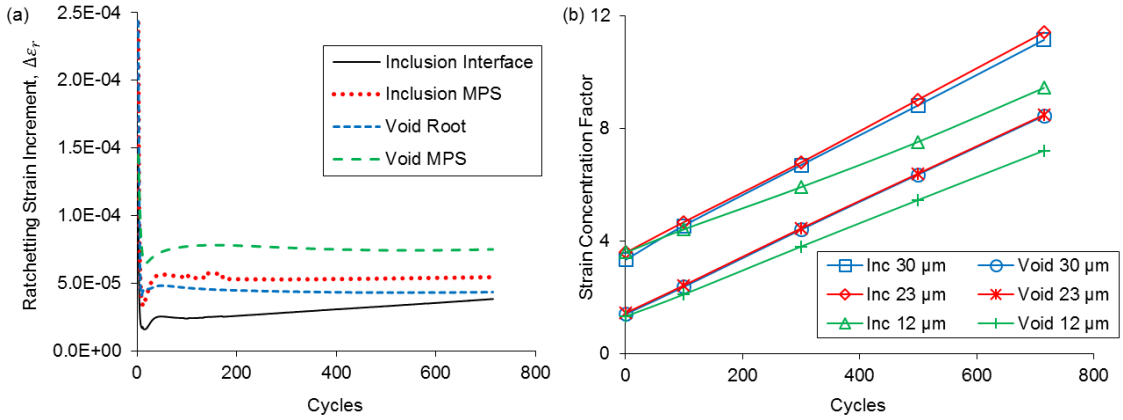

Figure 6.8 (a) Ratchetting strain increment with cycles for the 30 µm void and inclusion cases and (b) SNCF at the location of MPS for all models.

The calculated multiaxial failure strains and average triaxiality ratios for the various critical locations of each void and inclusion size are plotted in Figure 6.9, based on Equation 6.6 and the FE predicted triaxiality, with a comparison to the experimental uniaxial case. There is a significant attenuation of ductility as a result of the presence of a void and, furthermore, an inclusion in all areas, with larger voids and inclusions again having a greater influence.

Explicit modelling of decohesion of an inclusion was carried out to understand the effect on the localised behaviour of the matrix material surrounding an inclusion. The results, as per Figure 6.10, are similar to the void case in terms of the MPS distribution (Figure 6.6(a)), with increased maximum stress and strain. Rapid stress redistribution

occurs at the root (C), causing a large decrease in stress in the initial stress-strain loop (Figure 6.10 (b)). Ratchetting behaviour, similar to the void case, is observed also (Figure 6.6(b) and Figure 6.6(c)).

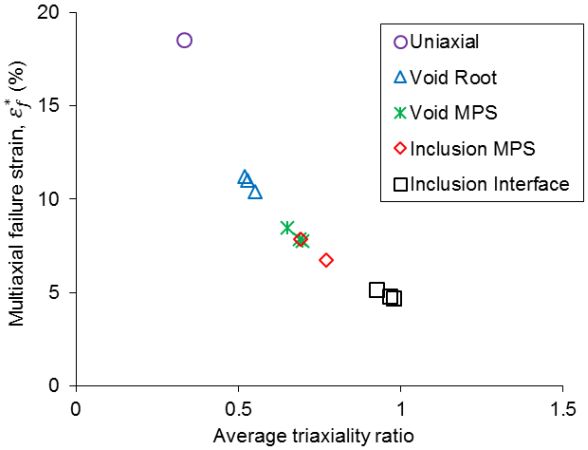

Figure 6.9 Multiaxial failure strain as a function of average triaxiality ratio at multiple locations, with a comparison to the uniaxial case.

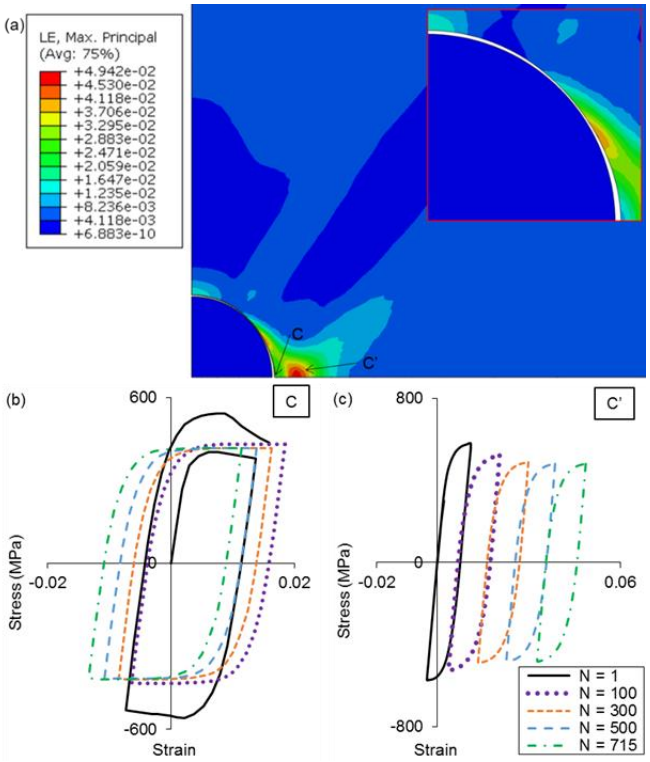

Figure 6.10 (a) Contour plot of the MPS at N = 715 for a 30 μm inclusion case with decohesion (inset is a magnified view of the decohesion), (b) stress-strain evolution at the top of inclusion-matrix interface (C) and (c) stress-strain evolution at the site of MPS (C'), and $\dot{\varepsilon}$ = 0.1 %/s, $\Delta\varepsilon$ = ± 0.5%, and T = 600 °C.

The predicted crack initiation lives for 30 µm void and inclusion cases (with and without decohesion), for combined ratchetting and LCF damage, are compared to the measured total fatigue life and assumed cycles to crack initiation, based on the transition from cyclic softening to fatigue induced damage (as per Chapter 5), in Figure 6.11. The predicted cycles to crack initiation are in line with those identified experimentally by Okamura *et al.* [206] for a maximum crack length of ~0.3 mm and N / N_f = 20% in a modified 9Cr-1Mo steel at 600 °C. LCF loading is predicted to be the dominant factor in crack initiation, with little change in the predicted value when ratchetting is included, indicating plastic strain-range is the dominant factor in crack initiation, as opposed to triaxiality ratio.

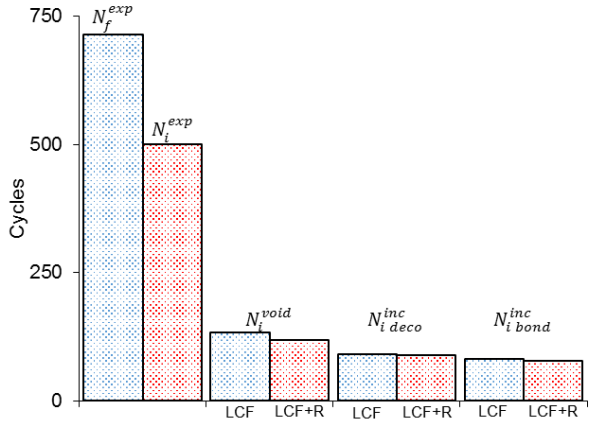

Figure 6.11 Comparison of 30 µm void and inclusion (with and without decohesion) crack initiation lives against measured total life.

6.3 Coupled Ostergren Life Prediction and Damage Model

6.3.1 Implementation of Fatigue Damage Model

Due to the minor effect of ratchetting predicted by the uncoupled methodology on cycles to crack initiation (Figure 6.11), damage due to ratchetting is not incorporated here. Therefore, the material model, as described in Section 6.2.1 is modified to include a coupled Ostergren critical-plane life prediction and damage methodology for cyclic loading. A flowchart of the constitutive damage UMAT, in conjunction with Abaqus, is presented in Figure 6.12.

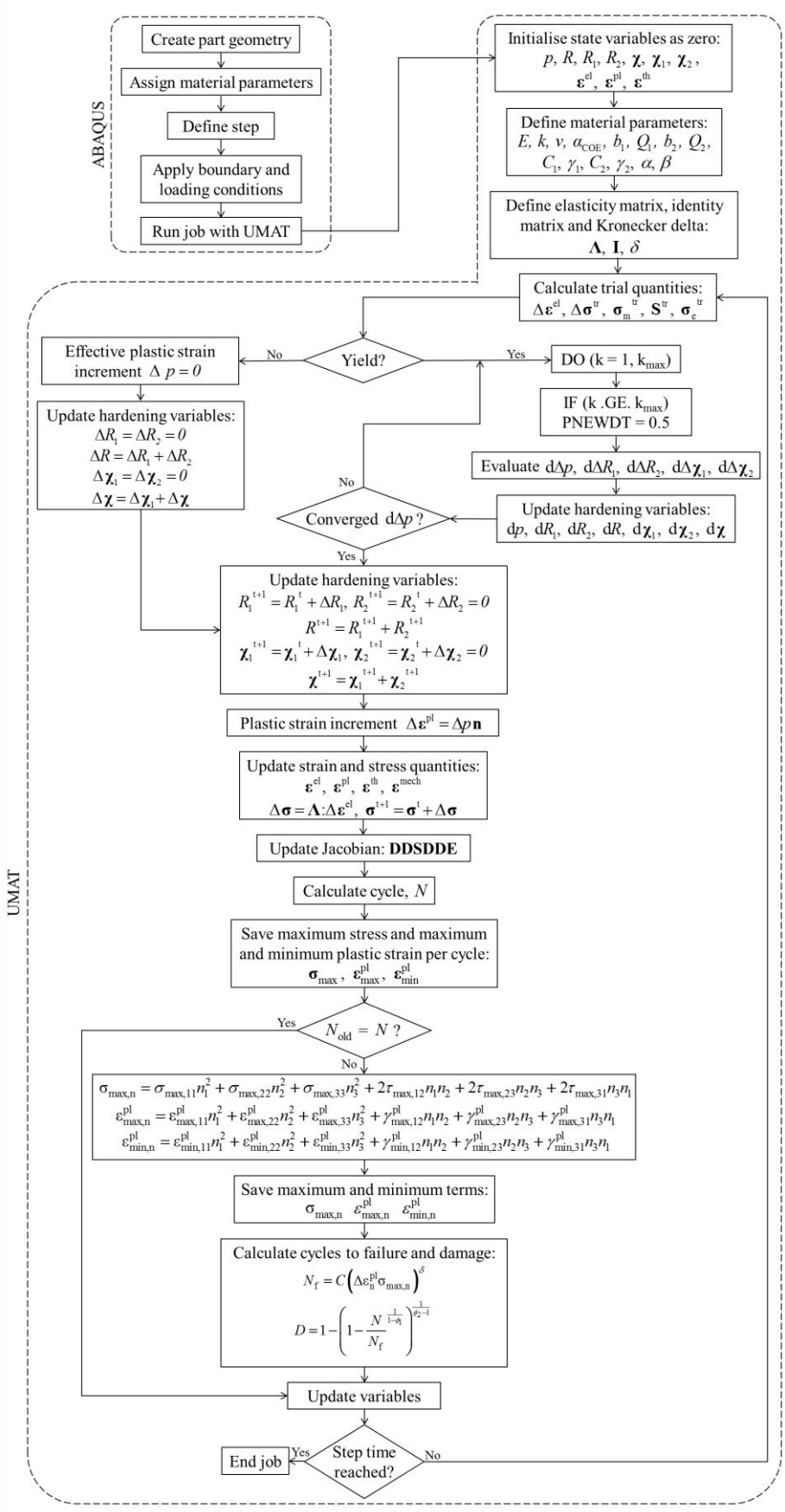

Figure 6.12 Flowchart for implicit implementation of the Ostergren critical plane UMAT, in conjunction with Abaqus.

The constitutive behaviour is defined by a hyperbolic sine viscoplastic flow rule, with isotropic and kinematic hardening; however, the plastic strain-rate tensor, $\dot{\boldsymbol{\varepsilon}}^{\mathrm{pl}}$ is now defined as:

$$\dot{\boldsymbol{\varepsilon}}^{\mathrm{pl}} = \frac{3}{2}\alpha \sinh\beta\left(\mathrm{J}_2\left(\tilde{\boldsymbol{\sigma}}-\boldsymbol{\chi}\right)-R-k\right)\frac{\tilde{\boldsymbol{\sigma}}-\boldsymbol{\chi}}{\tilde{\sigma}_{\mathrm{e}}} \tag{6.10}$$

where $\tilde{\boldsymbol{\sigma}} = \dfrac{\boldsymbol{\sigma}}{\left(1-D\right)}$ is the damaged stress tensor and D is fatigue damage. The kinematic [87] and isotropic [207,208] hardening laws are also modified to include damage.

$$\dot{\boldsymbol{\chi}}_{\mathrm{i}} = C_{\mathrm{i}}\dot{\boldsymbol{\varepsilon}}^{\mathrm{pl}}(1-D) - \gamma_{\mathrm{i}}\boldsymbol{\chi}_{\mathrm{i}}\dot{p} \tag{6.11}$$

$$\dot{R}_{\mathrm{i}} = b_{\mathrm{i}}Q_{\mathrm{i}}(1-D)\dot{p} - b_{\mathrm{i}}R_{\mathrm{i}}\dot{p} \tag{6.12}$$

The approach adopted to accumulate damage is to assume a Chaboche non-linear evolution [112] based on an evolving predicted value of number of cycles to failure, $N_{\mathrm{f}}\left(N\right)$:

$$D = 1-\left[1-\left(\frac{N}{N_{\mathrm{f}}\left(N\right)}\right)^{\frac{1}{1-\phi_1}}\right]^{\frac{1}{\phi_2-1}} \tag{6.13}$$

where ϕ_1 and ϕ_2 are damage constants. The use of an incremental damage term, $\mathrm{d}D/\mathrm{d}N$,

$$\frac{\mathrm{d}D}{\mathrm{d}N} = \frac{D\left(\dfrac{N}{N_{\mathrm{f}}}\right)^{\frac{1}{1-\phi_1}}\left(\dfrac{1}{N_{\mathrm{f}}}-\dfrac{N\delta\left(C\left(\frac{\mathrm{d}}{\mathrm{d}N}\Delta\varepsilon^{\mathrm{pl}}\right)\sigma_{\max}+C\left(\frac{\mathrm{d}}{\mathrm{d}N}\sigma_{\max}\right)\Delta\varepsilon^{\mathrm{pl}}\right)}{N_{\mathrm{f}}C\Delta\varepsilon^{\mathrm{pl}}\sigma_{\max}}\right)C\Delta\varepsilon^{\mathrm{pl}}{\sigma_{\max}}^{\delta}}{\left(1-\phi_1\right)\left(\phi_2-1\right)ND} \tag{6.14}$$

was also investigated and compared to the method described above (Equation 6.13). The predicted number of cycles to failure evolves with plastic strain, which in turn evolves due to (i) cyclic softening and (ii) damage accumulation. Liu *et al.* [105] investigated the use of the Coffin-Manson [100] and Ostergren [104] equations for prediction of cycles to failure for a nickel-based superalloy under thermo-mechanical fatigue (TMF) loading. The Coffin-Manson approach was found to be significantly non-conservative, and, therefore, the use of the Ostergren equation [198–200], based on a critical-plane methodology, is implemented here as follows:

$$N_{\mathrm{f}}\left(N\right)=C\left[\max_{\mathrm{n}}\left(\Delta\varepsilon_{\mathrm{n}}^{\mathrm{pl}}\left(N\right)\sigma_{\mathrm{max,n}}\left(N\right)\right)\right]^{\delta} \tag{6.15}$$

where N_{f} is number of cycles to failure, N is current cycle number and C and δ are the Ostergren constants. Although this work examines isothermal loading only, the use of the Ostergren equation allows application of the model to TMF loading conditions [199]. Maximisation of the Ostergren damage parameter with respect to plane orientation, n, requires identification of the maximum stress, $\sigma_{\mathrm{max,n}}$, and plastic strain-range, $\Delta\varepsilon_{\mathrm{n}}^{\mathrm{pl}}$, over a cycle. The cycle time is defined in the UMAT based on (a) the time for initial fatigue loading and (b) the time for one cycle, within which the maximum and minimum stress and strain components are identified and stored as state variables. The critical-plane approach requires calculation of the direction cosines over the range of candidate planes, spanning a 180° half-space incrementally (10° increments are used here), with the normal stresses and strains calculated on each candidate plane. The direction cosines are given by:

$$\begin{aligned} n_1 &= \sin\theta\sin\theta_{\mathrm{R}} \\ n_2 &= \sin\theta\cos\theta_{\mathrm{R}} \\ n_3 &= \cos\theta \end{aligned} \tag{6.16}$$

where θ and θ_{R} are two angles which uniquely define the candidate planes [199]. The associated normal stress and strain are given by:

$$\begin{aligned} \sigma_{\mathrm{n}} &= \sigma_{11}n_1^2+\sigma_{22}n_2^2+\sigma_{33}n_3^2+2\tau_{12}n_1n_2+2\tau_{23}n_2n_3+2\tau_{31}n_3n_1 \\ \varepsilon_{\mathrm{n}} &= \varepsilon_{11}n_1^2+\varepsilon_{22}n_2^2+\varepsilon_{33}n_3^2+\gamma_{12}n_1n_2+\gamma_{23}n_2n_3+\gamma_{31}n_3n_1 \end{aligned} \tag{6.17}$$

where τ_{ij} and γ_{ij} are the shear stress and shear strain for a given direction, as described schematically in Figure 6.13. This method allows calculation of number of cycles to failure (uniaxial test sample) and crack initiation (in the region of manufacturing defects), via Equation 6.15, for the identified critical Ostergren product.

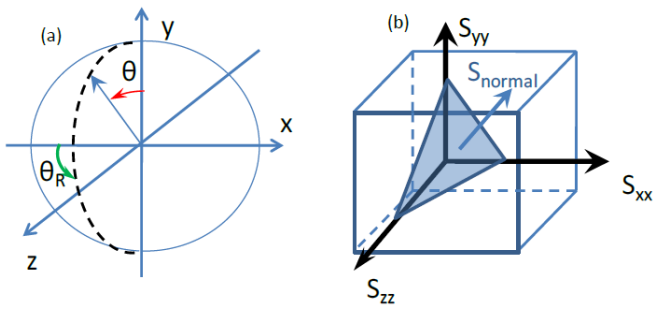

Figure 6.13 Schematic of (a) the angles, θ and θ_R, defining the candidate planes and (b) the normal stress vector, σ_n [86].

6.3.2 Material Parameter Identification

This model is applied to MarBN at both 600 °C and 650 °C. The complete constitutive and damage model requires identification of 17 material parameters; Young's modulus, E, Poisson's ratio, ν, initial cyclic yield stress, k, four isotropic (b_i and Q_i) and kinematic (C_i and γ_i) hardening parameters, two viscoplastic constants, α and β, and four life prediction (C and δ) and damage (ϕ_1 and ϕ_2) constants. Initial identification of the cyclic and viscoplastic material parameters for MarBN at 650 °C follows the method described in Chapter 5. The Levenberg-Marquardt algorithm, as part of the *lsqnonlin* non-linear optimisation toolbox in MATLAB, is used in conjunction with a uniaxial implementation of the constitutive material model in MATLAB to predict the cyclic viscoplastic and stress-relaxation response of MarBN at 650 °C. The material parameter optimisation procedure of Chapter 5 is modified here, whereby the overall final error is minimised with respect to (i) maximum stress evolution, (ii) cyclic response at initial and half-life cycles and (iii) stress-relaxation data. The identification of Ostergren and Coffin-Manson life prediction constants was described in Chapter 3. The damage constants (based on macroscale sample failure) are the same as those identified for MarBN at 600 °C in Table 3.4.

6.3.3 Results

Figure 6.14 shows calibration of the material parameters using MATLAB for MarBN at 650 °C, in terms of the maximum stress and plastic strain evolution with cycles. Validation is shown in Figure 6.14(b) and Figure 6.14(c) at different loading conditions (strain-rates and ranges) to those used for calibration for the initial and half-life cycles.

The resulting final identified cyclic viscoplastic material parameters for MarBN at 650 °C are shown in Table 6.1.

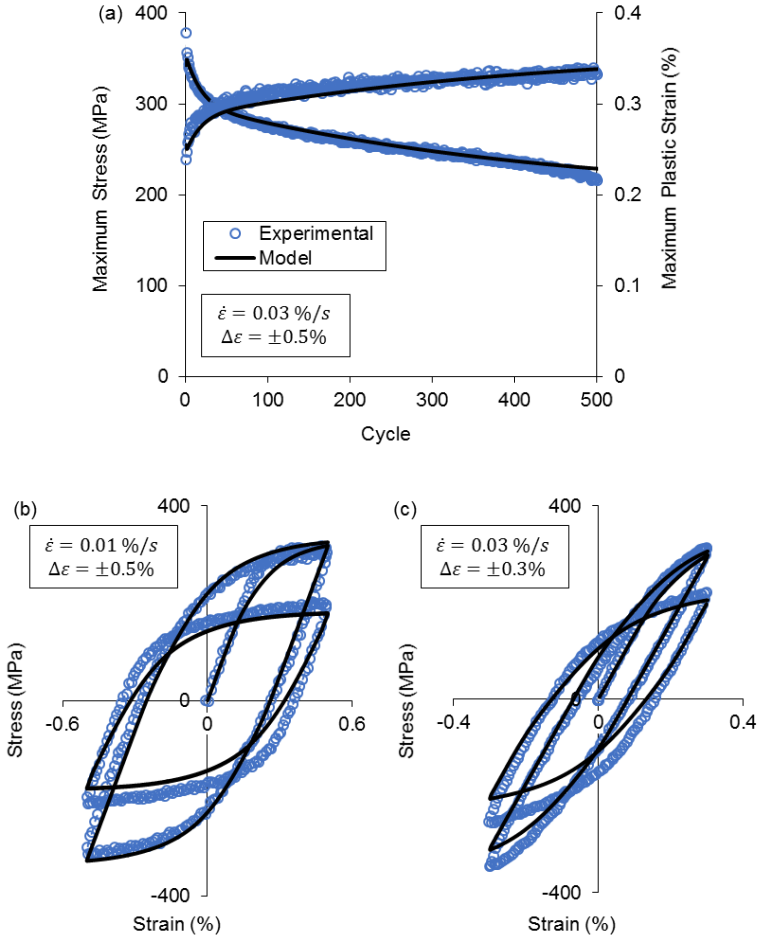

Figure 6.14 (a) Material parameter calibration and (b, c) validation at the initial and half-life cycles, for MarBN at 650 °C.

Table 6.1 MarBN cyclic viscoplastic material parameters at 650 °C.

E (GPa)	k (MPa)	Q_1 (MPa)	b_1 (-)	Q_2 (MPa)	b_2 (-)
133.1	50.0	-70.9	4.8	-100.1	0.2
C_1 (MPa)	**γ_1 (-)**	**C_2 (MPa)**	**γ_2 (-)**	**α (s^{-1})**	**β (MPa^{-1})**
181,747.0	2,428.9	40,912.3	545.9	3.8×10^{-7}	0.044

Figure 6.15 shows a comparison between using a single damage term (Equation 6.13) and the incremental damage approach (Equation 6.14) for uniaxial loading (Figure 6.15(a)) and an axisymmetric model of a 30 µm diameter inclusion (Figure 6.15(b)). In

both cases, a strain-rate of 0.1 %/s, strain-range of ±0.5% and temperature of 600 °C is applied. The final fatigue lives were predicted within 4% (uniaxial) and 1% (multiaxial) of one another, respectively, and hence, it was decided to use the simpler method for further studies, due to reduced computational expense and more rapid output of results for larger geometries e.g. FE modelling of 3D X-ray µCT defect distribution in Chapter 7.

Using this approach, calibration and validation of the UMAT under uniaxial cyclic loading conditions, across a range of strain-rates and strain-ranges at 600 °C and 650 °C, is performed using a single-element axisymmetric 2D model. The UMAT predicts essentially identical results to the uniaxial MATLAB code used for calibration and validation of the material parameters. Figure 6.16 shows a comparison of the UMAT-predicted critical-plane lives for MarBN, at a range of loading conditions and temperatures, compared to the experimental data presented in Chapter 3. The results are typically within ±15% of the experimentally measured cycles to failure (i.e. as a result of a 20% drop in load after the first 150 cycles of testing).

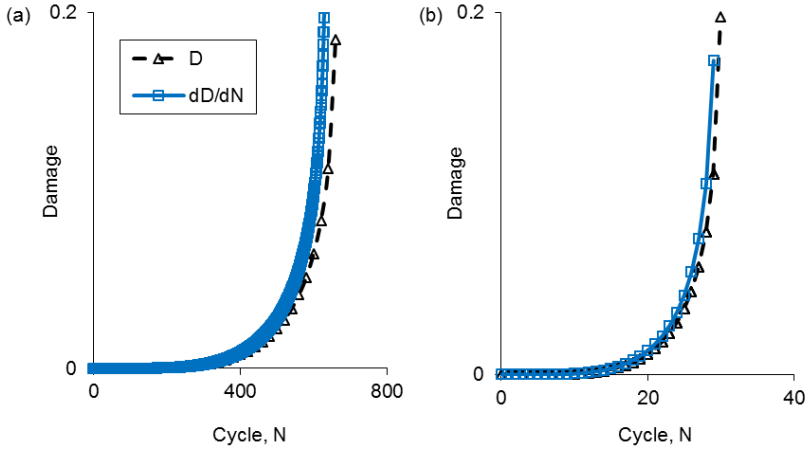

Figure 6.15 Damage evolution in MarBN for (a) a single-element uniaxial model and (b) an axisymmetric 2D model with an inclusion at the centre.

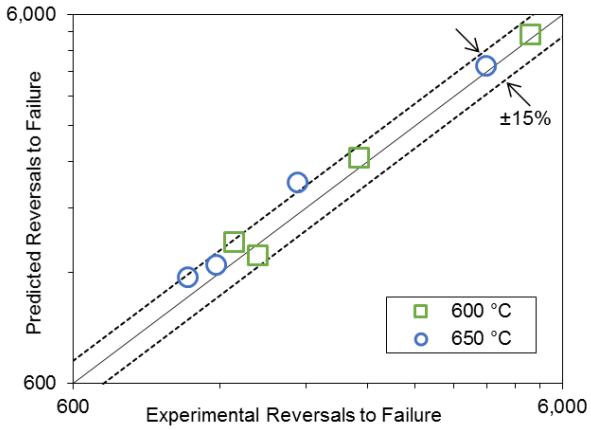

Figure 6.16 Predicted reversals to failure versus experimental data for MarBN at 600 °C and 650 °C under uniaxial cyclic loading.

In order to investigate the micro-scale effects of inclusions on damage and cracking, the coupled Ostergren life prediction and damage UMAT is applied to micro-scale models of single and multiple inclusions in a MarBN matrix. The model presented in Figure 6.3 is again adapted with frictionless, hard contact defined between the matrix and inclusion. As above, to accurately model decohesion, separation between the inclusion and matrix is allowed after contact. The models are run for 200 cycles, based on the limited numbers of cycles to fatigue crack initiation identified using the uncoupled method (Figure 6.11).

Figure 6.17 shows the predicted effect of strain-range on the MPS distribution after 200 cycles around the single inclusion at 650 °C, and similar results were obtained at 600 °C. Strain accumulation is predicted to occur at different rates in the region of the inclusion, depending on the applied strain-range. In Figure 6.18, the degree of decohesion is shown to increase with increasing strain-range for the same loading conditions as Figure 6.17.

In Figure 6.19, the cyclic evolution of damage is presented for an applied strain-range of ±0.5%. Figure 6.20 shows a comparison of (i) predicted cycles to crack initiation around the inclusion, and (ii) measured cycles to specimen failure. This is an attempt to quantify crack initiation life vis-à-vis measured total life.

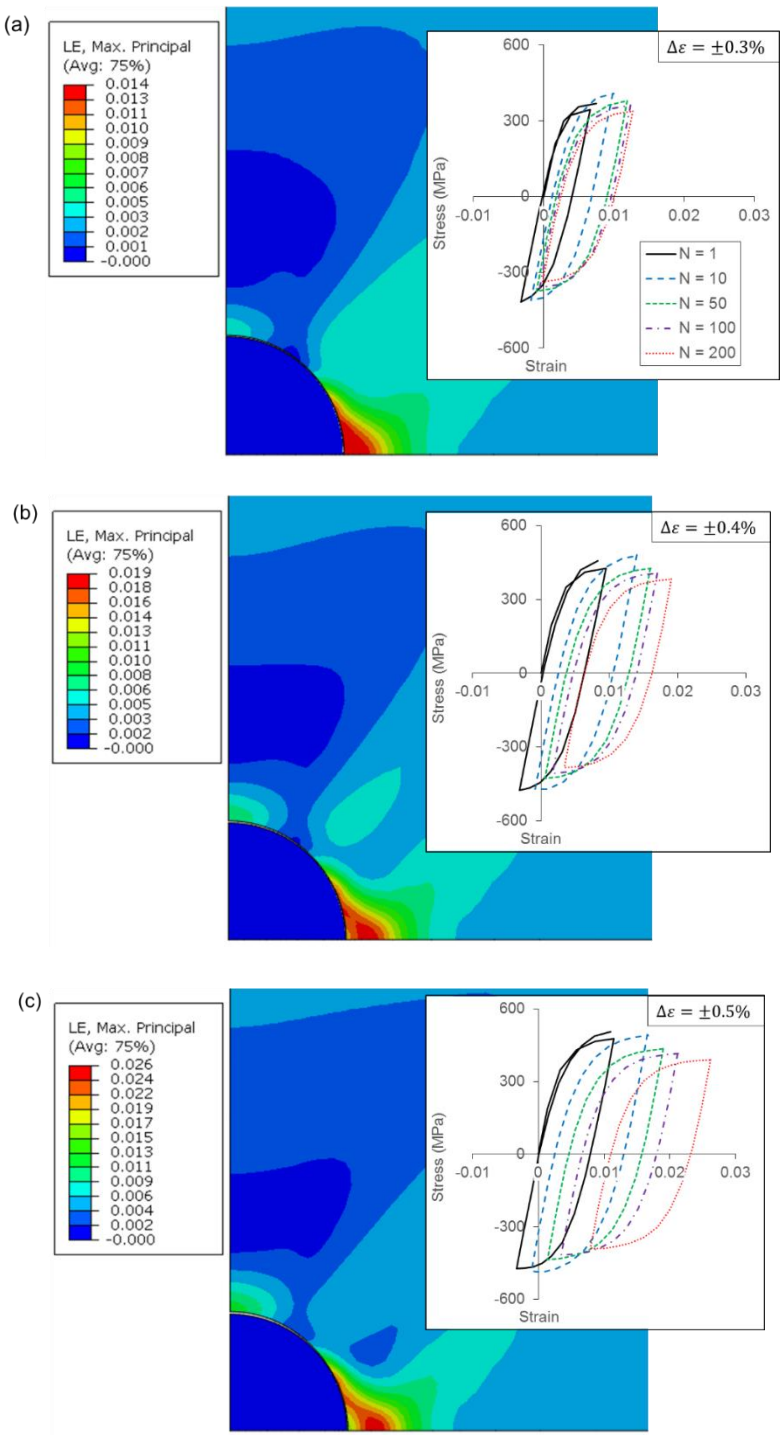

Figure 6.17 Maximum principal strain contour plots for MarBN at 650 °C, N = 200, $\dot{\varepsilon}$ = 0.1 %/s, and $\Delta\varepsilon$ = (a) ± 0.3%, (b) ± 0.4% and (c) ± 0.5%. The inset images show the stress-strain evolutions in the direction of loading at the MPS location.

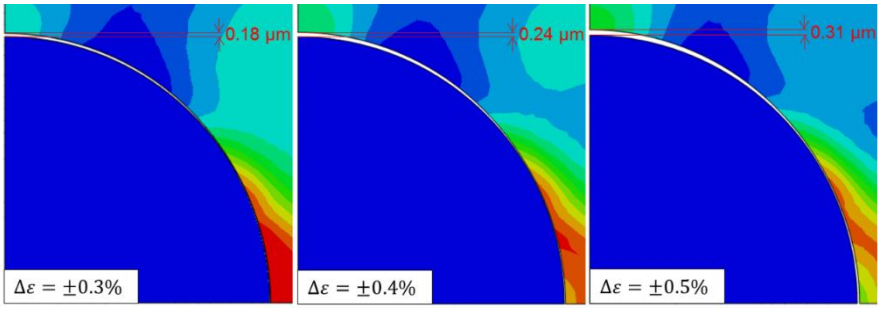

Figure 6.18 Comparison of the level of decohesion for MarBN across a range of strain-ranges at 650 °C, $\dot{\varepsilon}$ = 0.1 %/s and N = 200.

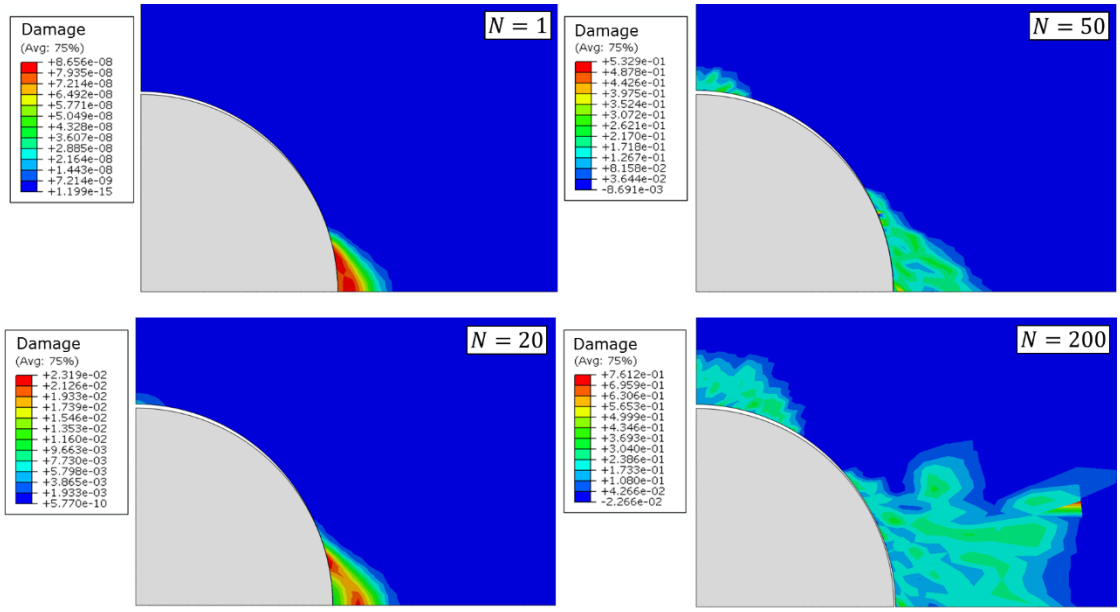

Figure 6.19 Contour plots of damage evolution with increasing cycles for MarBN at 650 °C, ($\dot{\varepsilon}$ = 0.1 %/s, $\Delta\varepsilon$ = ± 0.5%, and N = 200).

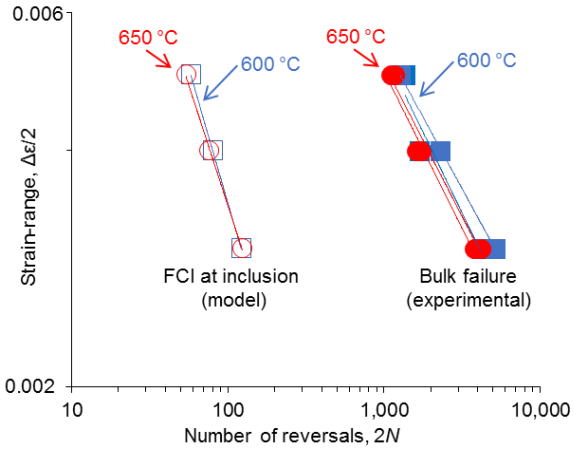

Figure 6.20 Comparison of model predicted cycles to fatigue crack initiation at an inclusion, compared to bulk experimental failure for various applied strain-ranges.

6.4 Uncoupled and Coupled Comparison

The two methods of computing fatigue damage, as described in Section 6.2 and Section 6.3, are compared in terms of MPS and von Mises stress distributions for a single inclusion case ($\dot{\varepsilon}$ = 0.1 %/s, $\Delta\varepsilon$ = ± 0.5% and T = 600 °C). Figure 6.21 indicates a more localised effect of inclusions, in terms of von Mises stress distribution, when damage is coupled. In Figure 6.22, the SNCF without damage is ~9.9 and this increases to ~10.7 in the coupled model, indicating a further increased rate of strain accumulation due to damage.

Figure 6.23 compares the stress and strain evolution for the models in Figure 6.22 at the location of MPS. A difference between the coupled and uncoupled methods of ~14% for maximum stress and ~1.5% for maximum strain occurs at 700 cycles. Figure 6.24 compares the predicted cycles to crack initiation using the coupled and uncoupled methods, as well as a comparison to experimental data. The number of cycles to experimental macroscale crack initiation corresponds to the transition from primary to secondary softening, as defined by Li *et al.* [209] for P91 steel at 600 °C, for micro-crack nucleation and coalescence. The coupled method predicts ~58 reversals to crack initiation, compared to the ~176 reversals predicted by the uncoupled method: a difference of ~67%, indicating the importance of including damage in computational models to more realistically predict the constitutive behaviour of the material, particularly in the region of manufacturing defects.

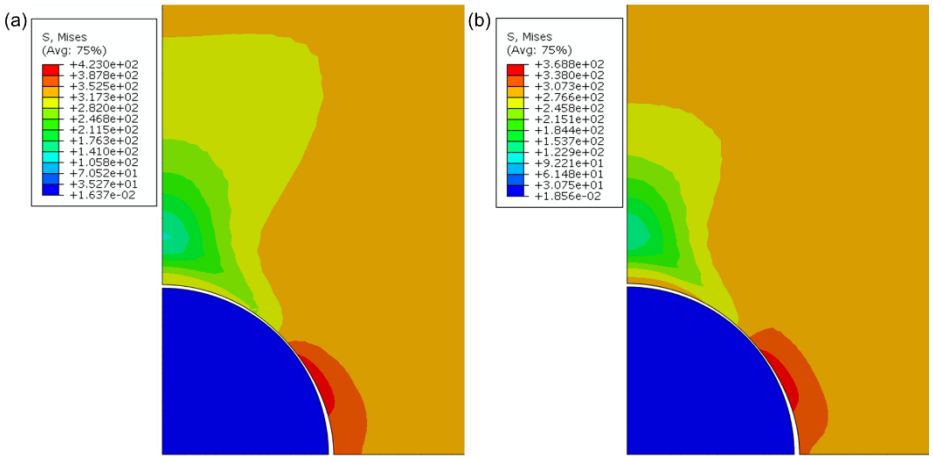

Figure 6.21 von Mises stress (MPa) for a single 30 µm inclusion model (a) without damage and (b) with damage.

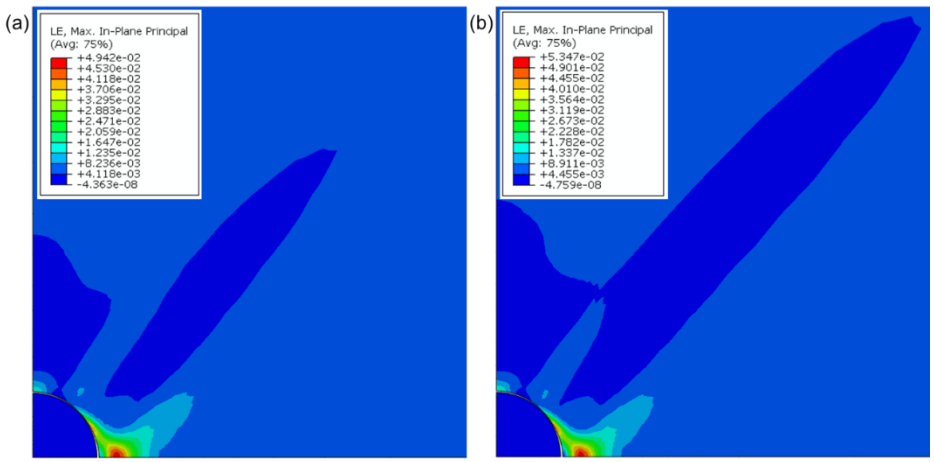

Figure 6.22 Maximum in-plane principal strain for a single 30 μm inclusion model (a) without damage and (b) with damage.

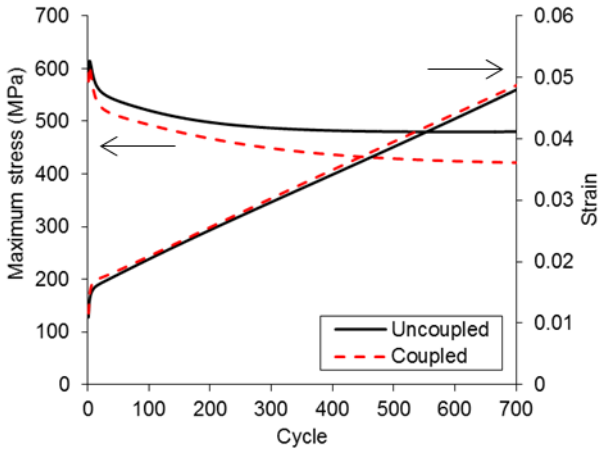

Figure 6.23 Comparison of the coupled and uncoupled methods in terms of maximum stress and strain evolution per cycle, in the direction of loading, at the location of MPS.

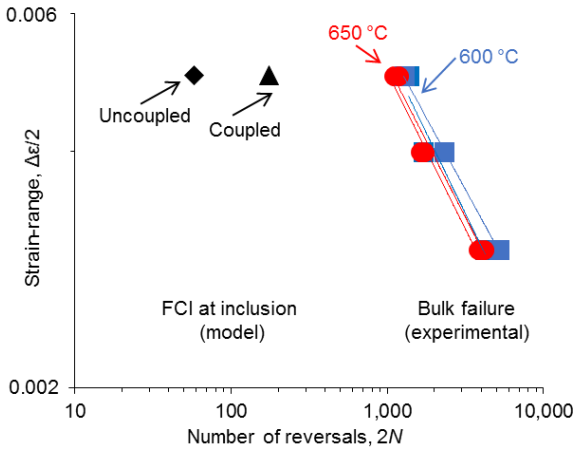

Figure 6.24 Model predicted number of cycles to crack initiation using the coupled and uncoupled methodologies ($\dot{\varepsilon}$ = 0.1 %/s, $\Delta\varepsilon$ = ± 0.5% and T = 600 °C), with comparison to experimental data ($\dot{\varepsilon}$ = 0.03 and 0.01 %/s).

6.5 2D Modelling of Multiple Inclusions

Figure 6.25(a) shows a scanning electron microscope (SEM) image of secondary cracking along the gauge length of a cast MarBN sample tested under HTLCF loading, highlighting in particular the presence of specific inclusions (I_1, I_2 and I_3). In order to develop a greater understanding of the interaction between inclusions, a 2D plane strain model of the three inclusions in a metal matrix has been developed, as shown in Figure 6.25(b). The modelling methodology is otherwise the same as that of Section 6.3 for a single inclusion. Simulations are conducted for temperatures of 600 °C and 650 °C, and at $\dot{\varepsilon}$ = 0.1 %/s, $\Delta\varepsilon$ = ± 0.5%. Based on the small numbers of cycles predicted for fatigue crack initiation around a single inclusion, as per previous sections, the model was run for 40 cycles. Inclusions are assumed to be circular and the influence of out-of-plane inclusions, that may affect the cracking behaviour, is neglected. 3D modelling of manufacturing defects will be performed in Chapter 7 to further investigate this effect. A combination of three and four node plane strain elements (CPE3 and CPE4) are used and mesh refinement is conducted in the region of the inclusions.

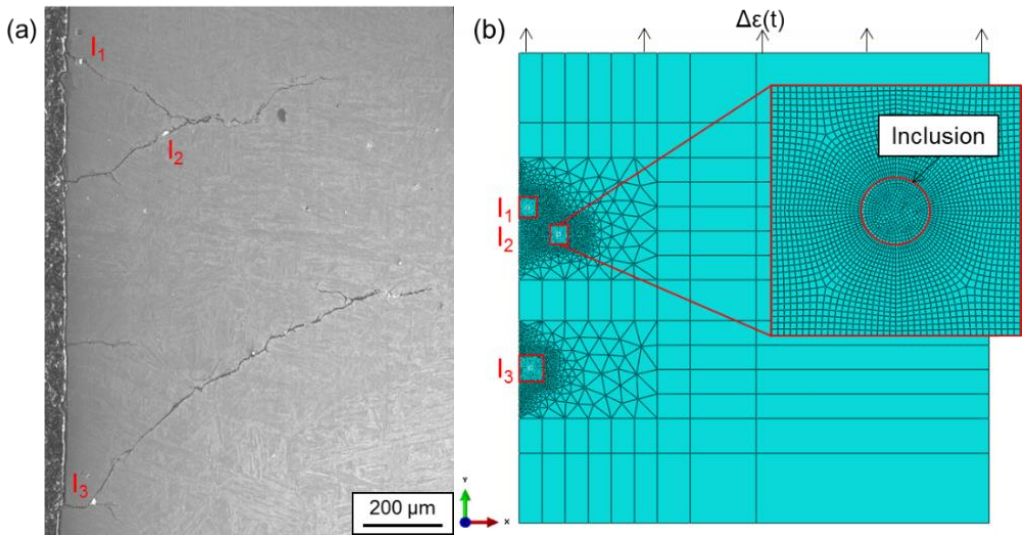

Figure 6.25 (a) SEM image of secondary cracking as a result of inclusions in a post-fatigue test MarBN sample and (b) corresponding 2D Abaqus model.

Figure 6.26 presents the predicted distributions of von Mises stress, MPS and damage at 40 cycles, focussing on the inclusions. Stress and strain concentrations can be seen around each inclusion, with a stress concentration factor (SCF) of approximately 2 and a SNCF of approximately 10, in relation to the maximum value of stress and strain in the unaffected matrix material (i.e. away from inclusions). This is shown to lead to an increase in damage in the region of inclusions, as well as interaction between inclusions I_1 and I_2.

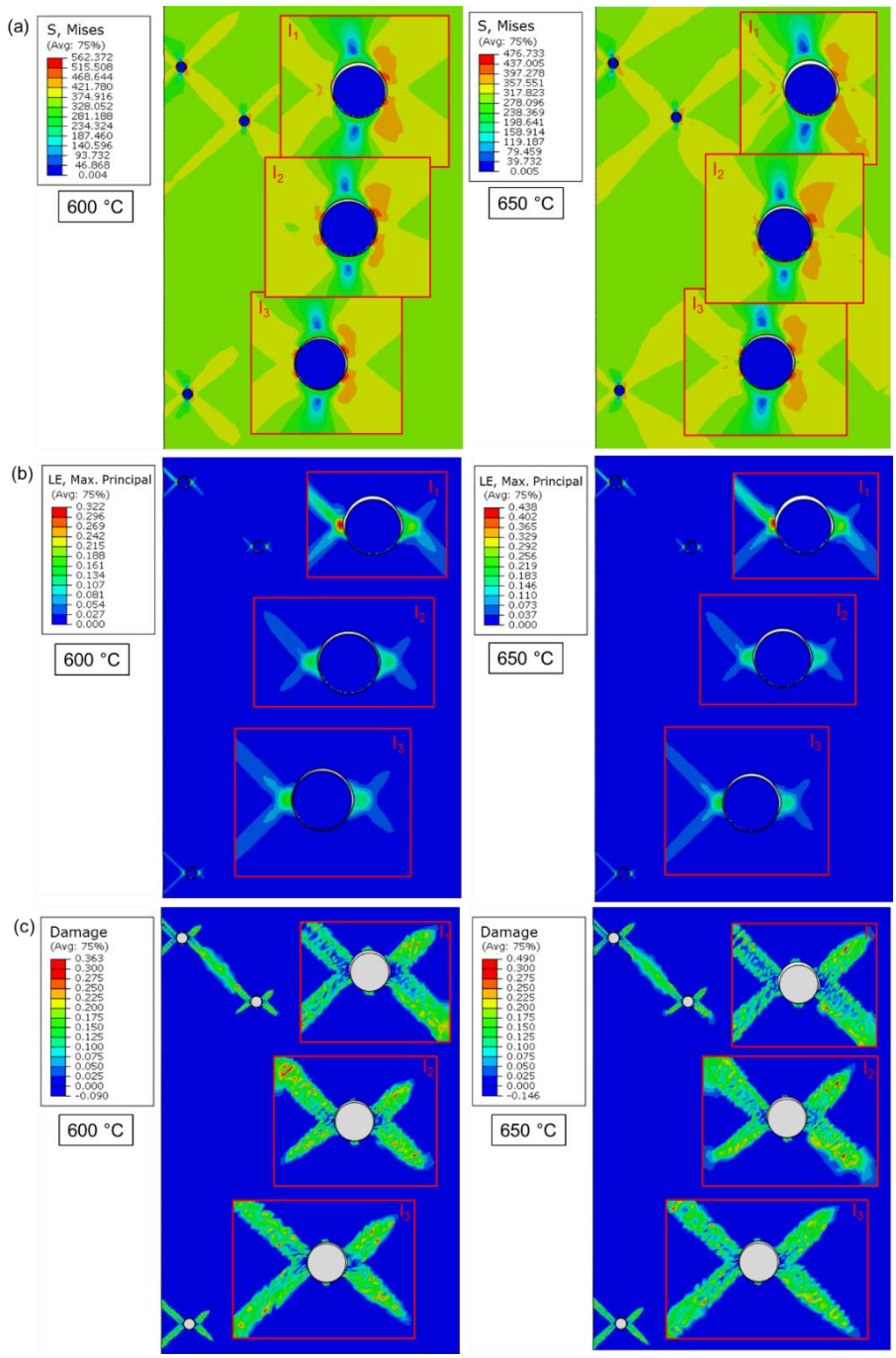

Figure 6.26 (a) von Mises stress (MPa), (b) maximum principal strain and (c) damage distribution around the inclusions in MarBN at 600 °C (left) and 650 °C (right) after 40 cycles ($\dot{\varepsilon}$ = 0.1 %/s and $\Delta\varepsilon$ = ± 0.5%).

Figure 6.27 examines the effect of zero strain, compression and tension, in terms of the MPS distribution and decohesion of the inclusion from the matrix, around inclusion I_1 at 600 °C and 650 °C after 40 cycles.

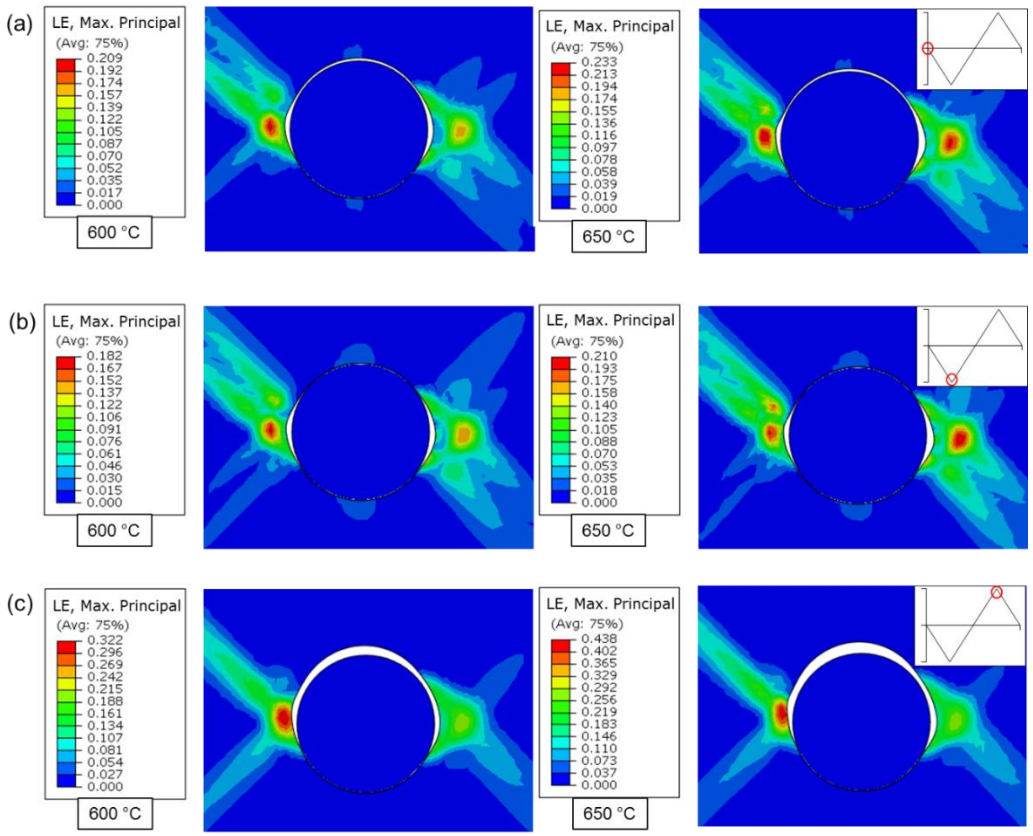

Figure 6.27 Maximum principal strain distribution around inclusion I_1 at 600 °C (left) and 650 °C (right) under (a) zero strain, (b) compression and (c) tension loading at N = 40.

6.6 Discussion

6.6.1 General

Chapter 3 and Chapter 4 identified manufacturing defects as key contributors to fatigue crack initiation and propagation, in terms of both location and geometry. Two modelling methodologies (coupled and uncoupled) have been presented in this chapter to quantify the effect of voids and inclusions in MarBN, based on localised stress and strain distributions, damage and cycles to fatigue crack initiation.

6.6.2 Uncoupled Methodology

From the contour plots presented in Figure 6.4 to Figure 6.7, multiaxial strain distributions are shown to occur around the defect, and strain redistribution occurs for the larger void and inclusion sizes with increasing cycles. Matrix deformation around a void, due to strain accumulation and material softening, is observed at later stages, whereas the presence of a fully bonded inclusion impedes deformation and produces

increased localised stresses and strains, compared to a void. The accumulation of such large strains in this region (SNCF up to ≈ 10 in Figure 6.8), as a result of strain accumulation, will inevitably lead to crack initiation and propagation.

Ratchetting, as a result of a non-zero mean stress, both at the interface and in the surrounding area, is shown to be highly complex for a void, varying from compressive to tensile as redistribution of the MPS location occurs, and is further complicated due to large cyclic softening of the 9Cr steel. Lower stress rates and combined creep-fatigue loading, more typical of plant conditions, have been found to increase the non-zero mean stress and ratchetting rate [210,211]. It should be noted that the Armstrong-Frederick model has been found previously to over-predict ratchetting [86,192,212,213], and future work may investigate the use of alternative kinematic hardening models, such as Ohno and Wang [214] for uniaxial and multiaxial applications. Nevertheless, the occurrence of localised ratchetting is further motivation to reduce the size and distribution of inhomogeneties in plant components. MarBN is a strain-rate dependent material at high temperature [9]; however, in terms of notched specimens, variation of stress triaxiality (Figure 6.9) was found to have the greatest influence on fracture strain, with negligible observed dependency on strain-rate, as observed experimentally for a broader range of strain-rates than those examined here [196,215–217].

Decohesion of inclusions near the gauge length is commonly observed experimentally in MarBN samples as a result of HTLCF testing (Chapter 3); therefore, modelling of inclusions, both with and without decohesion, is performed to understand the influence of this phenomena. For thick section components in plant, where inclusions are assumed to be more isolated from the surface, a fully bonded model is a better representation; whereas inclusions in thin-walled components (closer to the surface) are more likely to experience decohesion. Figure 6.10 presents results for the debonded case, and behaviour more similar to a void is predicted in terms of the MPS distribution. However, stresses and strain are elevated (compared to a void) and somewhat decreased compared to a fully bonded inclusion, as softening of the matrix material leads to reduced contact between the matrix and inclusion during fatigue loading, similar to the predicted void deformation.

The results shown here clearly indicate significant localised cyclic plasticity and ratchetting phenomena due to voids and inclusions in MarBN in all cases. In order to

estimate the effects of these phenomena on crack initiation, ratchetting and Coffin-Manson LCF cycles to crack initiation have been estimated for the void and inclusion models (Figure 6.11). The present models predict a dominant cyclic plasticity effect, despite the significant ratchetting and strain accumulation. The LCF void and inclusion crack initiation lives are ~19% and ~12%, respectively, of measured total life. Note that total experimental life, $N_{\mathrm{f}}^{\mathrm{exp}}$, for the present cyclic softening material, is defined as a 20% load drop from the end of primary softening [9]. Ratchetting further reduces local cycles to crack initiation by ~1% to 2% for voids and inclusions. The effects of ratchetting, stress triaxiality and multiaxial failure strain, in conjunction with void or inclusion diameter, distribution and loading indicate the complexity of this problem and resulting effect on fatigue life. Therefore, the reduction and elimination of manufacturing defects is a priority for increased resistance to fatigue crack initiation of power plant materials and components.

6.6.3 Coupled Methodology

To describe the continually evolving response of advanced materials at high temperature, a unified cyclic viscoplastic model has been modified to include damage and Ostergren multi-axial life prediction, as per Section 6.3. The hyperbolic sine flow rule allows the strain-rate effect at high temperature to be predicted from a single set of material parameters (Figure 6.14), as well as providing the ability to extrapolate to more common plant loading conditions. The damage model does not require a damage initiation threshold, as implemented in alternative models [218,219] and the material parameters required to predict cycles to failure and damage can be identified from the existing test data for calibration and validation of the cyclic viscoplastic material parameters. This model has been shown to accurately predict the uniaxial fatigue life of MarBN at 600 °C and 650 °C, generally within ±15% (Figure 6.16).

The ability to accurately model inclusions provides a greater understanding of what causes crack initiation and failure around these discontinuities. Figure 6.17 depicts the predicted MPS distribution around a single inclusion at the centre of a MarBN matrix, across different applied strain-ranges at 200 cycles. Substantial strain accumulation and redistribution is predicted to occur as the strain-range is increased. A strain concentration factor, defined here as the ratio of maximum local plastic strain-range to nominal applied strain-range, is approximately 2.5 in all cases after 200 cycles. The

evolution of damage (up to 200 cycles) is examined in Figure 6.19, and is predicted to initiate at the root of the inclusion-matrix interface and propagate perpendicular to the primary loading direction. A number of factors influence the complex distribution of damage around the inclusion, namely (i) the distribution and accumulation of strain, varying during tension and compression loading, (ii) shear band formation, (iii) cyclic softening and (iv) decohesion. Similar results are predicted at lower strain-ranges, but the area over which damage occurs is reduced. Cracking is predicted to occur in less than 150 reversals in all cases (Figure 6.20), with little difference in the predicted behaviour of the material at 600 °C and 650 °C; the main difference is a reduced maximum stress and an increase in plastic strain at higher temperatures, ultimately resulting in similar predictions for cycles to crack initiation.

A comparison of both the coupled and uncoupled life prediction methodologies (Figure 6.21 and Figure 6.22) indicate similar strain distributions in the region surrounding the inclusion, with a more localised stress concentration as a result of coupled damage. An increase in maximum strain occurs when damage and life prediction are included, in conjunction with greater stress degradation with cycles (Figure 6.23). As a result, the predicted number of cycles to crack initiation using the coupled method is reduced compared to the uncoupled method (Figure 6.24), and indicates the importance of not only a realistic constitutive model, but also the capability to predict damage accumulation and crack initiation in a continually evolving multi-axial model, where all stress and strain components are accounted for.

6.6.4 Multi-Inclusion Modelling

Extensive secondary cracking (greater than 0.5 mm) is observed in a post-HTLCF test MarBN sample around multiple inclusions (Figure 6.25(a)), as a result of static fracture at room temperature. Although SEM only provides a 2D slice of the sample, it is a valuable tool in understanding the influence of such discontinuities in the absence of 3D analysis methods. 2D material modelling of a similar geometry (Figure 6.25(b)) is performed to provide a greater insight into the influence of multiple inclusions, clustering and location. The high stress and strain concentrations (Figure 6.26(a) and Figure 6.26(b)) around each of the inclusions result in significant damage accumulation within 40 cycles (Figure 6.26(c)). In Figure 6.26(a) and Figure 6.26(c), a connection between inclusions I_1 and I_2 is predicted in terms of stress and damage distribution,

similar to the cracking observed experimentally. The close proximity of I_1 to I_2 leads to a further increase in stress and strain concentrations in this region at 600 °C. The stresses are reduced in the model at 650 °C, but the strains are further increased due to a higher rate of ratchetting, resulting in a similar damage distribution that both propagates towards the surface and predicts a link between inclusions I_1 and I_2. Experimentally, significantly longer crack propagation is observed around inclusion I_3 after nearly 850 cycles. This may be due to the complex shape of the inclusion and interaction between out-of-plane inclusions in the matrix, indicating the significance of shape on crack behaviour. This will be investigated in greater detail in Chapter 7.

The effect of different loading cases on inclusion I_1 (Figure 6.27) predicts that, under zero strain and after 40 cycles, decohesion of the matrix perpendicular to the primary loading direction will produce strain accumulation and redistribution. Although, quantitatively, similar predicted concentrations are observed for compression and tension loading (Figure 6.27(b) and Figure 6.27(c)), the levels of strain and decohesion are significantly greater under tension, slightly more so at 650 °C, as the material becomes more ductile. Irregular deformation of the surrounding MarBN material is observed, particularly in tension (Figure 6.27(c)), highlighting the influence of defect location on material deformation and void growth. The predicted levels of strain accumulation are substantially higher than for the single inclusion case, exceeding the experimentally measured uniaxial failure strain (18%) in all cases after 40 cycles, indicating the effects of location and clustering of inclusions in a matrix. This also leads to increased void formation and reduced effective matrix area capable of withstanding damage, and indicates the detrimental interaction effects of a limited number of inclusions, with dimensions even as small as 20 μm.

6.7 Conclusions

The key conclusions of this chapter are as follows:

- Application of a unified cyclic viscoplastic UMAT to void and inclusion geometries in a MarBN matrix, under HTLCF loading, predicts (i) large cyclic strain accumulation due to ratchetting at voids and inclusions (SNCF ≈ 10), (ii) significant and cyclically-evolving strain localisation in the region of defects (regardless of size), and (iii) high localised triaxiality ratios, particularly at inclusion-matrix interfaces, leading to reduced local material ductility.

- Development of a multi-axial fatigue life and damage accumulation model, in conjunction with a unified cyclic viscoplastic UMAT, allowing combined simulation of cyclic softening (due to microstructural degradation) and fatigue damage accumulation based on the current material response in that cycle.
- The presence of manufacturing defects is predicted to have a detrimental effect on cycles to crack initiation (less than 10% of total life). Size is not predicted to significantly affect initiation life; the key effect is the presence of voids or inclusions.

7 FATIGUE DAMAGE MODELLING OF MANUFACTURING DEFECTS IDENTIFIED VIA μCT SCANNING

7.1 Introduction

This chapter uses the cast and forged manufacturing defects, identified by micro-computed tomography (μCT) scanning (Chapter 4), and the Ostergren critical-plane fatigue damage user-material (UMAT) subroutine (Chapter 6), to predict crack initiation of MarBN high temperature low cycle fatigue (HTLCF) samples and realistic component geometries. The UMAT is extended for 3D applications here, and voxel representations of manufacturing defects allow high quality mesh generation, based on experimentally identified defect geometry and volume fraction.

7.2 Model Development

7.2.1 Introduction

Modelling of the experimentally identified defect distribution is impractical due to the significant meshing difficulties associated with multiple complex geometries, as well as the resulting mesh density necessary to accurately capture the geometry. As a result,

two methodologies have been developed here to create representative voxel models of cast and forged manufacturing induced defects in (i) HTLCF samples, tested at NUI Galway, and (ii) a valve chest sub-section (a typical plant component for cast martensitic steel). The volume fraction of manufacturing defects in the as-received material has been identified, via reconstruction of 3D X-ray µCT scanned HTLCF samples, as 0.03% and 0.002% for cast and forged MarBN, respectively.

7.2.2 Voxel-Type Defect Model Development

Figure 7.1 describes the process used for 3D model development of the cast and forged HTLCF gauge length models, whereby, in Abaqus, an STL of the largest defects (as per Figure 4.13(c)) is overlaid on a solid model of the HTLCF gauge length. Hexahedral meshing of the solid cylinder, to an element size of 40 µm (due to computational limitations) is performed and an input file is generated. A MATLAB code, implementing the nearest neighbour algorithm, has been written to identify overlapping regions between the solid cylinder model and defects. This data is written to an input file, in the form of voxel-type defects, and converted to an STL. In Autodesk Netfabb, Boolean subtraction of the voxel-type defects from the cylinder is performed. In NetGen, the cylinder (containing defects) is re-meshed to reduce the number of elements in regions away from the defects. Finally, material properties, loading and boundary conditions are applied in Abaqus. Material properties identified for MarBN at 600 °C (Chapter 5) are applied, as per the loading conditions applied to µCT scanned samples.

To model manufacturing defects in a sub-section model of a valve chest, as described in Figure 7.2, a Python script has been developed. This allows random distribution of unique manufacturing defects (as identified from 3D X-ray µCT scanning and modelled in the HTLCF geometries) throughout the solid model (in the Assembly module of Abaqus), based on a given volume fraction. Each translated instance is assigned a translation vector; however, this is not applied to the node data in the input file. Therefore, a MATLAB model to apply this translation to each node has been developed and applied here. The nearest neighbour analysis and following steps are then performed, as per Figure 7.1. The material properties for MarBN at 650 °C are applied to the valve chest sub-section (Chapter 6) to represent the maximum ultra-supercritical (USC) temperatures the component would experience. Although inclusions were found to further increase factors such as strain concentration factor (SNCF) (Figure 6.9(b))

and triaxiality ratio (Figure 6.10(b)) compared to voids, in this chapter, all manufacturing defects (including inclusions) are treated as voids due to the difficulties associated with modelling inclusion-matrix contact in Abaqus (Standard). Such issues include, for example, overclosure and penetration of nodes due to dissimilar meshes, inaccurate application of force and non-convergence, and increased mesh density and iterations, leading to longer analysis time [220].

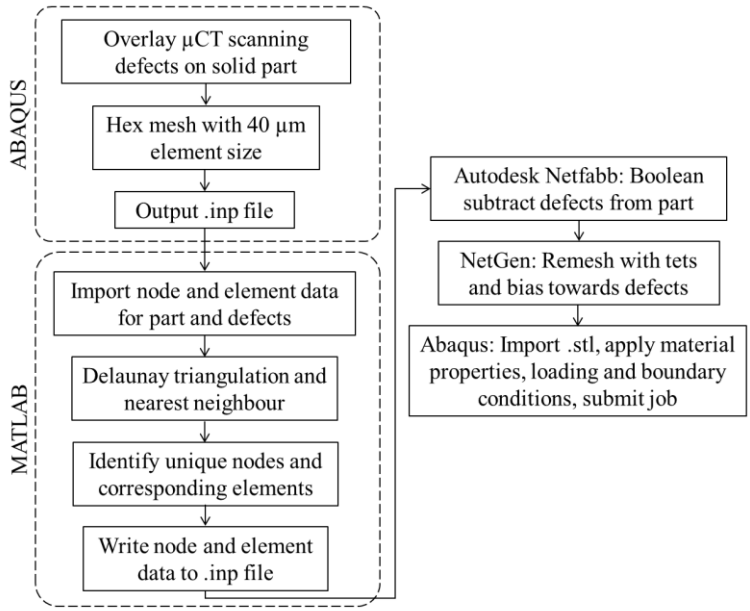

Figure 7.1 Flowchart for development of HTLCF geometry and valve chest sub-section Abaqus models, based on manufacturing defects identified via 3D X-ray µCT scanning.

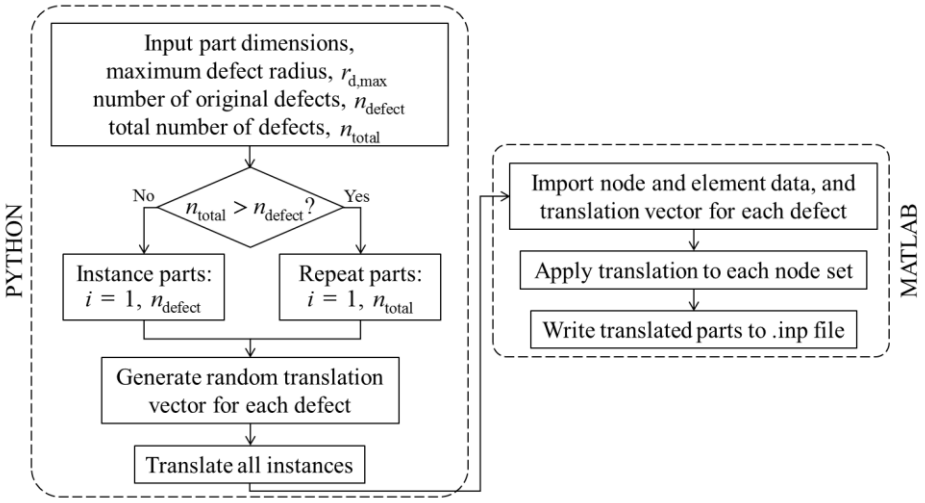

Figure 7.2 Flowchart for random distribution of defects in the Assembly module of Abaqus, and translation of each instance to create a part in Abaqus.

Figure 7.3 describes the boundary conditions applied to the cast and forged HTLCF models. In Figure 7.4, a comparison of the defects overlaid on the solid geometries can be seen, and the resulting refined mesh, with voxel-type defects for the cast (Figure 7.4(a)) and forged (Figure 7.4(b)) models. A defect-free model of the same geometry is also simulated for comparison.

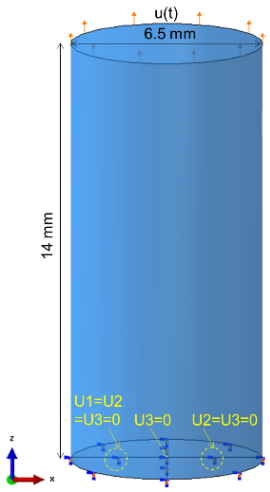

Figure 7.3 Boundary conditions applied to the HTLCF geometry for cyclic loading.

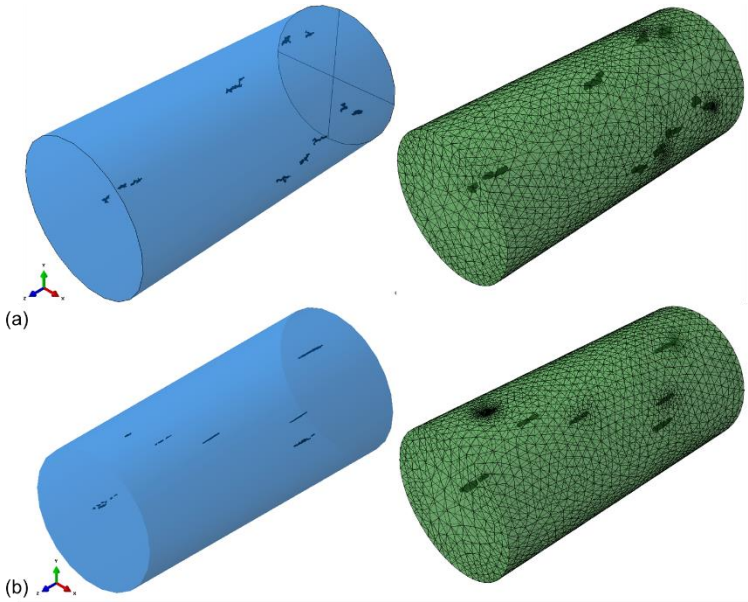

Figure 7.4 Experimentally-identified manufacturing defects overlaid on the solid model (left) and refined mesh with voxel-type defects (right) for (a) cast and (b) forged MarBN.

An image of a valve chest is shown in Figure 7.5(a), with the corresponding Abaqus model and 0.1° sub-section, highlighted in Figure 7.5(b). The loading and boundary conditions, as part of a cylindrical coordinate system, are described in Figure 7.5(c). In

Figure 7.6, defects (cast and forged) identified via 3D X-ray µCT scanning are randomly distributed throughout the sub-section (using a Python script), and compared to the voxel-type model. The forged defects are modelled in the direction of forging (Figure 7.6(b)), as well as rotated at 90° (Figure 7.6(c)) to investigate the influence of defect orientation in relation to cyclic loading. Once again, a defect-free model was simulated for comparison. Table 7.1 summarises the various models presented in this chapter, based on defect type, and the volume fraction of defects as a result of the voxel-type modelling methodology. In all cases, the volume fraction of defects is increased, in respect to the experimentally identified values for cast and forged MarBN, due to element size. However, they are in line with those identified by Hardin *et al.* [128] for cast steel (up to 0.587%), using radiographic analysis.

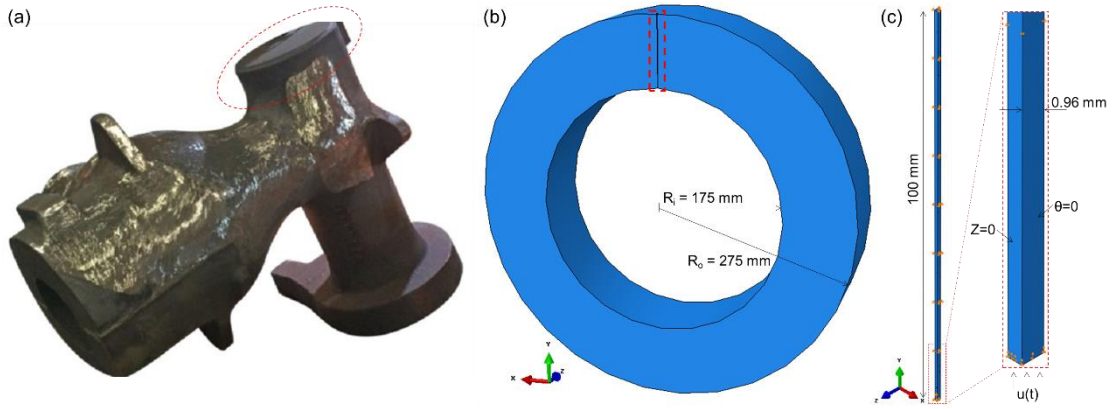

Figure 7.5 (a) Valve chest (pre-machining) [221], (b) Abaqus model with 0.1° sub-section highlighted (red box), and (c) sub-section dimensions, loading and boundary conditions.

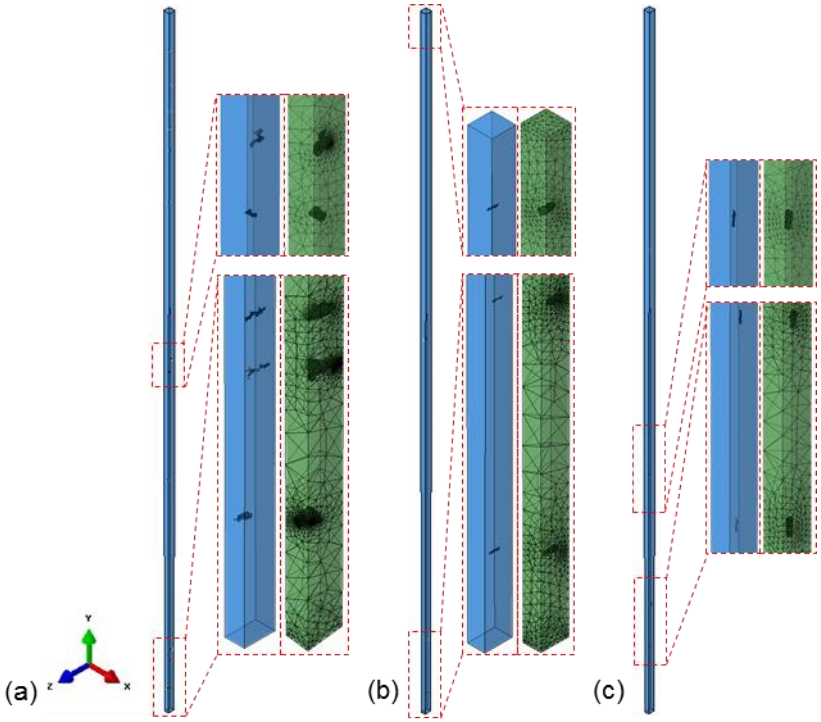

Figure 7.6 Sub-section model of the valve chest showing defects overlaid on the solid geometry and the resulting voxel representative mesh for (a) cast, (b) forged and (c) forged (90°) defects.

Table 7.1 Summary of the models presented in this chapter, the corresponding defect type and volume fraction of defects.

Model	**Defect Type**	V_f **(%)**
HTLCF	Defect-Free	0
	Cast	0.069
	Forged	0.026
Valve Chest	Defect-Free	0
	Cast	0.345
	Forged	0.047
	Forged (90°)	0.047

7.2.3 Mesh Refinement

The methodology described in the previous section allows for significant reduction in the number of elements in each model. Four-node tetrahedral elements (C3D4) are used in all cases, and the number of elements in each model (before and after refinement) is presented in Table 7.2, based on an original hexahedral element size of 40 µm. Further refinement of the original mesh (i.e. below 40 µm), to increase the geometric accuracy of the voxel-type defects, would result in even greater mesh densities than those presented here (~8.8 million and 1.2 million for the HTLCF geometry and valve chest sub-section, respectively). Such mesh sizes are unrealistic for simulation of cyclic loading of components, particularly in conjunction with a cyclic viscoplastic UMAT. Therefore, the ability refine the mesh, by over 90% in all cases, to generate both test samples and component geometries containing experimentally identified defects, is of great benefit for a broad range of applications. Mesh refinement (and bias towards defects) is performed using NetGen, and verification of mesh quality (warning and error free) is performed in Abaqus, based on standard shape factor and aspect ratio values.

Table 7.2 Number of elements in each original model (40 µm element size) and the refined model.

Model	Defect Type	Original Mesh	Refined Mesh	Reduction (%)
HTLCF	Cast	8,780,800	515,456	94.1
	Forged		201,422	97.7
Valve Chest	Cast	1,200,000	100,195	91.7
	Forged		72,826	93.9
	Forged (90°)		71,336	94.1

7.3 Results

7.3.1 High Temperature Low Cycle Fatigue Geometry

Due to the difficulties associated with viewing internal features using contour plots in Abaqus, the use of iso-surface plots, which produce a three-dimensional representation of a surface of constant value points, have instead been employed in this chapter to better describe the localised effect of manufacturing defects.

Figure 7.7 presents iso-surface plots of von Mises stress, concentrated at manufacturing defects in the cast and forged samples. von Mises Stress is increased by ~49% and

~46% in the cast and forged models, respectively, compared to the defect-free model after two cycles. In Figure 7.8, iso-surface plots of maximum principal strain, localised in the region of cast and forged defects, is presented after two cycles. The SNCF for maximum principal strain is ~11 and ~3 for the cast and forged models. In terms of both stress and strain, the area of iso-surfaces in the region of casting defects are shown to be more widespread than in the forged model, increasing the likelihood of crack initiation due to casting defects. Propagation of the stress and strain iso-surfaces across ligaments between defects is also observed, when closely located.

In Figure 7.9, iso-surface plots of localised damage at cast and forged manufacturing defects is presented, after two cycles. The predicted maximum value of damage in the cast model (~0.27) is four orders of magnitude higher than that of the forged (~0.00009). Damage is predicted to propagate across the ligaments between defects, similar to the stress and strain iso-surface plots.

Figure 7.10 compares iso-surface plots of cycles to crack initiation in the cast and forged models, with plot limits applied from zero to 100 cycles. Once again, the effect of cast manufacturing defects is predicted to be significantly worse in terms of component degradation. Crack initiation is predicted to occur at every casting defect after the second cycle. In contrast, minor cracking is predicted to occur in the forged sample at only two of the defects (one located at the surface), after twenty-two cycles.

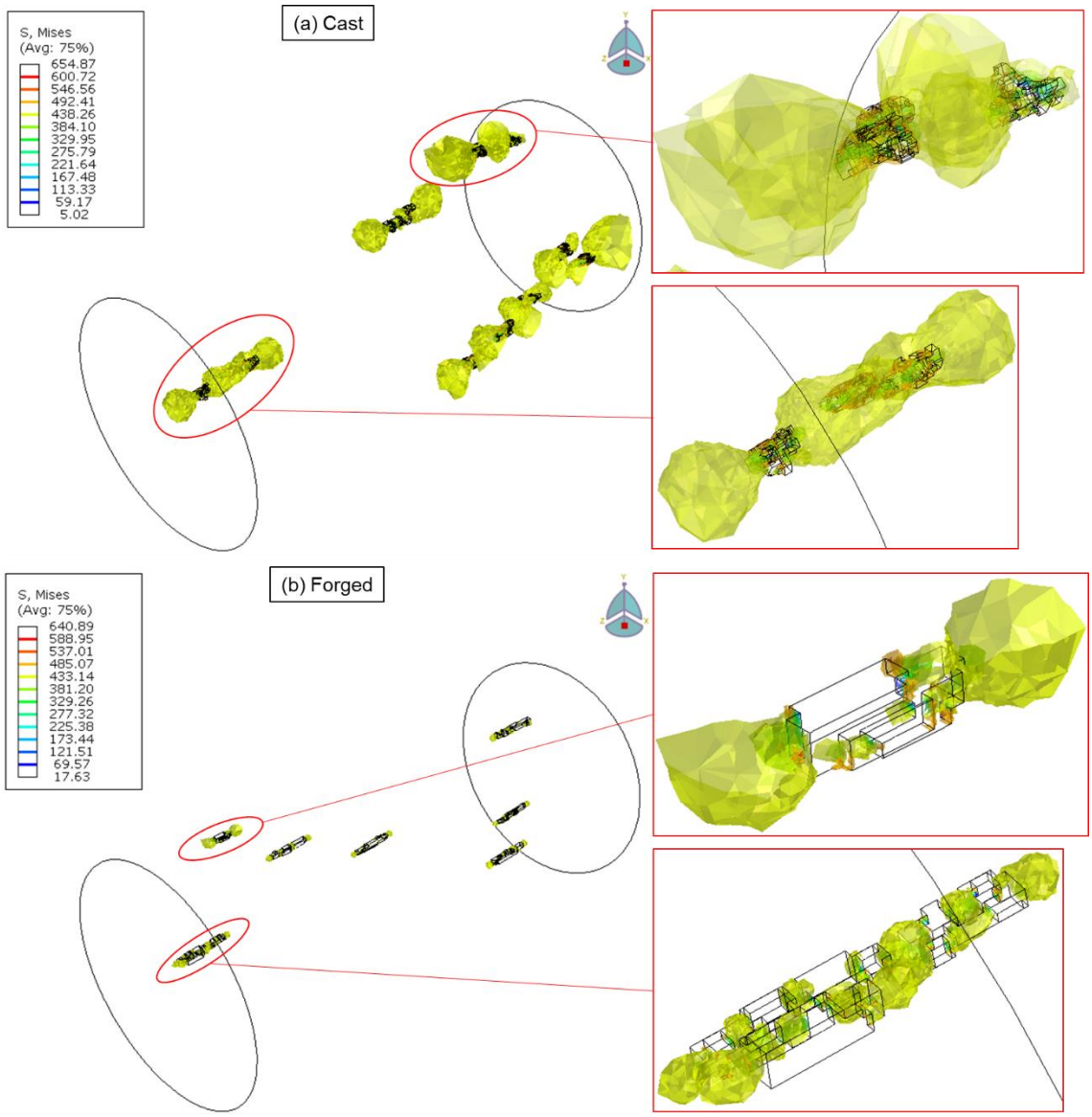

Figure 7.7 Iso-surface plot of von Mises stress (MPa) in (a) cast and (b) forged MarBN at 600 °C, $\dot{\varepsilon}$ = 0.1 %/s, $\Delta\varepsilon$ = ±0.5% and N = 2.

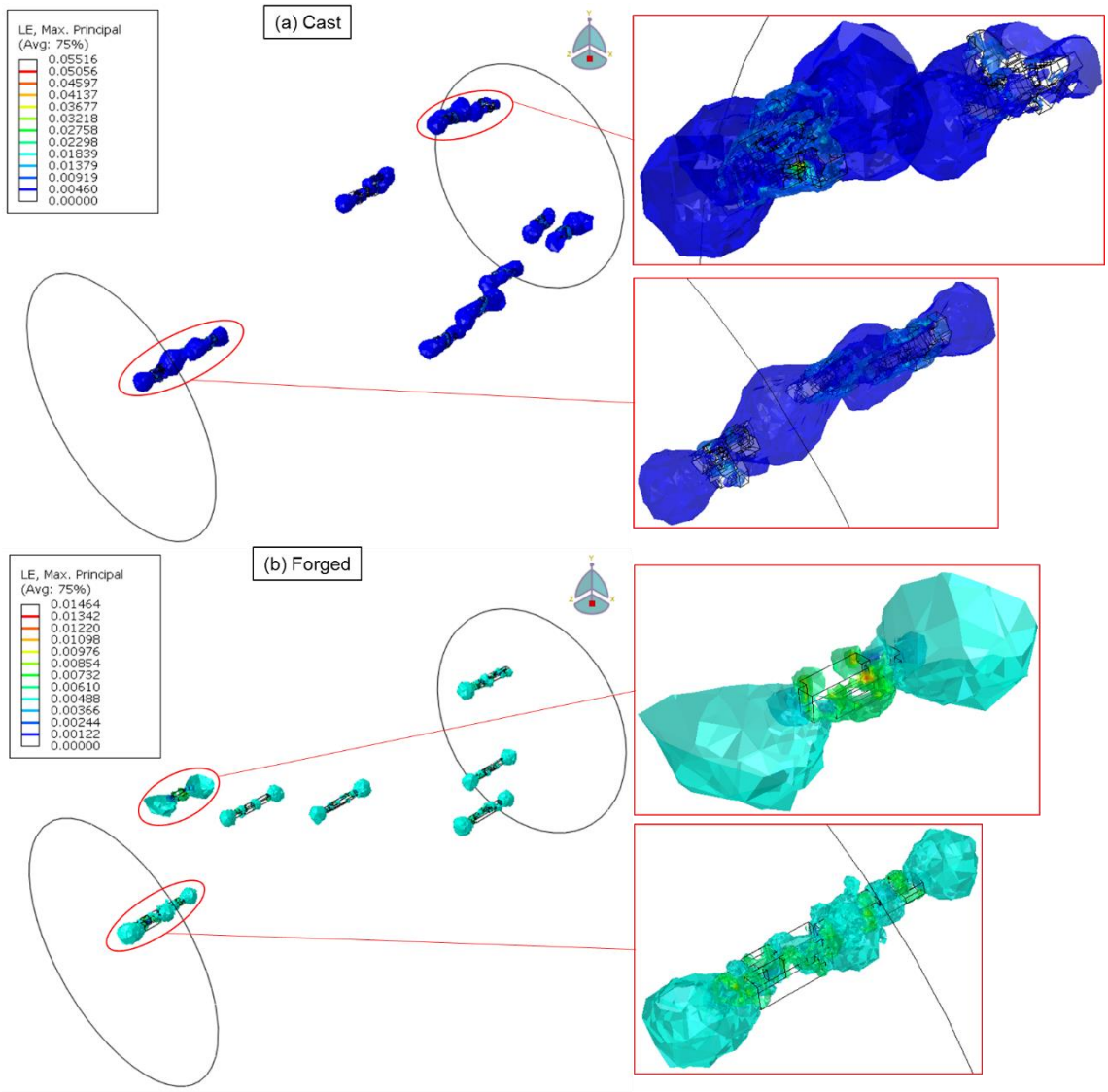

Figure 7.8 Iso-surface plot of maximum principal strain in (a) cast and (b) forged MarBN at 600 °C, $\dot{\varepsilon}$ = 0.1 %/s, $\Delta\varepsilon$ = ±0.5% and N = 2.

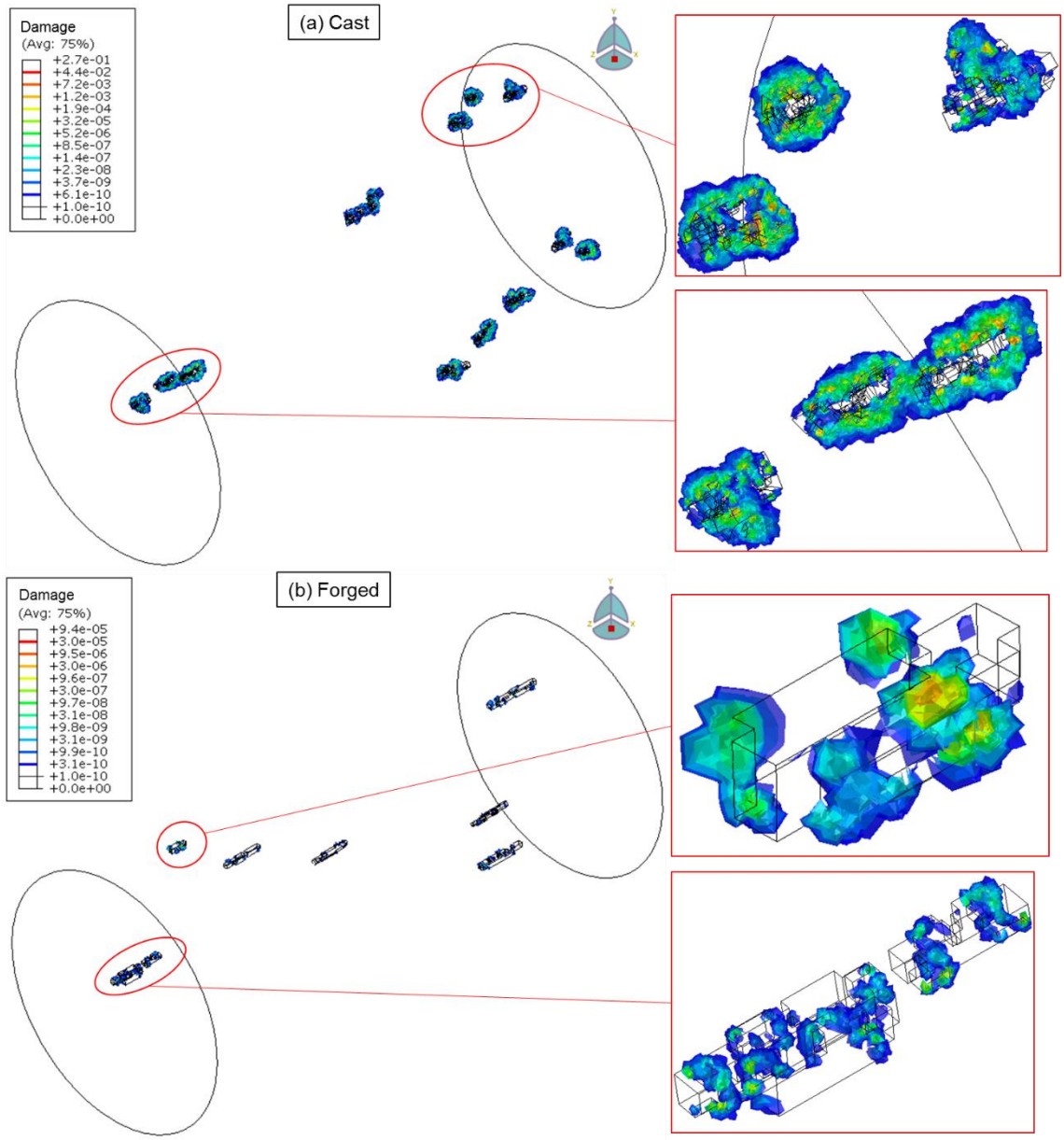

Figure 7.9 Iso-surface plot of damage in (a) cast and (b) forged MarBN at 600 °C, $\dot{\varepsilon}$ = 0.1 %/s, $\Delta\varepsilon$ = ±0.5% and N = 2.

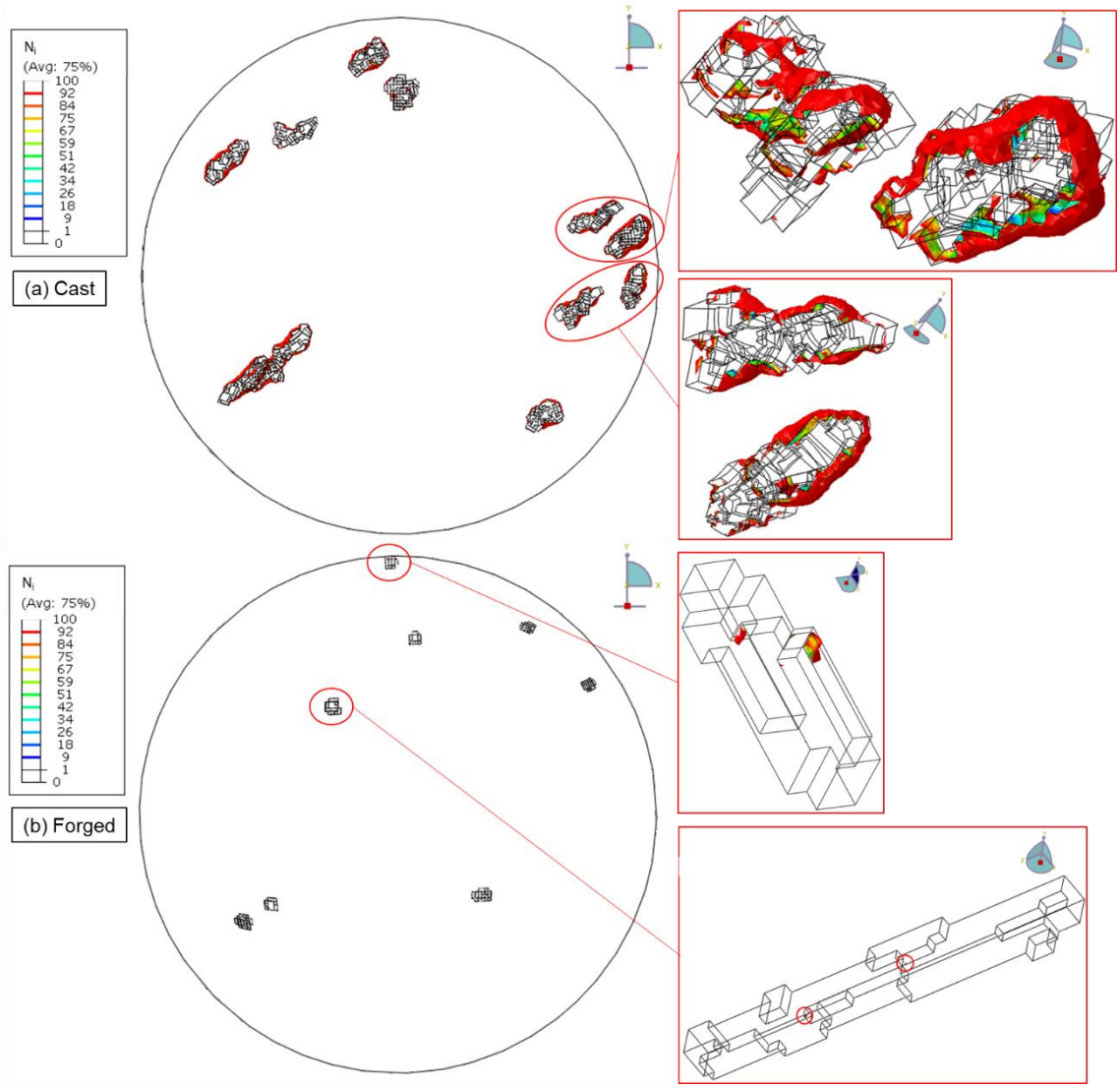

Figure 7.10 Iso-surface plot of cycles to crack initiation (limited from N = 0 to 100) in (a) cast and (b) forged MarBN at 600 °C, $\dot{\varepsilon}$ = 0.1 %/s, $\Delta\varepsilon$ = ±0.5% and N = 2.

Figure 7.11 is a symbol plot (i.e. magnitude and direction of vector or tensor variables at the integration point) of the maximum, intermediate and minimum principal stress and strain for the cast and forged MarBN models. The relative size of each arrow represents the magnitude of the result, and the direction relates to the global direction. Arrowheads pointing out indicate tensile loading, and the opposite occurs for compression. Manufacturing defects are shown to promote complex localised tensile and compressive out-of-plane loading.

Figure 7.12 compares the macroscale reaction force versus displacement, and stress versus strain, for the defect-free, cast and forged models during the initial cycle, with almost identical results in all cases. The predicted stress-strain response (Figure 7.12(b))

of each model is in agreement with the experimental data for Cast_02 (which underwent µCT scanning) also.

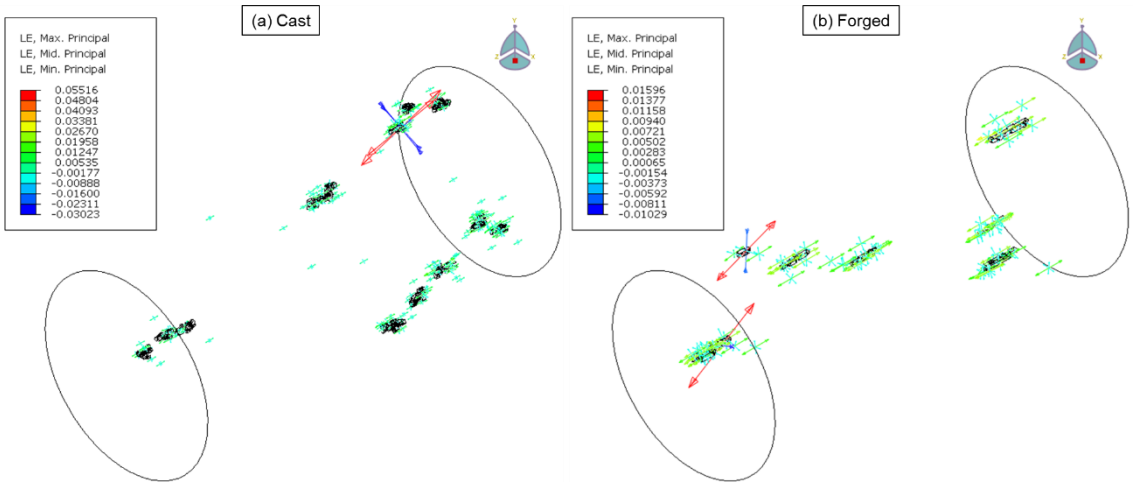

Figure 7.11 Symbol plot of maximum, intermediate and minimum principal strain in (a) cast and (b) forged MarBN at 600 °C, $\dot{\varepsilon}$ = 0.1 %/s, $\Delta\varepsilon$ = ±0.5% and N = 2.

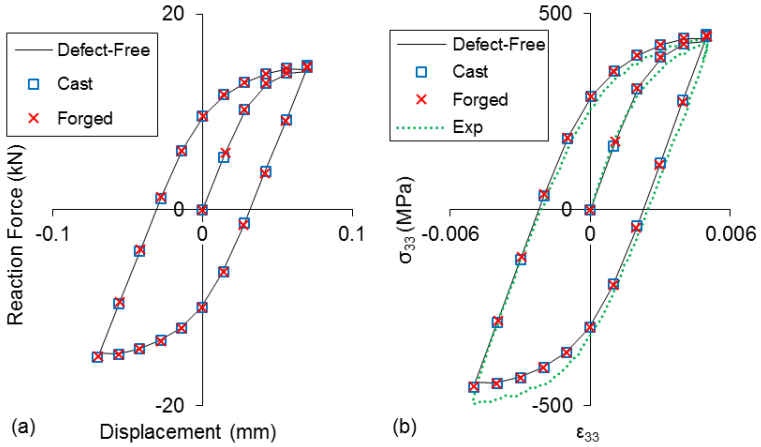

Figure 7.12 (a) Reaction force versus displacement and (b) stress versus strain, for the defect-free, cast and forged HTLCF models, with comparison to experimental data for Cast_02, at 600 °C, $\dot{\varepsilon}$ = 0.1 %/s, $\Delta\varepsilon$ = ±0.5% and N = 1.

However, in terms of the localised effect of defects, as presented in Figure 7.13, the stress-strain behaviour (taken at the location of maximum principal strain, one of the key areas for crack initiation) is significantly more complex for both the cast and forged models. A stress concentration factor (SCF) of ~6 and ~2, and a SNCF of ~10 and ~4 are identified for the cast and forged samples, respectively. Ratchetting is clearly observed in both samples in the shear y-z direction also. In Table 7.3, a summary of predicted cycles to crack initiation is presented for each model.

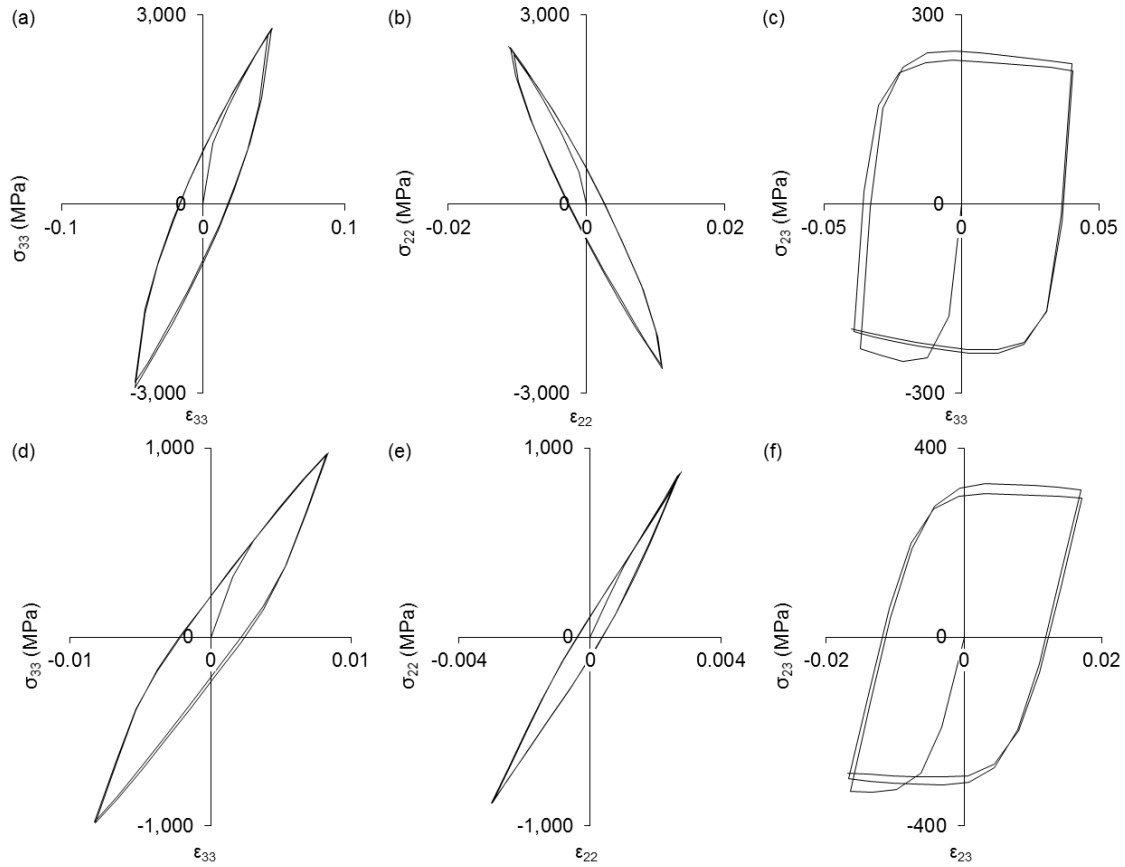

Figure 7.13 Stress versus strain in various loading directions at the location of maximum principal strain in the (a – c) cast and (d – f) forged MarBN models at 600 °C, $\dot{\varepsilon}$ = 0.1 %/s, $\Delta\varepsilon$ = ±0.5% and up to N = 2.

Table 7.3 Cycles to crack initiation for each HTLCF gauge length model, with corresponding volume fraction of defects.

Model	V_f **(%)**	N_i
Defect-Free	0	680
Cast	0.069	2
Forged	0.026	23

7.3.2 Valve Chest Sub-Section

In Figure 7.14 and Figure 7.15, iso-surface plots of the von Mises stress and maximum principal strain are presented for the cast, forged and forged (90°) samples, with a comparison to the defect-free model, after ten cycles. Overall, manufacturing defects are shown to increase the maximum stress and strain in the component, compared to a defect-free model. The greatest increase in von Mises stress occurs in the cast model (SCF ≈ 52%), followed by forged (90°) (~46%) and forged (~40%). In terms of maximum strain, the cast sample again has the highest level of strain in relation to the solid model (SNCF ≈ 5.7 times), then the forged (SNCF ≈ 3.5 times) and forged (90°) (SNCF ≈ 2.8 times).

Figure 7.16 shows iso-surface plots of localised damage at cast, forged and forged (90°) manufacturing defects after ten cycles, with the same maximum and minimum plot limits applied. As with the HTLCF geometry, the cast valve chest sub-section contains the highest level of damage, and as a result, leads to earlier and greater numbers of predicted crack initiation sites than the forged models. Figure 7.17 shows cycles to crack initiation for the cast, forged and forged (90°) models, highlighting the regions around manufacturing defects. The cast sample is predicted to have a broader region of cracking than that of either forged model.

In Figure 7.18, symbol plots of the predicted maximum, intermediate and minimum principal stress in the defect-free, cast, forged and forged (90°) MarBN models in a tensile state are presented. Once again, manufacturing defects are shown to cause complex localised stress and strain behaviour.

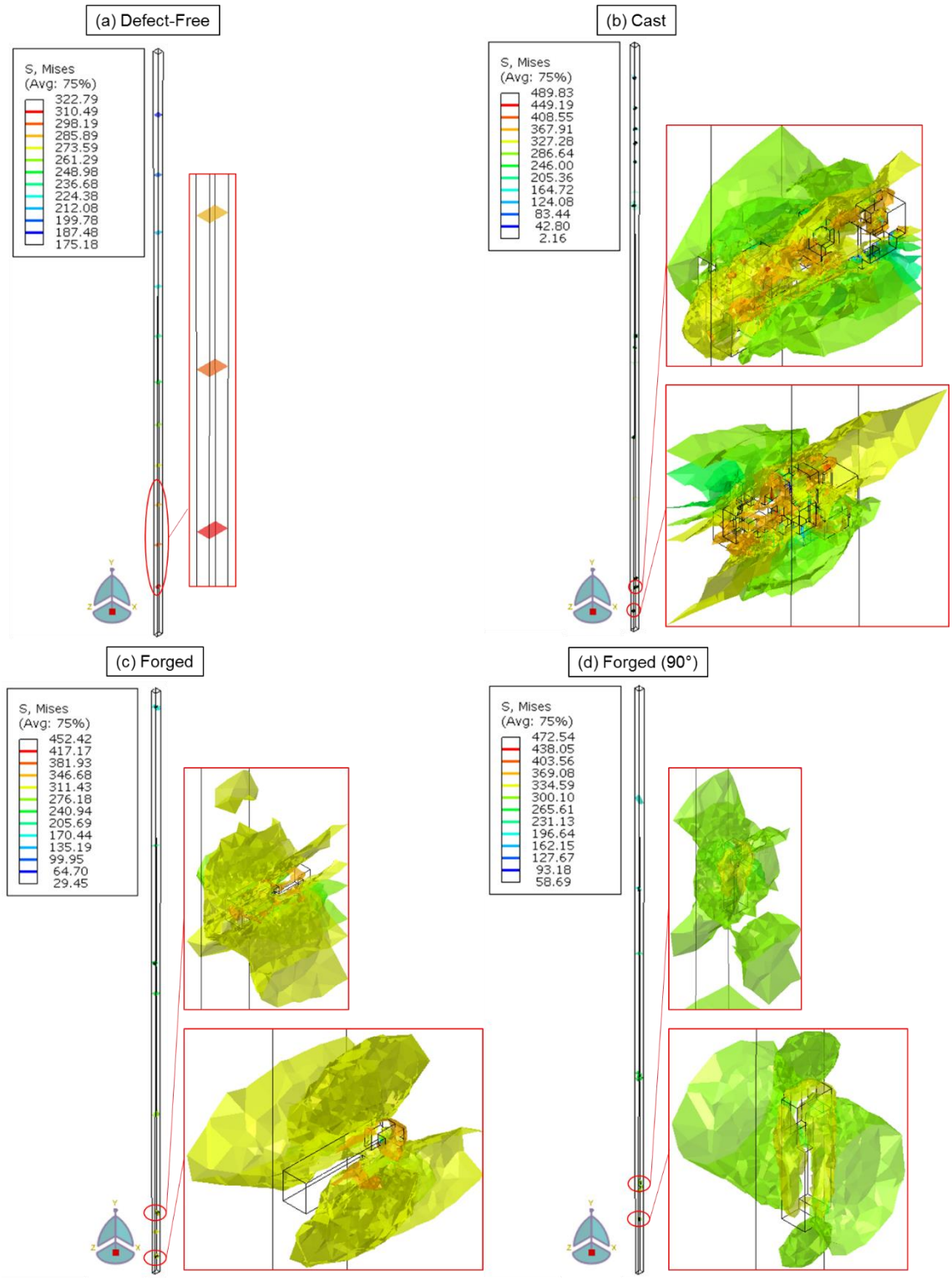

Figure 7.14 Iso-surface plot of von Mises stress (MPa) in the (a) defect-free, (b) cast, (c) forged and (d) forged (90°) MarBN model at 650 °C, $\dot{\varepsilon}$ = 0.1 %/s, $\Delta\varepsilon$ = ±0.5% and N = 10.

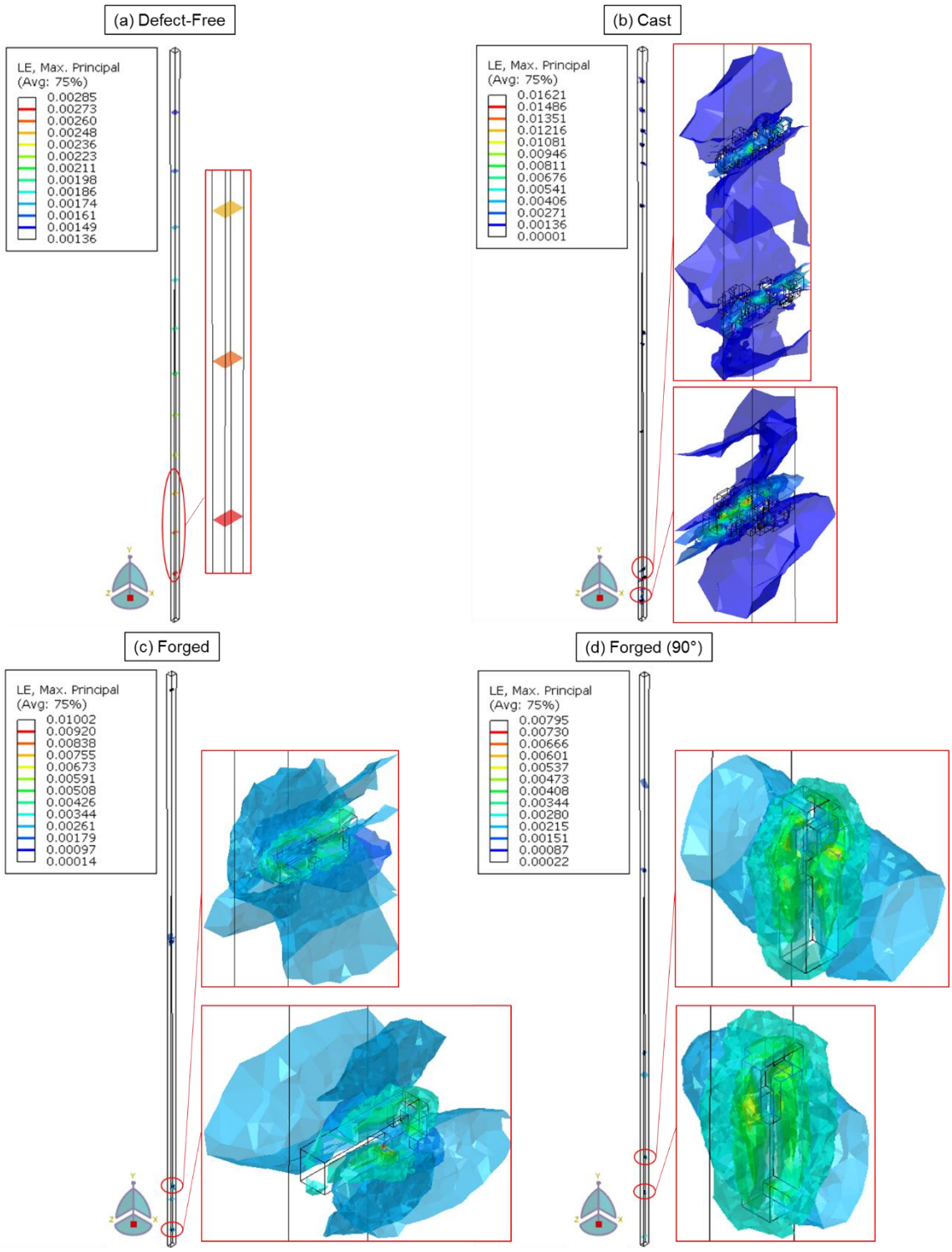

Figure 7.15 Iso-surface plot of maximum principal strain in the (a) defect-free, (b) cast, (c) forged and (d) forged (90°) MarBN model at 650 °C, $\dot{\varepsilon}$ = 0.1 %/s, $\Delta\varepsilon$ = ±0.5% and N = 10.

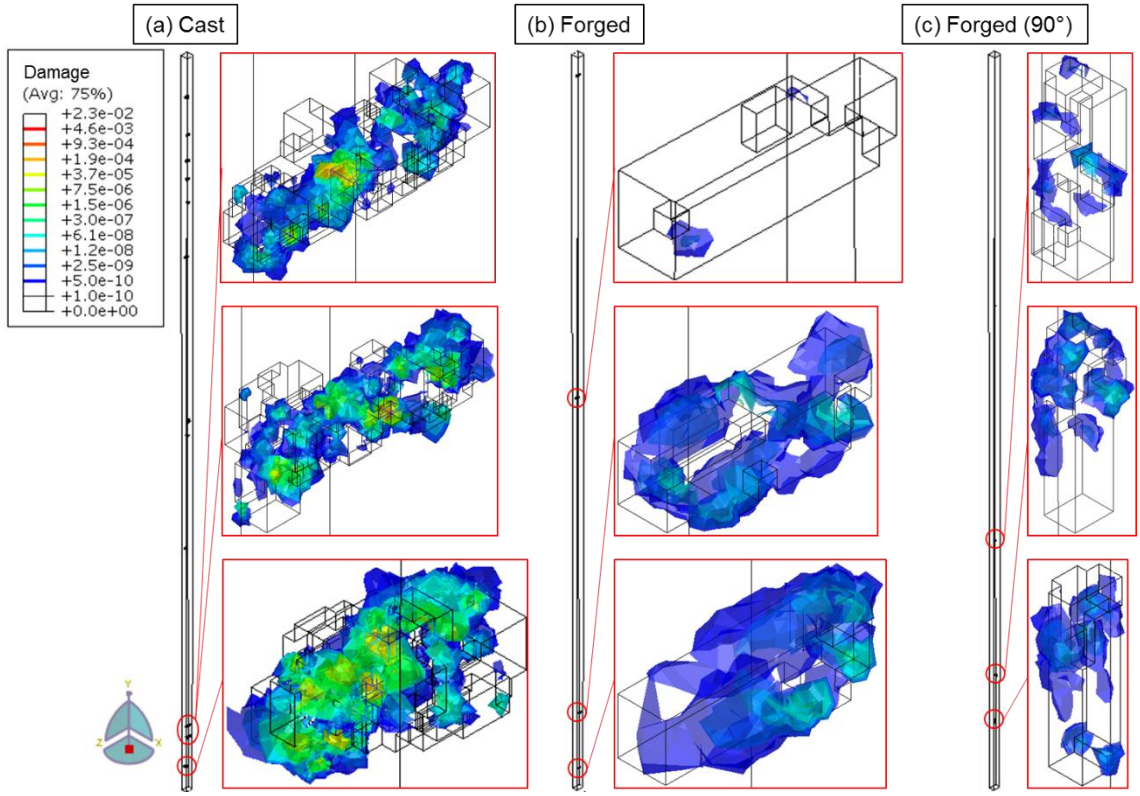

Figure 7.16 Iso-surface plot of damage in (a) cast, (b) forged and (c) forged (90°) MarBN at 650 °C, $\dot{\varepsilon}$ = 0.1 %/s, $\Delta\varepsilon$ = ±0.5% and N = 10.

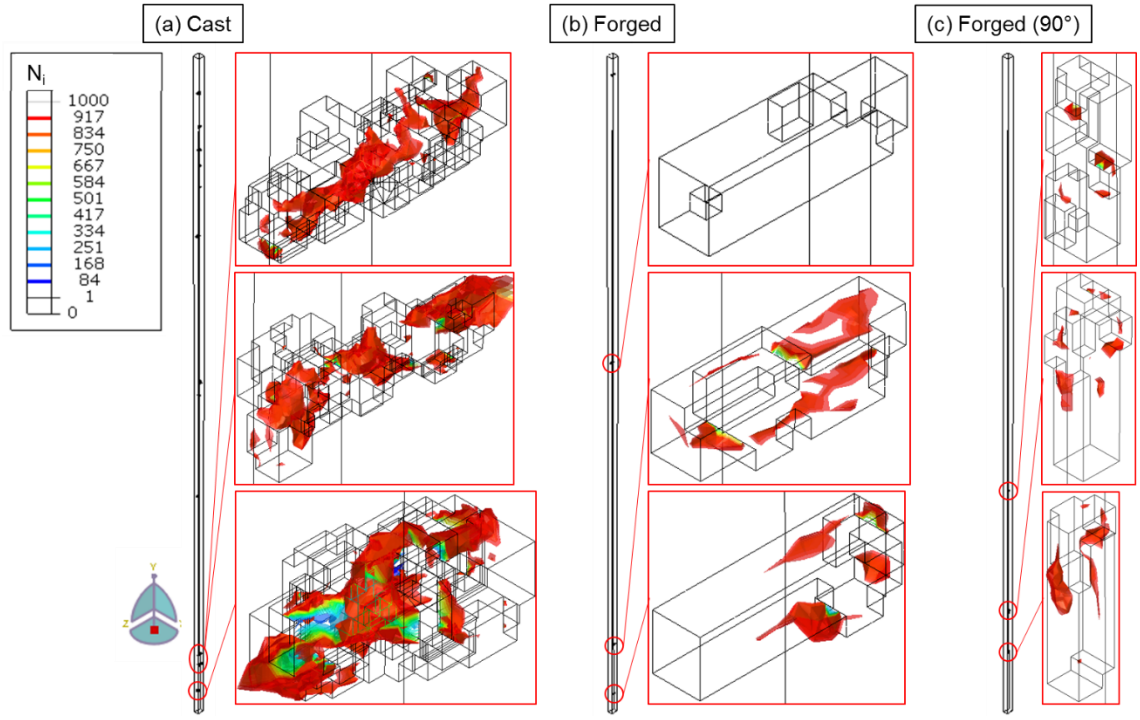

Figure 7.17 Iso-surface plot of cycles to crack initiation (limited from N = 0 to 1,000) in (a) cast, (b) forged and (c) forged (90°) MarBN at 650 °C, $\dot{\varepsilon}$ = 0.1 %/s, $\Delta\varepsilon$ = ±0.5% and N = 10.

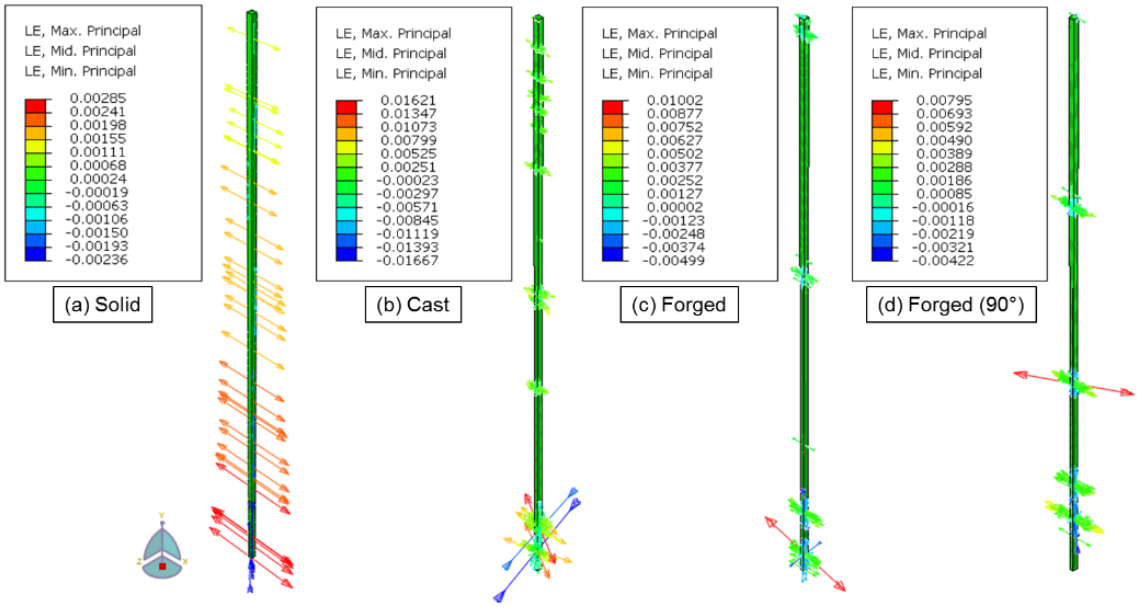

Figure 7.18 Symbol plots of maximum, intermediate and minimum principal strain in the (a) defect-free, (b) cast, (c) forged and (d) forged (90°) MarBN model at 650 °C, $\dot{\varepsilon}$ = 0.1 %/s, $\Delta\varepsilon$ = ±0.5% and N = 10.

Figure 7.19 depict macroscale stress versus strain for the defect-free, cast, forged and forged (90°) models, with identical behaviour in all cases. Plots of the localised stress-strain evolution are then presented (Figure 7.20 and Figure 7.21), at the location of maximum principal strain, in the cast, forged and forged (90°) models. Ratchetting is predicted in all models after ten cycles, particularly in the cast model. In Table 7.4, a summary of the number of cycles to crack initiation for each model is presented.

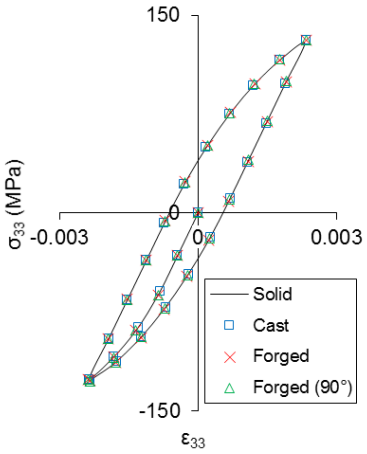

Figure 7.19 Stress versus strain for the cast, forged and forged (90°) valve chest MarBN models at 650 °C, $\dot{\varepsilon}$ = 0.1 %/s, $\Delta\varepsilon$ = ±0.5% and N = 1.

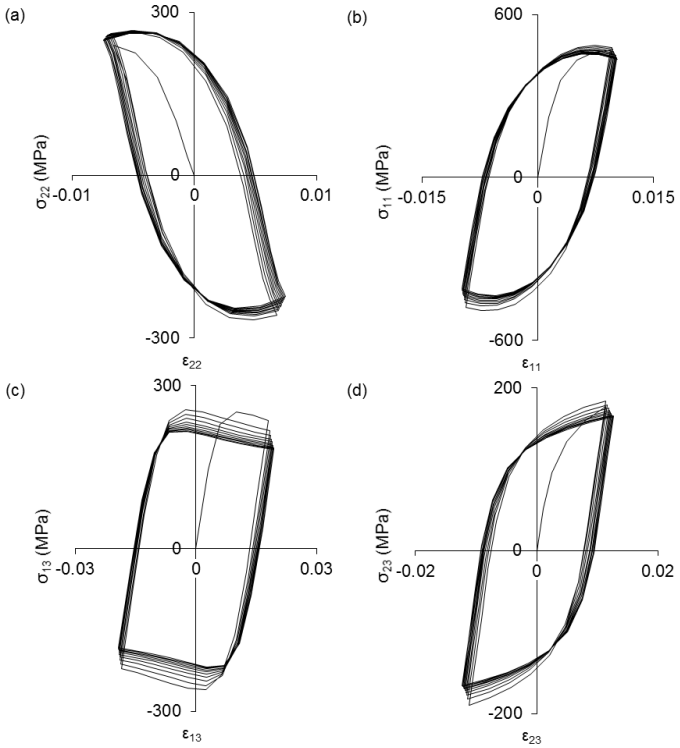

Figure 7.20 (a, b, c, d) Stress versus strain in various loading directions at the location of maximum principal strain in the cast MarBN model at 650 °C, $\dot{\varepsilon}$ = 0.1 %/s, $\Delta\varepsilon$ = ±0.5% and up to N = 10.

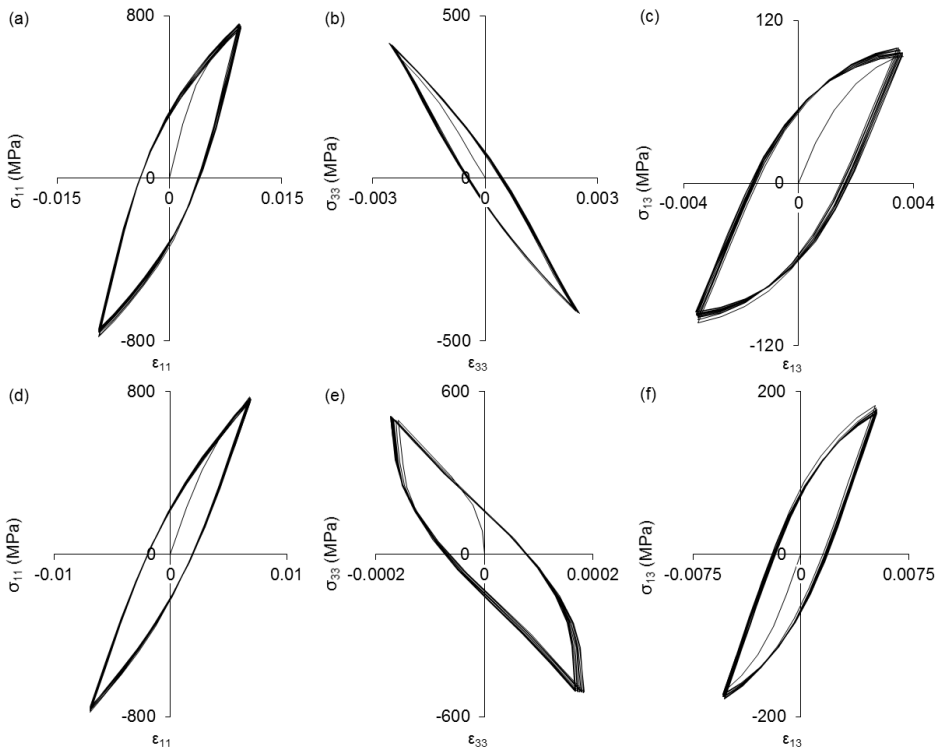

Figure 7.21 Stress versus strain in various loading directions at the location of maximum principal strain in the (a – c) forged and (d – f) forged (90°) MarBN models at 650 °C, $\dot{\varepsilon}$ = 0.1 %/s, $\Delta\varepsilon$ = ±0.5% and up to N = 10.

Table 7.4 Cycles to crack initiation for each valve chest sub-section model, with corresponding volume fraction of defects.

Defect Type	V_f **(%)**	N_i
Defect-Free	0	3,750
Cast	0.345	10
Forged	0.047	333
Forged (90°)	0.047	833

7.4 Discussion

7.4.1 Introduction

As was determined experimentally, the forged HTLCF life is approximately double that of the cast, despite very similar stress and plastic strain evolution, preceding sample failure (Figure 3.25). 3D X-ray µCT scanning was performed on cast and forged MarBN samples, before and after testing, to better understand the differences in the HTLCF performance of the materials (Figure 4.4 and Figure 4.9). In this chapter, advanced material modelling of complex manufacturing defects, identified as a result of 3D X-ray µCT scanning, in a HTLCF gauge length and valve chest sub-section model has been performed for MarBN at high temperature, in conjunction with an Ostergren critical-plane fatigue damage UMAT, for prediction of cycles to crack initiation and damage, to better understand the influence of complex (cast) and stringer-type (forged) defects under high temperature cyclic loading.

7.4.2 Methodology

Many attempts have been made to model manufacturing induced defects, using both mathematical and computational methods, with and without the use of computed tomography [129,133,222–226]. The key novelty of this chapter is the explicit modelling of manufacturing induced defects identified via 3D X-ray µCT scanning, and, in particular, investigation of the influence of defect geometry and resulting crack initiation and damage behaviour, based on two manufacturing methods i.e. casting and forging. A methodology has been developed to allow computational modelling of complex defect shapes and distributions, and has contributed to further understanding

the microscale mechanisms of degradation associated with the different types of cast and forged manufacturing defects.

A Python script was developed to generate random distributions of complex and unique defects throughout a plant component, based on a desired volume fraction; a key benefit is that 3D X-ray µCT scanning of each component is not required, particularly in the case of plant components, where scanning of the full part is unrealistic for such applications. Further initial mesh refinement, below 40 µm, in conjunction with increased computing power, would allow the topology of individual defects to be more accurately captured also. Nevertheless, the use of this methodology to create representative voxel-mesh geometries results in high quality mesh generation for analysis of complex components (i.e. without problems of poor element quality or element distortion). For example, this method could be extended to a superheater tube under oxidation or corrosion conditions [54], or a plant header under complex thermo-mechanical fatigue loading [227].

7.4.3 High Temperature Low Cycle Fatigue Sample Modelling

The role of spherical manufacturing defects in crack initiation was presented in Chapter 6 for MarBN at 600 °C and 650 °C. There are many benefits associated with 2D and 2D axisymmetric modelling, particularly due to reduced computational requirements; however, the out-of-plane loading occurring in the models presented in this chapter, for multiple complex defects distributed throughout a component (e.g. Figure 7.13), highlights the importance of 3D modelling in understanding microscale deformation mechanisms.

Significant localised stress and strain is predicted to occur in the region of all defects, particularly due to the increased complexity of defects in the cast sample (Figure 7.7 and Figure 7.8), resulting in ratchetting from the initial loading cycle. Similar strain concentrations to the cast model were predicted for a 30 µm spherical inclusion in an axisymmetric matrix in Figure 6.11 after 715 cycles; this highlights the significant effect of complex shaped geometries on the localised deformation of the matrix material in the initial loading cycles. Furthermore, calculation of the number of cycles to crack initiation is based on the full range of stress and strain-range components (whereas out-of-plane components would not be accounted for in 2D or 2D axisymmetric models),

and further contributes to more representative prediction of crack initiation and damage accumulation at defects under cyclic loading.

The cast material is predicted to crack significantly earlier (two cycles versus twenty-two) and more frequently than the forged model, with cracking predicted to occur at all casting defects within 100 cycles. In contrast, the majority of cracking in the forged model is limited to a single defect located at the surface. This highlights key information in relation to the importance of both defect shape and location.

7.4.4 Valve Chest Sub-Section Modelling

Complex distributions of stress and strain are again predicted to occur at defects in the valve chest models. The greatest increase in maximum stress and strain is predicted in the cast model, in relation to the defect-free model (Figure 7.14 and Figure 7.15). In the forged model, where defects are orientated at 90°, the maximum stress is increased compared to those aligned in the direction of forging; however, maximum strain is reduced by ~20%. This indicates the complex behaviour associated with even stringer-type defects and the effect orientation can have on the localised stress and strain behaviour. Similar stress-strain behaviour occurs for each forged sample (Figure 7.21), but increased levels of ratchetting are predicted in the cast sample across a range of loading directions (Figure 7.20). As a result, crack initiation in the cast model occurs at significantly earlier stages of loading compared to the forged model and, furthermore, the forged model with defects rotated at 90°. In terms of plant components, even for geometries as large as a valve chest, manufacturing defects less than 1 mm are found to have a significant micro-scale effect, particularly when located near the surface.

7.5 Conclusions

The key conclusions of this chapter are:

- A methodology has been successfully developed for 3D computational modelling of manufacturing defects, identified via 3D X-ray µCT scanning. This work represents a significant step towards realistic fatigue damage modelling of the non-uniform distribution of manufacturing-induced defects, in conjunction with a cyclic viscoplastic model (incorporating isotropic and kinematic hardening), and Ostergren life prediction of cycles to crack initiation and associated damage accumulation.

- The presence of manufacturing defects, including interaction between defects and with the component surface, is shown to be detrimental to both cylindrical HTLCF specimens and plant components, due to localised stress and strain concentrations (SNCF up to ~11).
- The complex geometry of casting defects, in contrast to forged stringer-type defects, causes more rapid damage accumulation and, hence, microscale crack initiation is predicted to occur as early as 2 and 10 cycles in the cast HTLCF geometry and valve chest sub-section, respectively.
- Forging has been shown to effectively reduce both the amount and complexity of manufacturing defects (Chapter 4); however, stringer-type defects are still predicted to cause crack initiation within 23 cycles in a HTLCF component, and 833 cycles (regardless of orientation) in a valve chest under high temperature cyclic loading conditions. Therefore, additional refinement of the manufacturing process would further benefit component performance, particularly for flexible USC loading conditions.

8 CONCLUSIONS AND RECOMMENDATIONS

8.1 Conclusions

This work has characterised the high temperature behaviour of cast and forged MarBN steel for low cycle fatigue, creep-fatigue, oxidation and corrosion loading conditions at 600 °C and 650 °C. Based on the range of experimental, microstructural (including 3D X-ray μCT scanning) and computational methodologies employed here, manufacturing defects are identified as a primary source of low-cycle fatigue crack initiation and propagation in cast and forged MarBN. The key achievements are as follows:

- To the author's knowledge, this is the first work to use 3D X-ray μCT scanning to characterise the effect of manufacturing process (i.e. casting and forging) on defect geometry and distribution in 9Cr steels. 3D X-ray μCT scanning of cast and forged MarBN, prior to and after high temperature low cycle fatigue testing, has confirmed manufacturing defects as key sources of void growth and fatigue cracking. The forging process is found to have a substantial effect on defect shape (i.e. complex to stringer) and volume fraction (~16 times less) compared to the cast material. The resulting macroscale impact is approximately double the number of cycles to failure for forged MarBN, under high temperature low cycle fatigue loading. This work provides insight into the complicated microscale effect of manufacturing defects and is additional motivation for material developers and steel manufacturers to further refine the manufacturing process (with particular focus on steps leading to manufacturing defect formation), and a view to prolonged in-service component performance.

- Coupled and uncoupled methods for prediction of cycles to failure in defect-free components, as well as crack initiation in the region of manufacturing defects, have been successfully developed. The coupled Ostergren life prediction and damage user-material (UMAT) subroutine was developed and applied to investigate the localised effect of complex manufacturing defects in MarBN steel under cyclic loading at high temperature. A methodology to simulate experimentally identified manufacturing defects in uniaxial test specimens and plant components, utilizing 3D X-ray μCT scanning, was also developed.
- Computational modelling of multiple complex defects in uniaxial and multiaxial component geometries has advanced the understanding of the effect of such discontinuities on MarBN under high temperature cyclic loading. Finite element modelling of (i) spherical voids and inclusions in an axisymmetric cast MarBN matrix, (ii) multiple inclusions in a 2D cast MarBN section, and (iii) 3D gauge length and valve chest sub-section models (with cast and forged manufacturing defects under high temperature cyclic loading) has been performed. In all cases, cycles to crack initiation at a defect is predicted as less than 12% of total experimentally-measured macroscale cycles to failure, due to significant stress concentrations and strain accumulation, and indicates that the presence alone of manufacturing defects is a key factor in fatigue crack initiation. Other factors include (i) defect geometry (particularly the complex shapes formed during casting), (ii) location (in terms of proximity to the gauge length and other defects), (iii) orientation (direction of primary loading e.g. forged defects rotated at 90° increased cycles to crack initiation by a factor of ~4), and (iv) volume fraction.
- Characterisation of the high temperature low cycle fatigue performance of cast MarBN, in conjunction with initial testing of forged MarBN, highlights the potential of this material for application in flexible power plants under ultra-supercritical (USC) loading conditions. This is due to the enhanced cyclic strength of both cast and forged MarBN at 600 °C, compared to rolled P91 steel, and comparable performance even as the temperature is increased to 650 °C. Furthermore, the fatigue life of cast MarBN is shown to be equivalent to rolled P91, and is approximately doubled as a result of forging. The short-term oxidation and corrosion performance for MarBN at 600 °C and 650 °C, compared to rolled P91 at 600 °C, indicates a similar rate of oxide scale growth

in all cases. This is important for the elevated loading conditions that components will be expected to endure at USC temperatures and pressures. However, creep-fatigue testing of cast MarBN is shown to reduce the fatigue life by ~25% and, in conjunction with an increased rate of cyclic softening and plastic-strain evolution, highlights the importance of a broad experimental test program, representative of flexible plant loading conditions.

- Microstructural analysis (i.e. scanning electron microscopy (SEM), energy dispersive X-ray (EDX) spectroscopy, backscatter electron (BSE) microscopy and transmission electron microscopy (TEM)) has identified manufacturing defects as a primary source of low-cycle fatigue crack initiation and propagation in cast and forged MarBN, particularly when located close to the surface. Their presence promotes oxide pit formation (as observed under oxidation, corrosion and high temperature loading scenarios) and contributes to a weakened matrix material. Such locations then become primary sites for crack initiation and component failure.
- The modified unified cyclic viscoplasticity modelling framework presented here captures the primary constitutive behaviour of 9Cr steels, i.e. cyclic plasticity and viscous effects (fatigue and creep-fatigue), isotropic (cyclic softening due to low angle boundary annihilation) and kinematic (back-stress as a result of dislocation pile-up at high angle boundaries and precipitates) hardening effects, and hyperbolic sine flow rule for strain-rate sensitivity. This model has been extended to include Coffin-Manson life prediction and Chaboche damage effects, an important step in realistic modelling of the constitutive and failure behaviour of the material. This model was applied to cast MarBN steel and P91 at high temperature, based on identification of material parameters from experimental data.
- A material parameter optimisation procedure has been developed, based on experimental data obtained from a program of high temperature experimental testing. This allows semi-automation of the high temperature low cycle fatigue parameters across a range of loading conditions, following initial identification. This test program is performed for material characterisation in GE Power and, therefore, the parameter optimisation methodology and material model is potentially of benefit for industrial applications, for rapid prediction of material

performance of 9Cr steels across a range of loading conditions, particularly in terms of damage accumulation and cycles to failure.

8.2 Recommendations for Future Work

The work presented in this thesis represents a significant step towards characterisation of (i) MarBN steel for flexible USC plant applications, (ii) the role of manufacturing process on defect volume fraction and geometry, and (iii) the influence of manufacturing induced defects on component failure in extreme conditions (e.g. high pressure, temperature and corrosive environments). Future work is required to further understand the complexities associated with high temperature cyclic loading and manufacturing of advanced 9Cr martensitic steels. This section provides the following recommendations to achieve these goals, using experimental and computational methods:

- Interrupted high temperature testing, in conjunction with 3D X-ray µCT scanning, to identify crack initiation and rates of crack growth at individual manufacturing defects, as validation of material modelling methods to predict crack initiation at defects. A similar program of 3D X-ray µCT scanning could be applied to rolled MarBN components to further investigate the influence of manufacturing process on defect geometry and volume fraction. Alternatively, the use of in-situ analysis methods (i.e. SEM, TEM and 3D X-ray µCT scanning) would provide detailed information on the evolution of microstructure evolution, and fatigue crack initiation and propagation during loading. Furthermore, use of the extended finite element method (XFEM) to simulate crack propagation, with comparison to reconstructed 3D X-ray µCT scanning, would be a significant development in the capability of predictive modelling methods. Similar methods have been developed by Grogan *et al.* [228] for composite materials.
- Crystal plasticity modelling of MarBN to explicitly include precipitates (e.g. $M_{23}C_6$ and Laves phase) and grain boundaries, in conjunction with simple and complex manufacturing defects, would provide greater insight into the effect of defects on microstructural evolution under cyclic loading e.g. [209,229]. Further application of such models to a broader range of loading conditions (e.g. effect of strain-rate and yield strength [95,97]), as well as component geometries (e.g. plant header [227] and T-joint [230]), to better understand the role of loading

and temperature on the microscale stress and strain behaviour, and fatigue crack initiation.

- Additional experimental testing, based on the test program of Chapter 3, with, for example, (i) lower strain-rates and strain-ranges, (ii) varied hold periods, (iii) thermo-mechanical fatigue loading, (iv) service-aged material and (v) notched samples, to further represent potential in-service flexible loading conditions and provide greater validation in terms of material modelling. This should include similar microstructural analysis methods to those employed here, to identify the primary strengthening and degradation mechanisms and influence of temperature and loading. Such experimental characterisation methods have been performed previously for P91 steel [90,92,193,231,232].
- Expansion of current creep test programs for MarBN weldments [21,132] to include the effect of flexible loading conditions, particularly in terms of understanding the primary failure mechanisms e.g. the methods of Farragher *et al.* [232]. This can be compared to the mechanisms of strengthening and degradation identified here for parent material MarBN, and extended to include welding-induced defects.
- Development of material models, based on experimental testing and microstructural analysis, to predict the influence of various microstructural parameters as a result of welding (e.g. dislocation density and volume fraction of precipitates at regions of interest, including the inter-critical heat affected zone) and effect of in-service loading, similar to the work of Mac Ardghail *et al.* [233,234].
- Chemical composition and heat treatment play a defining role in the high temperature performance of the material. Therefore, understanding the effect of varying these processes, using experimental characterisation methods, in conjunction with physically-based models, would provide a greater understanding for future material designers and manufacturers. For example, extension of a physically-based yield strength model, as developed by Barrett *et al.* [95], for complex loading of advanced 9Cr steels.
- Longer-term thermal aging studies for (i) oxidation, (ii) fireside and (iii) steam-side corrosion conditions could be performed to better understand the evolution behaviour of micro-scale phenomena in cast and forged MarBN (e.g. rates of precipitate coarsening, Laves phase formation and growth, and dislocation

density evolution). Addition of thermal effects in computational modelling for isothermal and thermo-mechanical fatigue loading, to quantify the role of temperature on the macro-scale and localised stress and strain behaviour (e.g. investigate the effect of thermal mismatch between inclusions and the matrix [54], in conjunction with a cyclic viscoplasticity model).

- Analysis of the detailed casting and forging techniques for manufacture of advanced martensitic steels, and specific processes related to defect formation. Furthermore, investigation of the influence of modification of various manufacturing steps, and characterisation of the resulting defect distribution, for example, to identify process-structure-property relationships.

9 REFERENCES

[1] Energy Roadmap 2050, (2012). http://ec.europa.eu/energy/en/topics/energy-strategy/2050- energy- strategy.

[2] S.A. Lefton, P.M. Besuner, D. Agan, The real cost of on/off cycling, Mod. Power Syst. 26 (2006) 11–13.

[3] Parsons Brinckerhoff, Technical Assessment of the Operation of Coal & Gas Fired Plants, (2014) 44.

[4] Sustainable Energy Authority Ireland, Energy in Ireland 1990-2016, 2017 Report, 2017.

[5] Organisation of the Petroleum Exporting Countries, World Oil Outlook, 2016. doi:10.1190/1.1439163.

[6] British Petroleum, British Petroleum Statistical Review of World Energy 2017, 2017. doi:http://www.bp.com/content/dam/bp/en/corporate/pdf/energy-economics/statistical-review-2017/bp-statistical-review-of-world-energy-2017-full-report.pdf.

[7] S. Zafar, Yuhuan 1,000 MW Ultra-Supercritical Pressure Boilers, (2015). https://www.power-technology.com/projects/yuhuancoal/.

[8] A. Di Gianfrancesco, Materials for ultra-supercritical and advanced ultra-supercritical power plants, 1st ed., Woodhead Publishing, Cambridge, 2016. doi:https://doi.org/10.1016/B978-0-08-100552-1.00001-4.

[9] R.A. Barrett, Experimental Characterisation and Computational Constitutive Modelling of High Temperature Degradation in 9Cr Steels Including Microstructural Effects, PhD Thesis. (2016) National University of Ireland Galway.

[10] R. Diehl, High Pressure Piping in Power Plants – Water Steam Cycles: Capital Markets Day “Power Services” at Moorburg Power Plant, (2010).

[11] A. Pickard, G. Meinecke, The Future Role of Fossil Power Generation, Siemens AG, Energy Sect. Erlangen, Ger. (2011) 20.

[12] J. Cochran, D. Lew, N. Kumar, Flexible Coal: Evolution from Baseload to Peaking Plant, Natl. Renew. Energy Lab. (2013) 10. doi:10.2172/1110465.

[13] E. Giacomazzi, The importance of operational flexibility in gas turbine power plants, EAI Energia, Ambient. e Innov. 6 (2013) 6. doi:10.12910/EAI2013-35.

[14] H.S. Leff, Thermodynamics of combined-cycle electric power plants, Am. J. Phys. 80 (2012) 515–518. doi:10.1119/1.3694034.

[15] S. Scully, Private Communication, (n.d.) ESB International.

[16] HRSG Tube Failure, (n.d.). https://www.tetra-eng.com/news/106-hrsg-tube-failure-guide-3rd-ed.

[17] Goodwin Steel Castings, Advanced Material Castings for High Temperature Coal Fired Steam Turbine Applications, (2011). http://www.goodwinsteelcastings.com/downloads/gsc-advanced-material-castings.pdf.

[18] IMPACT - Innovative Materials Design and Monitoring of Power Plant to Accommodate Carbon Capture, (2010). http://gtr.rcuk.ac.uk/projects?ref=100819.

[19] IMPULSE - Advanced Industrial Manufacture of Next-Generation MARBN Steel for Cleaner Fossil Plant, (2016). http://gtr.rcuk.ac.uk/projects?ref=102468.

[20] Private Communication, IMPEL Consortium, 2015.

[21] F. Abe, M. Tabuchi, H. Semba, M. Igarashi, M. Yoshizawa, N. Komai, A. Fujita, Feasibility of MARBN steel for application to thick section boiler components in USC power plant at 650 C, in: Proc. 5th Int. Conf. Adv. Mater. Technol. Foss. Power Plants, Oct., 2007: pp. 3–5.

[22] X. Wang, X. Li, Q. Li, F. Huang, H. Li, J. Yang, Control of stringer shaped non-metallic inclusions of CaO-Al2O3 system in API X80 linepipe steel plates, Steel Res. Int. 85 (2014) 155–163. doi:10.1002/srin.201300044.

[23] P.J. Ennis, A. Zielinska-Lipiec, O. Wachter, A. Czyrska-Filemonowicz, Microstructural stability and creep rupture strength of the martensitic steel P92 for advanced power plant, Acta Mater. 45 (1997) 4901–4907. doi:10.1016/S1359-6454(97)00176-6.

[24] K. Maruyama, K. Sawada, J. Koike, Strengthening mechanisms of creep resistant

tempered martensitic steel, ISIJ Int. 41 (2001) 641–653.

[25] L. Li, P. Zhu, G. West, R.C. Thomson, The Effect of Duration of Stress Relief Heat Treatments on Microstructural Evolution and Mechanical Properties in Grade 91 and 92 Power Plant Steels, Adv. Mater. Technol. Foss. Power Plants Proc. from Sixth Int. Conf. 2010 (ASM Int. (2011) 679–692.

[26] M.F. Ashby, D.R.H. Jones, Engineering Materials 1, Eng. Mater. 1. (1996) 322. doi:10.1016/B978-0-08-096665-6.00030-1.

[27] T.H. Hyde, W. Sun, C.J. Hyde, Applied Creep Mechanics, McGraw-Hill Professional, 2013.

[28] B.F. Dyson, Creep and fracture of metals: mechanisms and mechanics, Rev. Phys. Appl. 23 (1988) 605–613.

[29] C.G. Panait, W. Bendick, A. Fuchsmann, A.F. Gourgues-Lorenzon, J. Besson, Study of the microstructure of the Grade 91 steel after more than 100,000 h of creep exposure at 600 °C, Int. J. Press. Vessel. Pip. 87 (2010) 326–335. doi:10.1016/j.ijpvp.2010.03.017.

[30] P.J. Ennis, A. Czyrska-Filemonowicz, Recent advances in creep resistant steels for power plant applications, Sadhana. 28 (2003) 709–730. doi:10.1007/BF02706455.

[31] T.H. Hyde, A.A. Becker, W. Sun, J.A. Williams, Finite-element creep damage analyses of P91 pipes, Int. J. Press. Vessel. Pip. 83 (2006) 853–863. doi:10.1016/j.ijpvp.2006.08.013.

[32] A. Orlova, J. Bursik, K. Kucharova, V. Sklenicka, Microstructural development during high temperature creep of 9% Cr steel, Mater. Sci. Eng. A. 245 (1998) 39–48. doi:10.1016/S0921-5093(97)00708-9.

[33] C.G. Panait, A. Zielińska-Lipiec, T. Koziel, A. Czyrska-Filemonowicz, A.F. Gourgues-Lorenzon, W. Bendick, Evolution of dislocation density, size of subgrains and MX-type precipitates in a P91 steel during creep and during thermal ageing at 600°C for more than 100,000h, Mater. Sci. Eng. A. 527 (2010) 4062–4069. doi:10.1016/j.msea.2010.03.010.

[34] G. Dimmler, P. Weinert, E. Kozeschnik, H. Cerjak, Quantification of the Laves phase in advanced 9-12% Cr steels using a standard SEM, Mater. Charact. 51 (2003) 341–352. doi:10.1016/j.matchar.2004.02.003.

[35] D. Jandová, J. Kasl, E. Chvostová, Microstructure of CB2 Steel before and after Long-Term Creep Tests, Mater. Sci. Forum. 782 (2014) 311–318. doi:10.4028/www.scientific.net/MSF.782.311.

[36] A. Di Gianfrancesco, L. Cipolla, M. Paura, S.T. Vipraio, D. Venditti, S. Neri, M. Calderini, The role of boron in long term stability of a CrMoCoB (FB2) steel for rotor application, in: Adv. Mater. Technol. Foss. Power Plants Proc. from Sixth Int. Conf. August 31-September 3, 2010, St. Fe, New Mex. USA, 2011: p. 342.

[37] T. Hamaguchi, H. Okada, S. Kurihara, H. Hirata, M. Yoshizawa, A. Iseda, MICROSTRUCTURAL EVALUATION OF 9CR-3W-3CO-ND-B HEAT-RESISTANT STEEL (SAVE12AD) AFTER LONG-TERM CREEP DEFORMATION, in: Proc. ASME 2017 Press. Vessel. Pip. Conf., Waikoloa, Hawaii, 2017.

[38] F. Abe, Precipitate design for creep strengthening of 9% Cr tempered martensitic steel for ultra-supercritical power plants, Sci. Technol. Adv. Mater. 9 (2008) 013002. doi:10.1088/1468-6996/9/1/013002.

[39] J.P. Shingledecker, N.D. Evans, Creep-rupture performance of 0.07C-23Cr-45Ni-6W-Ti,Nb austenitic alloy (HR6W) tubes, Int. J. Press. Vessel. Pip. 87 (2010) 345–350. doi:10.1016/j.ijpvp.2010.03.011.

[40] F. Masuyama, History of power plants and progress in heat resistant steels, ISIJ Int. 41 (2001) 612–625.

[41] G.Y. Lai, High-temperature corrosion and materials applications, ASM International, Ohio, 2007. doi:10.1361/hcma2007p001.

[42] F. Abe, H. Kutsumi, H. Haruyama, H. Okubo, Improvement of oxidation resistance of 9 mass% chromium steel for advanced-ultra supercritical power plant boilers by pre-oxidation treatment, Eval. Program Plann. (2016). doi:10.1016/j.corsci.2016.10.008.

[43] R. Viswanathan, J. Sarver, J.M. Tanzosh, Boiler materials for ultra-supercritical coal power plants - Steamside oxidation, J. Mater. Eng. Perform. 15 (2006) 255–274. doi:10.1361/105994906X108756.

[44] C.P. O'Hagan, Experimental and Numerical Characterisation of Materials for Biomass Co-Firing, PhD Thesis. (2017) National University of Ireland Galway.

[45] J. Bischoff, L. Tan, O. Ridge, T. Allen, Influence of Alloy Microstructure on Oxide Growth in HCM12A in Supercritical Water, in: MRS Online Proc. Libr. Arch., 2008. doi:10.1557/PROC-1125-R06-05.

[46] H.O. Pierson, Handbook of Chemical Vapor Deposition: Principles, Technology and Applications, William Andrew Publishing LLC, New York, 1999.

[47] R.W.W. Neu, H. Sehitoglu, Thermomechanical fatigue, oxidation, and creep: Part I. Damage mechanisms, Metall. Trans. A. 20 (1989) 1755–1767.

[48] G.H. Meier, A review of advances in high-temperature corrosion, Mater. Sci. Eng. A. 120–121 (1989) 1–11. doi:10.1016/0921-5093(89)90712-0.

[49] M. Schütze, Modelling oxide scale fracture, Mater. High Temp. 22 (2005) 147–154. doi:10.1179/mht.2005.017.

[50] N. Birks, G.H. Meier, F.S. Pettit, Introduction to the High Temperature Oxidation of Metals, 2006. doi:10.2277/0521480426.

[51] K. Sawada, M. Fujitsuka, M. Tabuchi, K. Kimura, Effect of oxidation on the creep rupture life of ASME T23 steel, Int. J. Press. Vessel. Pip. 86 (2009) 693–698. doi:10.1016/j.ijpvp.2009.03.001.

[52] C.P.O. Hagan, S.B. Leen, R.F.D. Monaghan, A microstructural investigation into the accelerated corrosion of 347SS during biomass co-firing, Corros. Sci. 109 (2016) 101–114.

[53] C.P. O'Hagan, R.A. Barrett, S.B. Leen, R.F.D. Monaghan, Effect Of High Temperature Corrosion On The Service Life Of P91 Piping In Biomass Co-Firing, ASME 2015 Press. Vessel. Pip. Conf. (2015) 1–10. doi:10.1115/PVP2015-45612.

[54] C.P. O'Hagan, B.J. O'Brien, S.B. Leen, R.F.D. Monaghan, A microstructural investigation into the accelerated corrosion of P91 steel during biomass co-firing, Corros. Sci. 3 (2016). doi:10.1016/j.corsci.2016.03.028.

[55] B. Skrifvars, R. Backman, M. Hupa, K. Salmenoja, E. Vakkilainen, Corrosion of superheater steel materials under alkali salt deposits Part 1 : The effect of salt deposit composition and temperature, 50 (2008) 1274–1282. doi:10.1016/j.corsci.2008.01.010.

[56] B. Fournier, M. Sauzay, C. Caës, M. Noblecourt, M. Mottot, A. Bougault, V. Rabeau, A. Pineau, Creep-fatigue-oxidation interactions in a 9Cr-1Mo martensitic steel. Part I: Effect of tensile holding period on fatigue lifetime, Int. J. Fatigue. 30 (2008) 649–662. doi:10.1016/j.ijfatigue.2007.05.007.

[57] B. Fournier, Creep-fatgue-oxidation interactions in a 9Cr-1Mo martensitic steel . Part II : Effect of compressive holding period on fatigue lifetime, Int. J. Fatigue. 30 (2008) 663–676. doi:10.1016/j.ijfatigue.2007.05.008.

[58] B. Fournier, M. Sauzay, C. Caës, M. Noblecourt, M. Mottot, A. Bougault, V. Rabeau, J. Man, O. Gillia, P. Lemoine, Creep–fatigue–oxidation interactions in a 9Cr–1Mo martensitic steel. Part III: Lifetime prediction, Int. J. Fatigue. 30 (2008) 1797–1812.

[59] A.A. Saad, Cyclic plasticity and creep of power plant materials, Univ.

Nottingham. PhD Thesis (2012).

[60] V. Shankar, M. Valsan, K.B.S. Rao, R. Kannan, S.L. Mannan, S.D. Pathak, Low cycle fatigue behavior and microstructural evolution of modified 9Cr-1Mo ferritic steel, Mater. Sci. Eng. A. 437 (2006) 413–422. doi:10.1016/j.msea.2006.07.146.

[61] G. Golański, S. Mroziński, Fatigue life at 550 C temperature of aged martensitic cast steel, AASRI Procedia. 2 (2012) 249–255.

[62] S. Mroziński, G. Golański, A. Zielińska-Lipiec, Fatigue Resistance of GX12CrMoVNbN9-1 Cast Steel after Ageing Process, Mater. Sci. 20 (2014) 396–402.

[63] S. Mroziński, G. Golański, Elevated Temperature Low Cycle Fatigue Properties of Martensitic Cast Steel, Int. J. Eng. Technol. 13 (2013) 86–91.

[64] G. Golański, S. Mroziński, Low cycle fatigue and cyclic softening behaviour of martensitic cast steel, Eng. Fail. Anal. 35 (2013) 692–702. doi:10.1016/j.engfailanal.2013.06.019.

[65] J.S. Park, S.J. Kim, C.S. Lee, Effect of W addition on the low cycle fatigue behavior of high Cr ferritic steels, Mater. Sci. Eng. A. 298 (2001) 127–136. doi:10.1016/S0921-5093(00)01291-0.

[66] A. Nagesha, R. Kannan, G.V.S. Sastry, R. Sandhya, V. Singh, K. Bhanu Sankara Rao, M.D. Mathew, Isothermal and thermomechanical fatigue studies on a modified 9Cr-1Mo ferritic martensitic steel, Mater. Sci. Eng. A. 554 (2012) 95–104. doi:10.1016/j.msea.2012.06.021.

[67] V. Knežević, J. Balun, G. Sauthoff, G. Inden, A. Schneider, Design of martensitic/ferritic heat-resistant steels for application at 650 °C with supporting thermodynamic modelling, Mater. Sci. Eng. A. 477 (2008) 334–343. doi:10.1016/j.msea.2007.05.047.

[68] L. Korcakova, J. Hald, M.A.J. Somers, Quantification of Laves phase particle size in 9CrW steel, Mater. Charact. 47 (2001) 111–117. doi:10.1016/S1044-5803(01)00159-0.

[69] B. Fournier, F. Dalle, M. Sauzay, J. Longour, M. Salvi, C. Caes, I. Tournie, P.F. Giroux, S.H. Kim, Comparison of various 9-12%Cr steels under fatigue and creep-fatigue loadings at high temperature, Mater. Sci. Eng. A. 528 (2011) 6934–6945. doi:10.1016/j.msea.2011.05.046.

[70] Y. Takahashi, Study on Type-IV Damage Prevention in High-Temperature Welded Structures of Next-Generation Reactor Plants: Part I — Fatigue and

Creep-Fatigue Behavior of Welded Joints of Modified 9Cr-1Mo Steel, in: ASME 2006 Press. Vessel. Piping/ICPVT-11 Conf., 2006.

[71] F. Abe, Precipitate design for creep strengthening of 9% Cr tempered martensitic steel for ultra-supercritical power plants, Sci. Technol. Adv. Mater. 9 (2008) 13002.

[72] R.A. Barrett, P.E. O'Donoghue, S.B. Leen, A dislocation-based model for high temperature cyclic viscoplasticity of 9–12Cr steels, Comput. Mater. Sci. 92 (2014) 286–297.

[73] T. Simm, L. Sun, S. McAdam, P. Hill, M. Rawson, K. Perkins, The influence of lath, block and Prior Austenite Grain (PAG) size on the tensile, creep and fatigue properties of novel maraging steel, Materials (Basel). 10 (2017). doi:10.3390/ma10070730.

[74] R. Kaibyshev, Microstructural Evolution in 9%Cr Heat Resistant Steels under Creep Conditions, Mater. Sci. Forum. 715–716 (2012) 813–818. doi:10.4028/www.scientific.net/MSF.715-716.813.

[75] Z. Zhang, Z. Hu, S. Schmauder, Fatigue Behavior of 9 – 12 % Cr Ferritic-Martensitic Steel, Handb. Mech. Mater. (2018) 1–46.

[76] J. Hald, Microstructure and long-term creep properties of 9-12% Cr steels, Int. J. Press. Vessel. Pip. 85 (2008) 30–37. doi:10.1016/j.ijpvp.2007.06.010.

[77] S.P. Srinivas Prasad, R. Rajkumar, H.K. Hari Kumar, Numerical simulation of precipitate evolution in ferriticmartensitic power plant steels, Calphad Comput. Coupling Phase Diagrams Thermochem. 36 (2012) 1–7. doi:10.1016/j.calphad.2011.10.006.

[78] K. Guguloth, S. Sivaprasad, D. Chakrabarti, S. Tarafder, Low-cyclic fatigue behavior of modified 9Cr-1Mo steel at elevated temperature, Mater. Sci. Eng. A. 604 (2014) 196–206. doi:10.1016/j.msea.2014.02.076.

[79] H. Semba, F. Abe, Alloy design and creep strength of advanced 9% Cr USC Boiler steels containing high concentration of boron, Energy Mater. 1. (2006) 238–244.

[80] K. Sakuraya, H. Okada, F. Abe, BN type inclusions formed in high Cr ferritic heat resistant steel, Energy Mater. 1 (2006) 158–166.

[81] L. Li, R. MacLachlan, M.A.E. Jepson, R. Thomson, Microstructural Evolution of Boron Nitride Particles in Advanced 9Cr Power Plant Steels, Metall. Mater. Trans. A. 44 (2013) 3411–3418.

[82] F. Abe, M. Tabuchi, S. Tsukamoto, Alloy design of martensitic 9Cr-Boron steel

for A-USC boiler at 650 C—Beyond Grades 91, 92 and 122, Energy Mater. 2014. (2014).

[83] F. Abe, M. Tabuchi, M. Kondo, S. Tsukamoto, Suppression of Type IV fracture and improvement of creep strength of 9Cr steel welded joints by boron addition, Int. J. Press. Vessel. Pip. 84 (2007) 44–52. doi:10.1016/j.ijpvp.2006.09.013.

[84] J.L. Chaboche, G. Rousselier, On the plastic and viscoplastic constitutive equations—Part I: Rules developed with internal variable concept, J. Press. Vessel Technol. 105 (1983) 153–158.

[85] J.-L. Chaboche, G. Rousselier, On the plastic and viscoplastic constitutive equations—Part II: application of internal variable concepts to the 316 stainless steel, J. Press. Vessel Technol. 105 (1983) 159–164.

[86] T.F. Farragher, Thermomechanical Analysis of P91 Power Plant Components, PhD Thesis. (2014) National University of Ireland Galway.

[87] C.O. Frederick, P.J. Armstrong, A mathematical representation of the multiaxial Bauschinger effect, Mater. High Temp. 24 (2007) 1–26.

[88] G.H. Koo, J.H. Kwon, Identification of inelastic material parameters for modified 9Cr-1Mo steel applicable to the plastic and viscoplastic constitutive equations, Int. J. Press. Vessel. Pip. 88 (2011) 26–33. doi:10.1016/j.ijpvp.2010.11.004.

[89] W.Z. Wang Buhl, P., Klenk, A, A unified viscoplastic constitutive model with damage for multi-axial creep–fatigue loading, Int. J. Damage Mech. 24 (2015) 363–382. doi:10.1177/1056789514537007.

[90] A.A. Saad, C.J. Hyde, W. Sun, T.H. Hyde, Thermal-mechanical fatigue simulation of a P91 steel in a temperature range of 400–600 C, Mater. High Temp. 28 (2014) 212–218.

[91] J. Wang, P. Steinmann, J. Rudolph, A. Willuweit, A combined creep-viscoplastic constitutive model for modeling the thermal-mechanical behavior of high-Cr steel components 1 Introduction, (2013).

[92] C.J. Hyde, W. Sun, T.H. Hyde, A.A. Saad, Thermo-mechanical fatigue testing and simulation using a viscoplasticity model for a P91 steel, Comput. Mater. Sci. 56 (2012) 29–33.

[93] R.A. Barrett, P.E. O'Donoghue, S.B. Leen, An improved unified viscoplastic constitutive model for strain-rate sensitivity in high temperature fatigue, Int. J. Fatigue. 48 (2013) 192–204.

[94] R.A. Barrett, T.P. Farragher, C.J. Hyde, N.P. O'Dowd, P.E. O'Donoghue, S.B. Leen, A Unified Viscoplastic Model for High Temperature Low Cycle Fatigue of

Service-Aged P91 Steel, J. Press. Vessel Technol. 136 (2014) 21402.

[95] R.A. Barrett, P.E. O'Donoghue, S.B. Leen, A physically-based high temperature yield strength model for 9Cr steels, Mater. Sci. Eng. A. 730 (2018) 410–424. doi:10.1016/j.msea.2018.05.086.

[96] D. Li, R.A. Barrett, P.E.O. Donoghue, N.P.O. Dowd, B. Sean, A multi-scale crystal plasticity model for cyclic plasticity and low-cycle fatigue in a precipitate-strengthened steel at elevated temperature, (2016) 1–25.

[97] R.A. Barrett, P.E. O'Donoghue, S.B. Leen, A physically-based constitutive model for high temperature microstructural degradation under cyclic deformation, Int. J. Fatigue. 100 (2017) 388–406. doi:10.1016/j.ijfatigue.2017.03.018.

[98] M.H. Maitournam, C. Krebs, A. Galtier, A multiscale fatigue life model for complex cyclic multiaxial loading, Int. J. Fatigue. 33 (2011) 232–240. doi:10.1016/j.ijfatigue.2010.08.017.

[99] O.H. Basquin, The exponential law of endurance tests, Proc. ASTM. 10 (1910) 625–630.

[100] L.F. Coffin, Fatigue at high temperature, in: Fatigue Elev. Temp., ASTM International, 1973.

[101] K.N. Smith, P. Watson, T.H. Topper, A stress-strain function for the fatigue of metals, J. Mater. (1970) 767–778.

[102] T. Zhang, P.E. McHugh, S.B. Leen, Finite element implementation of multiaxial continuum damage mechanics for plain and fretting fatigue, Int. J. Fatigue. 44 (2012) 260–272.

[103] F. Ellyin, D. Kujawski, Plastic Strain Energy in Fatigue, J. Press. Vessel Technol. 106 (1984) 342–347.

[104] W.J. Ostergren, A damage foundation hold time and frequency effects in elevated temperature low cycle fatigue, J. Test Eval. (1967) 327–339.

[105] F. Liu, S.H. Ai, Y.C. Wang, H. Zhang, Z.G. Wang, Thermal-mechanical fatigue behavior of a cast K417 nickel-based superalloy, Int. J. Fatigue. 24 (2002) 841–846. doi:10.1016/S0142-1123(02)00010-5.

[106] L.M. Kachanov, Time of the rupture process under creep conditions, Izv Akad Nauk S S R Otd Tech Nauk. 8 (1958) 26–31. doi:citeulike-article-id:5466815.

[107] Y. Rabotnov, Creep Rupture, Springer, Berlin, 1968.

[108] M.A. Miner, Cumulative damage in fatigue, J. Appl. Mech. 67 (1945) A159–A164.

[109] V. Dattoma, S. Giancane, R. Nobile, F.W. Panella, Fatigue life prediction under variable loading based on a new non-linear continuum damage mechanics model, Int. J. Fatigue. 28 (2006) 89–95. doi:10.1016/j.ijfatigue.2005.05.001.

[110] J. Lemaitre, A course on damage mechanics, Springer-Verlag, Berlin, 1992.

[111] J. Lu, W. Sun, A. Becker, A.A. Saad, Simulation of the fatigue behaviour of a power plant steel with a damage variable, Int. J. Mech. Sci. 100 (2015) 145–157. doi:10.1016/j.ijmecsci.2015.06.019.

[112] J.L. Chaboche, P.M. Lesne, A Non-Linear Continuous Fatigue Damage Model, Fatigue Fract. Eng. Mater. Struct. 11 (1988) 1–17.

[113] J. Lemaitre, R. Desmorat, Engineering damage mechanics: Ductile, creep, fatigue and brittle failures, 2005. doi:10.1007/b138882.

[114] A. Nayebi, H. Ranjbar, H. Rokhgireh, Analysis of unified continuum damage mechanics model of gas turbine rotor steel: Life assessment, Proc. Inst. Mech. Eng. Part L J. Mater. Des. Appl. (2012) 1464420712456513.

[115] S.T. Kyaw, J.P. Rouse, J. Lu, W. Sun, Determination of material parameters for a unified viscoplasticity-damage model for a P91 power plant steel, Int. J. Mech. Sci. 115–116 (2016) 168–179. doi:10.1016/j.ijmecsci.2016.06.014.

[116] K. Priyaajit, A. Gautam, P.K. Sarkar, Fatigue damage estimation through continuum damage mechanics revisited, J. Mines, Met. Fuels. 64 (2016) 214–217. doi:10.1016/j.proeng.2016.12.248.

[117] R.W. Neu, H. Sehitoglu, Thermomechanical fatigue, oxidation, and Creep: Part II. Life prediction, Metall. Trans. A. 20 (1989) 1769–1783. doi:10.1007/BF02663208.

[118] J. Shang, T.H. Hyde, S.B. Leen, Finite element-based life prediction for high-temperature cyclic loading of a large superplastic forming die, 41 (2006) 539–559. doi:10.1243/03093247JSA236.

[119] S.-P. Zhu, H.-Z. Huang, Y. Liu, R. Yuan, L. He, An efficient life prediction methodology for low cycle fatigue–creep based on ductility exhaustion theory, Int. J. Damage Mech. (2012) 1056789512456030.

[120] K. Tanaka, T. Mura, A theory of fatigue crack initiation at inclusions, Metall. Trans. A. 13 (1982) 117–123. doi:10.1007/BF02642422.

[121] D. Hull, Fractography: observing, measuring and interpreting fracture surface topography, Cambridge University Press, 1999.

[122] D.R. Askeland, P. Webster, The Science and Engineering of Materials, Chapman & Hall, London, 1996. doi:10.2172/15009526.

[123] X. Xie, L. Zhang, M. Zhang, J. Dong, K. Bain, Micro-mechanical behavior study of non-metallic inclusions in P/M disk superalloy Rene'95, Superalloys. (2004) 451–458.

[124] Q.Y. Wang, C. Bathias, N. Kawagoishi, Q. Chen, Effect of inclusion on subsurface crack initiation and gigacycle fatigue strength, Int. J. Fatigue. 24 (2002) 1269–1274. doi:10.1016/S0142-1123(02)00037-3.

[125] I. Gustavsson, Fatigue limit model for hardened steels, Fatigue Fract. Eng. Mater. Struct. 15 (1992) 881–894.

[126] T. Billaudeau, Y. Nadot, G. Bezine, Multiaxial fatigue limit for defective materials : mechanisms and experiments, Acta Mater. 52 (2004) 3911–3920. doi:10.1016/j.actamat.2004.05.006.

[127] R. Prasannavenkatesan, J. Zhang, D.L. McDowell, G.B. Olson, H.J. Jou, 3D modeling of subsurface fatigue crack nucleation potency of primary inclusions in heat treated and shot peened martensitic gear steels, Int. J. Fatigue. 31 (2009) 1176–1189.

[128] R.A. Hardin, C. Beckermann, Effect of Porosity on the Stiffness of Cast Steel, Metall. Mater. Trans. A. 38 (2007) 2992–3006. doi:10.1007/s11661-007-9390-4.

[129] L. Babout, E. Maire, R. Foug, Damage initiation in model metallic materials : X-ray tomography and modelling, Acta Mater. 52 (2004) 2475–2487. doi:10.1016/j.actamat.2004.02.001.

[130] A. Isaac, F. Sket, W. Reimers, B. Camin, G. Sauthoff, A.R. Pyzalla, In situ 3D quantification of the evolution of creep cavity size, shape, and spatial orientation using synchrotron X-ray tomography, Mater. Sci. Eng. A. 478 (2008) 108–118. doi:10.1016/j.msea.2007.05.108.

[131] O. Kuwazuru, Y. Murata, Y. Hangai, T. Utsunomiya, S. Kitahara, N. Yoshikawa, X-Ray CT Inspection for Porosities and Its Effect on Fatigue of Die Cast Aluminium Alloy, J. Solid Mech. Mater. Eng. 2 (2008) 1220–1231. doi:10.1299/jmmp.2.1220.

[132] C. Schlacher, C. Béal, C. Sommitsch, S. Mitsche, P. Mayr, Creep and damage investigation of advanced martensitic chromium steel weldments for high temperature applications in thermal power plants, Sci. Technol. Weld. Join. 20 (2015). doi:10.1179/1743284714Y.0000000621.

[133] E. Pessard, F. Morel, A. Morel, D. Bellett, Modelling the role of non-metallic inclusions on the anisotropic fatigue behaviour of forged steel, Int. J. Fatigue. 33 (2011) 568–577. doi:10.1016/j.ijfatigue.2010.10.012.

[134] C. Temmel, B. Karlsson, M. Society, I. Steels, Fatigue Isotropy in Cross-Rolled , Hardened Isotropic-Quality, (2008). doi:10.1007/s11661-008-9467-8.

[135] A. Mbiakop, A. Constantinescu, K. Danas, On void shape effects of periodic elasto-plastic materials subjected to cyclic loading, Eur. J. Mech. / A Solids. 49 (2015) 481–499. doi:10.1016/j.euromechsol.2014.09.001.

[136] A. Mbiakop, A. Constantinescu, K. Danas, An analytical model for porous single crystals with ellipsoidal voids, J. Mech. Phys. Solids. 84 (2015) 436–467. doi:10.1016/j.jmps.2015.07.011.

[137] J.D. Eshelby, P.R.S.L. A, The Determination of the Elastic Field of an Ellipsoidal Inclusion , and Related Problems Article cited in :, Proc. R. Soc. London A Math. Phys. Eng. Sci. 241 (1957) 376–396. doi:10.1098/rspa.1957.0133.

[138] E. Pessard, F. Morel, D. Bellett, A. Morel, A new approach to model the fatigue anisotropy due to non-metallic inclusions in forged steels, Int. J. Fatigue. 41 (2012) 168–178. doi:10.1016/j.ijfatigue.2012.01.005.

[139] A. Melander, A finite-element study of the notch effect at surface inclusions, Int. J. Fatigue. 12 (1990) 154–164.

[140] E. Maire, O. Bouaziz, M. Di Michiel, C. Verdu, Initiation and growth of damage in a dual-phase steel observed by X-ray microtomography, Acta Mater. 56 (2008) 4954–4964. doi:10.1016/j.actamat.2008.06.015.

[141] G. Nicoletto, R. Konec, Characterization of microshrinkage casting defects of Al – Si alloys by X-ray computed tomography and metallography, Int. J. Fatigue. 41 (2012) 39–46. doi:10.1016/j.ijfatigue.2012.01.006.

[142] G. Nicoletto, G. Anzelotti, R. Kone, Procedia Engineering X-ray Computed Tomography vs . Metallography for Pore Sizing and Fatigue of Cast Al-alloys, (2010). doi:10.1016/j.proeng.2010.03.059.

[143] R.A. Hardin, C. Beckermann, Prediction of the Fatigue Life of Cast Steel Containing Shrinkage Porosity, Metall. Mater. Trans. A. 40 (2009) 581–597. doi:10.1007/s11661-008-9755-3.

[144] R.L. Klueh, Elevated-Temperature Ferritic and Martensitic Steels and Their Application To Future Nuclear Reactor, Oak Ridge Natl. Lab. (2004).

[145] F.B. Pickering, Historical developments and microstructure of high chromium ferritic steels for high temperature applications, Inst. Mater. 667 (1997) 1–30.

[146] The Difference Between Casting & Forging, ATC Gr. (2018). http://www.atcgroup.com.au/CustomCastingForging/TheDifferenceBetweenCastingForging.aspx.

[147] OLYMPUS Stream Motion Image analysis software, (n.d.). https://www.olympus-ims.com/en/microscope/stream2/.

[148] Nanoimages, SEM Technology Overview – Scanning Electron Microscopy, (n.d.). http://www.nanoimages.com/sem-technology-overview/.

[149] Hitachi, Instruction Manual for Model S-4800 Field Emission Scanning Electron Microscope, 2002.

[150] NanoScience, How an SEM works, (n.d.). https://www.nanoscience.com/technology/sem-technology/how-sem-works/.

[151] AMMRF, Background information - What is energy dispersive X-ray spectroscopy?, (2014). http://www.ammrf.org.au/myscope/analysis/eds/.

[152] AMMRF, Transmission Electron Microscope Training module, n.d. doi:10.1007/978-1-4757-2519-3_1.

[153] T.P. Farragher, S. Scully, N.P. O'Dowd, C.J. Hyde, S.B. Leen, High Temperature, Low Cycle Fatigue Characterization of P91 Weld and Heat Affected Zone Material, J. Press. Vessel Technol. 136 (2014) 21403.

[154] A. Plumtree, H.A. Abdel-Raouf, Cyclic stress-strain response and substructure, Int. J. Fatigue. 23 (2001) 799–805. doi:10.1016/S0142-1123(01)00037-8.

[155] F. Ellyin, Fatigue damage, crack growth and life prediction, Springer Science & Business Media, 2012.

[156] S. Murakami, Continuum damage mechanics: a continuum mechanics approach to the analysis of damage and fracture, Springer Science & Business Media, 2012.

[157] F.C. Campbell, Fatigue and fracture: understanding the basics, ASM International, 2012.

[158] S. Suresh, Fatigue of Materials, Cambridge University Press, Cambridge, 1998. doi:10.1017/CBO9780511806575.

[159] C.T. Rueden, J. Schindelin, M.C. Hiner, ImageJ2: ImageJ for the next generation of scientific image data, (2017) 18:529.

[160] X. Wang, Q. Xu, S.M. Yu, L. Hu, H. Liu, Y.Y. Ren, Laves-phase evolution during aging in 9Cr-1.8W-0.5Mo-VNb steel for USC power plants, Mater. Chem. Phys. 163 (2015) 219–228. doi:10.1016/j.matchemphys.2015.07.032.

[161] F. Abe, Effect of Boron on Microstructure and Creep Strength of Advanced Ferritic Power Plant Steels, Procedia Eng. 10 (2011) 94–99.

[162] F. Abe, M. Tabuchi, S. Tsukamoto, T. Shirane, Microstructure evolution in HAZ and suppression of Type IV fracture in advanced ferritic power plant steels, Int. J.

Press. Vessel. Pip. 87 (2010) 598–604. doi:10.1016/j.ijpvp.2010.08.005.

[163] S.K. Albert, M. Kondo, M. Tabuchi, F. Yin, K. Sawada, F. Abe, Improving the creep properties of 9Cr-3W-3Co-NbV steels and their weld joints by the addition of boron, Metall. Mater. Trans. A. 36 (2005) 333–343.

[164] G. Golanski, S. Mrozinski, Low cycle fatigue and cyclic softening behaviour of martensitic cast steel, Eng. Fail. Anal. 35 (2013) 692–702. doi:10.1016/j.engfailanal.2013.06.019.

[165] B. Fournier, M. Sauzay, C. Caës, M. Mottot, M. Noblecourt, A. Pineau, Analysis of the hysteresis loops of a martensitic steel. Part II: Study of the influence of creep and stress relaxation holding times on cyclic behaviour, Mater. Sci. Eng. A. 437 (2006) 197–211. doi:10.1016/j.msea.2006.08.087.

[166] H.O. Stephens, R.I., Fatemi, A., Stephens, R.R., Fuchs, Metal fatigue in engineering, (2000).

[167] F. Ellyin, M. Asme, A Total Strain Energy Density Theory for Cumulative Fatigue Damage, (2013).

[168] X. Wang, W. Zhang, J. Gong, M.A. Wahab, Low cycle fatigue and creep fatigue interaction behavior of 9Cr-0.5Mo-1.8W-V-Nb heat-resistant steel at high temperature, J. Nucl. Mater. 505 (2018) 73–84. doi:10.1016/j.jnucmat.2018.03.055.

[169] B. Xiao, L. Xu, L. Zhao, H. Jing, Y. Han, Tensile mechanical properties, constitutive equations, and fracture mechanisms of a novel 9% chromium tempered martensitic steel at elevated temperatures, Mater. Sci. Eng. A. 690 (2017) 104–119. doi:10.1016/j.msea.2017.02.099.

[170] B. Xiao, L. Xu, L. Zhao, H. Jing, Y. Han, Y. Zhang, Creep properties, creep deformation behavior, and microstructural evolution of 9Cr-3W-3Co-1CuVNbB martensite ferritic steel, Mater. Sci. Eng. A. 711 (2018) 434–447. doi:10.1016/j.msea.2017.11.061.

[171] J. Lu, Material Characterisation and Finite Element Modelling of the Cyclic Plasticity Behaviour of Steels, PhD Thesis. (2015) Univ. Nottingham.

[172] F.C. Campbell, Fatigue and Fracture: Understanding the Basics, 2012. doi:10.1017/CBO9781107415324.004.

[173] M. Sauzay, H. Brillet, I. Monnet, M. Mottot, F. Barcelo, B. Fournier, A. Pineau, Cyclically induced softening due to low-angle boundary annihilation in a martensitic steel, Mater. Sci. Eng. A. 400 (2005) 241–244.

[174] M. Sauzay, B. Fournier, M. Mottot, A. Pineau, I. Monnet, Cyclic softening of

martensitic steels at high temperature—Experiments and physically based modelling, Mater. Sci. Eng. A. 483 (2008) 410–414.

[175] B. Fournier, M. Sauzay, C. Caës, M. Noblecourt, M. Mottot, A. Bougault, V. Rabeau, A. Pineau, Creep–fatigue–oxidation interactions in a 9Cr–1Mo martensitic steel. Part I: Effect of tensile holding period on fatigue lifetime, Int. J. Fatigue. 30 (2008) 649–662.

[176] G.C. Wood, The oxidation of iron-chromium alloys and stainless steels at high temperatures, Corros. Sci. 2 (1962) 173–196. doi:10.1016/0010-938X(62)90019-7.

[177] A.S. Khanna, P. Rodriguez, J.B. Gnanamoorthy, Oxidation kinetics, breakaway oxidation, and inversion phenomenon in 9Cr-1Mo steels, Oxid. Met. 26 (1986) 171–200. doi:10.1007/BF00659183.

[178] K. Salmenoja, R. Backman, K. Makela, Corrosion in bubbling fluidized bed boilers burning chlorine containing fuels, in: 8th Int. Symp. Corros. Pulp Pap. Ind., 1995: pp. 198–206.

[179] R.R. Ke, R. Alkire, Initiation of corrosion pits at inclusions on 304 stainless steel, J. Electrochem. Soc. 142 (1995) 4056–4062. doi:10.1149/1.2048462.

[180] H.P. Nielsen, F.J. Frandsen, K. Dam-Johansen, L.L. Baxter, Implications of chlorine-associated corrosion on the operation of biomass-fired boilers, Prog. Energy Combust. Sci. 26 (2000) 283–298. doi:10.1016/S0360-1285(00)00003-4.

[181] K. Yokokawa, O. Kanemaru, H. Miyazaki, T. Ohba, F. Abe, Effect of W-Mo balance on the creep deformation behavior of 9Ct steel, Curr. Adv. Mater. Precesses. 12 (1999) 439–439.

[182] G. Golański, C. Kolan, J. Jasak, Degradation of the Microstructure and Mechanical Properties of High-Chromium Steels Used in the Power Industry, Creep. (2018). doi:10.5772/intechopen.70552.

[183] J.D. Boerckel, D.E. Mason, A.M. McDermott, E. Alsberg, Microcomputed tomography: Approaches and applications in bioengineering, Stem Cell Res. Ther. 5 (2014) 1–12. doi:10.1186/scrt534.

[184] J.P. Kruth, M. Bartscher, S. Carmignato, R. Schmitt, L. De Chiffre, A. Weckenmann, Computed tomography for dimensional metrology, CIRP Ann. - Manuf. Technol. 60 (2011) 821–842. doi:10.1016/j.cirp.2011.05.006.

[185] D.M. Grogan, S.B. Leen, C.O.A. Semprimoschnig, C.M.Ó. Brádaigh, Damage characterisation of cryogenically cycled carbon fibre / PEEK laminates, Compos. Part A. 66 (2014) 237–250. doi:10.1016/j.compositesa.2014.08.007.

[186] C. Gupta, H. Toda, C. Schlacher, Y. Adachi, P. Mayr, C. Sommitsch, K. Uesugi, Y. Suzuki, A. Takeuchi, M. Kobayashi, Study of creep cavitation behavior in tempered martensitic steel using synchrotron micro-tomography and serial sectioning techniques, Mater. Sci. Eng. A. 564 (2013) 525–538. doi:10.1016/j.msea.2012.12.002.

[187] L. Salvo, P. Cloetens, E. Maire, S. Zabler, J.J. Blandin, W. Ludwig, E. Boller, D. Bellet, C. Josserond, X-ray micro-tomography an attractive characterisation technique in materials science, 200 (2003) 273–286.

[188] A. Isaac, K. Dzieciol, F. Sket, A. Borbély, In-situ microtomographic characterization of single-cavity growth during high-temperature creep of leaded brass, Metall. Mater. Trans. A Phys. Metall. Mater. Sci. 42 (2011) 3022–3030. doi:10.1007/s11661-011-0781-1.

[189] Private Communication, IMPEL Consortium, 2018.

[190] I. Cruz-Matías, D. Ayala, D. Hiller, S. Gutsch, M. Zacharias, S. Estradé, F. Peiró, Sphericity and roundness computation for particles using the extreme vertices model, J. Comput. Sci. 30 (2019) 28–40. doi:10.1016/j.jocs.2018.11.005.

[191] Z. Zhan, A study of creep-fatigue interaction in a new nickel-based superalloy, PhD Thesis. (2004) University of Portsmouth.

[192] J.P. Rouse, W. Sun, T.H. Hyde, A. Morris, Comparative assessment of several creep damage models for use in life prediction, Int. J. Press. Vessel. Pip. 108–109 (2013) 81–87. doi:10.1016/j.ijpvp.2013.04.012.

[193] C.J. Hyde, W. Sun, T.H. Hyde, J.P. Rouse, T. Farragher, N.P. O'Dowd, S.B. Leen, Cyclic Viscoplasticity Testing and Modeling of a Service-Aged P91 Steel, J. Press. Vessel Technol. 136 (2014) 44501. doi:10.1115/1.4026865.

[194] B. Fournier, M. Sauzay, A. Pineau, Micromechanical model of the high temperature cyclic behavior of 9-12%Cr martensitic steels, Int. J. Plast. 27 (2011) 1803–1816. doi:10.1016/j.ijplas.2011.05.007.

[195] P.F. Giroux, F. Dalle, M. Sauzay, C. Caës, B. Fournier, T. Morgeneyer, A.F. Gourgues-Lorenzon, Influence of strain rate on P92 microstructural stability during fatigue tests at high temperature, Procedia Eng. 2 (2010) 2141–2150. doi:10.1016/j.proeng.2010.03.230.

[196] J.R. Rice, D.M. Tracey, On the ductile enlargement of voids in triaxial stress fields, J. Mech. Phys. Solids. 17 (1969) 201–217.

[197] M. Yatomi, a. D. Bettinson, N.P. O'Dowd, K.M. Nikbin, Modelling of damage development and failure in notched-bar multiaxial creep tests, Fatigue Fract. Eng.

Mater. Struct. 27 (2004) 283–295. doi:10.1111/j.1460-2695.2004.00755.x.

[198] D.F. Socie, Multiaxial fatigue damage models, Trans. ASME. J. Eng. Mater. Technol. 109 (1987) 293–298.

[199] W.S. Sum, E.J. Williams, S.B. Leen, Finite element, critical-plane, fatigue life prediction of simple and complex contact configurations, Int. J. Fatigue. 27 (2005) 403–416. doi:10.1016/j.ijfatigue.2004.08.001.

[200] T.P. Farragher, S. Scully, N.P. O'Dowd, S.B. Leen, Thermomechanical Analysis of a Pressurized Pipe Under Plant Conditions, J. Press. Vessel Technol. 135 (2013) 11204.

[201] R.A. Barrett, T.P. Farragher, N.P. O'Dowd, P.E. O'Donoghue, S.B. Leen, Multiaxial cyclic viscoplasticity model for high temperature fatigue of P91 steel, Mater. Sci. Technol. 30 (2014) 67–74.

[202] A.L.M. Tobi, J. Ding, G. Bandak, S.B. Leen, P.H. Shipway, A study on the interaction between fretting wear and cyclic plasticity for Ti – 6Al – 4V, Wear. 267 (2009) 270–282. doi:10.1016/j.wear.2008.12.039.

[203] C.H. Goh, D.L. McDowell, R.W. Neu, Plasticity in polycrystalline fretting fatigue contacts, J. Mech. Phys. Solids. 54 (2006) 340–367. doi:10.1016/j.jmps.2005.06.009.

[204] A. Melander, A finite element study of short cracks with different inclusion types under rolling contact fatigue load, Int. J. Fatigue1. 19 (1997) 13–24.

[205] K. Zhang, J. Aktaa, Characterization and modeling of the ratcheting behavior of the ferritic-martensitic steel P91, J. Nucl. Mater. 472 (2016) 227–239. doi:10.1016/j.jnucmat.2015.10.050.

[206] H. Okamura, R. Ohtani, K. Saito, K. Kimura, R. Ishii, K. Fujiyama, S. Hongo, T. Iseki, H. Uchida, Basic investigation for life assessment technology of modified 9Cr-1Mo steel, Nucl. Eng. Des. 193 (1999) 243–254. doi:10.1016/S0029-5493(99)00181-8.

[207] J.L. Chaboche, G. Rousselier, On the Plastic and Viscoplastic Constitutive Equations—Part I: Rules Developed With Internal Variable Concept, J. Press. Vessel Technol. 105 (1983) 153. doi:10.1115/1.3264257.

[208] J.L. Chaboche, G. Rousselier, On the Plastic and Viscoplastic Constitutive Equations—Part II: Application of Internal Variable Concepts to the 316 Stainless Steel, J. Press. Vessel Technol. 105 (1983) 159. doi:10.1115/1.3264258.

[209] D.F. Li, R.A. Barrett, P.E. O'Donoghue, N.P. O'Dowd, S.B. Leen, A multi-scale crystal plasticity model for cyclic plasticity and low-cycle fatigue in a precipitate-

strengthened steel at elevated temperature, J. Mech. Phys. Solids. 101 (2017) 44–62. doi:10.1016/j.jmps.2016.12.010.

[210] R. Halama, J. Sedlák, M. Šofer, Phenomenological Modelling of Cyclic Plasticity, Numer. Model. 1 (2012) 329–354.

[211] G. Kang, Ratchetting : Recent progresses in phenomenon observation , constitutive modeling and application, Int. J. Fatigue. 30 (2008) 1448–1472. doi:10.1016/j.ijfatigue.2007.10.002.

[212] M. Yaguchi, Y. Takahashi, Ratchetting of viscoplastic material with cyclic softening, part 2: application of constitutive models, Int. J. Plast. 21 (2005) 43–65. doi:10.1016/j.ijplas.2004.02.001.

[213] M. Abdel-Karim, N. Ohno, Kinematic hardening model suitable for ratchetting with steady-state, Int. J. Plast. 16 (2000) 225–240. doi:10.1016/S0749-6419(99)00052-2.

[214] N. Ohno, J.D. Wang, Kinematic hardening rules with critical state of dynamic recovery, part I: formulation and basic features for ratchetting behavior, Int. J. Plast. 9 (1993) 375–390. doi:10.1016/0749-6419(93)90042-O.

[215] P. Church, The effect of stress triaxiality and strain-rate on the fracture characteristics of ductile metals, J. Mater. Sci. 31 (1996) 453–461.

[216] O.S. Hopperstad, T. Børvik, M. Langseth, K. Labibes, C. Albertini, On the influence of stress triaxiality and strain rate on the behaviour of a structural steel . Part I . Experiments, Eur. J. Mech. 22 (2003) 15–32. doi:10.1016/S0997-7538(02)00006-2.

[217] T. Børvik, O.S. Hopperstad, T. Berstad, On the influence of stress triaxiality and strain rate on the behaviour of a structural steel . Part II . Numerical study, Eur. J. Mech. 22 (2003) 15–32. doi:10.1016/S0997-7538(02)00005-0.

[218] J. Lemaitre, J.P. Sermage, One damage law for different mechanisms, Comput. Mech. 20 (1997) 84–88. doi:10.1007/s004660050221.

[219] J. Lemaitre, J.P. Sermage, R. Desmorat, A two scale damage concept applied to fatigue, Int. J. Fract. 97 (1999) 67-81–81. doi:10.1023/A:1018641414428.

[220] Common difficulties associated with contact modeling in Abaqus/Standard, (n.d.). http://bobcat.nus.edu.sg:2080/English/SIMACAEITNRefMap/simaitn-c-contacttrouble.htm (accessed January 27, 2019).

[221] B. Polomski, R. Vanstone, R. Leese, Roberts, S, Continuous Development of MARBN Steel through Full-size component manufacture, in: 9th Int. Charles Parsons Turbine Gener. Conf., 2015.

[222] I. Koutiri, D. Bellett, F. Morel, E. Pessard, A probabilistic model for the high cycle fatigue behaviour of cast aluminium alloys subject to complex loads, Int. J. Fatigue. 47 (2013) 137–147. doi:10.1016/j.ijfatigue.2012.08.004.

[223] V. Le, F. Morel, D. Bellett, E. Pessard, N. Saintier, P. Osmond, Microstructural-based analysis and modelling of the fatigue behaviour of cast Al-Si alloys, Procedia Eng. 133 (2015) 562–575. doi:10.1016/j.proeng.2015.12.630.

[224] A. Gupta, S. Goyal, K.A. Padmanabhan, A.K. Singh, Inclusions in steel: micro–macro modelling approach to analyse the effects of inclusions on the properties of steel, Int. J. Adv. Manuf. Technol. 77 (2015) 565–572. doi:10.1007/s00170-014-6464-5.

[225] S. Romano, A. Brückner-Foit, A. Brandão, J. Gumpinger, T. Ghidini, S. Beretta, Fatigue properties of AlSi10Mg obtained by additive manufacturing: Defect-based modelling and prediction of fatigue strength, Eng. Fract. Mech. 187 (2018) 165–189. doi:10.1016/j.engfracmech.2017.11.002.

[226] D.M. Grogan, C.M.Ó. Brádaigh, S.B. Leen, A combined XFEM and cohesive zone model for composite laminate microcracking and permeability, Compos. Struct. 120 (2015) 246–261. doi:10.1016/j.compstruct.2014.09.068.

[227] T.P. Farragher, S. Scully, N.P. O'Dowd, S.B. Leen, Development of life assessment procedures for power plant headers operated under flexible loading scenarios, Int. J. Fatigue. 49 (2013) 50–61.

[228] D.M. Grogan, C.M.Ó. Brádaigh, J.P. Mcgarry, S.B. Leen, Damage and permeability in tape-laid thermoplastic composite cryogenic tanks, Compos. Part A. 78 (2015) 390–402. doi:10.1016/j.compositesa.2015.08.037.

[229] J. Lu, W. Sun, A. Becker, Material characterisation and finite element modelling of cyclic plasticity behaviour for 304 stainless steel using a crystal plasticity model, Int. J. Mech. Sci. 105 (2016) 315–329. doi:10.1016/j.ijmecsci.2015.11.024.

[230] M. Li, R.A. Barrett, S. Scully, N.M. Harrison, S.B. Leen, P.E. O'Donoghue, Cyclic plasticity of welded P91 material for simple and complex power plant connections, Int. J. Fatigue. 87 (2016) 391–404. doi:10.1016/j.ijfatigue.2016.02.005.

[231] C.J. Hyde, W. Sun, T.H. Hyde, An investigation of the failure mechanisms in high temperature materials subjected to isothermal and anisothermal fatigue and creep conditions, Procedia Eng. 10 (2011) 1157–1162. doi:10.1016/j.proeng.2011.04.192.

[232] T.P. Farragher, C.J. Hyde, W. Sun, T.H. Hyde, N.P. O'Dowd, S. Scully, S.B. Leen, High temperature low cycle fatigue behaviour of service-aged P91 material, in: 9th Int. Conf. Creep Fatigue Elev. Temp. IOM3, London, UK, 2012.

[233] P. Mac Ardghail, R.A. Barrett, N. Harrison, S.B. Leen, Predictions of ICHAZ Cyclic Thermo-Mechanical Response in GTAW Process for 9Cr Steels, in: ASME 2017 Press. Vessel. Pip. Conf., 2017: p. V06AT06A080-V06AT06A080.

[234] P. Mac Ardghail, N. Harrison, S.B. Leen, Through-process modelling of welding and service of 9Cr steel power plant components under load-following conditions, MATEC Web Conf. 165 (2018) 1–8. doi:10.1051/matecconf/201816521010.